

## **INFORMATION TO USERS**

**This manuscript has been reproduced from the microfilm master. UMI films the text directly from the original or copy submitted. Thus, some thesis and dissertation copies are in typewriter face, while others may be from any type of computer printer.**

**The quality of this reproduction is dependent upon the quality of the copy submitted. Broken or indistinct print, colored or poor quality illustrations and photographs, print bleedthrough, substandard margins, and improper alignment can adversely affect reproduction.**

**In the unlikely event that the author did not send UMI a complete manuscript and there are missing pages, these will be noted. Also, if unauthorized copyright material had to be removed, a note will indicate the deletion.**

**Oversize materials (e.g., maps, drawings, charts) are reproduced by sectioning the original, beginning at the upper left-hand corner and continuing from left to right in equal sections with small overlaps.**

**Photographs included in the original manuscript have been reproduced xerographically in this copy. Higher quality 6" x 9" black and white photographic prints are available for any photographs or illustrations appearing in this copy for an additional charge. Contact UMI directly to order.**

**ProQuest Information and Learning  
300 North Zeeb Road, Ann Arbor, MI 48106-1346 USA  
800-521-0600**

**UMI<sup>®</sup>**



**University of Alberta**

***Microstructural Characterization of Microalloyed Linepipe Steels***

by

***Udit Sharma*** ©

A thesis submitted to the Faculty of Graduate Studies and Research in  
partial fulfillment of the requirements for the degree of *Master of Science*

in

***Materials Engineering***

**Department of Chemical and Materials Engineering**

**Edmonton, Alberta, CANADA**

***Spring, 2001***



**National Library  
of Canada**

**Acquisitions and  
Bibliographic Services**

**395 Wellington Street  
Ottawa ON K1A 0N4  
Canada**

**Bibliothèque nationale  
du Canada**

**Acquisitions et  
services bibliographiques**

**395, rue Wellington  
Ottawa ON K1A 0N4  
Canada**

*Your file Votre référence*

*Our file Notre référence*

**The author has granted a non-exclusive licence allowing the National Library of Canada to reproduce, loan, distribute or sell copies of this thesis in microform, paper or electronic formats.**

**The author retains ownership of the copyright in this thesis. Neither the thesis nor substantial extracts from it may be printed or otherwise reproduced without the author's permission.**

**L'auteur a accordé une licence non exclusive permettant à la Bibliothèque nationale du Canada de reproduire, prêter, distribuer ou vendre des copies de cette thèse sous la forme de microfiche/film, de reproduction sur papier ou sur format électronique.**

**L'auteur conserve la propriété du droit d'auteur qui protège cette thèse. Ni la thèse ni des extraits substantiels de celle-ci ne doivent être imprimés ou autrement reproduits sans son autorisation.**

0-612-69409-7

**Canada**

# University of Alberta

## Library Release Form

Name of Author: **Udit Sharma**

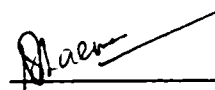
Title of Thesis: **Microstructural Characterization of Microalloyed Linepipe Steels**

Degree: **Master of Science**

Year this Degree Granted: **2001**

Permission is hereby granted to the University of Alberta Library to reproduce single copies of this thesis and to lend or sell such copies for private, scholarly or scientific research purposes only.

The author reserves all other publication and other rights in association with the copyright in this thesis, and except as herein before provided, neither the thesis nor any substantial portion thereof may be printed or otherwise reproduced in any material form whatever without the author's prior written permission.



Udit Sharma  
c/o Dr. S.K. Sharma  
M-9, Indra Nagar,  
Kanpur, 208026  
INDIA

Date: March 7/01

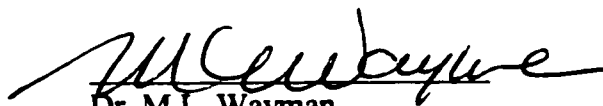
University of Alberta

Faculty of Graduate Studies and Research

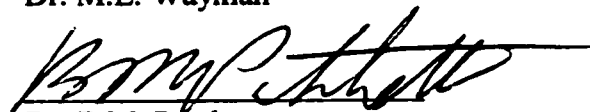
The undersigned certify that they have read, and recommend to the Faculty of Graduate Studies and Research for acceptance, a thesis entitled **Microstructural Characterization of Microalloyed Linepipe Steels** submitted by **Udit Sharma** in partial fulfillment of the requirements for the degree of **Master of Science in Materials Engineering**.



Dr. D.G. Ivey (Supervisor)



Dr. M.L. Wayman



Dr. B.M. Patchett



Dr. A. Meldrum

*October 6, 2000*

## **Abstract**

The aim of this study was to characterize the microstructure of microalloyed linepipe steels. The steels investigated were X70 (0.04 wt% C - 0.02 wt% Ti - 0.07 wt% Nb), X80 (0.04 wt% C - 0.025 wt% Ti - 0.09 wt% Nb) and Grade80 (0.06wt%C - 0.028wt%Ti – 0.09wt%Nb) steel. The present study focused on phase identification and quantification, distribution of alloying elements and inclusions and segregation effects. The steels were primarily composed of a mixed ferrite structure, i.e., polygonal ferrite and acicular ferrite/bainitic ferrite, with characteristic low angle grain boundaries and high dislocation densities. Pockets of retained austenite, exhibiting a Kurdjumov-Sachs orientation relationship (KS-OR) with the adjoining ferrite, were found in both steels.

Five general classes of precipitates were identified in all three steels: 1) Very large (2-10  $\mu\text{m}$ ) cuboidal TiN particles nucleated on inclusions; 2) large (0.1–1.0  $\mu\text{m}$ ) cuboidal TiN particles; 3) medium sized (30-50nm), irregular shaped Nb-Ti carbonitrides; 4) fine (<20nm), rounded precipitates of Nb carbonitrides with traces of Mo; 5) very fine dispersed precipitates (<5 nm in size).

Inclusion content and morphology were analyzed. The inclusions in X70 steels were found to be primarily CaS with significant amounts of Al, O, Ti, Fe and Mn. They were essentially spherical in shape with small elliptical distortions along the rolling direction and across the width of the plate. The morphology of the inclusions in the X80 steel was very similar; however, they showed higher Mn levels. The Grade80 steel showed stringers of MnS at the centerline, in addition to the Ca-Mn-S rounded inclusions.

## **Acknowledgements**

I would like to gratefully acknowledge Dr. Douglas Ivey for his supervision, guidance and encouragement throughout my program. He has been a constant source of inspiration and help throughout all these years and continues to do so. Indeed, I am deeply indebted to him.

Thanks also go to everyone else in the group who have extended their advice and co-operation. My discussions with Siamak –Akhlaghi and Jeff Bulger provided many ideas that I later incorporated into my thesis.

Dr. B.M. Patchett's, Dr. L.E. Collins' and Rob Mackenzie's suggestions were highly useful and my thanks to them.

Special thanks are extended to Tina Barker and John Malinski for help with SEM analysis and TEM work.

I wish to thank Wenzhen Sun for her constant support and invaluable advice. Her help is much appreciated.

Finally, I wish to acknowledge IPSCO Inc. and Natural Sciences and Engineering Research Council of Canada for funding this work.

# Table of Contents

<b>1</b>	<b>Introduction.....</b>	<b>1</b>
<b>2</b>	<b>Literature Survey.....</b>	<b>4</b>
2.1	Introduction.....	4
2.2	Development of Microalloyed Steels.....	5
2.2.1	<i>Factors Leading to Initial Development of the Microalloyed Steels....</i>	<i>6</i>
2.3	Microstructure of Microalloyed Steels.....	12
2.3.1	<i>Early Ferritic-Pearlitic Steels.....</i>	<i>12</i>
2.3.2	<i>Dual Phase Steels.....</i>	<i>14</i>
2.3.3	<i>Multiphase Steels.....</i>	<i>15</i>
2.3.4	<i>Ultra Low Carbon Sheet Steels.....</i>	<i>17</i>
2.4	Precipitates in Microalloyed Steels.....	19
2.5	Characterization of Precipitates.....	22
2.5.1	<i>Optical Metallography.....</i>	<i>22</i>
2.5.2	<i>SEM Characterization.....</i>	<i>23</i>
2.5.3	<i>TEM Characterization.....</i>	<i>25</i>
2.5.4	<i>High Resolution Electron Microscopy (HREM) Analysis of Precipitates.....</i>	<i>27</i>
2.5.5	<i>EELS for Identifying Precipitate Composition.....</i>	<i>28</i>
2.5.6	<i>Extraction of Precipitates by Electrochemical Means and Their Analysis by X-ray Diffraction.....</i>	<i>29</i>
2.6	Role of Alloying Elements in Microalloyed Steels.....	31

2.6.1	<i>Niobium (0-1%)</i> .....	31
2.6.2	<i>Titanium (0-0.3%)</i> .....	32
2.6.3	<i>Vanadium (0-0.05%)</i> .....	32
2.6.4	<i>Molybdenum (0-0.3%)</i> .....	33
2.6.5	<i>Chromium (0-0.3%)</i> .....	33
2.6.6	<i>Boron (10-20ppm)</i> .....	33
2.6.7	<i>Manganese (1-2%)</i> .....	34
2.7	Effect of Microalloying Elements on Mechanical Properties.....	34
2.8	Structural Aspects of Alloy Carbonitride Precipitation in Microalloyed Steels.....	36
2.8.1	<i>Interphase Precipitation Planar: IPP</i> .....	37
2.8.2	<i>Interphase Precipitation Curved: IPC - Irregular</i> .....	38
2.8.3	<i>Interphase Precipitation Curved: IPC - Regular</i> .....	38
2.8.4	<i>Interphase Precipitation Random: IPR</i> .....	39
2.8.5	<i>Interphase Precipitation Fibrous: IPF</i> .....	40
2.9	Inclusions in Steels.....	41
2.9.1	<i>Effect of Inclusions on Properties of Steels</i> .....	41
2.9.2	<i>Control of Inclusions in Steels</i> .....	45
2.10	Line Pipe Steels.....	50
2.10.1	<i>Nomenclature</i> .....	51
2.10.2	<i>Manufacture of Line-pipe Steel</i> .....	51
2.11	Pipemaking.....	54
2.11.1	<i>U-O-E Process</i> .....	54

2.11.2	<i>Spiral Welded Pipe</i> .....	54
2.12	Controlled Rolling.....	57
2.12.1	<i>Stages in Controlled Rolling of Microalloyed Steels</i> .....	58
2.13	Accelerated Cooling.....	61
2.13.1	<i>Effects of Accelerated Cooling on Strength of Microalloyed Plate</i> .....	61
2.13.2	<i>Effect of Accelerated Cooling on the Toughness of Microalloyed Plate</i> .....	64
2.14	Steckel Mills.....	65
2.14.1	<i>Characteristics of Rolling in a Steckel Mill</i> .....	65
2.14.2	<i>Control Systems in a Steckel Mill</i> .....	66
2.15	Types of Linepipe Steels.....	68
2.15.1	<i>Ferrite-Pearlite Steels</i> .....	69
2.15.2	<i>Bainite/Acicular Ferrite Steels</i> .....	70
2.15.3	<i>Multiphase Steels</i> .....	70
2.16	Practical Pipeline Steels.....	71
<b>3</b>	<b>Experimental</b> .....	<b>73</b>
3.1	Materials analyzed.....	73
3.2	Sample Preparation and Instruments Used.....	76
3.2.1	<i>Optical Metallography</i> .....	76
3.2.2	<i>Scanning Electron Microscopy (SEM)</i> .....	78
3.2.3	<i>Transmission Electron Microscopy (TEM): Thin Foils</i> .....	78
3.2.4	<i>TEM-Carbon Extraction Replicas</i> .....	80

<b>4</b>	<b>X70 Steels: Results.....</b>	<b>81</b>
4.1	Introduction.....	81
4.2	Grain Structure.....	81
4.3	Inclusions in X70 Steel.....	91
4.4	Precipitates in X70 Steel.....	98
4.4.1	<i>Very Large TiN Precipitates (2-10<math>\mu</math>m).....</i>	<i>98</i>
4.4.2	<i>Large Cuboidal Precipitates (0.1-1.0<math>\mu</math>m).....</i>	<i>101</i>
4.4.3	<i>Medium Sized Irregular Shaped Precipitates (30-50nm).....</i>	<i>104</i>
4.4.4	<i>Small Spherical Precipitates ( &lt;20nm).....</i>	<i>106</i>
4.4.5	<i>Very Small Precipitates (&lt;5nm).....</i>	<i>108</i>
<b>5</b>	<b>X80 Steels: Results.....</b>	<b>110</b>
5.1	Introduction.....	110
5.2	Grain Structure.....	110
5.3	Inclusions in X80 Steel.....	118
5.4	Precipitates in X80 Steel.....	125
5.4.1	<i>Very Large TiN Precipitates (2-10<math>\mu</math>m).....</i>	<i>125</i>
5.4.2	<i>Large Cuboidal Precipitates (0.1-1.0<math>\mu</math>m).....</i>	<i>127</i>
5.4.3	<i>Medium Sized Irregular Shaped Precipitates (30-50nm).....</i>	<i>129</i>
5.4.4	<i>Small Spherical Precipitates ( &lt;20nm).....</i>	<i>130</i>
5.4.5	<i>Very Small Precipitates (&lt;5nm).....</i>	<i>131</i>

<b>6</b>	<b>Grade80 Steels: Results.....</b>	<b>132</b>
6.1	Introduction.....	132
6.2	Grain Structure.....	132
6.3	Inclusions in Grade Steel.....	139
6.4	Precipitates in Grade80 Steel.....	147
6.4.1	<i>Very Large TiN Precipitates (2-10<math>\mu</math>m).....</i>	<i>147</i>
6.4.2	<i>Large Cuboidal Precipitates (0.1-1.0<math>\mu</math>m).....</i>	<i>148</i>
6.4.3	<i>Medium Sized Irregular Shaped Precipitates (30-50nm).....</i>	<i>150</i>
6.4.4	<i>Small Spherical Precipitates ( &lt;20nm).....</i>	<i>151</i>
6.4.5	<i>Very Small Precipitates (&lt;5nm).....</i>	<i>153</i>
<b>7</b>	<b>Results and Discussions.....</b>	<b>154</b>
7.1	Introduction.....	154
7.2	Thermomechanical Processing.....	154
7.3	Grain Structure.....	156
7.4	Segregation Effects.....	163
7.5	Inclusions.....	166
7.6	Precipitates.....	168
7.6.1	<i>Very Large TiN Precipitates (2-10<math>\mu</math>m).....</i>	<i>168</i>
7.6.2	<i>Large TiN Precipitates (0.1-1.0<math>\mu</math>m).....</i>	<i>170</i>
7.6.3	<i>Nb-rich Irregularly Shaped Precipitates (30-50nm).....</i>	<i>172</i>
7.6.4	<i>Small Spherical Precipitates (&lt;20nm).....</i>	<i>173</i>

7.6.5	<i>Very Small Precipitates (&lt;5nm)</i> .....	174
7.7	Mechanical Properties.....	175
<b>8</b>	<b>Conclusions</b> .....	<b>177</b>
<b>9</b>	<b>Future Work</b> .....	<b>181</b>
	<b>References</b> .....	<b>184</b>
	<b>Appendix A</b> .....	<b>195</b>

## List of Tables

Table 2-1	Typical chemical composition of ferrite-pearlite microalloyed steels (in wt%) [Kim83].....	13
Table 2-2	Typical chemical composition of dual phase microalloyed steel (in wt%) [Kim83].....	15
Table 2-3	Typical chemical composition of multiphase microalloyed steel (in wt%) [Kim83][DeArdo95].....	16
Table 2-4	Typical chemical composition of ULC sheet steel (in wt%) [DeArdo95].....	18
Table 3-1	Chemical composition of steels analyzed (in wt%).....	75
Table 3-2	Mechanical properties of steels analyzed.....	75
Table 3-3	Etchants used for optical metallographic examination.....	76
Table 3-4	Operating parameters for electrojet polishing.....	79
Table 4-1	Grain size as an average intercept length.....	83
Table 4-2	Aspect ratio of grains in X70 steel along the LS orientation.....	84
Table 4-3	Size and density distribution of TiN precipitates across the thickness of X70 plate.....	101
Table 5-1	Grain size as average intercept length.....	112
Table 5-2	Aspect ratio of grains for X80 steel along the LS orientation.....	113
Table 5-3	Density and size distribution of TiN precipitates across the thickness of X80 plate.....	127
Table 6-1	Grain size as average intercept length for Grade80 steel in LS orientation.....	135

Table 6-2	Aspect ratio of grains for Grade80 steel along the LS orientation.....	136
Table 6-3	Size and number distribution of TiN precipitates across the thickness of Grade80 plate.....	148
Table 7-1	Processing parameters for the three grades of steel.....	155
Table 7-2	Comparison of deformation and cooling rates for different grades of steel.....	158
Table 7-3	Distribution of grain size and grain shape across the thickness of the plate.....	162
Table 7.4	Distribution of MAC islands in the three grades of steels.....	164
Table 7.5	Distribution of 'pearlite-like' microstructure in the three grades of steels.....	165
Table 7-6	Characteristics of inclusions in the various grades of steel.....	167
Table 7-7	Distribution of large (2-10 $\mu$ m) TiN precipitates.....	169
Table 7-8	Density, size and volume fraction of precipitates in X70 and X80.....	172

## List of Figures

Figure 2-1	Development of microalloyed steels [Gladman97].....	11
Figure 2-2	Optical micrograph showing the typical microstructure of ferrite-pearlite microalloyed steel. Lighter areas: polygonal ferrite, darker areas: pearlite [Collins83].....	13
Figure 2-3	Optical micrograph showing microstructure of dual phase steels. Martensite islands surrounded by ferrite grains. [Kot-Bramfitt81].....	15
Figure 2-4	Microstructure of multiphase steel a) optical micrograph shows non-equiaxed grain structure. b) TEM BF image shows presence of acicular grains of ferrite [Collins83].....	17
Figure 2-5	Ti <sub>4</sub> S <sub>2</sub> C <sub>2</sub> type precipitates in ULC steels [DeArdo95].....	18
Figure 2-6	Temperature dependence of precipitation and dissolution of microalloy carbonitrides [Sage83].....	19
Figure 2-7	Solubility of carbides, nitrides of Ti, Nb and V in steel [Sellars84].....	20
Figure 2-8	Optical micrograph of precipitates in a 0.06C-0.03Nb-0.015Ti microalloyed steel. Only the larger precipitates are visible [Zhou96].....	23
Figure 2-9	SEM micrograph of square precipitates along the grain boundary of a boron microalloyed steel [Juarez-Islas94].....	24
Figure 2-10	a) SEM micrograph showing a TiN precipitate with a core of CaS.	

	b) Corresponding concentration profile across the precipitate [Saikaly99].....	24
Figure 2-11	TEM BF micrographs showing interaction of carbonitride precipitates with dislocations in a thin foil steel sample [Wellner81].....	26
Figure 2-12	TEM micrographs of precipitates of various size range and morphologies as observed by the carbon replica method [Feng89][Lehtinen89] [Kestenbach89].....	26
Figure 2-13	a) Titanium nitride precipitate observed on carbon replica. b) Corresponding electron diffraction pattern (fcc TiN – zone axis [110]) and c) EDX spectrum [Saikaly99].....	27
Figure 2-14	HREM image obtained from a large precipitate. The value measured from the interplanar distance corresponds to $\cong 0.36\text{nm}$ [Juarez- Islas94].....	28
Figure 2-15	PEELS spectrum of a titanium carbonitride from a carbon replica. The carbon and nitrogen peaks are widely separated and easily identifiable [Saikaly99].....	29
Figure 2-16	a) The slime cell for collection of precipitates by dissolution of metal matrix, b) Flow chart of the chemical treatment of the slime [Read90].....	30
Figure 2-17	X-ray diffraction spectrum from the residue. The accompanying table of lattice parameters identifies the residue as consisting mainly of NbC [Read90].....	30

Figure 2-18	Interphase precipitation planar (IPP) in a V steel [Smith88].....	37
Figure 2-19	Curved irregularly spaced sheets of precipitates in a microalloyed steel illustrating the ‘Interphase precipitation curved-irregular’ mode of precipitation [Smith88].....	38
Figure 2-20	a) Schematic depicting the ‘Quasi-ledge model’ of precipitation, b) CDF image of V(C,N) showing IPC (regular) dispersion in V steel [Smith88].....	39
Figure 2-21	a) and b) Schematic illustrating the uncoordinated and coordinated pinning of the $\alpha/\gamma$ interface by carbonitride precipitates, c) CDF image of Nb(C,N) precipitates with apparent random dispersion in a Nb steel [Smith88].....	40
Figure 2-22	Effect of S on CVN shelf energy absorption in a Si-Al killed 0.19C-1.2Mn hot-rolled steel [Nicholson86].....	43
Figure 2-23	Deformation in converting the plate to expanded pipe [Sage83].....	50
Figure 2-24	U-O-E process of pipemaking.....	54
Figure 2-25	Spiral submerged metal arc welding (SMAW) pipemaking.....	55
Figure 2-26	Schematic of production of microalloyed line pipe.....	56
Figure 2-27	CCT diagram of a typical microalloyed steel [Collins85].....	62
Figure 2-28	Schematic depicting the typical setup of a Steckel mill 1. Crop shear and entry side guides; 2. Drum type crop shear; 3. Coiler furnace; 4. 4-high reversing stand; 5. Laminar cooling section [Kramer97] .....	67

Figure 3-1	Sketch showing the relationship between rolling direction and pipe axis in a spiral welded pipe.....	74
Figure 3-2	Schematic showing the various orientations examined.....	74
Figure 3-3	Schematic showing preparation of thin foil samples for transmission electron microscopy.....	79
Figure 3-5	Extraction of precipitates by the carbon replica method.....	80
Figure 4-1	Optical micrograph of X70 steel, etched with nital, showing mixed grain structure consisting of polygonal ferrite (PF) and acicular ferrite (AF).....	82
Figure 4-2	Grain structure of X70 steel in an optical microscope, a) near the center , X70-LS-mid; and b) near the surface, X70-LS-top (etched with nital).....	82
Figure 4-3	Schematic showing calculation of grain size through average intercept length of random lines.....	83
Figure 4-4	Measurement of aspect ratio of grains by comparing the average intercept length of grains along the rolling direction and perpendicular to it.....	84
Figure 4-5	Optical micrograph of X70 steel along the rolling direction, showing segregation (darker areas) at the centerline. The sample was etched with 2% nital.....	85
Figure 4-6	Optical micrographs of X70 steel etched with modified LaPera's etch showing the presence of martensite austenite constituent (MAC) as tiny white islands in the ferrite matrix (tan).....	86

Figure 4-7	Secondary electron SEM micrographs of X70 steel etched with picral, a) showing the presence of pearlite like constituent at grain boundaries of ferrite. b) martensitic areas.....	87
Figure 4-8	Optical micrographs of X70 steel etched with picral showing distribution of this pearlite like microstructure at c) near the centerline and d) near the surface of plate.....	87
Figure 4-9	a) TEM bright field (BF) image from a thin foil of X70 steel showing elongated, acicular grains with low angle grain boundaries. The matrix is composed primarily of bcc ferrite. b) Selected area diffraction (SAD) pattern from region shown in a).....	88
Figure 4-10	a) TEM BF image of thin foil from X70 showing ferrite grains possessing high dislocation density. b) Small precipitates nucleated on dislocations.....	89
Figure 4-11	a) BF image from X70 steel showing a cluster of ferrite grains surrounding a grain of austenite (no.4), b) SAD pattern from grain 1( $\alpha$ ) and 4( $\gamma$ ). c) Indexed pattern of one shown in b).....	90
Figure 4-12	a) Rounded non-metallic inclusions in X70 steel. b) Some inclusions acted as nucleation site for TiN cuboidal precipitates. c) EDX spectrum from one of the larger inclusions. Fe is mainly from the matrix.....	92
Figure 4-13	Planar intercept area of inclusions in X70 steel along the LS orientation.....	94

Figure 4-14	Planar intercept area of inclusions in X70 steel along the ST orientation.....	95
Figure 4-15	Aspect ratio of inclusions in X70 steel along the LS orientation.....	96
Figure 4-16	Aspect ratio of inclusions in X70 steel along the ST orientation.....	97
Figure 4-17	Optical micrograph of X70 LS mid etched in nital, showing faceted and cuboidal, copper colored TiN precipitates.....	98
Figure 4-18	a) Back scattered electron (BSE) SEM micrograph of a cuboidal precipitates in X70 showing a dark particle at the center. b) EDX spectrum from the shell. c) EDX spectrum from particle in the center.....	99
Figure 4-19	Counting the size and number of very large TiN precipitates through the random intercept method.....	100
Figure 4-20	a) TEM BF image from a carbon replica showing 2 large cuboidal precipitates in X70. b) SAD pattern from the larger cuboid shows it to be fcc NaCl-type. c) EDX spectrum from the same precipitate shows it to be Ti rich, with some Nb.....	102
Figure 4-21	a) TEM BF image of a large cuboidal precipitate in X70. b) SAD pattern identifying it as fcc NaCl type. c)-f) Composition profiles from various positions of the precipitate as marked in a).....	103
Figure 4-22	a) TEM BF of an irregular shaped precipitate in X70, b) DP identifies it to be fcc, NaCl type, lattice parameter close to NbC, c) EDX indicated presence of Nb with Ti.....	104

Figure 4-23	Distribution of cuboidal (0.1-1.0 $\mu$ m) and irregular shaped (30-50nm) precipitates in a ferrite grain.....	105
Figure 4-24	a) TEM DF image of small spherical precipitates in X70 steel. b) Ring diffraction pattern from a cluster of precipitates. c) EDX spectrum from a group of precipitates .....	107
Figure 4-25	a) TEM DF image of thin foil sample of X70 showing small precipitates along a line. b) SAD pattern from central ferrite grain in (a), showing extra spots near the central spot. The spot used for obtaining the DF image is encircled.....	108
Figure 5-1	Optical micrograph of X80 steel etched with 2% nital, showing acicular/ferritic (AF) grain structure with mixed grain size. Small regions of polygonal ferrite (PF) are also visible.....	111
Figure 5-2	Grain structure of X80 steel in an optical microscope, a) near the center , X80-LS-mid; and b) near the surface, X80-LS-top (etched with nital).....	111
Figure 5-3	Optical micrograph of X80 steel etched with 2% nital, along the rolling direction, showing no segregation at the centerline. Some TiN cuboidal precipitates are visible.....	113
Figure 5-4	Optical micrographs of X80 steel etched with modified LaPera's etch showing the presence of martensite austenite constituent (MAC) as tiny white islands in the ferrite matrix (tan).....	115

<b>Figure 5-5</b>	<b>Optical micrographs of X80 LS steel etched with picral showing distribution of pearlite like microstructure at a) near the centerline and b) near the surface of plate.....</b>	<b>116</b>
<b>Figure 5-6</b>	<b>TEM BF image from a thin foil sample of X80 steel showing the presence of a polygonal ferrite grain with many smaller subgrains in it. The adjoining SAD patterns show that the subgrains are separated by low angle grain boundaries (<math>\sim 2^\circ</math>).....</b>	<b>117</b>
<b>Figure 5-7</b>	<b>a) Secondary electron SEM micrograph of a spherical non-metallic inclusions in X80 steel, b) EDX spectrum from it shows the inclusion to be consisting mainly of Ca,Mn and S with Ti, Al, Mg, Mn. Fe is from the matrix.....</b>	<b>118</b>
<b>Figure 5-8</b>	<b>Polished and unetched X80 steel in the LS orientation depicting the size and distribution of non-metallic, Ca-Mn-S inclusions.....</b>	<b>119</b>
<b>Figure 5-9</b>	<b>Planar intercept area of inclusions in X80 steel along the LS orientation.....</b>	<b>121</b>
<b>Figure 5-10</b>	<b>Planar intercept area of inclusions in X80 steel along the ST orientation.....</b>	<b>122</b>
<b>Figure 5-11</b>	<b>Aspect ratio of inclusions in X80 steel along the LS orientation.....</b>	<b>123</b>
<b>Figure 5-12</b>	<b>Aspect ratio of inclusions in X80 steel along the ST orientation.....</b>	<b>124</b>
<b>Figure 5-13</b>	<b>TiN cuboidal precipitate in X80 steel with a non-metallic inclusion at its interior and another attached to its side.....</b>	<b>125</b>

Figure 5-14	a) Secondary electron SEM micrograph of a TiN cuboidal precipitate with inclusions attached to the sides, b)-d) EDX from the various areas as marked in a).....	126
Figure 5-15	Large cuboidal precipitates in X80 associated with a second particle growing epitaxially from one of the edges: a) Irregularly shaped second particle. b) Faceted second particle.....	128
Figure 5-16	EDX spectra from the large precipitates in X80 steel (Figure 5-15a). a) Larger, cuboidal particle which is richer in Ti and b) smaller irregularly shaped particle richer in Nb.....	128
Figure 5-17	SAD pattern from the pair of precipitates from Figure 5-16b. The crystallographic orientation is the same with a slight mismatch in d spacing as shown. The outer spots are from TiN and inner from NbC. The rings are from the amorphous carbon film supporting the precipitates.....	129
Figure 5-18	TEM BF image of X80 carbon replica showing irregular shaped, Nb rich precipitates at the grain boundaries and within the ferrite grains.....	130
Figure 5-19	TEM BF micrograph of carbon replica from X80 steel showing presence of small (<10nm), spherical precipitates of NbC in the matrix.....	131
Figure 5-20	TEM BF image from thin foil X80 showing extremely small (<5nm) precipitates spread throughout the grain and at grain boundary.....	131

Figure 6-1	Optical micrograph of Grade80 steel in LS orientation, etched with nital, showing the typical grain structure. Some areas appear as massive lath shaped with poorly defined substructure, as pointed out by the upper arrow. The dark spherical particles are the non-metallic inclusions present in the steel.....	133
Figure 6-2	Secondary electron SEM micrograph of Grade80 steel showing subgrains in a large grain, as marked by the line.....	134
Figure 6-3	TEM BF image of a Grade80 thin foil showing a) lathlike grain structure. b) SAD pattern from adjoining grains shows presence of low angle grain boundaries through splitting of spots as marked by the arrow.....	134
Figure 6-4	a) Centerline segregation in Grade80 steel. The presence of elongated inclusions at the centerline is indicated by the arrow (etched with nital).....	136
Figure 6-4	b)TiN faceted precipitates in Grade80 steel at the centerline.....	137
Figure 6-5	Optical micrograph of Grade80 steel etched with picral showing presence of pearlite-like microstructural constituent.....	137
Figure 6-6	TEM BF image from a thin foil of Grade80 showing the presence of numerous dislocations in a grain of ferrite.....	138
Figure 6-7	a) TEM BF micrograph of Grade80 steel showing acicular ferrite grains, b) SAD pattern from one acicular grain identifies it to be bcc ferrite.....	139

Figure 6-8	a) Optical micrograph from centerline of Grade80 steel showing a long stringer, b) near the surface of the plate the inclusions are a mix of spherical particles and short stringers. (Etched with nital).....	140
Figure 6-9	EDX spectra from inclusions in Grade80 steel. a) The elongated inclusion was composed mainly of Mn and S with traces of Ti, the large Fe peak is from the matrix; b) the small rounded inclusions consisted of considerable amount of Ca in addition to Mn and S and traces of Ti and Mg. The large Al and O peaks have contributions from the polishing powder ( $Al_2O_3$ ).....	141
Figure 6-10	Planar intercept area of inclusions in Grade80 steel along the LS orientation.....	143
Figure 6-11	Planar intercept area of inclusions in Grade80 steel along the ST orientation.....	144
Figure 6-12	Aspect ratio of inclusions in Grade80 steel along the LS orientation.....	145
Figure 6-13	Aspect ratio of inclusions in Grade80 steel along the ST orientation.....	146
Figure 6-14	a) TEM BF image of cuboidal precipitates from a carbon replica. b) SAD pattern from one precipitate. c) EDX spectrum from the same precipitate in (b).....	149
Figure 6-15	a) TEM BF image of carbon replica from Grade80 LS showing medium sized, irregular shaped precipitates along with a cluster of	

	smaller rounded precipitates marked by an arrow. b) Indexed SAD pattern from precipitate 'a' .....	150
Figure 6-15	c) EDX spectrum from precipitate 'a' in (a).....	151
Figure 6-16	a) TEM BF image of small, rounded precipitates in Grade80 steel. b) Ring pattern from cluster of small precipitates indexed to be NbC. c) EDX spectrum from one of the small precipitate shows it to be Nb-rich with traces of Mo, Ti and O. The O peak is from the oxidation products formed on Cu support grid.....	152
Figure 6-17	TEM BF image of a ferrite grain showing extremely small precipitates spread throughout the grain, as seen by arrows pointing to extremely small spots .....	153
Figure 7-1	TEM BF micrographs from thin foils of X70 and Grade 80 showing differences between a) acicular ferrite and b) bainitic ferrite.....	157
Figure 7-2	CCT diagrams for a) X70 and b) X80 steels [CANMET98].....	160
Figure 7-3	Relationship of precipitation of Ti and Nb carbides, nitrides with temperature for a microalloyed steel [Gladman97].....	169

# Chapter 1: Introduction

Over the past several years, a newer class of microalloyed steels has been developed which possess high strength and toughness. These are the Grade70 steels and beyond, where ## is a number denoting the Specified Minimum Yield Strength (in ksi). In earlier steels, the major contributors to strength were enhanced levels of carbon and alloying additions. However, the richer chemistry led to lower toughness and problems in welding due to higher carbon equivalent ( $C_{eq}$ ) values. During the early 1980s thermomechanical rolling of steels was carried out in several mills around the world. Although, the theoretical foundations of the process had been laid out a couple of decades earlier, implementation had to wait for developments in mill technology and capacity. The new process involved controlling the temperature and deformation of the steel during rolling to control the phase transformations and grain growth (shape, size and distribution). Primarily V, Nb and Ti in small amounts (total < 1wt%) were used as the alloying additions to tailor the microstructure during controlled rolling. This enabled fabrication of superior products with leaner chemistries and attendant improvements in toughness and welding.

This blend of high strength, good toughness and improved weldability finds application in pipelines for oil and natural gas transport where the thin walled pipe leads to considerable cost savings when installation of several hundreds of kilometers of pipeline is required. The objective of the work in this thesis is to characterize the microstructure of three grades of microalloyed steels; X70 (0.04wt%C; 0.02wt%Ti and 0.07wt%Nb), X80 (0.04wt%C; 0.025wt%Ti and 0.09wt%Nb) and Grade80 (0.06wt%C; 0.038wt%Ti and 0.09wt%Nb).

This work focuses on phase identification and quantification, distribution of alloying elements and inclusions and segregation effects. Although, many researchers have studied various facets of microalloyed steels' processing and individual microstructural features, the motivation for this work was to characterize the microstructure in its entirety and to draw meaningful correlations between the

chemistry/processing and resultant microstructure and the evolution of physical properties on the basis of this microstructure. The study was organized to characterize the microstructure on a macroscopic level (low magnifications) and then focus on the individual microstructural features using more powerful techniques (like scanning and transmission electron microscopy). This experimental process gives an overview of the entire structure and ensures selection of representative areas and avoidance of artifacts. This philosophy can be better appreciated in the light of the fact that while these products (steel plates) are typically tens of meters in length, many of the microstructural components are in the size range of few tens of nanometers to a few microns.

Many different types of characterization and analytical tools were used to ascertain the microstructure. Initial microscopic examinations were made with conventional optical metallography. Scanning electron microscopy (SEM) was used to observe the grain structure of these steels to give a general overview of the grain shape and size distribution. However, a limitation of SEM is that the crystal structure information is not obtainable. The next step was to observe thin foil samples in the transmission electron microscope (TEM). One difficulty consistently encountered in the observation of the thin foils was the magnetic effect of the steel samples, which caused electron beam alignment problems. Carbon replicas were employed to prevent these effects.

The thesis is divided into 9 chapters. Along with a comprehensive literature survey on microstructural characterization of microalloyed steels, some information on the manufacture, types and characteristics of line pipe steels is presented in Chapter 2.

The experimental methods and details of the various techniques used for characterization are included in Chapter 3.

Chapter 4 presents the results of analysis for X70 steel. The findings are categorized according to different microstructural features including overall grain structure, inclusion content and morphology and types and distribution of precipitates. Similar treatment is repeated for X80 and Grade80 steels in Chapters 5 and 6 respectively.

The steels for this study were chosen to be generally similar, but with sufficient differences in chemistry and processing conditions to give rise to measurable differences in microstructure and physical properties. By analyzing these structures together and correlating them with their constituent chemistries and thermomechanical processing schedules, it is possible to explain the evolution a particular kind of microstructure and origin of differences, if any. An effort is made along these lines in Chapter 7 of this thesis. The chapter also tries to relate the differences in mechanical properties (strength and toughness) to the differences in microstructure of each grade of steel.

Finally, the work is concluded in Chapter 8 and recommendations for future work are made in Chapter 9.

## **Chapter 2: Literature Survey**

### **2.1 Introduction**

Microalloyed steels can be defined as "steels containing essentially less than 0.1% of the alloying additions used singly or in combination, and in which yield strength increments of two or three times that of plain carbon steels can be obtained" [Gladman97].

The name microalloyed steels was first applied to a class of higher strength low carbon steels containing small additions of niobium and/or vanadium. A rational definition now would include aluminum, vanadium, titanium along with niobium treated steels.

Boron had been used as a hardenability enhancing agent for many years prior to the development of niobium steels, but the term microalloyed had never been applied to these hardenable engineering type steels. Similarly, aluminum treated steels were used to produce a good combination of strength and toughness but they were never referred to as microalloyed steels. Presumably 'microalloyed steels' as a name was reserved for steels containing small additions of an alloying element that would produce grain refinement and/or precipitation strengthening by formation of relatively stable carbides and nitrides.

Thus microalloyed steels typically contain niobium, titanium and vanadium and their specific effects may be influenced by other alloying additions like aluminum, boron or any of the other more conventional alloy elements used in steel manufacture. The effects of microalloying elements are also strongly influenced by thermal and thermo-mechanical treatments [Gladman97].

## **2.2 Development of Microalloyed Steels**

Availability of niobium played a major role in development of these kinds of steels. Although niobium had been considered as an additive to steel prior to 1940, there was not any serious development at that time, due to low availability and high price of niobium. Also there was lack of proper understanding of the use of niobium. At that time the known resources of niobium were few and the niobium produced was in demand for use in tool steels as a substitute for tungsten, and in stainless steels as a stabilizing agent against intergranular corrosion because of its high affinity for carbon and nitrogen.

The price of niobium fell from \$14 US per pound to \$3 US per pound with the discovery of large ore deposits in Canada in 1954 and in Brazil in 1958.

Trials to study the effect of additions of niobium were introduced in the mid 1950's. Soon it became the focus of research and developmental activity in every major steel-producing country throughout the world.

One of the major factors contributing to the interest in these steels was the fact that niobium (and vanadium) showed a low affinity for oxygen, so additions could be made to the semi-killed steels. This should be appreciated in the light of the fact that in the late 1950's and early 1960's the commercial use of continuous casting was not predominant and all steels were ingot cast. This led to a low product yield (about 75% yield for fully killed steel) compared to semi-killed steel with a yield of 95%-98%. This was reflected in steel prices, so that additions such as niobium (or vanadium) that could be made using a semi-killed steel would produce cheaper high strength steels. This was an important factor because normalized steels, grain refined by aluminum additions, were already in existence, but had to be produced as fully killed steels due to high affinity of aluminum for oxygen [Gladman97].

In terms of research on these steels, it had already been established that the as-rolled niobium steels were significantly strengthened by fine precipitates of niobium carbides [Stuart83][Gladman97]. The nature of the precipitation reaction in the as rolled condition had not then been fully understood.

By 1966, the mechanism of 'interphase' precipitation had been discovered, together with the important role of transformation temperature, in controlling the size and spacing of the 'interphase' precipitated particles [Gladman97][Krishnadev75].

### **2.2.1 Factors Leading to Initial Development of the Microalloyed Steels**

Several factors contributed to the initial development of microalloyed steels. These have been summarized below.

- 1) Materials cost saving could be obtained directly by application of microalloyed steels.
- 2) In-service benefits could be obtained in the development of lighter transport vehicles with higher payloads.
- 3) The need for higher strength linepipe that was easily weldable provided an expanding market for higher yield strength steels.
- 4) The extensive use of welding as the principal fabrication method meant that conventional ways of increasing strength (increased carbon and alloy contents) would result in more expensive and much less practicable welding procedures, while the new microalloyed steels with their generally lower carbon and alloy levels (for a given strength) could often be welded using existing procedures.

- 5) The strength increase could be obtained relatively cheaply as both niobium and vanadium, not being readily oxidized, could be added to semi-killed steels, thus avoiding the cost increase associated with the yield losses of prime material attached to fully killed ingot cast steels.

Another significant development occurred in the period between 1963 and 1967: the controlled-rolling process was developed. This enabled fine-grained microstructure to be obtained in the 'as-rolled' condition.

It was realized at this time that niobium had another important effect in steels. Small additions of niobium could dramatically reduce the rate of recrystallization of austenite during hot-rolling. Other microalloys such as vanadium and titanium were also found to be capable of producing some retardation of austenite recrystallization, but their effect was considerably smaller than that of niobium.

Many instances of lamellar tearing in the weldments in pressure vessels, marine fabrication and structural applications were reported in the late 1960s. The cause of this phenomenon was found to be a delamination along arrays of non-metallic inclusions aligned parallel to the plate surfaces. This led to control of sulfide and oxide inclusions and their shape. Inclusion shape control additives such as rare earths, titanium, zirconium and calcium were tried with varying degree of success [Gladman97][Hilty75-1][Hilty75-2].

At this time (late 1960's and early 1970's) other factors were also coming into the scenario. There were large scale developments in gas and oil industries in remote and hostile areas of Alaska, Siberia and the North Sea [Mihelich74][Goetz77]. Pipeline diameter was being increased. This required higher strength steels to avoid thicker walled pipes that were accompanied by punitive welding costs. These pipelines were prone to longitudinal burst, which could carry on for kilometers. Thus steels with improved longitudinal and transverse toughness and sufficient resistance to cleavage were required. As a result various desulfurization practices were developed. These

included hot metal desulfurization in the transfer ladle from the blast furnace, lime injection and slag control. These ultimately replaced simple inclusion shape control methods.

Throughout the 1970's, attention was on compositional and processing refinements that would produce given strength levels at lower cost, or would extend the strength ranges that were attainable.

Some of the main efforts in this direction were [Gladman97]:

- 1) Use of controlled residual levels to reduce the transformation temperature of plate and linepipe steels, while maintaining a ferrite-pearlite transformation product. Refinement of the interphase particle distribution and increase in the strength levels were obtained, while maintaining adequate levels of toughness.
- 2) Development of titanium precipitation strengthened steels, where somewhat higher addition levels (0.15% -0.20%) could be used to develop hot strip product yield strengths of 350-700 MPa. The important feature was that same steel could yield virtually the full range of yield strengths depending on processing conditions.
- 3) Continuous hot strip mills were developed with various cooling facilities e.g. water cooling sprays, laminar flow cooling, etc. The temperature (and hence the austenite to ferrite transformation temperature) could be selected and closely controlled over a wide range.

The late 1970's saw the introduction of a fundamentally different type of steel, known as 'dual phase' steel [Kot-Bromfitt81][Bittence78]. These steels had a microstructure of ferrite and martensite and exhibited high work hardening rates. The connection with microalloying additions was that the work hardening characteristics

were improved by the refinement of the martensite island size, and the microalloyed dual phase steels showed distinct advantages over coarser structures. These steels have occupied a niche in cold formed components for the automobile industry.

The importance of cooling rate and cooling temperature was well appreciated in hot strip mills, and the substitution of cooling sprays during cooling for expensive alloying additions to give the same transformation temperature in other product forms such as plates, bars and sections became an area for development [Almond79].

The first on-line accelerated cooling system was installed in 1980 in a Japanese plate mill [Tsukada82]. The process has since then been incorporated in heavy section mills.

In the mid 1980's attention was focused on higher carbon steels. Vanadium was being used in medium/high carbon steel forgings with the aim of attaining the same strength levels in air cooled forgings as were obtained in quenched and tempered products [Naylor89]. In many forgings the deformation is inhomogeneous with some parts only slightly deformed or perhaps not deformed at all. In such regions of the forging, the structure will be typical of the soaking temperature and will be coarse grained with an attendant loss in toughness. The solution to this problem was found in use of titanium nitride as a grain refining agent, now known as the 'titanium nitride technology'. Very low titanium levels are essential, and are required to be sub-stoichiometric with respect to the nitrogen. The very high stability of titanium nitride can give rise to very fine stable nitrides when the titanium content is restricted, and grain coarsening temperature can be obtained. Thus, even parts of the forging that have no deformation will have a reasonably fine grained structure, with improved properties.

Although titanium nitride technology can be applied to weldments in restricting the size of coarse grained heat affected zone (HAZ), it is not effective in inhibiting grain growth at solidus temperatures.

Later developments, started in the late 1980's, include the use of titanium oxide particles. Such steels can develop superior toughness levels in the HAZ. The exact mechanism for this effect is unclear. It may be associated with seeding of acicular ferrite by titanium oxide particles during the cooling of weld, rather than by grain growth inhibition at welding temperature.

In the early mid-1980s 'interstitial free' (IF) steels were developed. Niobium and titanium have been used as scavengers for interstitial carbon and nitrogen in stainless steels, to avoid chromium carbide precipitation. Steelmaking processes that produce relatively low interstitial C and N ( <0.005 wt%) mean that relatively small additions of microalloy elements would allow carbo-nitride precipitation to give an interstitial free steel.

The carbon management process ( i.e., control of interstitial carbon levels and formation of carbides) led to the development in mid 1980's of bake hardening steels. In these steels the carbon and/or nitrogen levels in interstitial solid solution is controlled at about 0.001 wt%. Figure 2-1 summarizes the development of microalloyed steels discussed above [Gladman97].

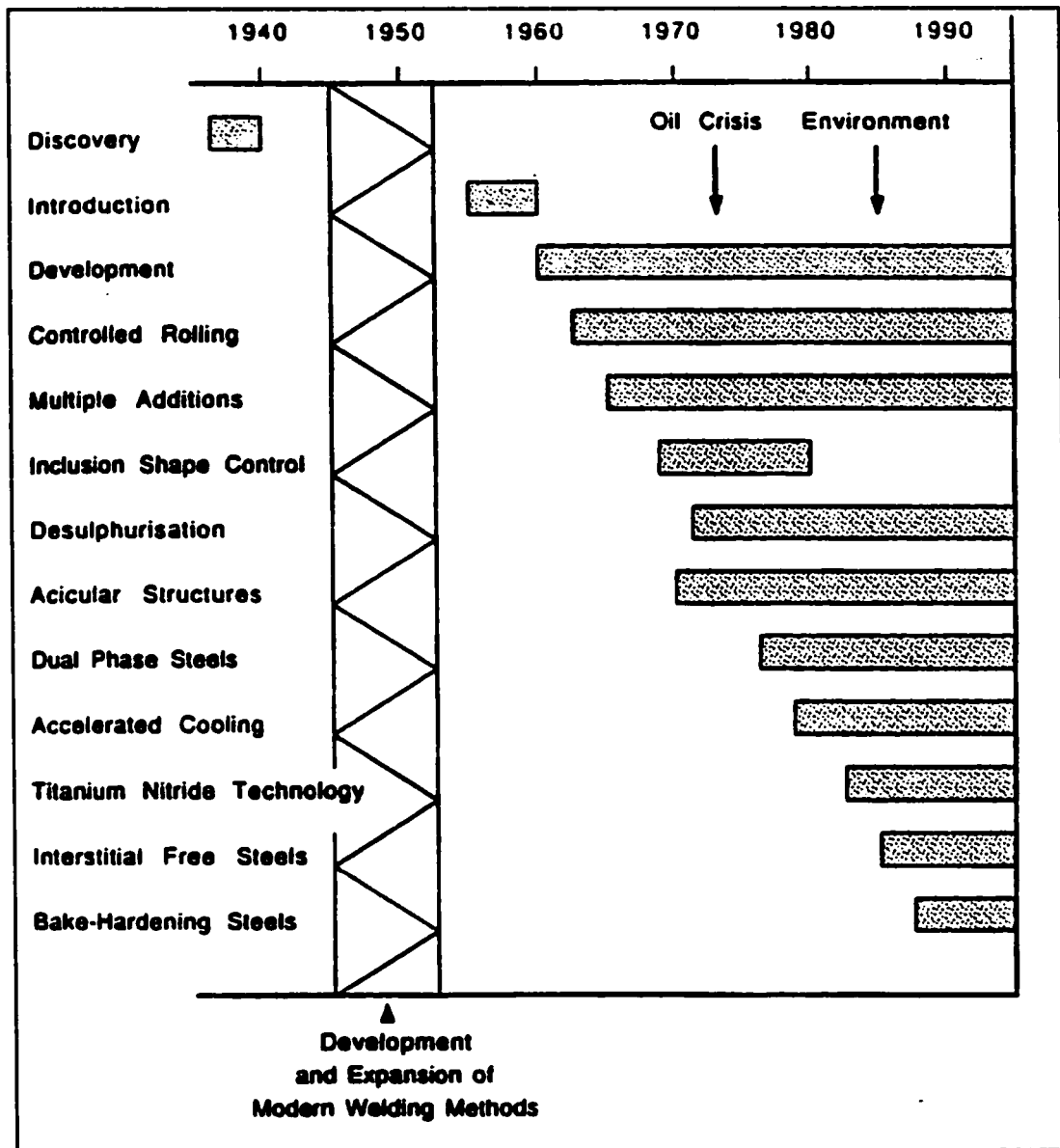


Figure 2-1 Development of microalloyed steels [Gladman97].

## **2.3 Microstructure of Microalloyed Steels**

The microstructure of steels is often described as being ferritic, bainitic or martensitic. However the microstructures are often if not always, complex and heterogeneous in nature. Even when precipitates and non-metallic inclusions are disregarded, the remaining matrix is often found to be composed of a mixture of phases and microconstituents [DeArdo88].

### **2.3.1 Early Ferritic-Pearlitic Steels**

Pearlite was perhaps the first microconstituent shown to have a large effect on properties. As early as 1935, the influence of pearlite content on strength, ductility and notch toughness was clearly recognized [DeArdo88][DeArdo95][Kim83].

In the early 1970's pearlite was recognized as contributing to the deterioration of resistance to both ductile and brittle fracture in notched impact tests in hot rolled line-pipe steels. [DeArdo95]. A negative influence of pearlite was observed on the fracture appearance transition temperature (FATT).

The negative influence of pearlite or carbon content on weldability in linepipe steels also was recognized at that time [Aronson67][Rothwell78]. This was essentially true for the heat affected zone (HAZ) associated with multipass arc welding, a technique widely used since World War II.

Ductility and formability are very important in strip and sheet steels. Pearlite was found to be detrimental to properties such as ductility.

The outlook for high strength hot rolled steel in mid 1960's was not entirely encouraging. Pearlite needed for strengthening was also responsible for lowering several other critical properties. This led to a large research effort to find ways of lowering carbon content of steel while still maintaining high strength, i.e. finding

substitute mechanisms for the composite strengthening of pearlite. Thus microalloyed steels were developed. From this time onwards carbon was no longer requisite for strength. Table 2-1 and Figure 2-2 show, respectively, the typical chemical composition [Kim83] and microstructure of a ferrite pearlite steel [Collins83].

Table 2-1 Typical chemical composition of ferrite-pearlite microalloyed steels (in wt%) [Kim83].

C	Mn	Si	S	P	V	Nb	Ti	Al	N
0.2 - 0.5	0.8 - 1.5	0.2 - 0.4	~0.05	~0.02	0.1-0.2	0 - 0.05	-	0.01 - 0.02	0 - 0.02

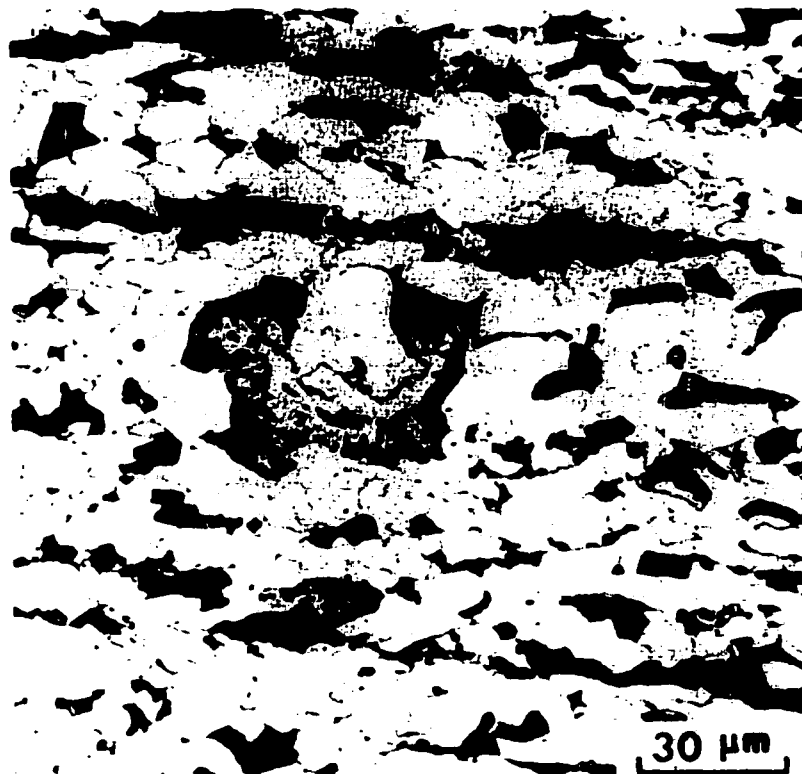


Figure 2-2 Optical micrograph showing the typical microstructure of ferrite-pearlite microalloyed steel. Lighter areas: polygonal ferrite, darker areas: pearlite [Collins83].

### **2.3.2 Dual Phase Steels**

This type of structure was a result of the response to the oil embargo in the early 1970's. Dual phase steels are modified ferrite pearlite steels in which the pearlite has been converted to martensite by inter-critical annealing followed by cooling to room temperature. A typical dual phase steel contains about 15 vol% martensite. When compared to a similar high strength ferrite-pearlite steel the presence of martensite results in lowering of the yield strength, an increase in the tensile strength and also an increase of the total elongation and stretch formability [DeArdo95][Gladman97][Lawson80].

The enhanced ductility and stretch formability exhibited by the dual phase steel can be attributed to [Kot-Bramfitt81]:

- 1) The nature and behavior of martensite, i.e., its ductility and cohesion with the ferrite.
- 2) The low carbon content in ferrite following slow cooling from the intercritical annealing temperature.
- 3) The transformation of retained austenite.

Controlled rolling was developed at this time. It was shown that it was possible to exert substantial control over the final microstructure and properties through creative alloy design and processing.

Table 2-2 and Figure 2-2 show respectively, the typical chemical composition [Kim83] and microstructure [Kot-Bramfitt81] of dual phase steels.

Table 2-2 Typical chemical composition of dual phase microalloyed steel (in wt%) [Kim83].

<b>C</b>	<b>Mn</b>	<b>Si</b>	<b>S</b>	<b>P</b>	<b>Cr</b>	<b>Mo</b>	<b>V</b>	<b>Al</b>	<b>N</b>
0.05 - 0.15	1.0 - 1.5	0.4 - 1.3	0.005 - 0.01	0.01 - 0.015	0 - 0.5	0 - 0.3	0 - 0.6	0 - 0.05	0 - 0.007



Figure 2-3 Optical micrograph showing microstructure of dual phase steels. Martensite islands surrounded by ferrite grains. [Kot-Bramfitt81].

### 2.3.3 Multiphase Steels

#### 2.3.3.1 Multiphase Plate Steels

It is extremely difficult to obtain yield strengths in excess of 550 MPa in a ferrite-pearlite microalloyed microstructure in thicknesses typical of linepipe grades, e.g., 18 mm, even with controlled rolling.

The combination of controlled rolling, accelerated cooling and increased hardenability led to mixed microstructures consisting of ferrite and lower bainite. The higher strengths found in these multi phase steels have been attributed to a combination of [DeArdo95][Kim83]:

- 1) fine dispersion of bainite;
- 2) significant grain refinement of ferrite;
- 3) very effective precipitation strengthening and;
- 4) very high dislocation densities in ferrite.

### 2.3.3.2 Multiphase Bar Steels

The first use of multiphase microstructures in bar and rod steels was described in 1983 [Heritier84]. The goal was to replace the medium carbon low alloyed steels which had to be treated to generate the required mechanical properties. It was found that low C Mn-Nb-B steels exhibited a dual phase microstructure containing bainitic ferrite and martensite-retained austenite constituent (MAC).

Another development of the as rolled microstructure consisted of a very fine microstructure of ferrite of 5 $\mu$ m grain size and 20% lower bainite. This steel was called BHS-1 [DeArdo95].

Table 2-3 and Figure 2-4 show respectively, the typical chemical composition [Kim83][DeArdo95] and microstructure of dual phase steels [Collins83].

Table 2-3 Typical chemical composition of multiphase microalloyed steel (in wt%) [Kim83][DeArdo95].

<b>C</b>	<b>Mn</b>	<b>Si</b>	<b>S</b>	<b>V</b>	<b>Nb</b>	<b>Ti</b>	<b>Mo</b>	<b>Al</b>	<b>B</b>
0.02 - 0.08	1.7 - 2.2	0.1 - 0.4	<0.005	0 - 0.05	0.04 - 0.09	0 - 0.03	0 - 0.3	0 - 0.06	0 - 0.001

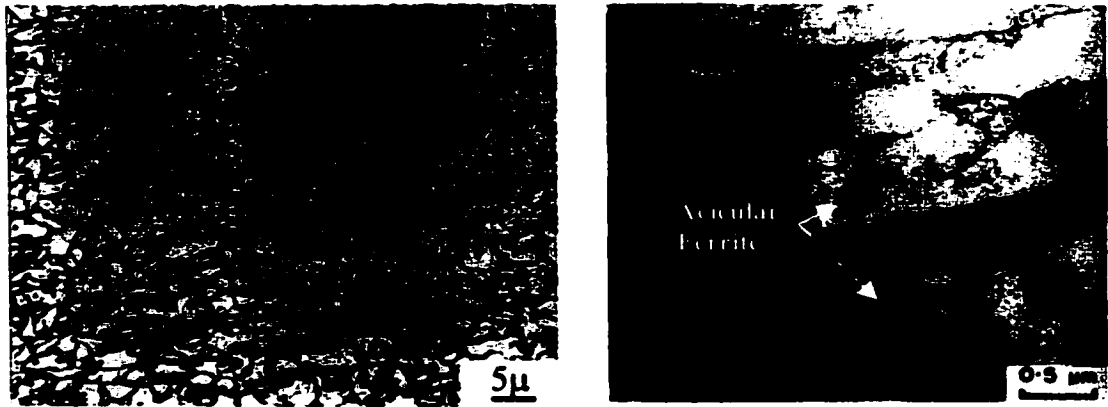


Figure 2-4 Microstructure of multiphase steel a) optical micrograph shows non-equiaxed grain structure. b) TEM BF image shows presence of acicular grains of ferrite [Collins83].

#### 2.3.4 Ultra Low Carbon Sheet Steels

The ultra low carbon or interstitial free steels were developed for enhanced deep drawability. Whereas vacuum degassing of the liquid steel can lower the C content to 40 PPM by weight, most of the remaining carbon must be removed through stabilization by the addition of strong carbide forming elements such as Ti or Nb. Recent work has shown that stabilization of C occurs by a different mechanism in some ULC steels where the atom ratio of carbon to sulfur is near one. In this case the carbon is initially and predominantly removed from the solid solution by in-situ transformation of  $\text{TiS}$  to  $\text{Ti}_4\text{C}_2\text{S}_2$ . The reaction is then followed by the epitaxial precipitation of MC on fully transformed  $\text{Ti}_4\text{C}_2\text{S}_2$  [DeArdo88][DeArdo95]. Table 2-4 and Figure 2-5 show the typical composition of ULC steel and  $\text{Ti}_4\text{C}_2\text{S}_2$  precipitate growth [DeArdo95].

Table 2-4 Typical chemical composition of ULC sheet steel (in wt%)  
[DeArdo95].

C	Mn	Si	S	P	Cr	Al	Ti	Nb	N
0.002-0.003	1.0 - 1.5	0.03-0.05	0.002-0.005	0 - 0.06	0 - 1.0	0.02 - 0.05	0 - 0.01	0 - 0.01	0.001

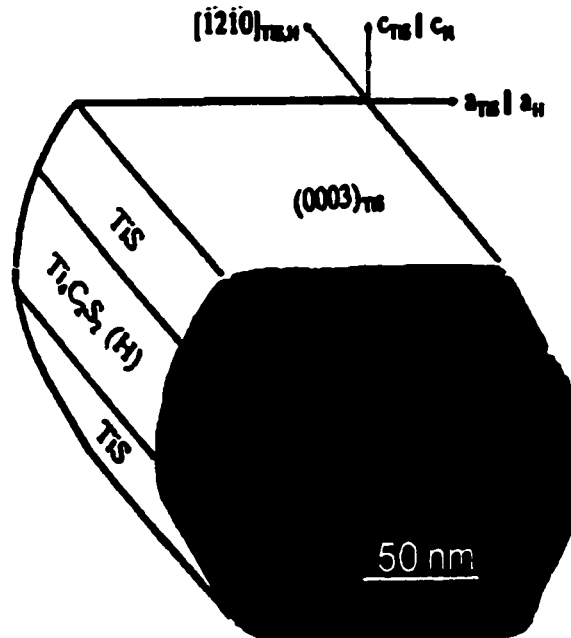


Figure 2-5  $\text{Ti}_4\text{S}_2\text{C}_2$  type precipitates in ULC steels [DeArdo95].

## 2.4 Precipitates in Microalloyed Steels

The most important precipitates in microalloyed steels are Nb, V and Ti carbides and nitrides. Nb, V and Ti are all strong carbide (nitride) formers. "The functions of microalloying elements result partly from their effect in the solid solution, but mostly from their effects as precipitates. There is little evidence to indicate their influence is related to precipitate morphology or their composition per se. Their effect is therefore a function of their size and the temperatures at which they exist in relation to the transformation temperature of steel (the dynamic transformation temperature in the case of as-rolled steels)" [Sage83].

The temperature at which most common microalloy compounds exist in relation to the transformation temperature is illustrated in Figure 2-6 [Sage83]. The upper part depicts the temperatures when the precipitates start coming out of the solution when steel is cooled down from high temperatures. The lower part shows temperature ranges over which the precipitates start dissolving on reheating the steel.

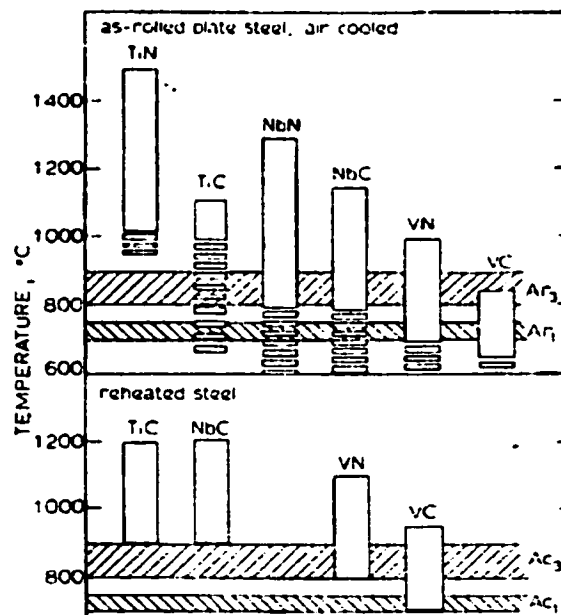


Figure 2-6 Temperature dependence of precipitation and dissolution of microalloy carbonitrides [Sage83].

The temperatures at which the precipitates form and their growth rate is influenced by the rate of cooling (and hence plate thickness) and the presence of alloys in solid solution, such as Cr, Mn and Mo, all of which tend to suppress precipitation and therefore refine the precipitate. This can be understood from the Figure 2-7 which shows solubility products of Nb, Ti and V along with Al, C and N [Sellars84]. It is seen that VC is the least stable precipitate and is taken into solution at relatively low temperatures. TiN is more stable and virtually insoluble in the austenite except at very high temperatures.

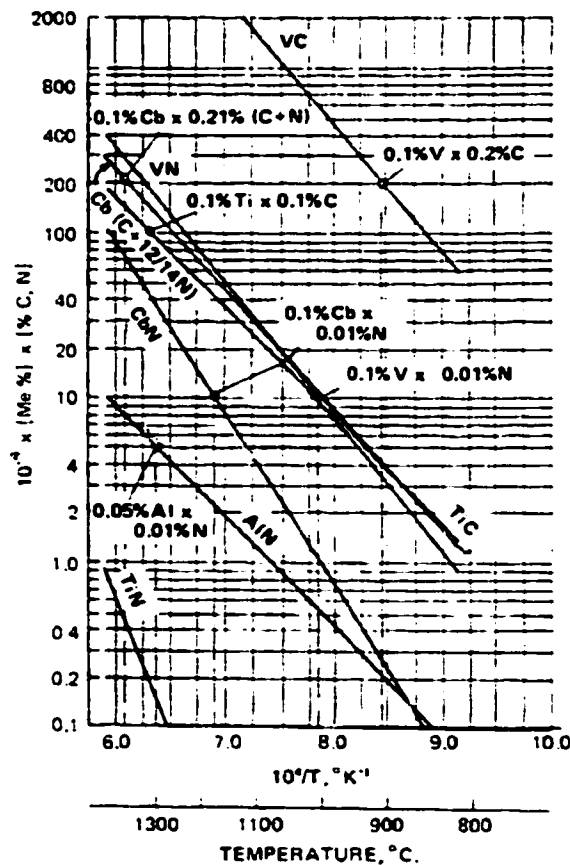


Figure 2-7 Solubility of carbides, nitrides of Ti, Nb and V in steel [Sellars84].

The carbides and nitrides are mutually soluble in each other and with both carbon and nitrogen present in the steel, carbonitrides with compositions depending on the steel compositions are formed. Carbides or nitrides remaining out of the solution during reheating can restrain grain growth whenever the volume fraction and particle size meet the critical conditions for pinning of grain boundaries.

## **2.5 Characterization of Precipitates**

Many different techniques have been used to analyze and quantify the precipitates in microalloyed steels. These include scanning electron microscopy (SEM), transmission electron microscopy (TEM) and high resolution electron microscopy (HREM), along with more conventional methods like optical microscopy. Other methods like electrical resistivity measurements, chemical and electrochemical dissolution techniques and evaluation of the loss of secondary hardening potential on tempering have also been used.

Some specific examples of each type are illustrated to provide a flavor of the characteristics of each technique and important results about precipitate morphology, size and precipitation behavior are described.

### **2.5.1 Optical Metallography**

Until a few decades ago most of the metallurgical studies were made with the optical microscope as it was the only option available. With the advent of more sophisticated techniques like electron microscopy, optical microscopy has been replaced to a large extent. However it is still used as the primary examination method for initial metallographic observations. Figure 2-8 shows micrographs of large precipitates in a microalloyed steel [Zhou96]. The most obvious limitation of this type of technique is the poor resolution.



Figure 2-8 Optical micrograph of precipitates in a 0.06C-0.03Nb-0.015Ti microalloyed steel. Only the larger precipitates are visible [Zhou96].

### 2.5.2 SEM Characterization

Scanning electron microscopy has been used extensively in identifying and characterizing the grain structure of microalloyed steels. However, it has not been very successful in characterizing the precipitates in these steels. The main reason behind this limitation is the small size of the carbonitride precipitates occurring in microalloyed steels. The majority of the precipitates are in the size range of 10-250nm. Depending on the beam energy the interaction volume of the electron beam in the sample is typically around  $1\mu\text{m}^3$ . It is possible to observe and image the precipitates of sizes belonging to the upper end of the limit ( $\sim 200\text{nm}$ ), as in Figure 2-9 [Juarez-Islas94]. Chemical analysis through EDX suffers from masking of precipitates by the matrix. For smaller precipitates the problem is more acute.

Sometimes larger precipitates (1-10 $\mu\text{m}$ ) do exist in the microstructure and here SEM is very useful in analyzing them as they are often lost during TEM sample preparation. Figure 2-10 shows an image of one such cuboidal precipitate nucleated on a round particle at its center. The accompanying composition profile identifies the core as CaS and the shell as Ti-rich [Saikaly99].

Another major limitation of SEM is that it is not possible to identify the lattice structure of crystalline materials. For all these reasons, TEM is the major tool employed to characterize precipitates in microalloyed steels.

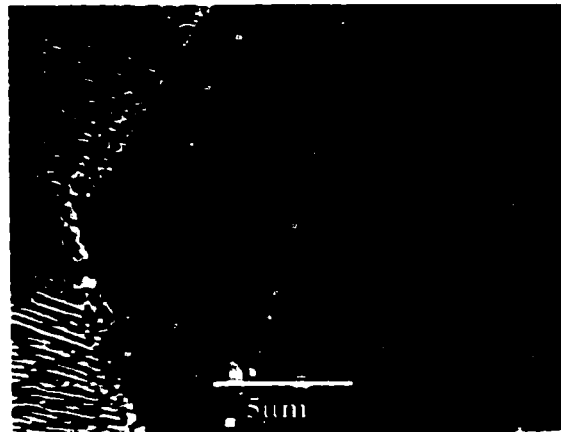
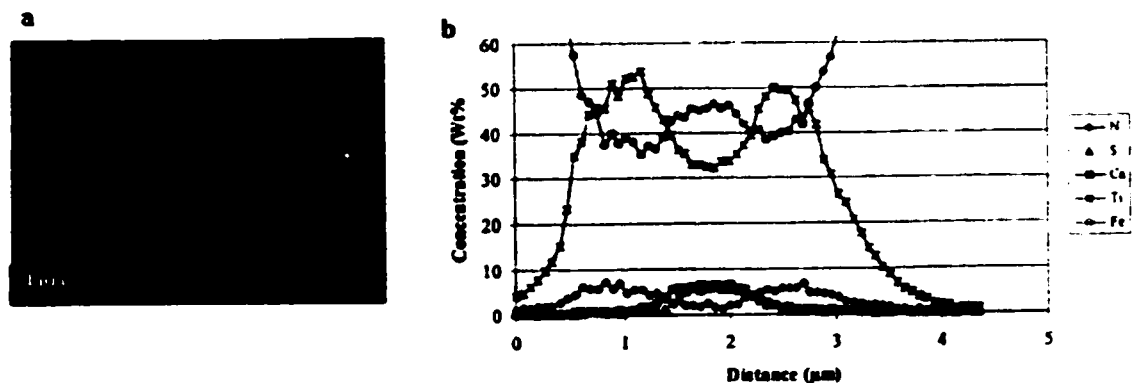


Figure 2-9 SEM micrograph of square precipitates along the grain boundary of a boron microalloyed steel [Juarez-Islas94].



### **2.5.3 TEM Characterization'**

As explained in the previous section, transmission electron microscopy has obvious advantages over other, lower resolution techniques like optical and scanning electron microscopy. It is possible to study the precipitate structure at high resolution and since most of the current TEMs are equipped with various analytical tools like EDX and electron energy loss spectroscopy (EELS), it is possible to image the precipitates and at the same time obtain their chemical composition (through EDX and EELS) and their crystal structure (through diffraction). Thus it is possible to characterize a precipitate completely in an analytical TEM. There have been a host of conferences and research publications on this topic and extensive literature is available on identification of precipitates in different types of microalloyed steels [Gaugry85][Read90][Wellner81][Zhou96] [Zou91][Mishra98].

Generally two different techniques are adopted when preparing samples for transmission electron microscopy. Either the material is thinned to electron transparency through mechanical and electrochemical means or carbon replicas are used to lift off the precipitates from the surface of an etched sample. Both the techniques have their individual advantages and disadvantages. While in the thin foil it is possible to observe the precipitates in relation to grains and other microstructural features within the grains like dislocations, inclusions, twins etc. (Figure 2-11) [Wellner81], sometimes the precipitates are so small that they are effectively masked by the matrix or there is a large interference from surrounding material hindering their precise identification. Also, because the steel samples are ferromagnetic, microscope alignment difficulties arise, particularly in sample tilting and beam alignment. In this case, the carbon replicas can be quite useful. There is no interference from the iron matrix as the precipitates are supported on a thin carbon film. It is possible to observe all size ranges of precipitates as Figure 2-12 shows [Feng89][Lehtinen89][Kestenbach89]. Figure 2-13 shows a cuboidal precipitate from which a diffraction pattern and EDX spectrum were obtained, identifying it as a titanium carbonitride [Saikaly99].



Figure 2-11 TEM BF micrographs showing interaction of carbonitride precipitates with dislocations in a thin foil steel sample [Wellner81].

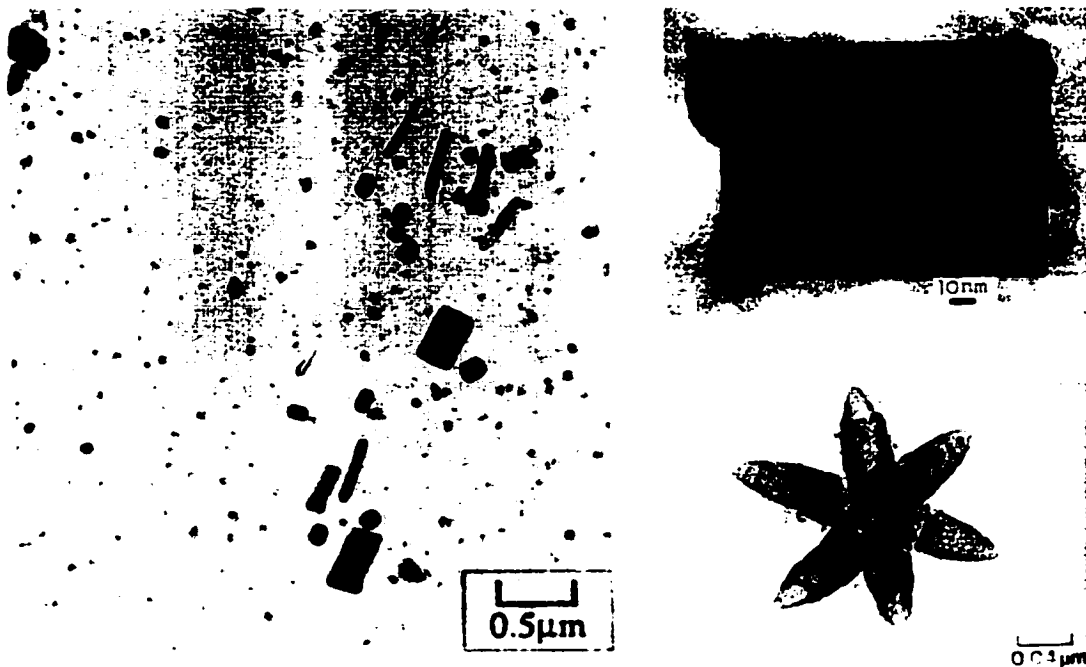


Figure 2-12 TEM micrographs of precipitates of various size range and morphologies as observed by the carbon replica method [Feng89][Lehtinen89][Kestenbach89].

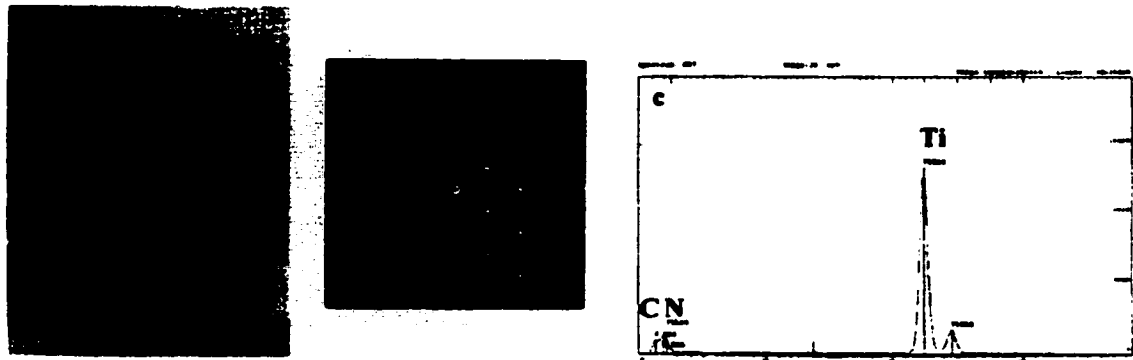


Figure 2-13 a) Titanium nitride precipitate observed on carbon replica. b) Corresponding electron diffraction pattern (fcc TiN – zone axis [110]) and c) EDX spectrum [Saikaly99].

#### 2.5.4 High Resolution Electron Microscopy (HREM) Analysis of Precipitates

HREM is a technique not commonly employed in characterization of precipitates in a microalloyed steels. However some researchers have used it to corroborate their observations from other sources, such as conventional TEM. Juarez et. al [Juarez-Islas94] identified some precipitates in TEM, which had an interplanar spacing of 0.34nm. This distance was found to be similar to the distance measured from lattice fringes in a HREM image (0.36nm) as shown in Figure 2-14. These precipitates were identified in this way to be  $B_{13}C_2$  and  $B_4C$  type.

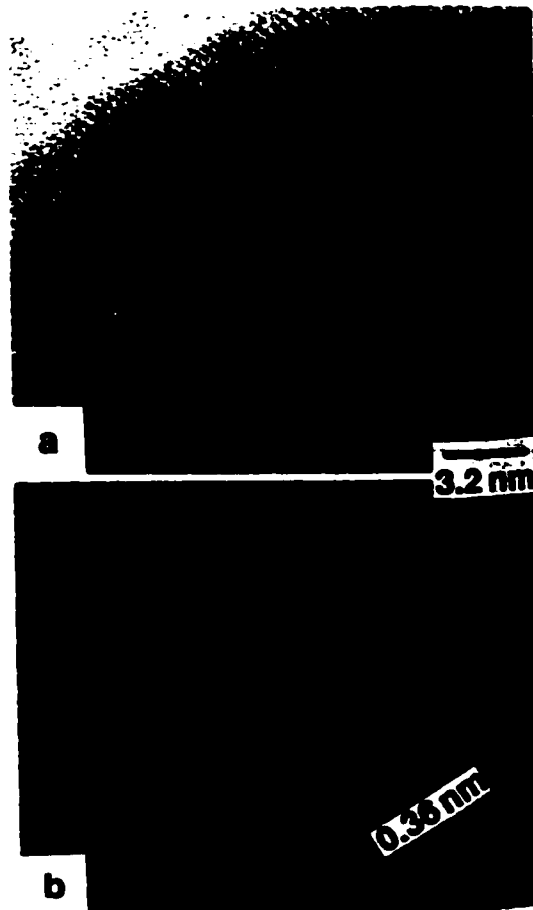


Figure 2-14 HREM image obtained from a large precipitate. The value measured from the interplanar distance corresponds to  $\approx 0.36\text{nm}$  [Juarez-Islas94].

### 2.5.5 Electron Energy Loss Spectroscopy (EELS) for Identifying Precipitate Composition

The most common types of precipitates in contemporary microalloyed steels are carbonitrides, carbides or nitrides of Ti, Nb or V. Sometimes it is difficult to characterize such precipitates properly using EDX, since the energy resolution ( $\sim 130\text{eV}$ ) of EDX spectra is not sufficient to clearly distinguish the nitrogen peak from that of carbon. EELS spectra are better suited for study of these Nb,Ti(C,N) precipitates. Figure 2-15 shows a parallel electron energy loss spectrum (PEELS) spectrum of a precipitate from a carbon replica. Ti, C and N peaks are clearly seen [Saikaly99].

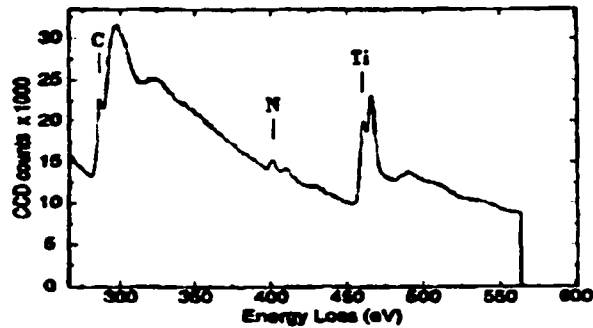


Figure 2-15 PEELS spectrum of a titanium carbonitride from a carbon replica. The carbon and nitrogen peaks are widely separated and easily identifiable [Saikaly99].

### 2.5.6 Extraction of Precipitates by Electrochemical Means and Their Analysis by X-ray Diffraction

An electrolytic dissolution technique using a 'slime' cell can be used to extract precipitates and has the advantage of being a bulk method. The residue obtained following chemical treatment of the dissolved steel was analyzed using scanning and transmission electron microscopy and x-ray diffraction [Read90]. Figure 2-16 shows the slime cell and the chemical extraction method.

Figure 2-17 shows the x-ray diffraction spectrum of residue and the results of lattice parameter calculations [Read90]. From the figure it is obvious that the particles were very similar to NbC with slight variations in lattice parameter, which might be due to nitrogen replacing carbon and forming carbonitrides.

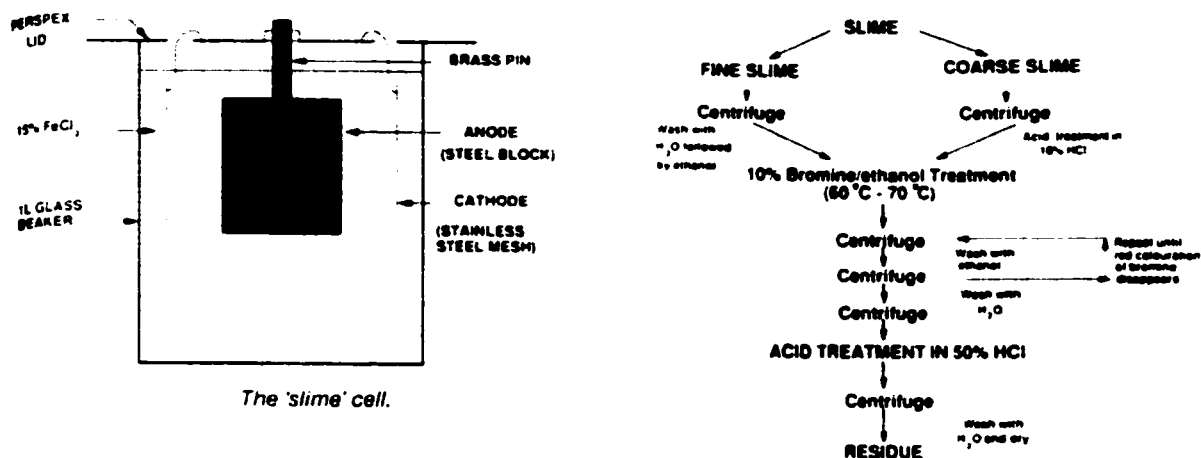


Figure 2-16 a) The slime cell for collection of precipitates by dissolution of metal matrix, b) Flow chart of the chemical treatment of the slime [Read90].

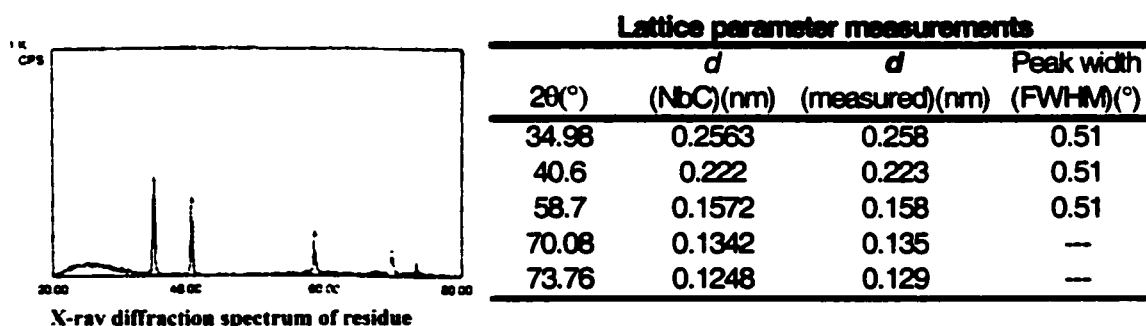


Figure 2-17 X-ray diffraction spectrum from the residue. The accompanying table of lattice parameters identifies the residue as consisting mainly of NbC [Read90].

## **2.6 Role of Alloying Elements in Microalloyed Steels**

The information presented in this section was gathered from these references: [Brownrigg73][Cochrane81][Collins83][Feng90][Kniessl93][Kuziak95][Manohar96][Mangonon76][Paju89][Paju91][Penolba96][Sage83]. All compositions are in wt%.

### **2.6.1 Niobium (0-1 %)**

- Niobium (columbium) is a strong carbonitride former. The role of niobium in the  $\gamma \rightarrow \alpha$  transformation is complex. Carbonitrides of Nb may precipitate in austenite, during transformation or in the ferrite after the transformation is complete. In solution, niobium reduces the  $A_{r3}$  temperature ( $\cong 8^\circ\text{C}/0.01\% \text{Nb}$ ) and ferrite nucleation rates, thus shifting the CCT curve to longer times and lower temperatures.
- Nb retards austenite recrystallization during rolling through the strain induced precipitation of fine Nb(C,N) particles.
- Nb has a strong affinity for N and if any nitrogen is available in austenite it precipitates as NbN, thereby reducing its effectiveness in suppressing the  $\gamma \rightarrow \alpha$  transformation.
- Very small and finely dispersed precipitates of NbC form after coiling of strip at around  $600^\circ\text{C}$  during manufacture of plates for pipeline. These provide extra precipitation strengthening. However the precipitates have a detrimental effect on the impact toughness.

### **2.6.2 Titanium (0-0.3%)**

- Titanium is also a very strong carbonitride former. TiN is a very stable compound which forms at high temperatures and does not dissolve at temperatures even as high as 1400°C. Thus, when the steel is reheated to around 1200°C-1250°C the TiN particles pin the grain boundaries of austenite thereby preventing growth of recrystallized austenite grains to abnormally large sizes. This leads to a finer initial austenite grain size for the  $\gamma \rightarrow \alpha$  transformation and consequently a finer final ferrite grain size.
- Ti is also added to prevent the formation of NbN. Since TiN forms at higher temperatures, it ties up any excess nitrogen. This tying up of nitrogen also prevents the formation of BN in boron containing steels. Boron is essential for increased hardenability and if taken out of solution as BN, its effectiveness is sacrificed.
- Depending on the initial content some titanium also precipitates as titanium carbides in ferrite, contributing to precipitation strengthening. However TiC is detrimental to toughness.

### **2.6.3 Vanadium (0-0.05%)**

- Vanadium has a greater solubility in austenite than Nb. It is more likely to remain in solution prior to transformation.
- Vanadium causes an increase in the ferrite start temperature and shifts the ferrite nose in the CCT diagram to shorter times. The higher transformation temperature promotes formation of polygonal ferrite.
- Vanadium also depresses the bainite and pearlite transformation thereby promoting the formation of MAC in the higher carbon austenite remaining after the ferrite reaction.

#### **2.6.4 Molybdenum (0-0.3%)**

- Molybdenum acts as a solid solution strengthener.
- It also plays an important role in precipitate strengthening. Molybdenum increases the solubility of Nb(C, N) strongly. Hence, it is possible to retain some of the Nb in solution after controlled rolling, for hardenability and/or ferrite precipitation hardening.
- Molybdenum strongly retards the transformation kinetics of transformation ( $\gamma \rightarrow \alpha$ , pearlite) particularly in the temperature range 600°C-700°C. It displaces the pearlite and ferrite regions to longer times in the CCT diagram. This promotes the formation of low-temperature microstructures, acicular ferrite, bainite and MAC.

#### **2.6.5 Chromium (0-0.3%)**

- Chromium stabilizes austenite in steel. It delays the transformation and promotes the formation of low temperature products.
- Chromium is not as effective as molybdenum in suppressing the  $\gamma \rightarrow \alpha$  transformation.

#### **2.6.6 Boron (10-20ppm)**

- Boron additions very strongly suppress the  $\gamma \rightarrow \alpha$  transformation. Boron shifts the CCT diagram to right (increasing hardenability) allowing the formation of bainite and martensite.
- The mechanism of suppression of  $\gamma \rightarrow \alpha$  transformation is believed to be through inhibition of ferrite nucleation at austenite grain boundaries.
- Boron has a strong synergistic effect with both Mo and Nb and the presence of either of these elements delays the formation of ferrite.

### **2.6.7 Manganese (1-2%)**

- Manganese acts as a solid solution strengthener.
- It tends to suppress the transformation temperature of austenite. Therefore it leads to a finer microstructure.
- Larger additions of Mn (1.5 - 2%) may lower the transformation temperature so much that acicular or bainitic products are obtained.

## **2.7 Effect of Microalloying Elements on Mechanical Properties**

As explained in the earlier sections, microalloying elements have two major effects on controlling the final properties of steel. Through controlled rolling they form stable carbides and nitrides, which prevent recrystallization and grain growth of austenite. This leads to a very fine pancake shaped austenite, which later transforms to fine grained ferrite providing higher toughness and strength to the steel [DeArdo88][Dogan88] [Kim83][Meyer96][Shehata82].

The other effect of the microalloying elements is through dispersion strengthening. The fine carbonitrides (50nm to  $\sim 1\mu\text{m}$ ) provide adequate hindrance to dislocation motion and hence high strength values.

Therefore, in assessing the effect of microalloying elements on mechanical properties of steels, we have to take into account their indirect effect on the production of microstructure. The varying amounts of different phases constituting the final microstructure have a direct influence on the mechanical properties along with the size, shape and density of precipitates.

In general the total yield strength can be described as a contribution from all strengthening mechanisms [Sage83].

$$\sigma_y = \sigma_l + \sigma_{ss} + \sigma_{ppt} + \sigma_{disl} + \sigma_{tex} + k_y d^{-1/2} \quad (1)$$

where

- $\sigma_y$  = yield strength
- $\sigma_l$  = lattice friction stress
- $\sigma_{ss}$  = solid solution strengthening
- $\sigma_{ppt}$  = precipitation strengthening
- $\sigma_{disl}$  = dislocation strengthening
- $\sigma_{tex}$  = texture strengthening
- $d$  = ferrite grain diameter
- $k_y$  = constant

Pontremoli et. al. [Pontremoli86] give another relation for linepipe steels having acicular ferritic (AF) and martensite-retained-austenite (MAC) structures:

$$\sigma_2[\pm 25 \text{ MN/m}^2] = 534 + 0.62AF + 6.87MAC \quad (2)$$

$$UTS [\pm 3 \text{ MN/m}^2] = 654 + 9.12MAC \quad (3)$$

Where  $\sigma_2$  = stress for 2% plastic strain

The microalloying precipitates do not affect the properties in isolation. The effect of various other parameters such as rolling temperature, rolling speed and cooling conditions must be considered.

## **2.8 Structural Aspects of Alloy Carbonitride Precipitation in Microalloyed Steels**

Carbonitrides of alloying elements precipitate in both austenite and ferrite during the controlled processing of microalloyed steels. They have a significant influence on mechanical properties. Commercial microalloyed steels have been studied extensively by electron microscopy to establish the various models of carbonitride precipitation that occur in austenite or ferrite during isothermal treatment or commercial processing [Smith88]. Alloy carbonitrides form at the  $\alpha/\gamma$  interface and grow in ferrite in the Baker-Nutting (BN) orientation relationship.

$$\begin{aligned} \{100\}_{\text{CN}} &\parallel \{100\}_{\alpha} \\ \langle 110 \rangle_{\text{CN}} &\parallel \langle 100 \rangle_{\alpha} \end{aligned} \quad (4)$$

However, at temperatures higher or lower than the interphase range ferrite can form which is, at least initially, free of precipitates. Under certain conditions austenite can decompose to a fine dispersion of alloy carbonitrides arranged in sheet form in a ferrite matrix. The sheets or layers form at the  $\alpha/\gamma$  interphase boundary by repeated nucleation of carbonitride particles as the transformation front moves through the austenite. Initially all these precipitates forming at the  $\alpha/\gamma$  interface were grouped as one category. Recent studies have identified five different interphase models in microalloyed steels. These are:

- 1) Interphase precipitation - planar: IPP
- 2) Interphase precipitation - Curved (irregular): IPC-Irregular.
- 3) Interphase precipitation - Curved (regular): IPC- Regular.
- 4) Interphase precipitation - Random: IPR.
- 5) Interphase precipitation – Fibrous: IPF.

### 2.8.1 Interphase Precipitation Planar: IPP

This kind of precipitation is associated with ferrite growth by a ledge mechanism at a semicoherent  $\alpha/\gamma$  interface. The carbonitrides are nucleated in a random array over the interface and continue to grow until another ferrite ledge moves over them and the process is repeated.

The nucleation of carbonitrides is controlled by diffusion of particular solute atoms and the supersaturation of carbon. At higher temperatures carbon rapidly partitions to the austenite, decreasing the degree of supersaturation of the ferrite. At lower temperatures the carbon partitions more slowly to the austenite. Thus planar interphase precipitation occurs over an optimum temperature range where the following conditions apply

- Ferrite grows by a ledge mechanism along semi-coherent boundaries at an appropriate rate.
- The diffusivities of the carbide/ nitride forming elements are relatively high.
- Carbon atoms buildup at the  $\alpha/\gamma$  interface as they are rejected from ferrite.

Figure 2-18 shows a BF TEM image of planar interphase precipitation in a V steel. The sheets are regular spaced and planar. The precipitates are uniform in size.

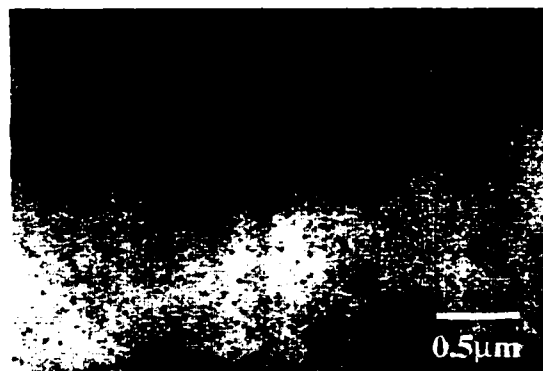


Figure 2-18 Interphase precipitation planar (IPP) in a V steel [Smith88].

### 2.8.2 Interphase Precipitation Curved: IPC - Irregular

Interphase precipitation is not always associated with planar semi-coherent interfaces. It has also been observed as fine alloy carbonitrides randomly distributed within curved sheets in ferrite. It is accepted that this form of precipitation is associated with migrating incoherent  $\alpha/\gamma$  boundaries. Solute builds up ahead of the moving boundaries and this solute drag slows the movement sufficiently for carbonitride precipitation. These carbonitrides effectively pin the grain boundary until selective coarsening occurs, allowing the interface to escape by bowing between the particles. This process is repeated resulting in curved irregularly spaced sheets of precipitates (Figure 2-19) [Smith88].



Figure 2-19 Curved irregularly spaced sheets of precipitates in a microalloyed steel illustrating the 'Interphase precipitation curved-irregular' mode of precipitation [Smith88].

### 2.8.3 Interphase Precipitation Curved: IPC - Regular

Interphase precipitation at curved incoherent boundaries also occurs with small and relatively regular spacings. Rick and Howell [Smith88] showed that regular sheet spacing originates from a quasi ledge migration along a heavily pinned, incoherent boundary. Under certain conditions, precipitation at the migrating incoherent boundary may be so prolific that it is immobilized and the growth

continues by bowing of interface segments normal to the growth direction forming quasi-ledges. Figure 2-20a demonstrates the process of formation of these quasi ledges when the interface bows between occasional widely spaced particles. An example of such regularly spaced, curved precipitation is shown in Figure 2-10b.

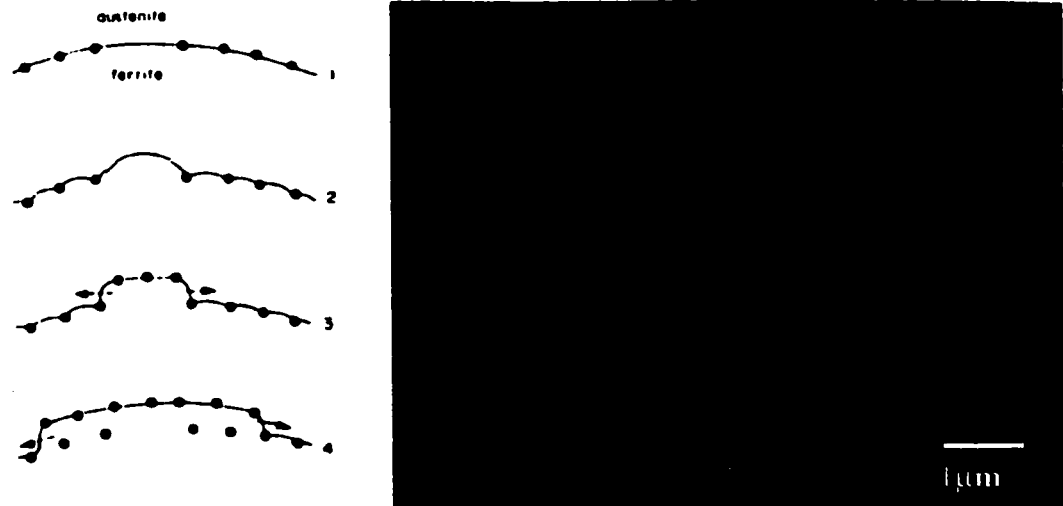


Figure 2-20 a) Schematic depicting the 'Quasi-ledge model' of precipitation, b) CDF image of V(C,N) showing IPC (regular) dispersion in V steel [Smith88].

#### 2.8.4 Interphase Precipitation Random: IPR

In this type of precipitation the particles do not follow any regular spacing but precipitate randomly all over, within the grain (Figure 2-21b). Characteristic sheets of precipitate form only when precipitation and pinning of the interface are co-ordinated along a section of the interface. In other cases a random distribution of particles develops. Figure 2-21a shows a schematic of this mechanism.

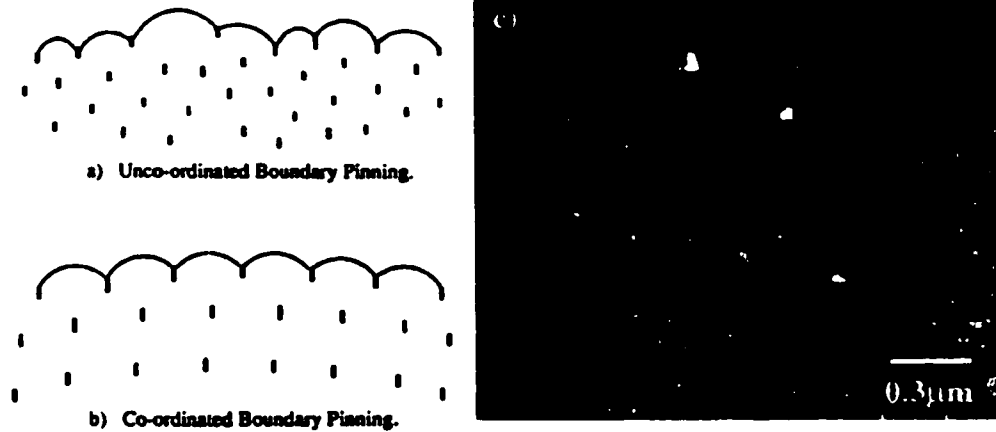


Figure 2-21 a) and b) Schematic illustrating the uncoordinated and coordinated pinning of the  $\alpha/\gamma$  interface by carbonitride precipitates, c) CDF image of Nb(C,N) precipitates with apparent random dispersion in a Nb steel [Smith88].

### 2.8.5 Interphase Precipitation Fibrous: IPF

IPF occurs in steels with large alloy concentrations. A fibrous morphology can occur under slow transformation. The morphology is similar to pearlite, except it is fibrous instead of lamellar and the fibers are straight and do not branch. The fibers form approximately perpendicular to the migrating  $\alpha/\gamma$  interface. This type of morphology is restricted to alloys with relatively high alloy content, in which the transformation temperature and supersaturation are high and the polymorphic transformation is slow. The structure is associated with slow moving, curved, incoherent structures and therefore the particles exhibit no orientation relationship with the austenite.

## **2.9 Inclusions in Steels**

The effect of inclusions on the properties of steel was being considered as early as the late 1930's, when Sims advocated the importance of sulfide inclusion shape control [Snape74]. However, for a long time the focus was confined to specialty, low tonnage, high performance alloy steels. Plate steels produced in tonnage quantities had high levels of sulfur by today's standards and process control was erratic. Later it was found that aluminum had the power to alter the character of both oxide and sulfide inclusions and thus affect the ductility of steel. Further work showed that this effect was not peculiar to aluminum but was characteristic of any similar strong deoxidizer. In fact this was an effect of deoxidation itself. Strong deoxidizers are chemically active elements with a strong affinity for nitrogen, carbon and sulfur besides oxygen. Thus, superimposed on deoxidation, there were changes in the composition of inclusions. Based on these observations titanium and calcium were used to form sulfides in place of manganese sulfides. These are perhaps the most stable sulfides known and improved the properties of steel considerably.

Since then the steelmaking processes have improved tremendously and it is possible to control the sulfur and oxygen levels in present day steels to extremely low levels. The introduction of HSLA and microalloyed steels with stringent requirements on properties such as formability, toughness and ductility in transverse and through thickness directions provided the impetus for development of these technologies.

### **2.9.1 Effect of Inclusions on Properties of Steels**

Inclusions can have extremely large effects on certain properties but negligibly small effects on others. While yield strength and ultimate tensile strength are relatively unaffected by inclusions there is significant effect on other properties [Nicholson86]. These include:

- 1) properties in which a ductile fracture mechanism is involved, such as impact fracture upper-shelf energy, plane strain fracture toughness, sheet metal formability, cold heading and bendability.
- 2) properties in which tessellated stresses around the inclusions are important, e.g., fatigue.
- 3) properties in which inclusions affect surface characteristics, e.g., polishability, pitting corrosion and coating adherence.
- 4) Machinability.

To understand the effect of inclusions on properties of steels the inclusions are considered as [Gladman92]:

- 1) “*holes*: the inclusions act as discontinuities in the metal matrix and can be regarded as holes.
- 2) *pressurized holes*: under certain service conditions involving hydrogen, the inclusions may become pressurized voids.
- 3) *self pressurized holes*: certain inclusions may generate their own internal pressures within the discontinuities or holes”.

#### **2.9.1.1 Properties Involving Ductile Fracture**

The general principles involved in the ductile fracture process include void nucleation at second phase particles such as inclusions, void growth and void coalescence. It has been shown that the strain required for ductile fracture is dependent on volume fraction of the inclusions and their shape. Different types of inclusions have different relative plasticities during hot working and so their effect on ductility can be very different. Elongated inclusions have the least effect on ductility when the tensile or straining axis is parallel with the long axis of inclusion, and the largest effect when straining is normal to the long axis.

### 2.9.1.2 Impact Toughness

The impact toughness of the steel can be improved largely by controlling the amount and shape of non-metallic inclusions, particularly sulfides. Figure 2-22 shows the effects of morphology of sulfides on impact toughness [Nicholson86]. The steels with lower sulfur content had relatively fewer inclusions and consequently higher impact toughness. The inclusions that were not cross rolled lead to anisotropic values for toughness.

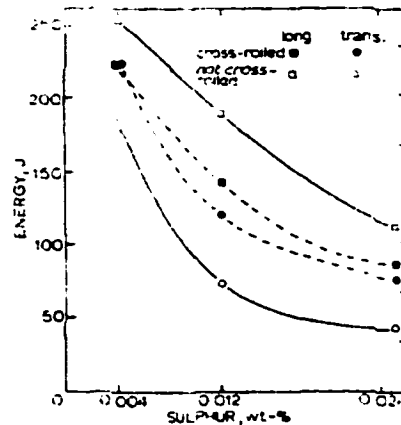


Figure 2-22 Effect of S on CVN shelf energy absorption in a Si-Al killed 0.19C-1.2Mn hot-rolled steel [Nicholson86].

Initial attempts to improve the fracture toughness involved the use of rare earth additives. This resulted in replacement of manganese sulfide by rare earth sulfides that are virtually undeformed by hot working. However, because of the large affinity of oxygen for rare earth additives there was danger of reoxidation and reduced steel cleanliness. In the past few years this practice has been replaced by improved and cheaper desulfurization practices involving calcium treatment. Sulfur contents of 0.001wt% are not uncommon now. At these sulfur levels, the sulfides, which may be CaS or (Ca,Mn)S are also shape controlled because of low plasticity of Ca bearing sulfides.

### **2.9.1.3 Bendability of Strip**

HSLA steels are used for automobile parts, e.g., chassis members. These require good transverse bendability. Since these steels are microalloyed with titanium, vanadium or niobium, advantage is taken of the dual role of titanium addition in producing high strength levels with inclusion shape control.

### **2.9.1.4 Sheet Metal Forming**

Although the formability of steel is largely controlled by plastic anisotropy and work hardening characteristics, the presence of large elongated inclusions can result in premature fracture. Similar remedies, i.e., inclusion shape control and desulfurization are used for control.

### **2.9.1.5 Cold Heading**

In most bar products, the inclusions are elongated along the bar axis, and therefore have relatively small effects on longitudinal ductility. However, when the bar material is subjected to cold heading operations, as in manufacture of bolts or screws, the bar is subjected to a large compressive axial strain and a corresponding large circumferential tension. This tension is perpendicular to long axis of inclusions and may lead to cracking.

### **2.9.1.6 Tessellated Stresses and Fatigue**

Tessellated stresses arise around inclusions as a result of their thermal expansion coefficients, which differ considerably from the metal matrix. Those inclusions that have a much lower coefficient of expansion, e.g., alumina and calcium aluminates, develop circumferential tensile stresses which are harmful to rolling contact fatigue. On the other hand the inclusions which have a higher coefficient of expansion, e.g., MnS have no significant effect.

### **2.9.1.7 Surface Effects: Pitting Corrosion**

There is considerable evidence that non-metallic inclusions, particularly sulfides can act as nucleating sites for pitting corrosion in both carbon and stainless steels.

### **2.9.1.8 Machinability**

The inclusions play an important role in controlling machinability. The sulfide inclusions act as chip breakers, thereby reducing tool forces and provide a lubricating film between tool and chip. Therefore deoxidants are avoided where possible in free-machining steels.

## **2.9.2 Control of Inclusions in Steels**

There are two main ways to exercise control over the inclusions occurring in steel; either through production of cleaner steels or through steels with inclusions of controlled chemistry and morphology. At present both these approaches are the focus of advancements in secondary steelmaking in ladle refining technology. The main reasons for these trends are as follows [Nicholson86]:

- 1) **Productivity and costs:** By transferring the function of temperature and composition adjustment to the ladle, the primary furnace can be operated more efficiently for melting and decarburizing. Preheating of ladles allows tapping of the steel at lower temperatures. This leads to savings in refractory cost for the primary furnace.
- 2) **Continuous casting:** Continuous casting is being used increasingly. The process requires tight temperature and inclusion control. The non-metallics present in steel may deposit on the ladle and tundish nozzles and

cause partial or total blockage. The ladle acts as a buffer between the primary melter and the caster.

### **2.9.2.1 Slag Control**

The control of slag composition is a basic prerequisite of all ladle refining processes. A variety of techniques have been applied to prevent blast furnace slag entering the ladle. The most successful is the refractory plug device by Mannesman. In electric arc furnace steelmaking, a reduction in slag carry-over to ladle is achieved by changing the orientation of the taphole such that it enters the bath below the slag level more or less tangentially to the furnace bottom.

### **2.9.2.2 Deoxidation**

While other factors like teeming and temperature are important, the key to inclusion control is deoxidation practice. This is true in some measure for sulfides as well as oxides. To control deoxidation in ladle the total environment is controlled, i.e., steel bath, surrounding refractories, slag cover, gaseous atmosphere and stirring conditions.

To produce ultraclean steel the requirements are:

- 1) powerful deoxidation to reduce the dissolved oxygen content to a very low level (<5ppm) and thus prevent precipitation of oxides during solidification.
- 2) stable refractories, in particular, stability at high temperatures and ultra-low oxygen activities.
- 3) non-oxidizing slag, i.e., free from unstable oxides such as MnO and FeO. This implies efficient separation of the oxidizing tapping slag and replacement by a synthetic slag of suitable composition.

- 4) appropriate stirring conditions to promote the deoxidation reactions and assist in separation of the deoxidation product.

#### **2.9.2.2.1 Vacuum Carbon Deoxidation**

The steel is subjected to reduced pressure in the undeoxidized condition. This promotes the oxygen-carbon reaction and reduces the oxygen content of steel.

#### **2.9.2.2.2 Deoxidation Using Slags**

It is possible to increase the degree of deoxidation by the use of suitable slags when deoxidants such as silicon or aluminum are added. At the same time the nature of the deoxidation product is changed.

#### **2.9.2.3 Sulfide and Sulfur Control**

The main stimulus for this has been the demand for improved properties in offshore and pipeline steels. A typical specification requires a limit of 0.002wt%S maximum. While it is possible to produce very low sulfur content steel via the blast furnace- basic oxygen furnace steelmaking (BOS) route by desulfurizing the hot metal, it is usually necessary to treat the steel after tapping to obtain the lowest levels of sulfur and acceptable inclusion modification. Injection of calcium alloys (calcium silicide or calcium carbide) has been widely used for this purpose. However, it is necessary first to deoxidize the steel thoroughly with aluminum. Deep injection of calcium is necessary because of its high vapor pressure and to increase the residence time of the calcium vapor. Ultra low levels of sulfur and oxygen can be obtained and the inclusions produced are in the form of very small scattered globular calcium aluminates and Ca-Mn sulfides.

In some cases the steel specification precludes the use of calcium silicides or calcium carbides (i.e., silicon and carbon constraints). Here the basic reducing slags based on the  $\text{CaO-Al}_2\text{O}_3\text{-SiO}_2$  system are very effective in desulfurizing steel.

#### **2.9.2.4 Ladle Refining Processes**

##### **2.9.2.4.1 Ladle Bubbling**

Bubbling of an inert gas, usually argon or nitrogen, through a plug in the ladle bottom or via a deeply immersed lance is a widely used method of stirring the metal to facilitate temperature and composition adjustment. The rising gas bubbles trap the non-metallic inclusion particles and carry them to the surface where they are adsorbed in a suitable top slag. At the same time the column of gas bubbles stirs the bath and causes inclusion collision, growth and floatation. Vigorous gas injection can break up the slag cover and promote thorough mixing of slag and metal. With a top slag of appropriate chemistry, it is possible to intensify deoxidation and achieve a high degree of desulfurization very quickly.

##### **2.9.2.4.2 Vacuum Degassing**

Vacuum degassing is useful for deoxidizing the steel as it promotes the carbon-oxygen reaction at low temperatures to remove oxygen as a gaseous rather than solid product. Also vacuum degassers promote agglomeration and floatation of inclusions and addition of deoxidants in an environment which is not exposed to atmosphere.

##### **2.9.2.4.3 Ladle Additions**

Since the 1970's there have been many advances in ladle injection techniques in steelmaking. This has been largely due to introduction of calcium treatment for steels. Calcium boils at  $1487^\circ\text{C}$  and injection of powder into the ladle using argon as

the carrier gas is an established procedure. Calcium is added in the form of calcium silicide or calcium carbide.

#### **2.9.2.4.4 Ladle Heating Systems**

To reduce the superheat in a primary furnace and to control the teeming temperature more accurately, heating the steel in the ladle is becoming more common. A refining slag is put on the ladle, and electrodes of the arc heating system buried in it, to ensure efficient heat transfer and protection of ladle refractories from arc radiation and flare. Any residual iron in the slag is reduced by graphite electrodes. The process is capable of producing ultraclean, low sulfur steel.

## 2.10 Line Pipe Steels

Unlike many other structures, line pipe (except when quenched and tempered in the pipe form) is used in the cold worked condition. The process of cold working plays a critical role in determining the properties of the pipe. In some steels it lowers the strength of the pipe compared to plate, and in others it increases the strength. In almost all steels it reduces the steel toughness [Sage83].

In pipe forming, the inner layers of the plate are deformed in compression, the deformation increasing from zero at the neutral axis to a maximum at the surface. The outer part of the plate is deformed in tension.

During expansion, the inner layers of a pipe wall are deformed in tension and the outer layers receive further deformation in tension. In the flattening of a pipe section to provide test-pieces, the inner layers are deformed in tension and the outer layers in compression. Figure 2-23 summarizes these deformations [Sage83].

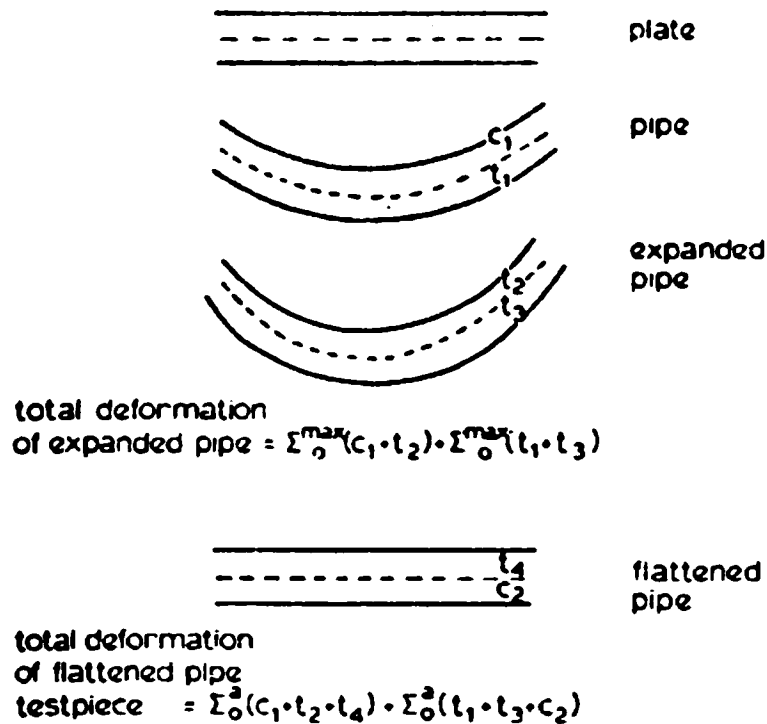


Figure 2-23 Deformation in converting the plate to expanded pipe [Sage83].

The properties of line pipe, like all structural steels, are controlled by the microstructure which in turn is determined by:

- 1) The effects of alloying elements on the kinetics of transformation and the formation of intermetallic compounds, i.e., the effects on the basic structure.
- 2) The effect of secondary constituents on the structure, such as inclusions, which are in turn controlled by
- 3) Steelmaking and casting processes and hence by the plant available for making and treating steel.

#### **2.10.1 Nomenclature**

The line pipe steels are usually named based on the yield strength levels attainable in them. The rules for nomenclature (as specified by American Petroleum Institute, API), are to denote the steel as X## where X denotes that it is a microalloyed line pipe steel and ## is a two digit number corresponding to the specified minimum yield strength (SMYS) in ksi.

For example X70 steel has a SMYS of 70 ksi or about 480MPa.

#### **2.10.2 Manufacture of Line-pipe Steel**

The sequence below describes a typical route adopted by present day manufacturers of line pipe. There may be differences in the initial steelmaking practices where instead of scrap based steelmaking, the blast furnace iron making route is adopted. However, the latter steps are more or less similar in all the processes [Collins95][Kostic96].

### **2.10.2.1 Steelmaking and Refining**

The steel is produced in an electric arc furnace with a typical capacity of 100-200 tonnes. The charge is a mix of steel scrap. Care is taken in selection and sorting of scrap to control the amount of residual and tramp elements allowed by the metallurgical requirements. To prevent nitrogen adsorption, special measures like airtight furnaces and foamy slag practices are often employed. Steel temperature is controlled from tap to casting to ensure optimal ladle and caster practices. During tapping of steel, deoxidizing and desulfurizing additions of Al, Si and synthetic basic slag are made. Deoxidizing and desulfurizing is enhanced by in situ argon bottom stirring.

Once the steel is in the ladle, calcium treatment is carried out. Ca-Si is injected by a top inserted lance. The amount of calcium to be added depends on the amount of sulfur present in the steel. This addition enables production of low-sulfur steel with good control of Ca content. The final calcium to sulfur ratio is controlled to modify the MnS inclusions into non-deformable, hard spherical particles instead of long stringers. This ensures higher toughness and less susceptibility to hydrogen induced cracking (HIC).

### **2.10.2.2 Continuous Casting**

With new advances in process control, currently almost all the slabs are cast through a continuous caster. The older practice of ingot casting and then rolling to slabs is rapidly becoming obsolete. Depending on the mill capacity the casting dimensions can be anywhere from a width of 2000mm to 4000mm. The thickness is typically around 200-300mm. Various measures are taken in design of the caster mould, containment rolls and cooling rates to ensure cleanliness and homogeneity of the steel required for manufacture of skelp for pipe making.

### **2.10.2.3 Hot Rolling**

The slabs are reheated in a walking beam gas fired reheat furnace (up to 1250°C) and then rolled in a 2-high reversing breakdown mill. The average rolling temperature is around 900°C-1000°C. Here, typically the thickness is reduced to about 30mm (from 200mm). The slab is now referred to as 'transfer bar'.

### **2.10.2.4 Controlled Rolling**

The transfer bar is often given a controlled roll treatment in a Steckel mill. This is typically a 4 high mill with heated coilers at either side. This ensures an excellent temperature control throughout the finishing operation. This control is essential because manufacture of linepipe steel is a thermomechanical controlled rolling process, which coupled with proper chemistry, provides the steel with the required properties. It is necessary to give proper deformation at certain temperatures to control grain deformation and recrystallization and for the onset of a particular precipitation sequence. The average rolling temperatures are in the 700°C-750°C range.

### **2.10.2.5 Online Accelerated Cooling (OLAC)**

After finish rolling the steel is cooled with a laminar flow of water and then coiled at a temperature of about 600°C.

## 2.11 Pipemaking

Two routes are available for manufacture of pipe from plate, depending on the size (diameter) of the final product.

### 2.11.1 U-O-E Process

Smaller diameter pipes (< 100cm diameter) are fabricated this way. The name of this process refers to the way the flat plat is deformed to a U and then finally the ends closed together as an O. The ends are seam welded and this weld runs along the longitudinal axis of the pipe [Tominaga2-24]. Figure 2-24 illustrates the schematic of the process.

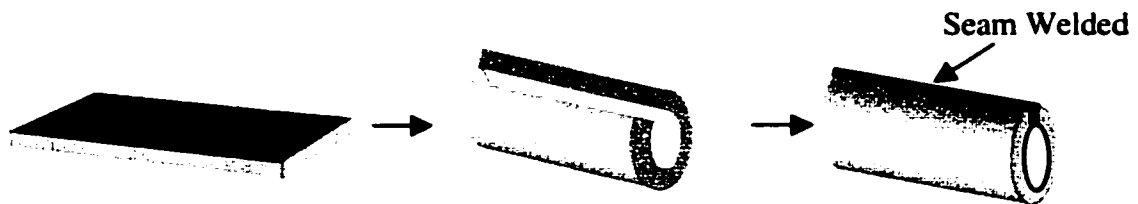


Figure 2-24 U-O-E process of pipemaking.

### 2.11.2 Spiral Welded Pipe

For larger diameter pipes (> 100cm diameter) the U-O process is not very suitable due to the large deformation forces required. Therefore large diameter pipes are fabricated as a spirally welded product. The coiled skelp is unwound and fed into a cropper to cut the edges of the coil to produce a square edge. The skelp is then sent through leveling rolls and a trimmer where about 20mm is removed from each side. The sheared edge is milled to a small angle ( $\sim 10^\circ$ ) to produce a good match for welding when the pipe is spiraled. The helical weld seam is produced using double submerged arc welding [Hanada86]. Figure 2-25 illustrates the schematic of the process.

After welding, the weld beads are ground to produce a smooth surface. The pipe is then x-ray tested, hydro-tested and inspected ultrasonically. It is then wrapped with polymer insulation coating.

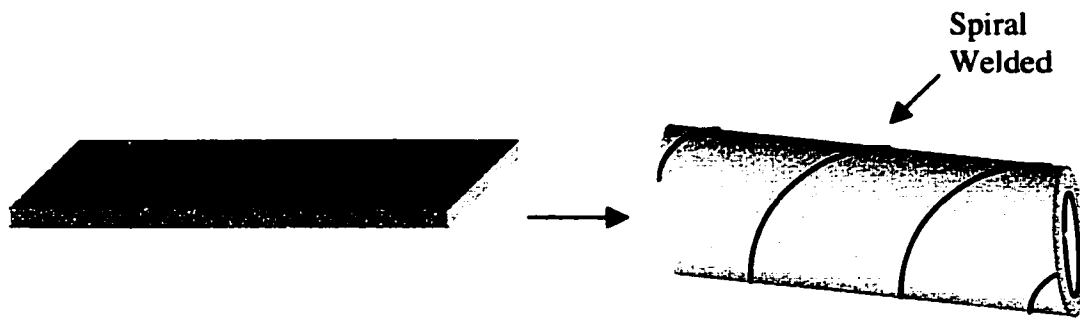


Figure 2-25 Spiral submerged metal arc welding (SMAW) pipemaking.

Figure 2-26 shows the schematic of pipe forming process from the beginning.

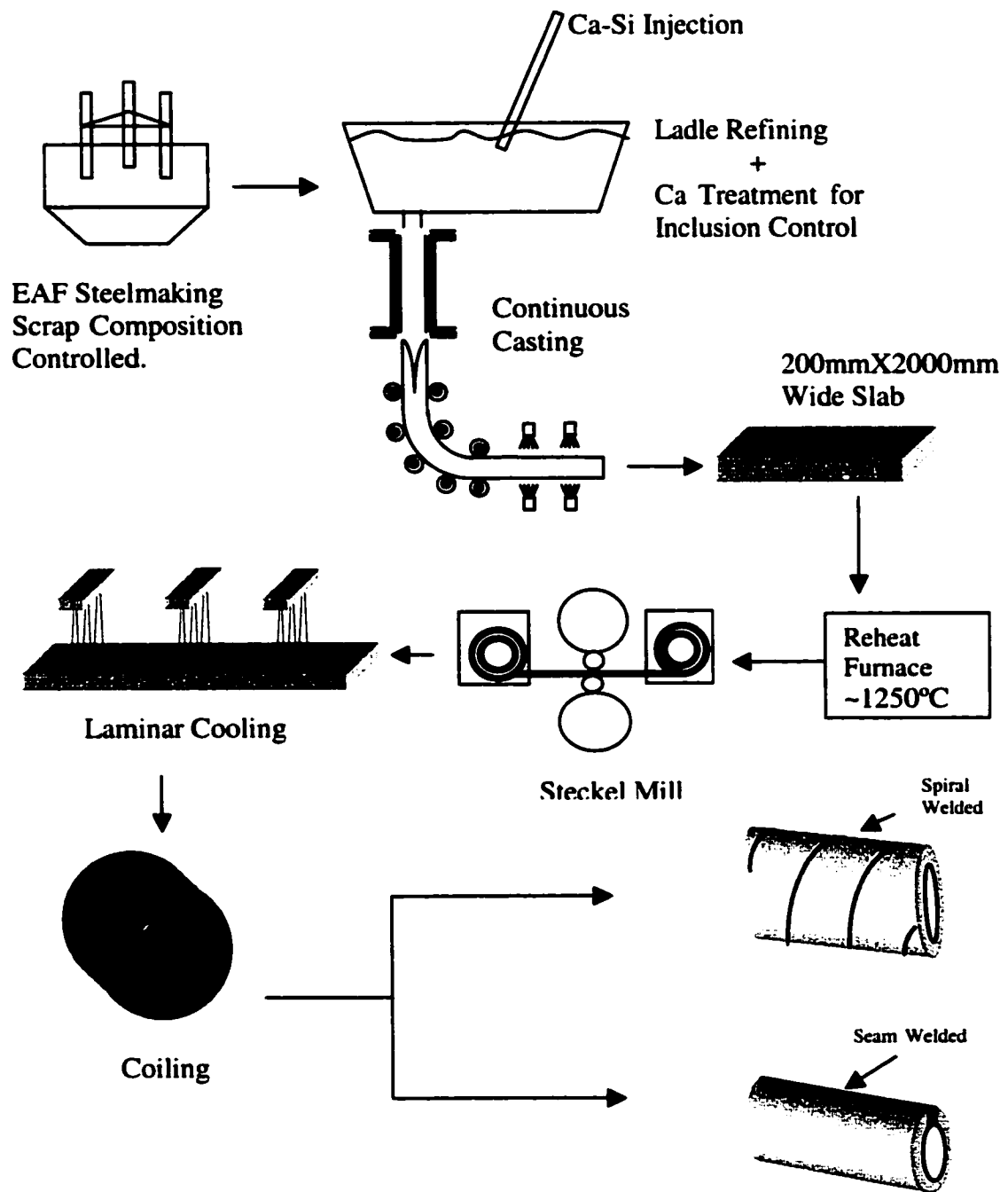


Figure 2-26 Schematic of production of microalloyed line pipe.

## **2.12 Controlled Rolling**

The need for grain refinement stimulated the development of controlled rolling techniques to produce steels with high strength and good toughness. Grain refinement is the only strengthening mechanism that increases strength and lowers the ductile to brittle transition temperature (DBTT) simultaneously. All other mechanisms like precipitation hardening and second phase strengthening, which increase the strength, are detrimental to toughness [DeArdo88].

Controlled rolling is ideally suited for microalloyed steels, because good control can be exercised on the precipitation sequence by controlling the temperature and deformation of steel. Also, the microalloying additions, when in solution, control the transformation of austenite to ferrite. Generally, microalloying elements increase the temperature where complete recrystallization occurs and retard the recrystallization of austenite below this temperature. The precipitate particles of these microalloying additions restrict the grain growth of austenite by retarding the grain boundary movement through pinning them. This leads to a highly deformed, fine austenite grain structure. Since the initial austenite grain size is smaller, the resulting ferrite grain structure after the  $\gamma \rightarrow \alpha$  transformation is finer still [DeArdo88][Morrison95].

The effect of microalloying elements in grain refinement is a function of the solubility of their precipitates in austenite. There is little evidence to indicate that the influence is related to precipitate morphology or their composition per se. Their effect is a function of their size and the temperature at which they exist in relation to the transformation temperature. When the steel is reheated, the TiN due to its low solubility in austenite does not dissolve or precipitates at high temperatures ( $\sim 1200^\circ\text{C}$ ). This stops the grains of austenite from growing to a large size, by their grain boundary pinning. Also, since the Ti ties up any extra nitrogen present in steel at high temperatures, it allows the Nb to remain in the solution. Nb in solution is very effective in depressing the transformation temperature of  $\gamma \rightarrow \alpha$ . Therefore the

formation of low temperature transformation products like bainite is favored. Also, Nb(C,N) forms at lower temperatures ( $\sim 800^{\circ}\text{C}$ ) and precipitates on strain bands, dislocations, grain boundaries as part of strain induced precipitation. This fine dispersion of precipitates is essential for the high strength in these steel. Hence, the temperature dependence of solubility dictates the onset of precipitation at different stages of rolling and at different regions in the microstructure.

### **2.12.1 Stages in Controlled Rolling of Microalloyed Steels**

Controlled rolling is typically divided into four stages, although only two or three stages may be involved in practice. The information in this section is based on [Kim83][Sage83][Sangal92].

#### **2.12.1.1 Deformation in the Austenite Recrystallization Region**

The initial austenite grain size controls the grain size of unrecrystallized austenite in the second stage and hence controls the ferrite size. The fineness of the ferrite is essential to the strength and toughness of all steels. Therefore, it is desirable to refine the austenite grain size as much as possible by consecutive deformation and recrystallization. The reheating temperature and solubility of microalloy precipitates have a strong influence on the grain size of initial and recrystallized austenite. A low reheating temperature leads to reduced rates of grain boundary movement. At higher reheat temperatures, most of the microalloy precipitates dissolve in the austenite. Some of the precipitates (like TiN) do not dissolve until very high temperatures (up to  $1300^{\circ}\text{C}$ ). These precipitates stop the grain boundary movement of recrystallizing austenite, thereby keeping austenite grains size to a finer scale.

Precipitates formed during deformation (strain-induced precipitation) inhibit the grain growth of recrystallized austenite in the same manner. The degree of deformation applied also influences the grain structure. The smallest recrystallized grain size can be obtained by using deformation just above the critical amount

required for completion of recrystallization. Below the critical amount of deformation, partial recrystallization occurs resulting in a duplex austenite structure, comprising of fine recrystallized grains with large, deformed but unrecrystallized grains. This duplex austenite grain structure is to be avoided as it leads to a non-uniform ferrite structure after transformation and cannot be removed by subsequent rolling.

#### **2.12.1.2 Deformation in the Non-recrystallization Region**

The rolling is performed at a temperature below which the austenite does not recrystallize ( $T_{nr}$ ) and above the  $A_{r3}$  temperature. In this regime the recrystallization of austenite grains is suppressed enough so that rolling produces deformed, elongated austenite grains. It was shown first by Irani et al. that austenite grains are rolled into 'pancake' shaped structures.

Microalloying elements retard the recrystallization of austenite either by a solid solution effect (solute drag) or by the pinning effect of strain induced precipitates. Deformation in this temperature range also produces deformation bands within the austenite grains. These two factors, the elongated grains of austenite and deformation bands within them, influence ferrite nucleation by providing preferential nucleation sites. With increasing amount of deformation, the austenite grains become more elongated, increasing their length to thickness ratio, and the number of deformation bands increases and their distribution becomes uniform, giving rise to a fine and uniform final structure. During transformation, ferrite grains nucleate on both sides of the deformed austenite grain and develop a grain size approximately half the minor axis of the pancaked austenite grains.

#### **2.12.1.3 Deformation in the $\alpha+\gamma$ Two Phase Region**

This stage of rolling is a complex process. Ferrite nucleates from heavily deformed austenite and is itself deformed. The ferrite is warm worked and may or

may not recover and recrystallize. This produces, besides equiaxed grains (if recrystallized), regions of high dislocation density and dislocation substructure. As the amount of deformation is increased, there is enhanced recovery and recrystallization of deformed ferrite and substructure volume increases in the mixed structure. This leads to increased yield and tensile strength along with lower DBTT, but lower impact energy. The lowering of DBTT by controlled rolling in the  $\alpha+\gamma$  two phase region is partly due to the presence of fine recrystallized ferrite grains and subgrains but is primarily due to the occurrence of separation (splitting) sometimes associated with crystallographic texture.

#### **2.12.1.4 Deformation in Ferrite Range**

This is not a very common practice. However in some cases the rolling is continued to as low as 690°C. Little has been reported on structure of steels rolled at such low temperature. It has been shown that the ferrite pearlite steels of similar composition sometimes give a continuous stress strain curve and sometimes discontinuous curve in a tensile test [Sage83]. Rolling in this region cold works the ferrite, which could explain the continuous stress strain curve. It is also possible that recovery could occur or heavy deformation may result in recrystallization, leading to a discontinuous curve.

## **2.13 Accelerated Cooling**

Accelerated cooling was developed in the early 1960s to reduce the length of run out tables on hot strip mills. The unexpected benefits derived from the initial uses led to large research and development efforts in the area. At present, it is a mature field with the physical metallurgy principles involved in microstructure control well established. Controlled cooling is an integral part of thermomechanical processing of microalloyed steels. It is routinely used in the production of virtually all types of steel products: strips, plates and long products [DeArdo88-2][Pereloma96-2].

Some of the benefits associated with accelerated cooling of flat products are as follows [DeArdo88-2][Collins]:

- Increased strength: coiled strip of high strength microalloyed steel.
- Better formability in coiled strip of drawing quality aluminum killed (AK) steel.
- Higher strength plate product with no deterioration in toughness.
- Improved weldability of plate product with no sacrifice in base plate properties.

Accelerated cooling for line pipe results in faster cooling rates and lower coiling temperatures. This influences the microstructure in two ways. Firstly less ferrite and pearlite and more bainite are formed and secondly, all microstructural features are present on a finer scale [Pereloma96-3].

### **2.13.1 Effects of Accelerated Cooling on Strength of Microalloyed Plate**

There are at least four sources of higher strength in accelerated cooled steels, which are discussed in the following sections [DeArdo88-2][Pereloma96-2] [Pereloma96-3].

### 2.13.1.1 The Formation of Fine Dispersion of Bainite

As evident from the CCT diagram in Figure 2-27, a high cooling rate is successful in avoiding the ferrite + pearlite nose, leading to a final microstructure which is a mixture of ferrite + bainite.

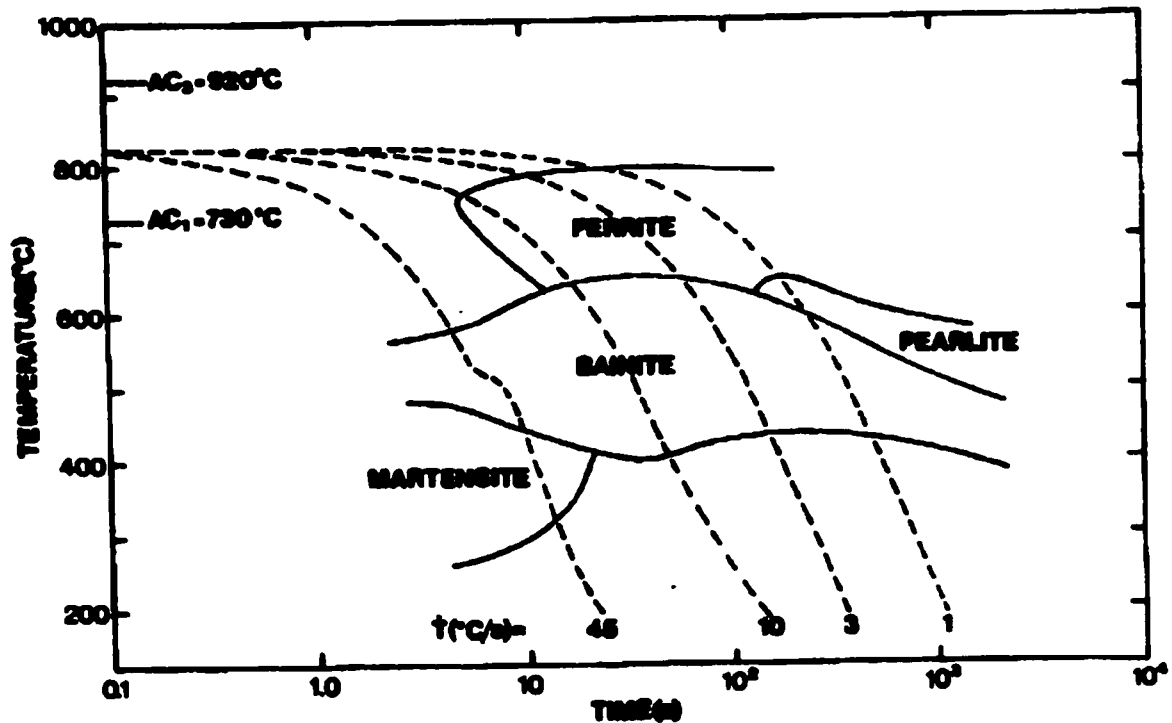


Figure 2-27 CCT diagram of a typical microalloyed steel [Collins85].

### 2.13.1.2 Significant Grain Refinement of Ferrite

The final grain size of ferrite is dependent on the rate of nucleation, growth and coarsening. The nucleation rate of ferrite is controlled by the number of sites for nucleation, i.e.  $S_v$ , times the nucleation rate for that specific site. The  $S_v$  factor is determined by state of austenite at the time of transformation, i.e., the degree of controlled rolling. The specific nucleation rate is determined by the transformation

temperature, i.e., the supercooling. Traditionally the transformation temperature of significance for ferrite nucleation is taken to be the transformation start or  $A_{r3}$  temperature and the driving force for nucleation is  $(T = A_{e3} - A_{r3})$ . However, recent work shows that not the transformation start temperature but some temperature that characterizes the temperature range over which the transformation occurs is the critical factor [DeArdo88-2]. In accelerated cooling this temperature range is lower, hence finer ferrite produced.

Grain coarsening can be described by the following relation by Fullman [DeArdo88 ]

$$D^2 - D_0^2 = k_0 t \exp(-Q / RT) \quad (5)$$

$D$  is the average grain size,  $D_0$  is initial grain size before coarsening,  $k_0$  is a constant,  $t$  is the time available for coarsening and  $RT$  have the usual meaning.  $Q$  is the activation energy for the process. Hence as the temperature of the transformation is lowered by accelerated cooling, both ferrite and the precipitates which accompany the transformation are less inclined to coarsen.

### 2.13.1.3 More Effective Precipitation Hardening

The strength increments due to precipitation can be described by the Orowan, Ashby relationship [DeArdo88]:

$$\Delta Y_{Sp} = K \frac{f^{1/2}}{D} \quad (6)$$

$K$  is a constant,  $f$  is the volume fraction of precipitates and  $D$  the mean planar intercept diameter of the precipitates. Due to accelerated cooling precipitates formed are finer and more dispersed. This leads to low values of  $D$  and higher strength.

#### **2.13.1.4 Higher Dislocation Density in Ferrite**

As the temperature of the transformation is decreased as a result of accelerated cooling, the ferrite formed has a very high dislocation density. There are two sources of this very high dislocation density. One source is the volume expansion that accompanies the FCC-BCC transformation. The other source is the austenite to bainite transformation which is a shear assisted transformation with accompanying volume changes. Both these factors contribute to formation of highly dislocated grains.

#### **2.13.2 Effect of Accelerated Cooling on the Toughness of Microalloyed Plate**

Accelerated cooled steels show improvement in resistance to brittle fracture in ferrite-bainite plate even though these are substantially stronger than their predecessors. Also, the formability or resistance to ductile fracture is much improved despite increasing strength level. This may be attribute to two factors:

- 1) Extra grain refinement of ferrite leads to better fracture toughness.
- 2) The low temperature transformation product formed by accelerated cooling, i.e., bainite is distributed as a fine, homogenous constituent. Therefore, although bainite itself is hard, its distribution is much less damaging than compared with large nodules or colonies of pearlite formed in air cooled steels.

## **2.14      Steckel Mills**

Steckel mills are used for thermomechanical rolling of microalloyed steels to meet the growing demand of exact mechanical properties, narrow dimensional tolerances and high surface quality. A steckel mill is a 4-high reversing mill with heated coil boxes on either side. This produces conditions approaching isothermal rolling and consequently better control of precipitation behavior [Collins95][Kramer97].

As has been the topic of various conferences and past the two decades of research into the field, microalloyed steels derive their desirable microstructure and properties from control of precipitation at various stages of deformation and transformation. The precipitation is strongly dependent on temperature. It is difficult in continuous cooling in conventional reversing mills to control the temperature and thereby precipitation accurately. Steckel mills with heated coil boxes meet these objectives very closely.

### **2.14.1      Characteristics of Rolling in a Steckel Mill**

After the plate has been rolled down to transfer bar in a roughing mill it is sent to the 4-high reversing finishing mill. Figure 2-28 shows the setup of a Steckel mill [Kramer97]. The strip is threaded onto the mandrel of one of the coiling furnaces through an entry side pinch roll unit. The delivery-side pinch roll unit feeds the strip to the delivery-side coiling mandrel. After the first few wraps have been coiled, the tension is established and the mandrel moves with the same speed as the mill. Constant strip tension is applied during rolling, based on the strip width and gage. Insufficient tension may cause operating problems, whereas excessive tension can result in width necking.

As the tail end of the strip enters the stand the mill is braked in such a way that the tail end clears the roll gap but is not coiled on the mandrel. The roll gap is automatically preset for the next pass and rolling is carried out in reverse.

During each reversing phase the ends of the strip are subjected to faster cooling than its body. This leads to a temperature drop of as high as 250°C at both ends of the strip, in a 7 rolling pass schedule. As a result of these temperature drops, the rolling force along the strip length increases at the strip ends. This characteristic is typical of Steckel mills. To keep the temperature drop to a minimum, the main drive motor and finishing mill equipment are designed in such a way to enable fast reversing capabilities. At present, reversing times of below 3s have been reached.

## **2.14.2 Control Systems in a Steckel Mill**

To counteract the variation in rolling forces, which are typical of a Steckel mill, different control systems are employed.

### **2.14.2.1 Automatic Gage Control**

In conventional hot strip mills, an electromechanical screwdown system is typically used for gage control. However, the demands placed on gage control of a Steckel mill system are much greater due to better dimensional homogeneity requirements. To achieve this, hydraulic roll gap systems are used. They allow virtually any desired adjustment speed. The response time for small position movement can be as low as 40ms. Such systems allow the effect of temperature drops at the strip ends to be efficiently counteracted.

### **2.14.2.2 Roll Alignment Control (RAC)**

If the strip flow is off center with respect to the rolls or there are temperature differences across the strip width, it may lead to skew positioning of the work roll and thus to a wedge shaped roll gap. To avoid this condition, Steckel mills are equipped with a RAC that keeps the loaded roll gap parallel, even when there are changing differential rolling forces. The differential rolling forces measured along the width of

the strip are converted to a steering (or leveraging) signal for the hydraulic roll gap setting.

### 2.14.2.3 Profile, Contour and Flatness Control

Automatic gage control with a hydraulic gage setting ensures that a point on the width of the strip is controlled to a specified gage length all across the length of the strip. However, elastic deformation of the mill stand, thermal expansion of the rolls and wear on the rolls may lead to changes in gage across the width of the strip. This is referred to as the strip profile. It is desirable to keep the strip profile to a pre-specified value, within narrow tolerances. To improve strip flow during subsequent cold rolling, a profile exhibiting a parabolic shape across the width of the strip is required. This is achieved through use of a S-shaped roll contour.

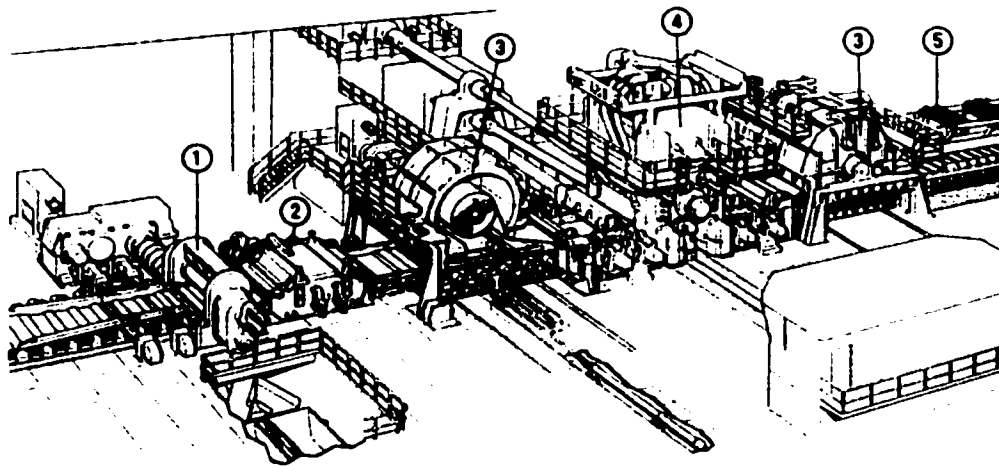


Figure 2-28 Schematic depicting the typical setup of a Steckel mill; 1. Crop shear and entry side guides; 2. Drum type crop shear; 3. Coiler furnace; 4. 4-high reversing stand; 5. Laminar cooling section [Kramer97].

## **2.15 Types of Linepipe Steels**

In general, the microstructural features of microalloyed linepipe steels are too complex to enable a definite comparison to be made between the microstructure and the resultant mechanical properties. General classification is made, based on their major constituent and deformation behavior. The microalloyed steels can be classified into three different types each having a different basic structure that has a profoundly different effect on the mechanisms of deformation and the relationship between plate and pipe properties [DeArdo88][Kim83][Sage83].

- 1) Ferrite-pearlite microalloyed steels, but with low or reduced pearlite content, which exhibit a discontinuous stress-strain curve in the tensile test.
- 2) Bainite/acicular ferrite microalloyed steels. These have an increased work hardening coefficient and exhibit a continuous stress-strain curve.
- 3) Multiphase microalloyed steels. These contain a matrix of polygonal ferrite and a major portion of a second phase, such as low-carbon bainite (also referred to as acicular ferrite) and/or islands of martensite and retained austenite. These exhibit continuous stress-strain curves.

The distinction between bainite/acicular ferrite steels and multiphase steels based solely on their microstructure might not be so marked, because bainite/acicular ferrite steels sometimes contain a considerable amount of other phases such as polygonal ferrite and/or martensite. However, there is a major difference in metallurgical design principles. Bainite/acicular ferrite steels are designed primarily to obtain high strength and good toughness through high dislocation density and a finer effective grain size of bainite/acicular ferrite matrix. On the other hand, multiphase steels utilize the concept of a composite in that the matrix of fine polygonal ferrite is responsible for good toughness, while strong second phases of bainite and/or martensite are responsible for high strength.

### **2.15.1 Ferrite-Pearlite Microalloyed Steels**

Ferrite-pearlite microalloyed steels obtain their strength mainly from grain refinement and precipitation strengthening. Additional strength can be obtained by deformation in the  $\alpha+\gamma$  two phase region. These steels invariably contain vanadium and niobium as alloying additions. The major role of these additions is to refine the ferrite grain size, but they also have the additional important function of increasing the strength of ferrite pearlite steels by precipitation hardening.

It is important to control the sequence of precipitation, as not all the precipitates have the same strengthening effect. Precipitates that form in austenite, either retained particles undissolved during reheating treatment or particles formed by strain induced precipitation are too coarse and widely spaced to contribute effectively to the strength. However they may have the important effect of preventing the austenite grains from growing to abnormally large sizes at the time of reheating. On the other hand, interphase particles formed at the  $\alpha/\gamma$  interphase during transformation and precipitates formed in ferrite during cooling are smaller and more finely distributed. These contribute significantly to strength. Thus it is necessary to retain some microalloying elements in austenite for subsequent precipitation in ferrite. The cooling rate after controlled rolling has a strong effect on the degree of precipitation. Too slow a cooling rate allows the particles to coalesce, thereby making them less effective for strengthening. With faster cooling rates, no precipitation may occur and microalloying elements remain in the solution.

During pipe forming operations with steels in cold worked conditions, the steels undergo at least one reversal of stress during the pipe forming, expansion and test-preparation operations. Strong barriers to dislocations, such as precipitates create back-stresses due to dislocation pile-ups, which can be wiped out by reverse straining that leads to permanent softening. Thus with ferrite pearlite steels it is commonly observed that some loss in strength occurs between plate and pipe. This phenomenon was noticed first by Bauschinger and named after him.

### **2.15.2 Bainite/Acicular Ferrite Microalloyed Steels**

In linepipe technology, the distinction between acicular ferrite and low-carbon bainite is vague. Sometimes the terms are used to denote the same structure. Generally acicular ferrite is defined as a highly substructured, non-equiaxed ferrite that forms in continuous cooling by a mixed diffusion and shear mode of transformation that begins at a temperature slightly higher than the upper bainite transition temperature.

Bainite/acicular ferrite microalloyed steels have a good combination of strength and toughness due to a high dislocation density and fine effective grain size. In addition to the high strength and good toughness, these steels have the advantage of continuous yielding. An additional increase in strength results from pipe forming. Continuous yielding is a consequence of high density of mobile dislocations present in the ferrite laths. The loss in strength due to permanent softening of precipitation or dislocation strengthened steels is partially offset by the increased work hardening characteristic of steel that increases the tensile strength of the deformed material (i.e., the pipe).

### **2.15.3 Multiphase Microalloyed Steels**

Multiphase microalloyed steels consist of a polygonal ferrite matrix with dispersions of second phase particles. The second phase can be acicular ferrite, bainite, martensite or a combination of these depending on the alloy compositions and process variables. The strength of multiphase steels is generally determined by the volume fraction and type of the second phase. In steels of this type, the hard areas of the second phase, under stress, introduce a high density of mobile dislocations in the surrounding polygonal ferrite matrix. The work hardening coefficient is therefore high, deformation takes place below the yield strength of the plate, and a continuous stress strain curve results. The multiphase steels have a higher initial work hardening rate than ferrite- pearlite and bainite/acicular ferrite steels. This causes the multiphase

steels to have a high yield strength, approaching ultimate tensile strength, after pipe forming.

## **2.16 Practical Pipeline Steels**

- **X60**

Pipes for gas or oil are made on the specifications based on API 5LX60, usually produced as controlled rolled ferrite-pearlite 0.03% Nb steels. Adequate strength is achieved from ferrite grain refinement and there is little loss of strength between plate and pipe [Sage83].

- **X65**

These are made mostly as controlled rolled 0.03Nb-0.06Ti-0.09V steels. Strength is achieved by a combination of fine grain size and precipitation strengthening. Approximately 5-% of the strength from precipitation is lost during pipemaking, and plates with a minimum of 470MPa are normally produced for this strength of pipe Sage[83].

- **X70**

These steels are used in pipe for gas transport and are made as controlled rolled 0.03Nb-0.06Ti-0.09V steels with special rolling practices involving a low reheating temperature and/or heavy primary rolling to produce an extra fine austenite and hence a fine ferrite size. Some grades contain chromium to produce bainite in the structure and increase the work-hardening capacity [Sage83].

- **X80**

This is the newest class of steels in commercial usage today. A typical composition is 0.09Nb-0.06Ti-0.06V. The underlying microstructure is very different from the earlier classes. These steels have a matrix of composed mainly of acicular ferrite with

small amounts of bainite and martensite-austenite constituents [Gärtner92]. The steels are characterized by a very fine dispersion of carbo-nitride precipitates of Nb and Ti (and V in cases).

- **X100**

These are the linepipe steels of future. Many mill trials are underway at present to develop these steels from the laboratory to commercial production. The impetus for development of X100 steel is further reduction in wall thickness for linepipe, superior field weldability and higher toughness at lower temperature. These steels are Low C-Mo-Nb containing steels [Collins98][Nagae99].

## **Chapter 3: Experimental**

### **3.1 Materials Analyzed**

Three types of steels were analyzed, X70, X80 and Grade80. The material was provided by IPSCO, Regina, Canada. The X70 and X80 steels are intended for manufacture of linepipe. Here the two digit number (70 or 80) refers to its specified minimum yield strength (SMYS) in ksi. The Grade## nomenclature is used for plate steels. The plates are used for various applications in the construction industry and for thick plate trucks and industrial movers for carrying heavy loads. The two varieties of steel are very similar in composition and processing. The major difference is that for linepipe the C levels are kept a little lower to have better weldability and alloy additions are slightly higher to achieve the SMYS.

The X70 and X80 steels were provided as portions of large diameter pipes (>1000mm diameter). Smaller pieces were cut using a band saw from them in the LS, ST and LT orientations. Care had to be taken when obtaining specimens of particular orientation with respect to the rolling direction of the initial plate. As the large diameter pipes were spirally welded, the rolling direction (RD) was not parallel to the longitudinal to pipe axis (LPA) direction. Figure 3-1 illustrates this relationship schematically. The rolling direction on the pipe could be easily identified by the weldments on the surface when plate was being spiralled for welding into a pipe. For plate steel (Grade80) the case was simpler. The rolling direction was along the length of the plate. Figure 3-2 shows the different areas that were analyzed to observe the differences, if any, due to rolling, different cooling rates at the surface and interior and unsymmetrical deformation (compression inside and tension on the outside surface) when the plate was converted to pipe.

In all three cases the material was obtained from the middle of the length of the plate.

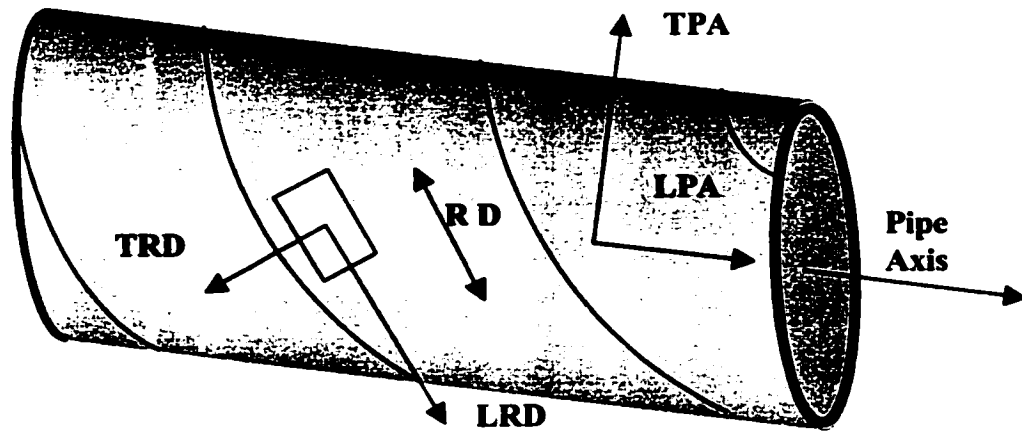


Figure 3-1 Sketch showing the relationship between rolling direction and pipe axis in a spiral welded pipe.

#### Areas observed

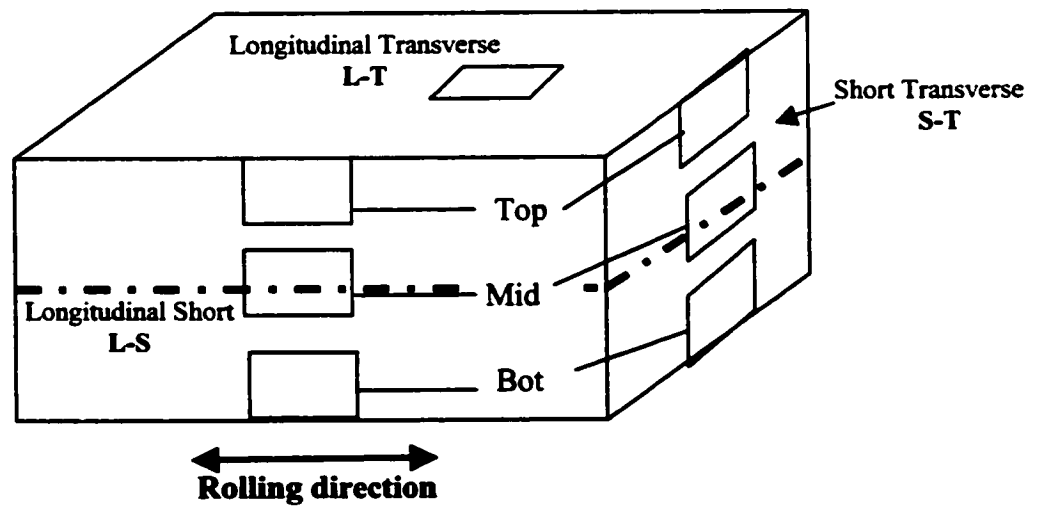


Figure 3-2 Schematic showing the various orientations examined.

Table 3-1 and Table 3-2 summarize the chemical composition and physical properties of the steels analyzed.

Table 3-1 Chemical composition of steels analyzed (in wt%).

Element	Grade80	X70	X80
C	0.062	0.040	0.033
Mn	1.640	1.745	1.820
S	0.010	0.001	0.004
P	0.014	0.010	0.011
Si	0.164	0.281	0.274
Cu	0.426	0.193	0.294
Ni	0.331	0.064	0.121
Cr	0.201	0.058	0.056
V	0.040	0.001	0.003
Nb	0.090	0.067	0.091
Mo	0.306	0.194	0.256
Ti	0.028	0.023	0.024
Al	0.027	0.045	0.038
N	0.012	0.010	0.010
Ca	0.002	0.004	0.003
B	0.0004	0.0002	0.0002

Table 3-2 Mechanical properties of steels analyzed.

Properties	Grade80	X70	X80
Yield Strength	587 MPa (LRD) 637 MPa (TRD)	545 MPa	568 MPa
UTS	770 MPa (LRD) 815 MPa (TRD)	642 MPa	668.5 MPa
Charpy, full size	140J @ RT (LRD) 75J @ RT (TRD)	375J @ RT	235 J @ RT

## 3.2 Sample Preparation and Instruments Used

### 3.2.1 Optical Metallography

Small, about 15mmX15mmX10mm, pieces were cut using a band saw, from three different orientations L-S, S-T and L-T as explained earlier in Figure 3-2. These were then mounted in one and a quarter inch bakelite mounts using the hot press method. Once mounted the samples were ground and polished. Initial rough grinding was done on belt grinder to make the surfaces smooth and parallel. The surface was ground successively using wet, SiC embedded polishing wheels in the sequence of 240, 320, 400 and 600 mesh size grit. Before final polishing with 0.05 $\mu$  alumina, the surface was pre-polished using 3 $\mu$  diamond paste. After the surface was prepared in this way to a smooth, mirror finish devoid of any scratches, it was etched to reveal its microstructure. Different etchants were used to reveal the various microstructural features present. Table 3-3 highlights the types of etchants used.

Table 3-3 Etchants used for optical metallographic examination.

Etchant	Composition
Nital	2% Nitric acid in ethanol
Picral	4% Picric acid in ethanol
Modified LaPera's	a) 10% HCl in water b) Saturated solution of picric acid (4%) in 100ml ethanol c) 1g sodium metabisulphite and 1g EDTA in 100 ml water. Sample etched for 10s in a) and then for 45 sec in a mixture of equal parts of b) and c)

The etched specimens were studied in either of the two different types of optical microscopes present in the department lab. The first was an Olympus PME3 model microscope coupled to image analysis software through a CCD camera. However, it only had a maximum magnification of 400X. It was useful in studying the microstructure at lower magnifications and for counting non-metallic inclusions through the software. The other microscope was a Zeiss Ultraphot-3 attached to a

polaroid camera and a video-capture system. Magnifications up to 2000X were obtainable using an oil immersion lens. This was used to study the finer microstructural features not readily apparent in the other microscope.

For studying non-metallic inclusions automatic image analysis was used [Shehata86]. The surface was prepared to 0.05 $\mu$  finish as usual. However, samples were used unetched to provide a bright background for the darker inclusions. The prepared samples were used immediately (within 1-2 hours of polishing), because if left in air they showed signs of degradation and pitting. This gave rise to artifacts and errors in counting the actual population distribution of the inclusions. Also, since the inclusions were water soluble, care had to be taken to use the minimal amount of water in polishing and cleaning of the surface. The samples were immediately dried after polishing, however, some of the smaller inclusions dissolved. During image analysis, the pits left behind were included in the inclusion count. Figure 3-2 shows the areas from which data was collected to give a representative count and ascertain if any differences arose due to directional rolling.

70 images were captured for image analysis from each of the regions: LS-mid, LS-top and LS-Bot (amounting to a total of more than 200 inclusions at each particular region) to give a good, statistically representative sample. The images were captured in 8-bit grayscale mode and calibrated using the in-built calibration standards of the software application. After calibration a cutoff value of graylevel was chosen (0-140) which delineated the second phase from the lighter background. This cutoff level was kept constant for all subsequent observations. Once the features had been identified this way, the software could perform a host of measurements including area, aspect ratio, roundness, density, ferret diameters, etc. Since it was found in few trials that almost all the inclusions in X70 and X80 were spherically shaped, area and aspect ratio measurements gave a good indication of the shape and size distribution of the inclusions. Other properties, like 'roundness', for example, reflected the 'aspect ratio' owing to the simple shape of the inclusion. The case for Grade80 was a little different. Some elongated inclusions were found in the centerline

of the plate. However, it was not possible to delineate them from the matrix using the software due to low contrast. These were counted manually. The other areas, i.e., top and bottom surfaces, had rounded inclusions similar to X70 and X80 and were counted as such.

### **3.2.2 Scanning Electron Microscopy (SEM)**

The sample preparation for SEM was very similar to that for optical metallography. However, the samples were etched for longer times (2-3 times longer) to enhance contrast. The SEM used was a Hitachi S-2700 equipped with an ultra-thin window (UTW) Ge x-ray detector. All observations were made at 20kV. SEM was useful in providing a general overview of the grain shape and size and in studying the non-metallic inclusions. Some of the larger precipitates were easy to characterize in the SEM, but owing to the large interaction volume of the electron beam ( $\sim 1\mu\text{m}^3$ ) it was not possible to study the smaller precipitates ( $<0.5\mu\text{m}$ ). It was not possible to analyze the crystal structures of the constituent phases in the SEM, so thin foils and carbon replicas were analyzed by transmission electron microscopy (TEM) for high resolution characterization.

### **3.2.3 Transmission Electron Microscopy (TEM): Thin Foils**

Again, the samples were cut in three different orientations, L-S, S-T and L-T (Figure 3-2). A thin (about 1mm) section of the material, about  $1\text{cm}^2$  in area, was sliced from the required orientation, using a band saw. It was then ground to a thickness of 70-100  $\mu\text{m}$  on SiC paper. 3mm diameter discs were punched out using a disc punch specifically made for this purpose. These discs were then electropolished in a Tenupol twin jet electropolisher. This produced a small perforation in the middle of the disc whose edges were electron transparent. The polisher had an automatic termination system which stopped the polishing as soon as the smallest perforation was detected. This was done to ensure the retention of narrow areas at the edge of the perforation, which are thin enough (50-100nm) to be transparent to electrons in the

TEM. Once perforated, the samples were immediately extracted from the polisher and dipped in ethanol to clean off the residual etchant and prevent oxidation of the surface. If required, the samples were further thinned in a Gatan model 600 ion mill. Ion milling was also useful for cleaning any residues from the surface of the thin foil. Milling was done at low incidence angles ( $12^{\circ}$ - $15^{\circ}$  to the surface) with an argon beam and low beam energies (3-4 kV) to minimize specimen damage and any artifacts. Times from 0.5 to 1 hr were used for ion milling. Figure 3-3 shows a schematic of the thin foil process. Table 3-4 shows the operating conditions for electropolishing of thin foil samples.

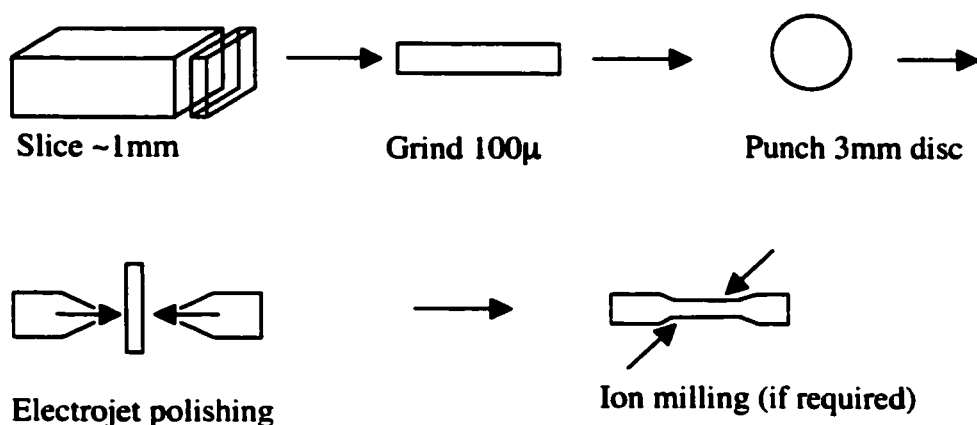


Figure 3-3 Schematic showing preparation of thin foil samples for transmission electron microscopy.

Table 3-4 Operating parameters for electrojet polishing.

Parameters	Values
Potential difference	40-60V
Current	20-80mA
Temperature	around -60 degreeC
Time	10s to 1min
Etching Solution	15% perchloric acid in ethanol

The TEM used was a JEOL EM2010 equipped with UTW Ge x-ray detector. The TEM was operated at 200kV. The ferromagnetic behavior of the thin foil caused TEM operation problems, particularly with regards to tilting and alignment. Also, it was difficult to observe very small precipitates due to the masking effect of the iron matrix. This was alleviated by preparing carbon replicas.

### 3.2.4 TEM-Carbon Extraction Replicas

Figure 3-5 depicts the sequence of operations in making a carbon replica. The steel was polished to a  $0.05\mu$  surface finish as for optical metallography. It was then etched with 10% nital to remove the iron matrix. The precipitates and inclusions were not affected by the etchant and stood proud of the surface. A thin film of carbon was then deposited by evaporating carbon from a rod under vacuum. A Hitachi carbon evaporator was used for this purpose. The deposited film was cut into small pieces (about 1.5mm X 1.5mm) using a scalpel on the surface of the specimen. The film was then delaminated from the surface of the metal using a 10% nital solution. The nital seeps beneath the carbon film and detaches it from the surface. The small segments of carbon film float in the solution. These were then transferred to baths of 100% ethanol, 50% ethanol + 50% water and 100% water successively. This ensured that the film did not break and was stretched wide and flat due to the surface tension of the water. It was then 'fished' out by supporting it on a perforated Cu grid held by tweezers. After drying on filter paper, the sample with small precipitates supported on carbon film was ready for observation in the TEM.

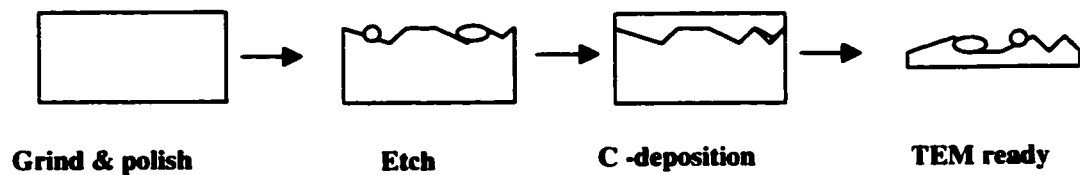


Figure 3-5 Extraction of precipitates by the carbon replica method.

## **Chapter 4: X70 Steel: Results**

### **4.1 Introduction**

X70 steel was the steel observed and analyzed first and most extensively. The insights gained from its study served as a basis for further study of other grades and provided some common grounds for comparison of various microstructural features across the various grades (X70, X80 and Grade80). To study the X70 (and subsequently other grades) a stepwise plan was charted out. The philosophy was to study first the coarser microstructural features present on a larger scale and then focus on the finer details using various analytical tools and techniques, as and when required. Consequently, initial metallographic observations were performed on low power optical microscopes and later studies were made using higher resolution SEM and TEM.

### **4.2 Grain Structure**

On observation in the optical microscope it was found that the grains in X70 steel were highly deformed and irregular in shape. This is what is typically referred to as the acicular grain structure in line pipe terminology. The grains were neither equiaxed, nor of uniform size. On the other hand they were highly deformed and of mixed size in nature. Therefore it is extremely difficult if not impossible to assign a grain size number based on the ASTM classification. Figure 4-1 shows an optical micrograph of typical microstructure of X70 steel along the rolling direction, etched with 2% nital. The micrograph was taken in LS orientation, near the middle of the thickness away from the centerline or edges to represent the bulk microstructure. The matrix is primarily composed of acicular grains with interspersed areas of polygonal ferrite.

There were areas near the centerline of the plate where large grains, elongated along the rolling direction existed (Figure 4-2a). The areas near the surface of the plate showed a more refined and equiaxed grain structure (Figure 4-2b).

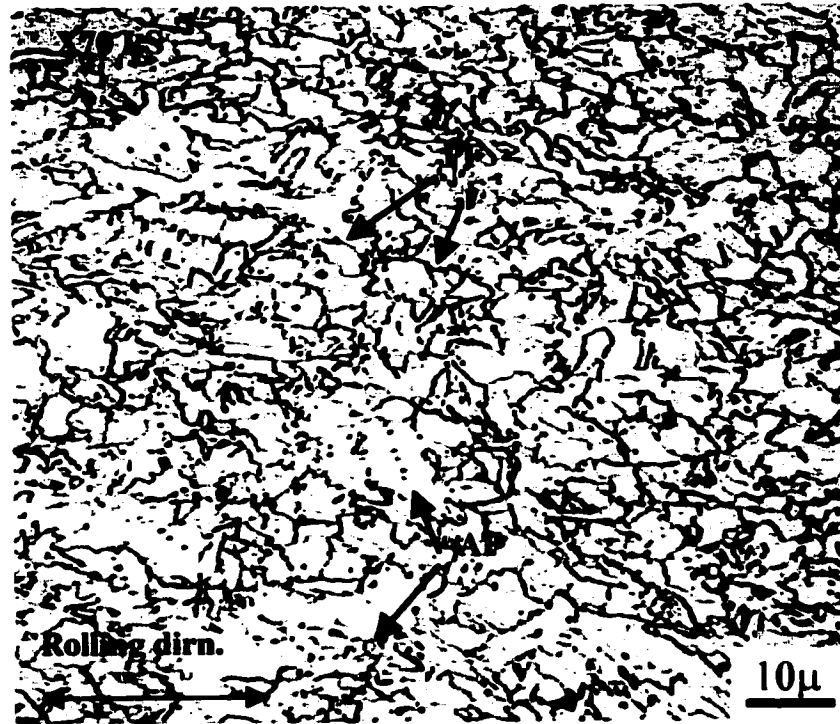


Figure 4-1 Optical micrograph of X70 steel, etched with nital, showing mixed grain structure consisting of polygonal ferrite (PF) and acicular ferrite (AF).

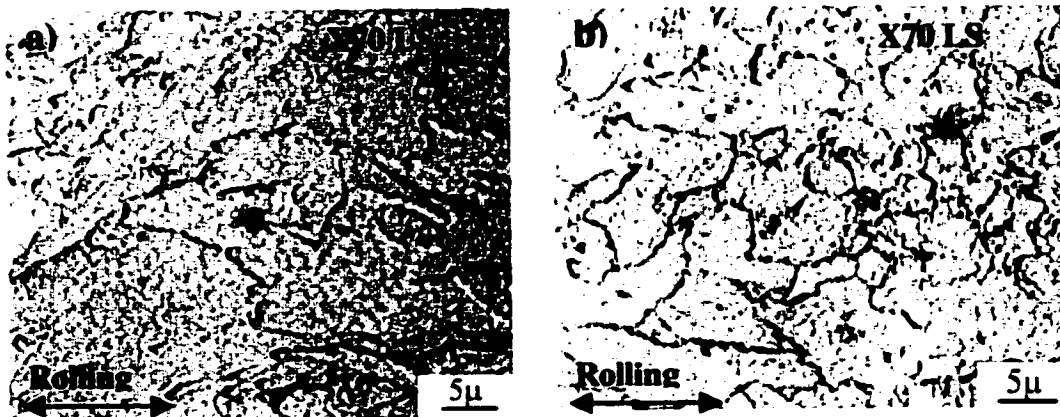


Figure 4-2 Grain structure of X70 steel in an optical microscope, a) near the center , X70-LS-mid; and b) near the surface, X70-LS-top (etched with nital).

Although measuring the grain size by the ASTM method was not feasible, a method of random intercepts was used to study and assign an apparent grain size. Some researchers have utilized automatic image analysis to calculate mean grain size [Shehata82-2]. However, it was found to be not feasible in our case as the software was incapable of delineating individual grain boundaries. Three areas, each of  $1600\mu\text{m}^2$  were selected and 30 random lines drawn for each. The number of grains intercepted by each line was counted and the inverse of this quantity provided an estimate of the grain size. About 500 grains were counted in all. The standard deviation gave an approximation of the degree of the mixed nature of grain sizes. A lower standard deviation implied that grains were more or less within a narrow size range and a large deviation reflected a cluster of large and small grains. Figure 4-3 shows a schematic of the grain size measurement and Table 4-1 shows the results obtained from near the centerline and near the surface of the plate. It is apparent that the grains are larger and of more mixed nature at the center than at the surface.

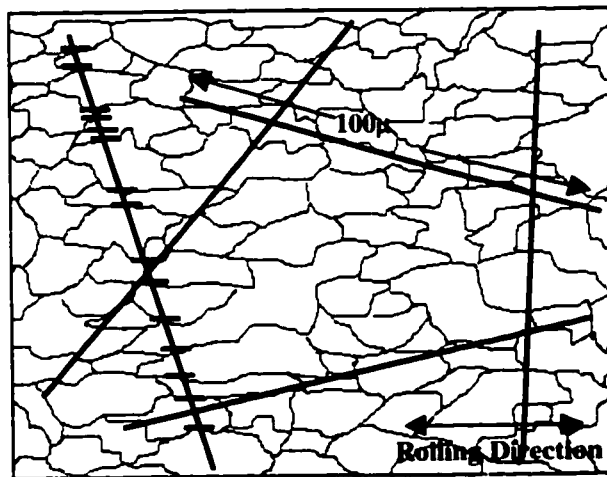


Figure 4-3 Schematic showing calculation of grain size through average intercept length of random lines.

Table 4-1 Grain size as an average intercept

Grain Size	X70	
	Center	Surface
Average intercept length ( $\mu\text{m}$ )	9.0	6.6
Standard deviation ( $\mu\text{m}$ )	4.2	2.1

A similar approach was employed to study the aspect ratio of the acicular grains. Instead of randomly oriented lines, directions along the rolling direction and perpendicular to it were chosen (Figure 4-4). More than 200 grains were counted to give a statistically representative count. Table 4-2 shows that grains are slightly more elongated in the center compared with the surface.

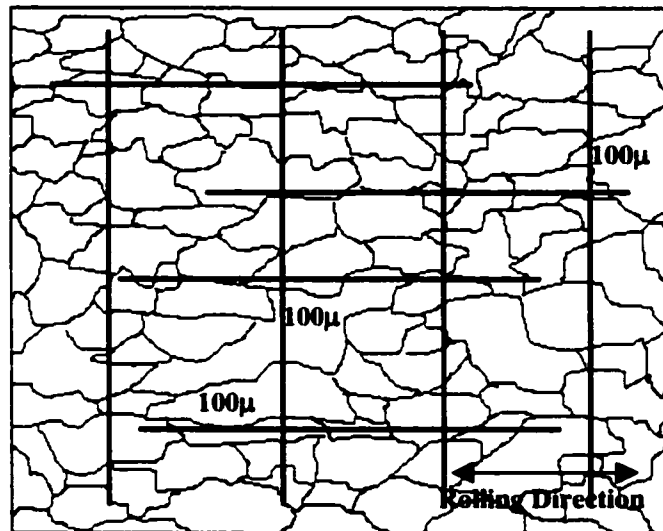


Figure 4-4 Measurement of aspect ratio of grains by comparing the average intercept length of grains along the rolling direction and perpendicular to it.

Table 4-2 Aspect ratio of grains in X70 steel along the LS orientation.

	<b>X70</b>	
	<b>Center</b>	<b>Surface</b>
<b>Aspect Ratio</b>	<b>2.2</b>	<b>1.8</b>

Figure 4-5 shows an area of X70 steel at the centerline. There appears to be some kind of segregation at the centerline as indicated by the arrow.



Figure 4-5 Optical micrograph of X70 steel along the rolling direction, showing segregation (darker areas) at the centerline. The sample was etched with 2% nital.

Use of modified LaPera's etch revealed the various constituent phases in the microstructure by coloring the ferrite tan, martensite and retained austenite white and bainite/carbide black. It was found to be most useful in the identification of martensite/retained austenite constituent. These regions are not easily differentiated through other etchants like nital and picral. Figure 4-6 shows the distribution of MAC at the center of thickness of plate and near the surface. MAC was found to be concentrated more at the centerline where the MAC islands were larger and clustered together. However, tiny, finely dispersed islands were observed throughout the thickness of the plate.

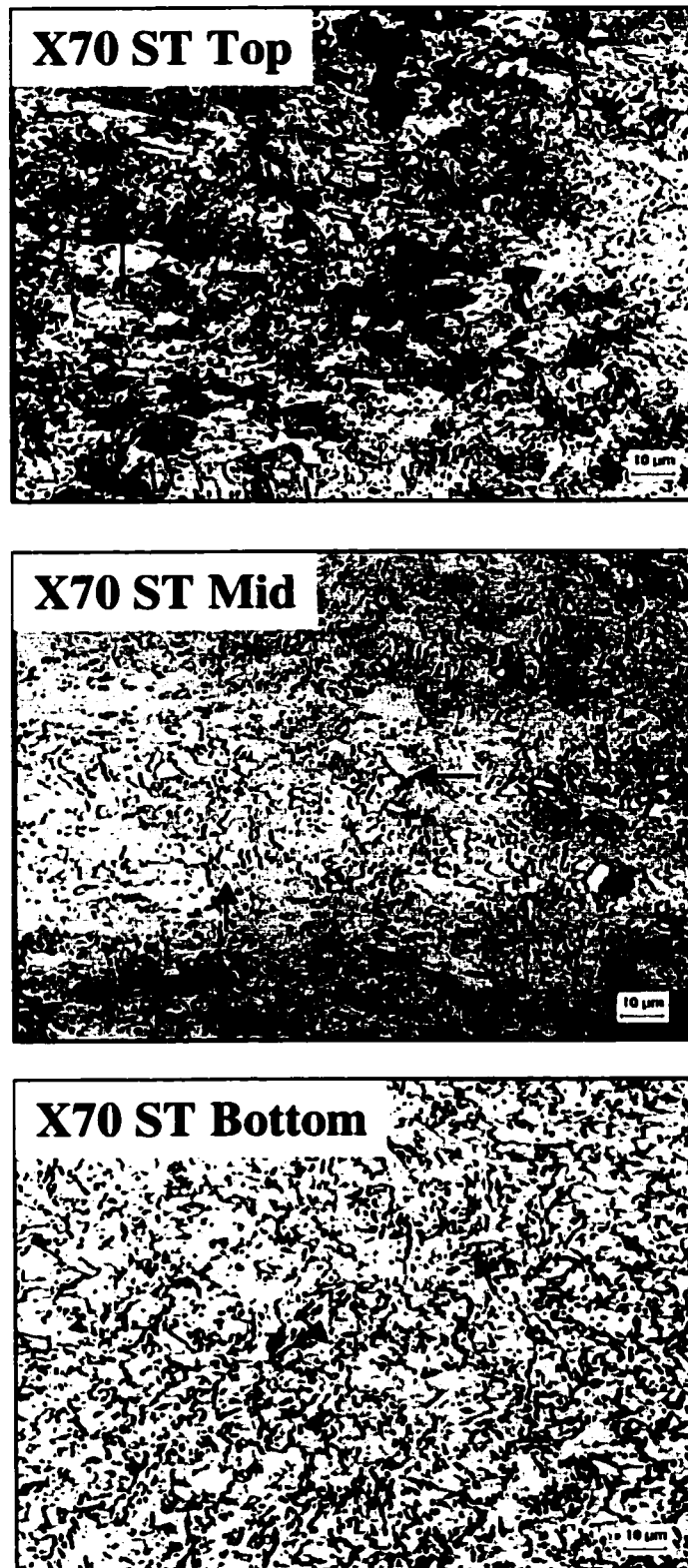


Figure 4-6 Optical micrographs of X70 steel etched with modified LaPera's etch showing the presence of martensite austenite constituent (MAC) as tiny white islands in the ferrite matrix (tan).

When etched with picral (4%) for sufficiently long times (greater than 2 min), X70 revealed pearlite-like microstructures at areas between the ferrite grains (Figure 4-7). Some of the brighter, single lamellar structures have been identified as martensite in the literature [17]. Figures 4-8a and 4-8b show the relative size and distribution of these “pearlitic” regions in the center and at surface of the plate respectively. These regions were coarser and more sparsely distributed in the center as compared with the surface region.

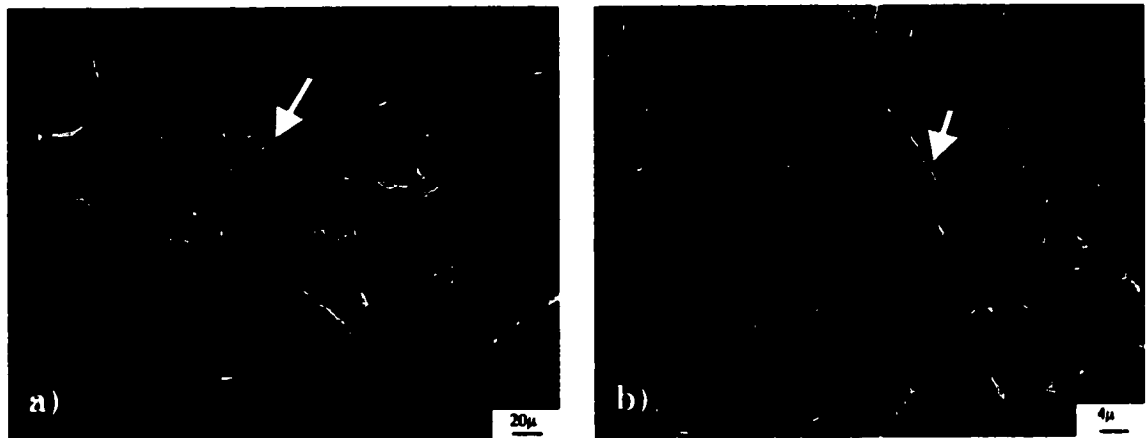


Figure 4-7 Secondary electron SEM micrographs of X70 steel etched with picral, a) showing the presence of pearlite like constituent at grain boundaries of ferrite, b) martensitic areas.

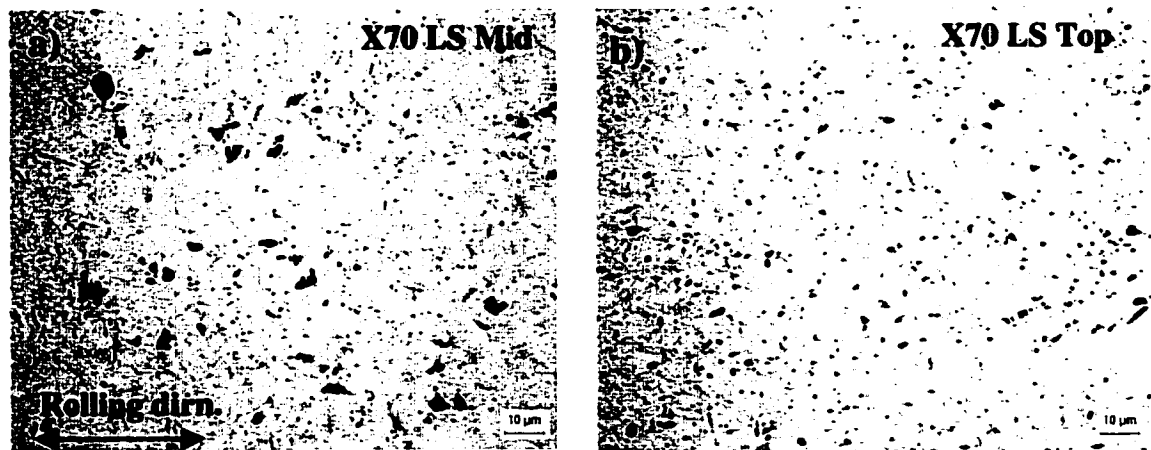


Figure 4-8 Optical micrographs of X70 steel etched with picral showing distribution of this pearlite like microstructure at c) near the centerline and d) near the surface of plate.

While optical microscopy and SEM were useful in identifying the microstructure on a larger scale they have their limitations in terms of resolution and analytical capabilities. Although, using different kinds of etchants helps in identifying various phases, still some ambiguity exists. More powerful tools like TEM have to be used to observe very fine microstructural features like dislocations, subgrains and precipitates. In addition to the higher resolution possible, most TEMs at present are equipped with analytical tools like EDX to perform chemical analysis of the areas being observed. Diffraction patterns help in identifying the crystal structure of the phase under observation.

To ascertain the crystal structure of the constituent phases in X70 steel, thin foils were analyzed in the TEM. A major portion of the microstructure consisted of acicular grains of bcc ferrite (Figure 4-9a), with many of them exhibiting low angle grain boundaries. Figure 4-9b shows the SAD pattern from two adjoining grains as marked by the circle in Figure 4-9a. The closely spaced diffraction spots indicate presence of a low angle grain boundary. Generally the grains possessed high dislocation densities (Figure 4-10a) and several small precipitates were observed associated with these dislocations (Figure 4-10b). This indicates that dislocation networks provide heterogeneous sites for the nucleation of small precipitates during coiling of the plate. This fine dispersion of precipitates leads to higher strength levels in the final product [Collins83][Tiwary95].

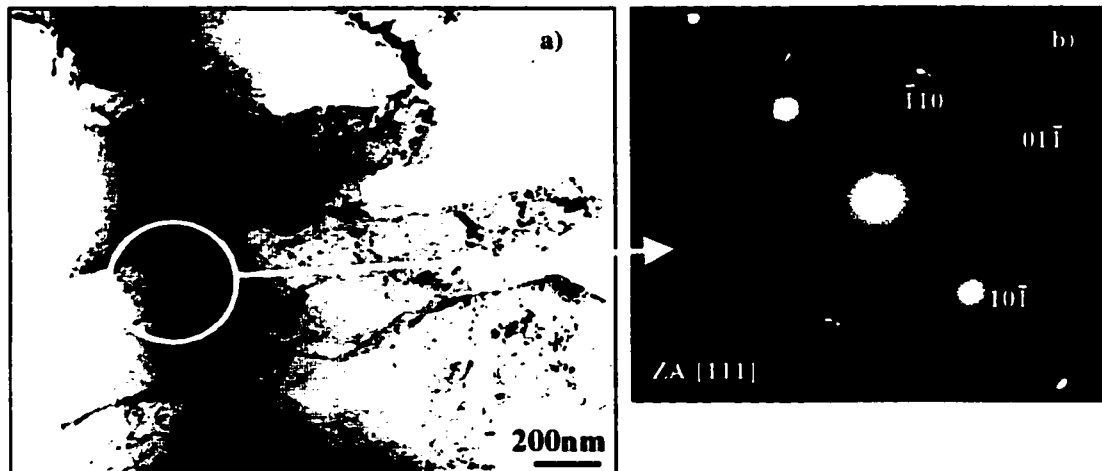


Figure 4-9 a) TEM bright field (BF) image from a thin foil of X70 steel showing elongated, acicular grains with low angle grain boundaries. The matrix is composed primarily of bcc ferrite. b) Selected area diffraction (SAD) pattern from region shown in a)

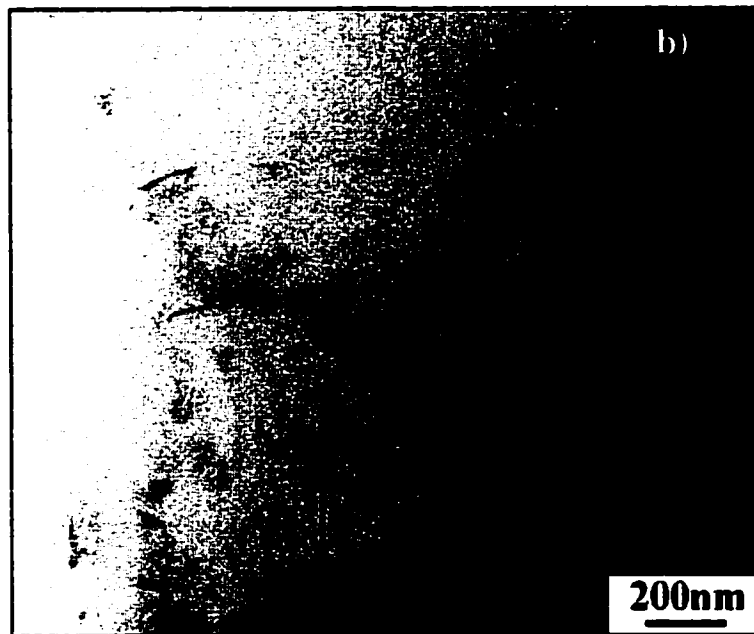
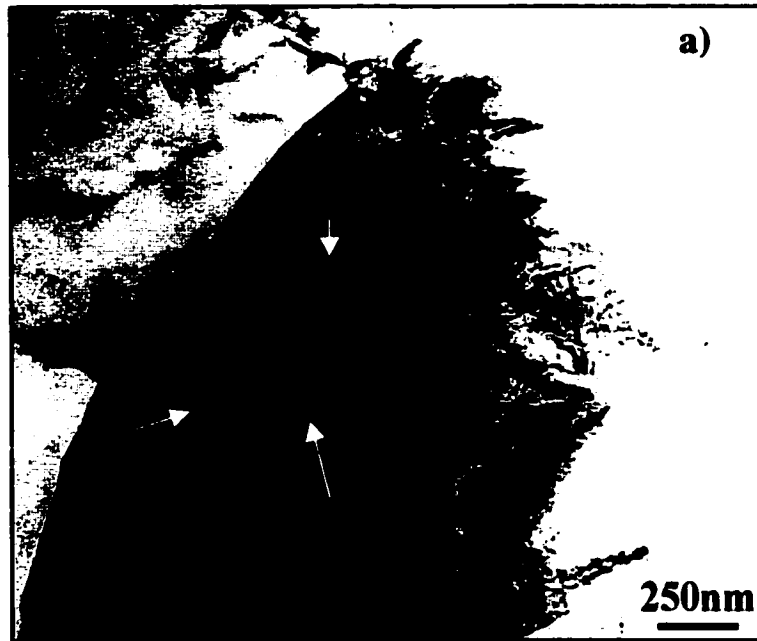


Figure 4-10 a) TEM BF image of thin foil from X70 showing ferrite grains possessing high dislocation density. b) Small precipitates nucleated on dislocations.

Pockets of retained austenite (seen as white areas with the modified LaPera's etch) were found to exist between clusters of ferrite grains. These grains of austenite showed Kurdjumov-Sachs orientation relationship (KS-OR) with their adjoining ferrite grains [Purdy84]. Figure 4-11a shows such a cluster. Here the grain labeled as 4 was austenite with all the surrounding grains ferrite. Ferrite grain 1 nucleated on austenite grain 4 and grew outwards. Figure 4-11b is the SAD pattern from grains 1 and 4 as indicated. The grains follow the KS-OR as illustrated in Figure 4-11c.

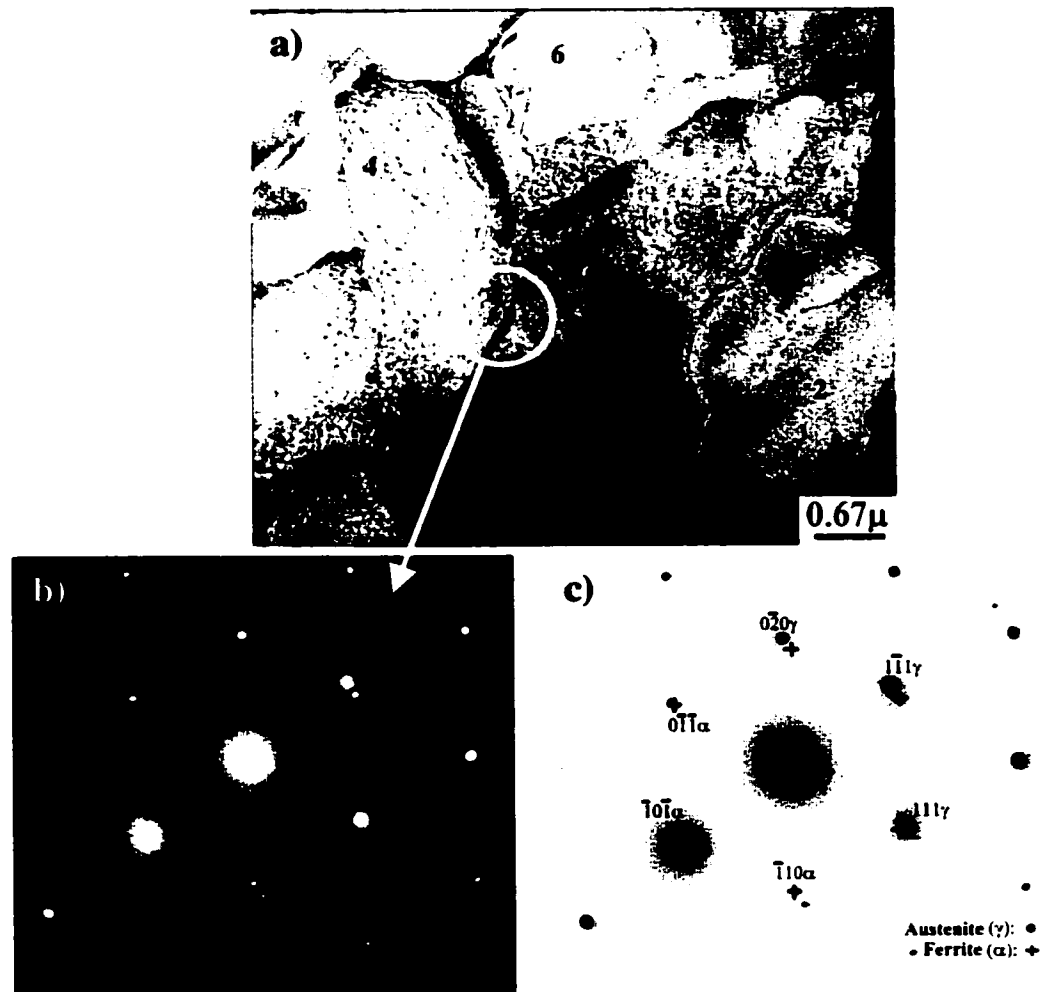


Figure 4-11 a) BF image from X70 steel showing a cluster of ferrite grains surrounding a grain of austenite (no.4), b) SAD pattern from grain 1(α) and 4(γ). c) Indexed pattern of the one shown in b).

### 4.3 Inclusions in X70 Steel

The inclusions in X70 steel were approximately rounded in shape (Figure 4-12 a), indicating the efficacy of S control and Ca treatment. Many of these non-metallic inclusions acted as nucleation site for large cuboidal TiN precipitates. Figure 4-12 b is an optical micrograph of one such inclusion. Energy dispersive x-ray (EDX) analysis performed on the inclusions in the SEM showed them to consist primarily of Ca and S. However, many of the larger inclusions had some Al, Ti, Nb and Mg too, along with some Mn (Figure 4-12 c). The EDX system of the SEM used by the author did not measure O content directly but as a residual content. The levels were generally 20-35at%. Therefore, in the spectrum the O peaks are not seen at all or with smaller intensities than expected. Most probably the inclusions are a mix of any or all of the oxides and sulfides (CaO-CaS-MnS-Al<sub>2</sub>O<sub>3</sub>-Ti(C,N)S). Other researchers have found or predict similar compositions for inclusions in microalloyed steels [Banks79] [Collins] [Gladman92].[Shehata85].

Image analysis was used to identify and count the inclusions present in various regions of the plate, with respect to the rolling direction and thickness of the plate as depicted previously in Figure 3-2. Seventy observations were made on each area (e.g.,LS-Top) with each observation corresponding to an area of 1600 $\mu\text{m}^2$ . Statistical analysis was performed to ascertain the distribution of these inclusions in terms of size (planar intercept area) and shape (aspect ratio). When the size is measured as planar intercept areas from the two perpendicular areas (LS and ST in this case) then it directly corresponds to the volume of these spherical particles. Similarly by measuring the aspect ratio on the two perpendicular faces LS and LT a good estimate of the shape of the inclusion can be made. The graphs below (Figure 4-13 to 4-16), show the shape and size distribution of CaS inclusions in X70 steel.

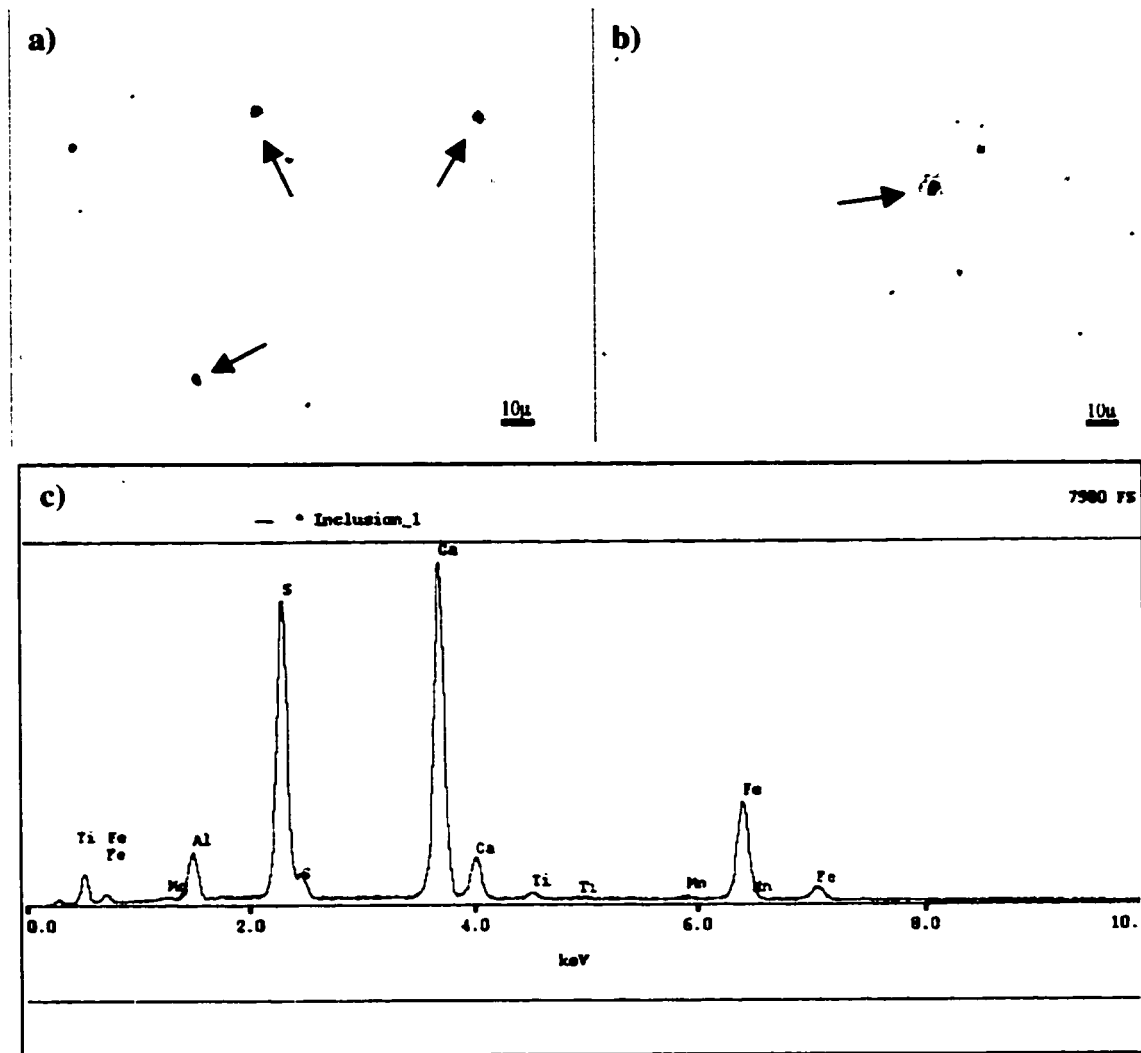


Figure 4-12 a) Rounded non-metallic inclusions in X70 steel. b) Some inclusions acted as nucleation sites for TiN cuboidal precipitates. c) EDX spectrum from one of the larger inclusions. Fe is mainly from the matrix.

The following observations can be made:

- Looking at the aspect ratios in the LS and ST direction, the inclusions are seen to be more or less spherical. There are no long stringers present in the X70 steel.
- Most of the inclusions have areas  $\leq 3\mu\text{m}^2$  with about 70% of them having areas  $\leq 2\mu\text{m}^2$ .

- The nominal planar density of inclusions in the LS orientation is about  $1.5 \times 10^5/\text{cm}^2$ .
- There is no appreciable difference in distribution of inclusions across the thickness of the plate. This implies good mixing in liquid steel and good casting practice.
- Looking at the aspect ratios, it can be seen that the particle shape is close to being spherical; however, they are slightly elongated along the rolling direction and across the width of the plate (average aspect ratio between 1.5 and 2). This deformation arises when the slab is being rolled. The fact that the inclusions have maintained their spherical shape and are not flattened out indicates that they are sufficiently hard to resist the roll deformation forces and avoid stringer formation. Stringers are to be avoided due to the role they play in hydrogen induced cracking (HIC).

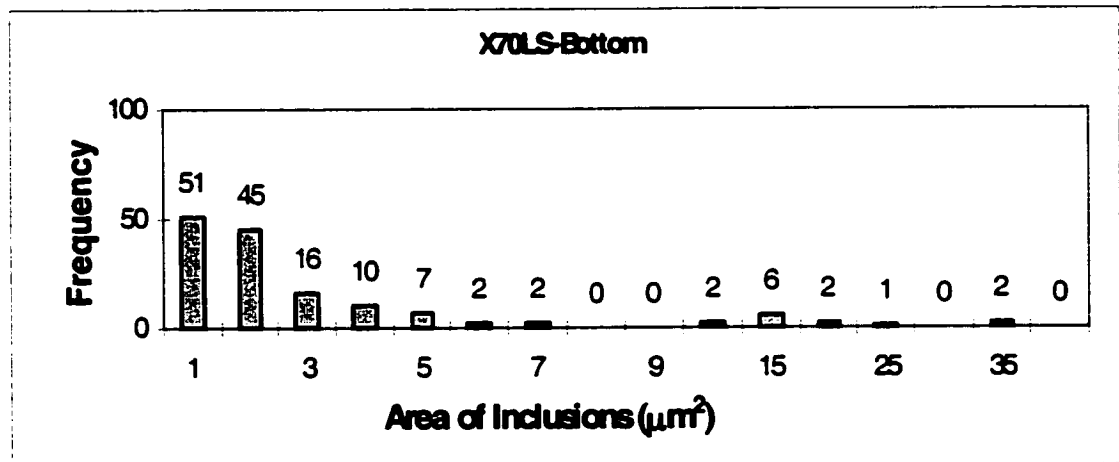
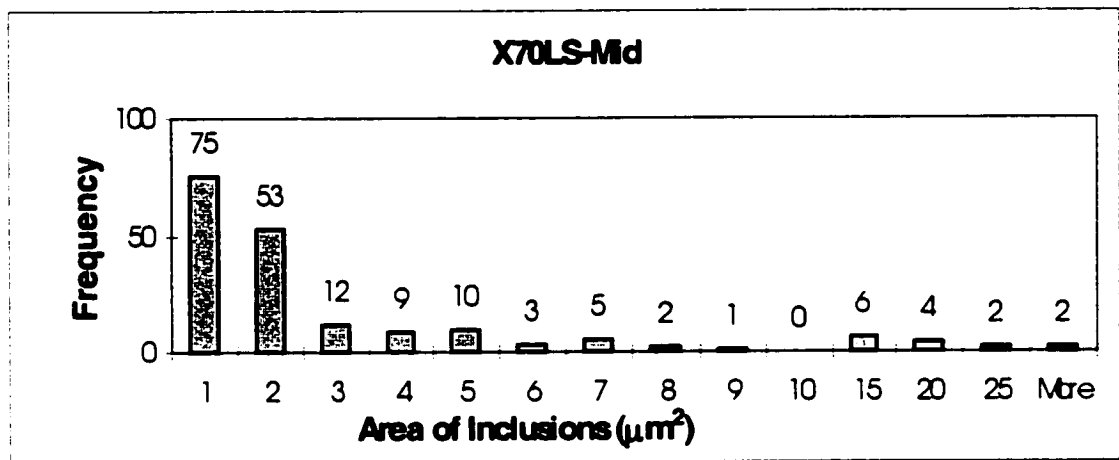
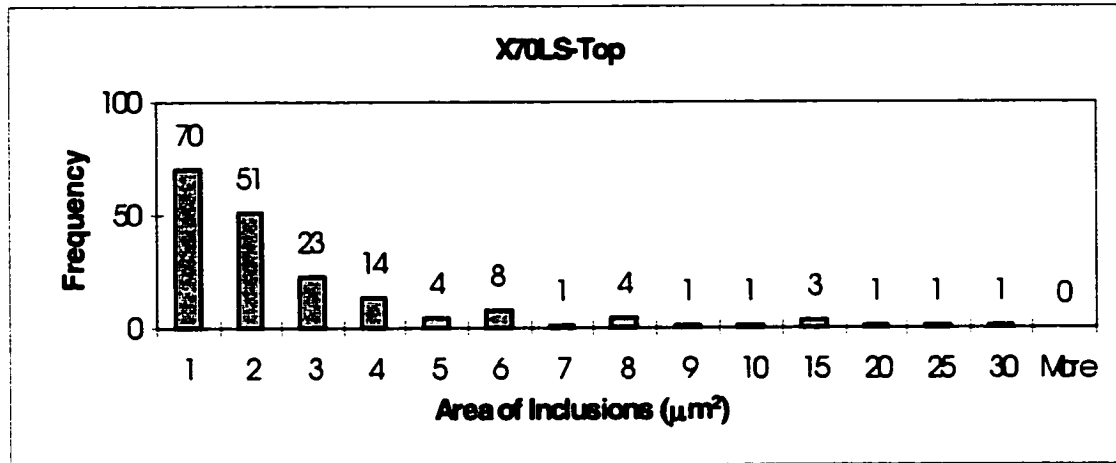


Figure 4-13: Planar intercept area of inclusions in X70 steel along the LS orientation.

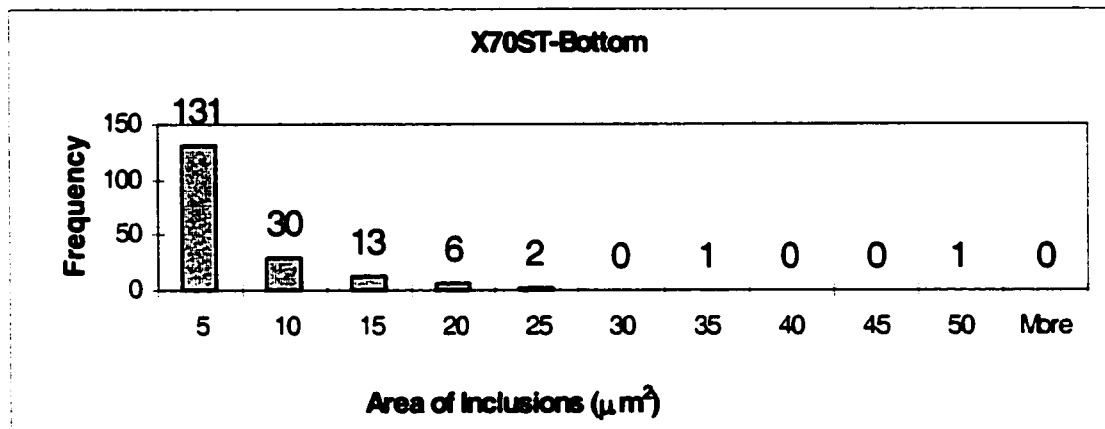
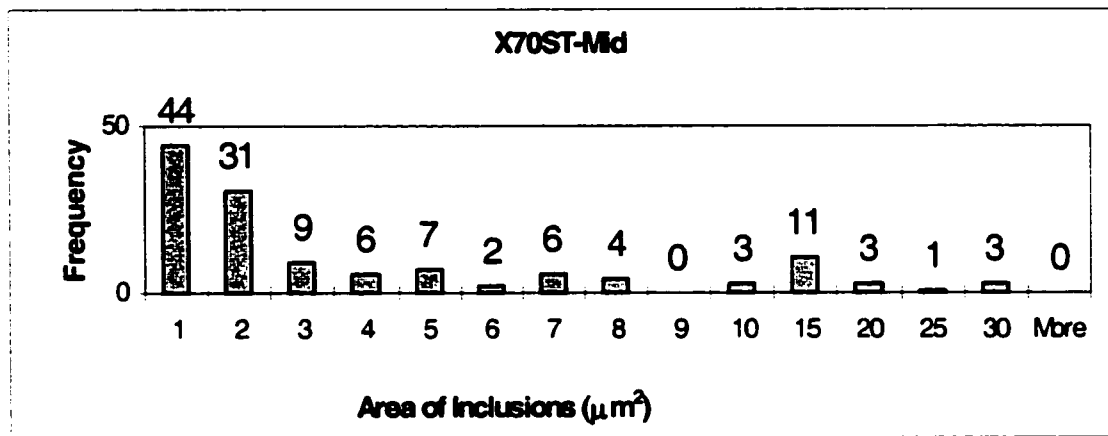
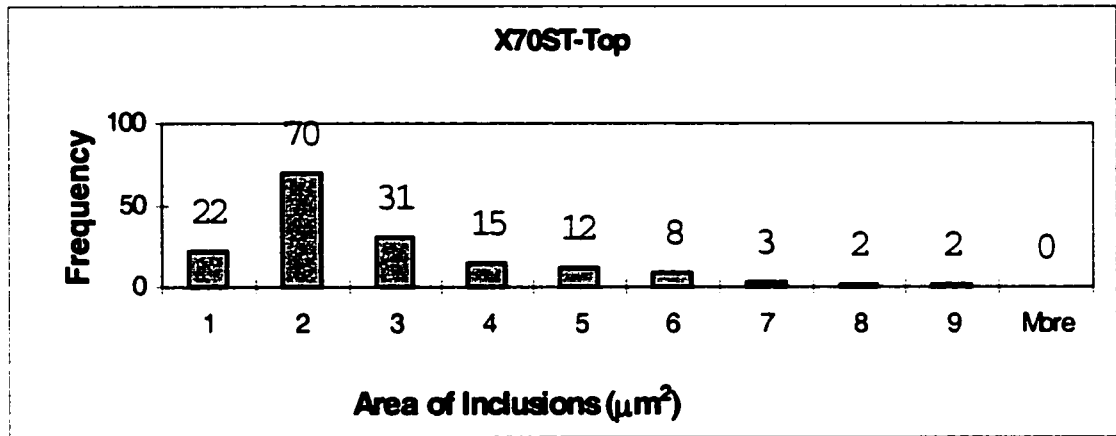


Figure 4-14 Planar intercept area of inclusions in X70 steel along the ST orientation.

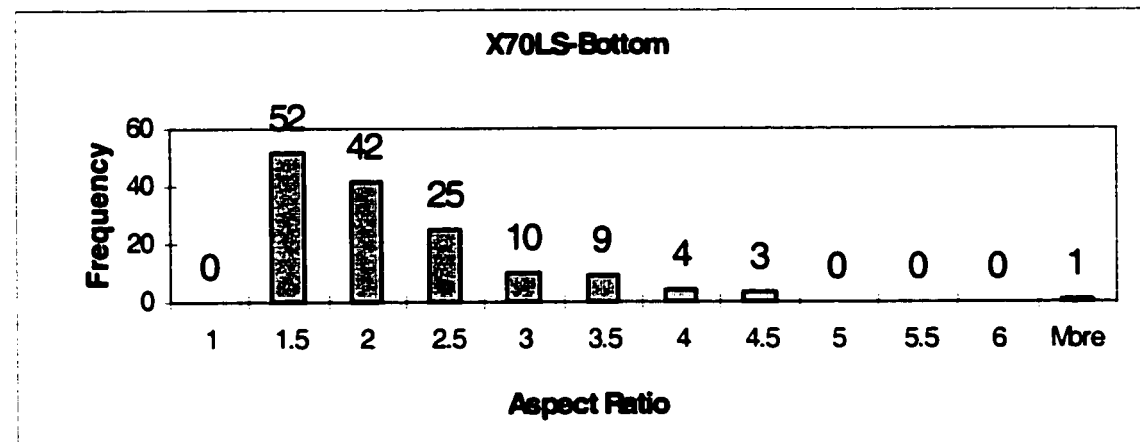
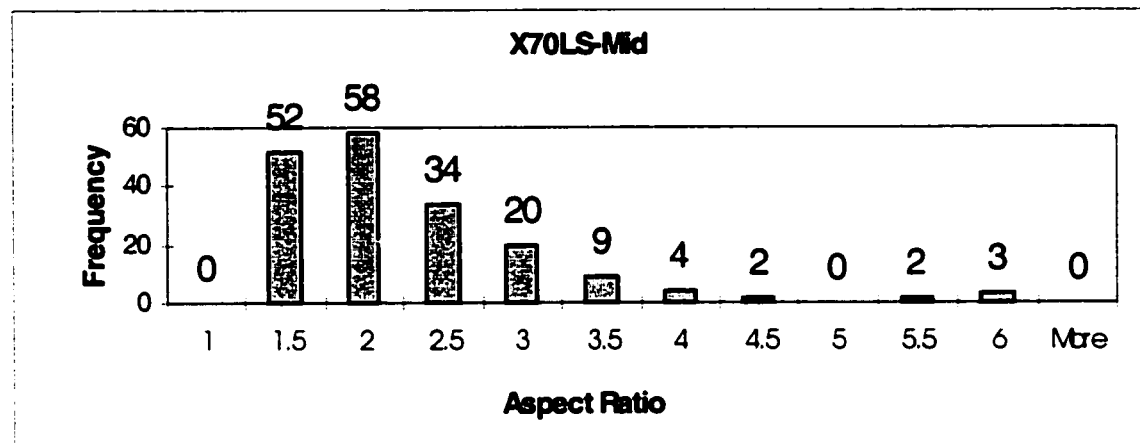
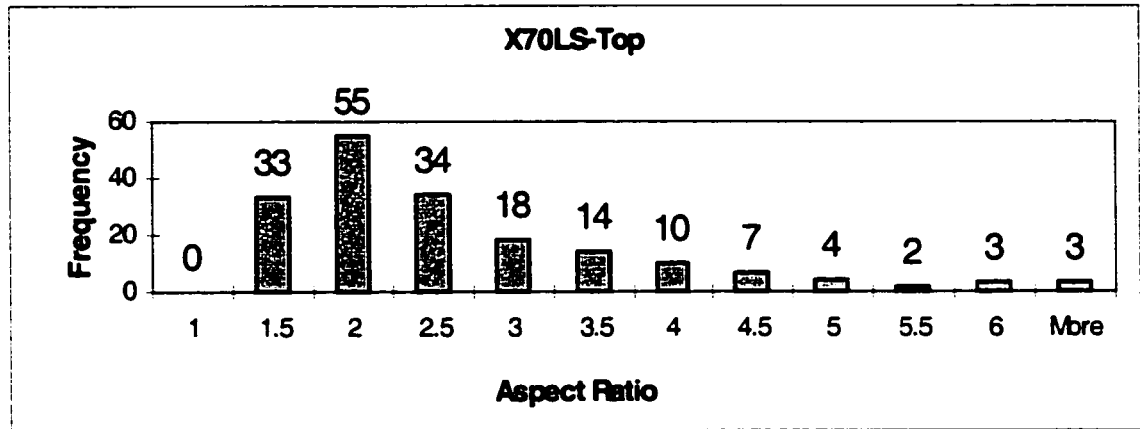


Figure 4-15 Aspect ratio of inclusions in X70 steel along the LS orientation.

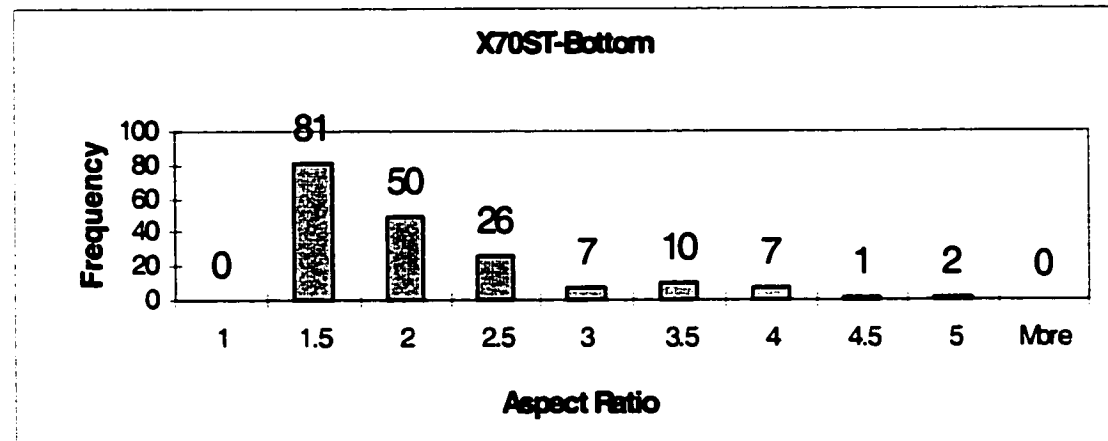
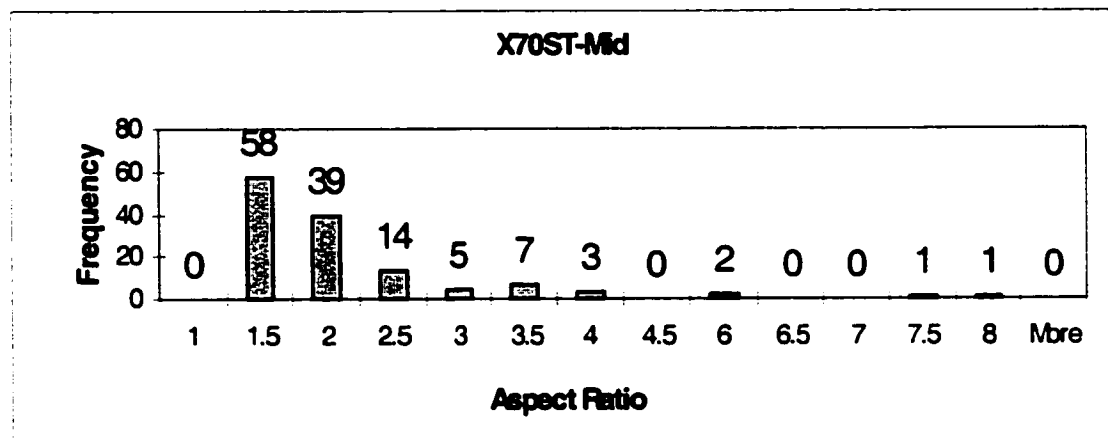
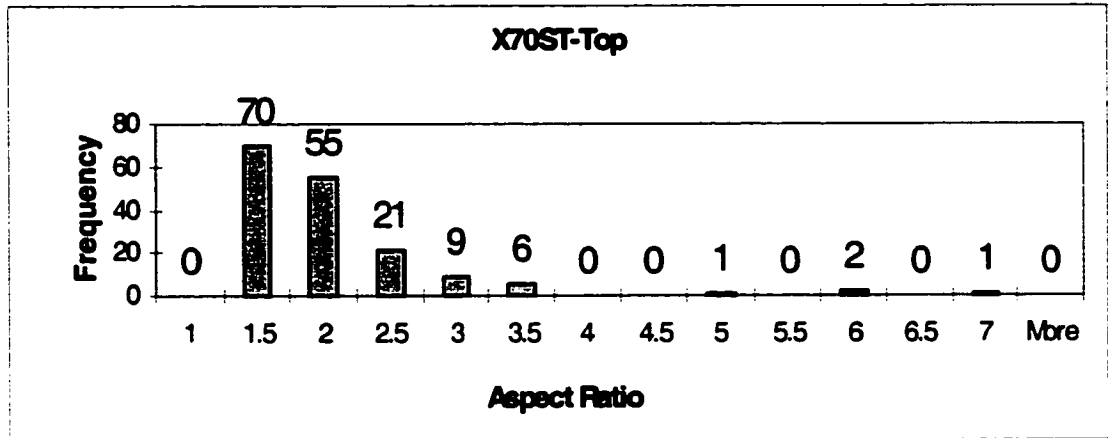


Figure 4-16 Aspect ratio of inclusions in X70 steel along the ST orientation.

## 4.4 Precipitates in X70 Steel

Five kinds of precipitates were observed in the X70 steel. They were classified into these divisions based on their size, shape, composition and the various stages of rolling during which they precipitate out from the solution.

### 4.4.1 Very Large TiN Precipitates (2-10 $\mu$ m)

This class of precipitates was large enough to be seen at low magnifications in an optical microscope. A key identifying characteristic was their copper color. The majority of these precipitates were cuboidal in shape with a dark interior. Some of them were observed in irregular shapes too. However, virtually all had facets suggesting that there are certain crystallographic planes which are of low surface energy with respect to the iron matrix. Figure 4-17 shows an optical micrograph of X70 steel in the LS orientation, depicting copper colored, faceted precipitates.

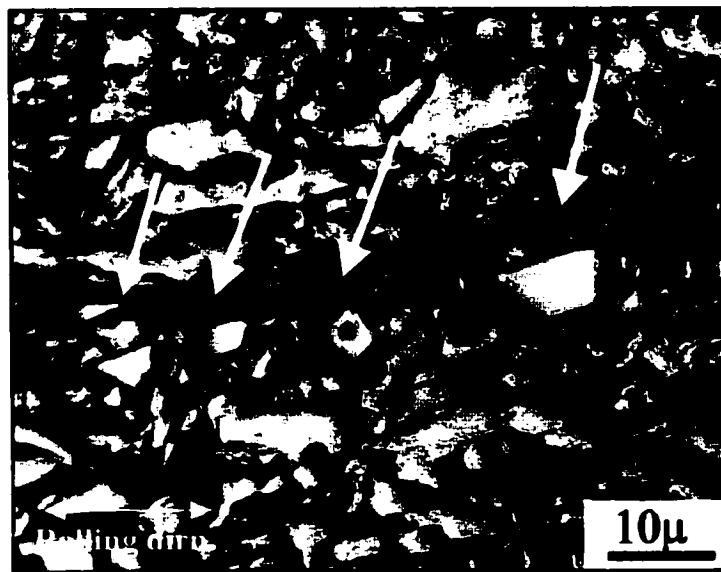


Figure 4-17 Optical micrograph of X70 LS mid etched in nital, showing faceted and cuboidal, copper colored TiN precipitates.

Figure 4-18 a shows an SEM micrograph of one such cuboidal precipitate with a dark center. EDX analysis of the shell indicated that it consisted primarily of Ti with

small amounts of Nb (Figure 4-18b). Due to the detection limitations of EDX detector in the SEM, no N peak could be observed. However, precipitation of Ti as TiN is favored thermodynamically at higher temperatures (1000°C-1400°C). The large size of these precipitates and the characteristic copper color indicates them to be TiN. The core contained Ca and S, with smaller amounts of Al and Ti (Figure 4-18c). The size and morphology of the particles suggest that they formed during solidification and remained undissolved during reheating. Itman et al. [Itman97] and Zhou and Priestner [Zhou96] have observed similar precipitates in their studies and identified them to be primarily TiN with size in the range of 2 $\mu$ m or higher. It appears that the TiN particle nucleated on the non-metallic inclusion of CaS and grew to a cuboidal shape. Most of the particles were seen with a core in their interior. The others showed a smooth surface, which may arise if the intercepting plane of polish does not pass through the center of the cuboid but near the surface.

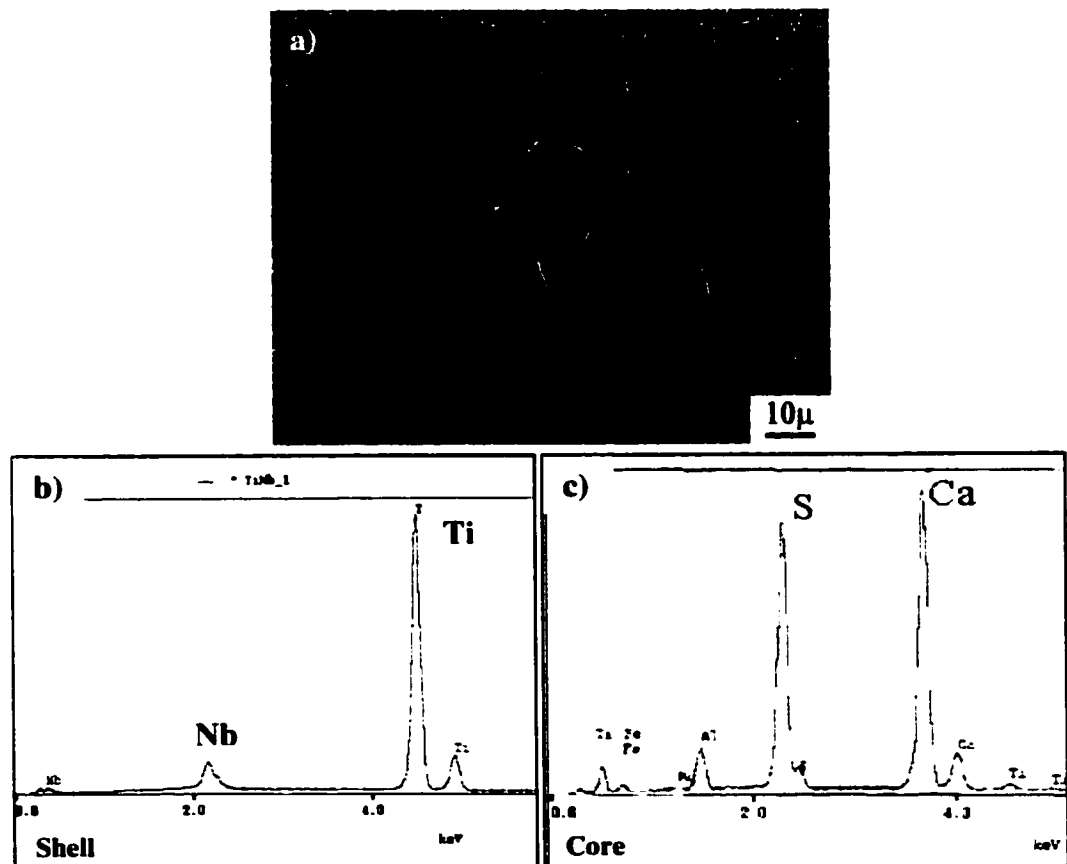


Figure 4-18 a) Back scattered electron (BSE) SEM micrograph of a cuboidal precipitates in X70 showing a dark particle at the center. b) EDX spectrum from the shell. c) EDX spectrum from particle in the center.

To ascertain whether there was any preferential distribution of the very large TiN precipitates across the thickness of the plate, a method of random sampling and random intercepts was followed to count the number and size of these precipitates. 50 areas were chosen at random near the centerline and near the surface of the plate in the LS orientation and the number of particles contained in them counted. Each area was  $1600\mu\text{m}^2$ . This gave a very crude approximation of areal density of the precipitates. The average intercept length gave an approximation of the relative sizes. Figure 4-19 illustrates this methodology and Table 4-2 shows the results.

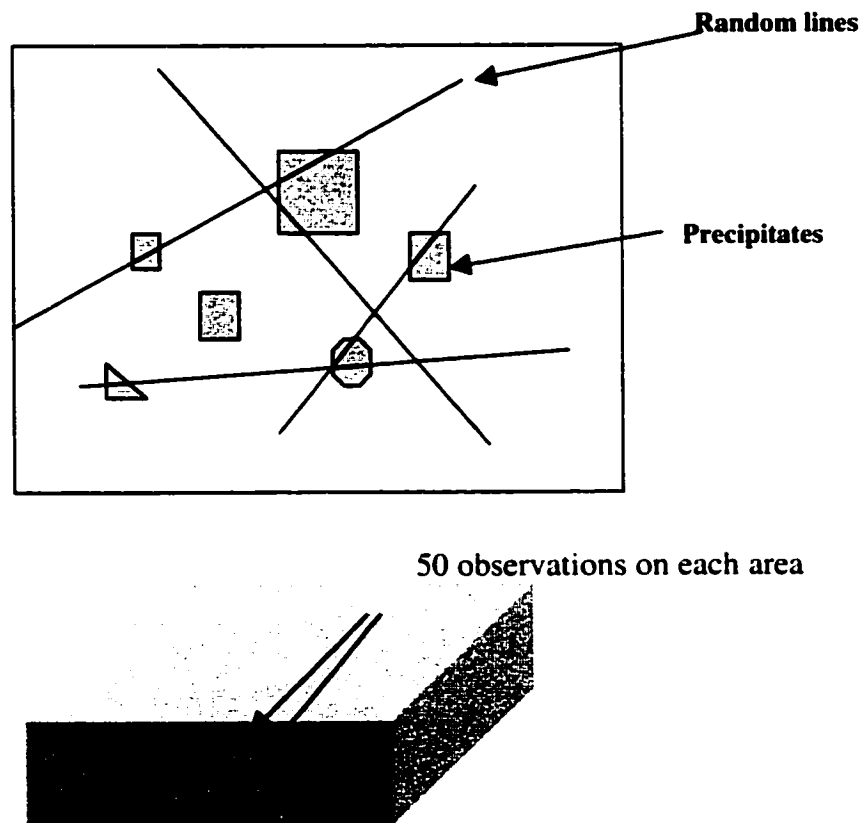


Figure 4-19 Counting the size and number of very large TiN precipitates through the random intercept method.

Table 4-3: Size and density distribution of TiN precipitates across the thickness of X70 plate.

TiN Precipitates	X70	
	Center	Surface
Density (#/cm <sup>2</sup> )	3400	1600
Average Size (μm)	3.9	3.1
Std. Dev (μm)	1.8	0.7

#### 4.4.2 Large Cuboidal Precipitates (0.1-1.0μm)

Cuboidal in shape (Figure 4-20a), these were present both at the grain boundaries and in the interior of the ferrite grains. The precipitates were identified in the TEM. They consisted primarily of Ti but had some Nb as well (Figure 4-20c). The Nb levels were slightly higher in comparison to the type 1 precipitates. The EDX spectrum in Figure 4-20c also shows presence of C and N indicating them to be carbides or nitrides or mixed carbonitrides. However, the C peak was comparatively very high due to the carbon film of the extraction replica. In many cases the N peak was not very prominent due to detector resolution limitations. Hence it was difficult to identify these precipitates as carbides or nitrides just from the EDX spectrum. SAD patterns were obtained to study the lattice structure. The crystal structure was fcc, NaCl type (Figure 4-20b). All the precipitates TiN, TiC, NbN and NbC have this same cubic crystal structure, fcc NaCl type, the difference being variations in lattice parameter. Nb and Ti are mutually soluble in the lattice as are C and N. As such, the lattice parameter of these precipitates did not exactly match either of the individual carbides or nitrides but was somewhere intermediate to them. Based on their solubilities and the temperature at which the various precipitates come out from the solution we find that TiN is the first to come out of the solution [Gladman97]. Hence these precipitates were primarily TiN. The major difference between these and the class 1 precipitates, besides the size, was that these did not have any non-metallic particle at their core. Liu and Jonas [Liu89] predict formation of N rich nuclei for

Ti(C,N) precipitates based on thermodynamics and solubilities of the components in the austenite.

Some of the cuboidal precipitates grow to large sizes in X70 steel (1-2  $\mu\text{m}$ ) and a TEM bright field image of one such precipitate is shown in Figure 4-21a. Some researchers have reported that these large precipitates consist of a core of TiN and a shell of NbC [Zou91]. EDX analysis was performed at various locations as shown in Figures 4-21c to 4-21f and it was found that the entire particle was similar in composition.

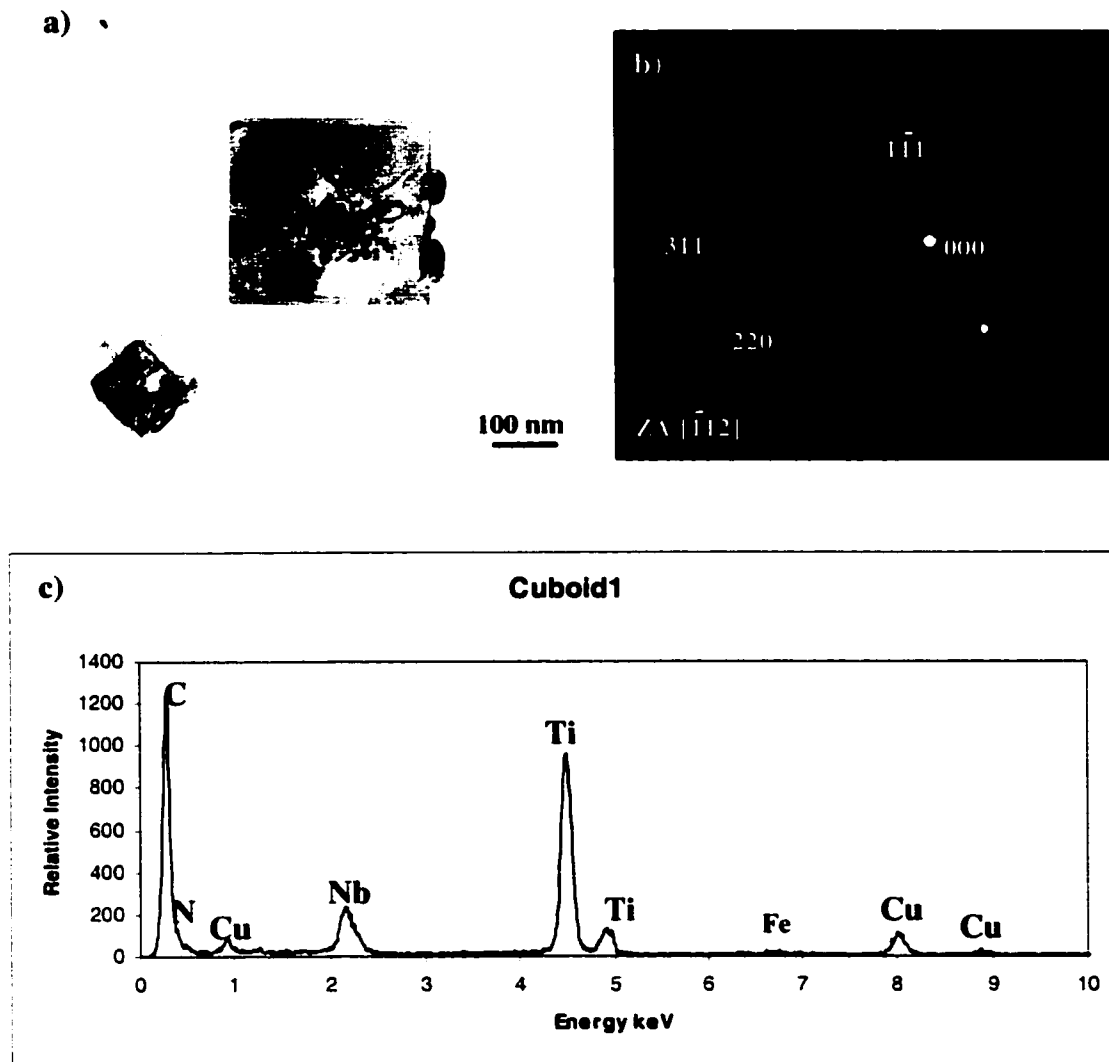


Figure 4-20 a) TEM BF image from a carbon replica showing 2 large cuboidal precipitates in X70. b) SAD pattern from the larger cuboid shows it to be fcc NaCl-type. c) EDX spectrum from the same precipitate shows it to be Ti rich, with some Nb.

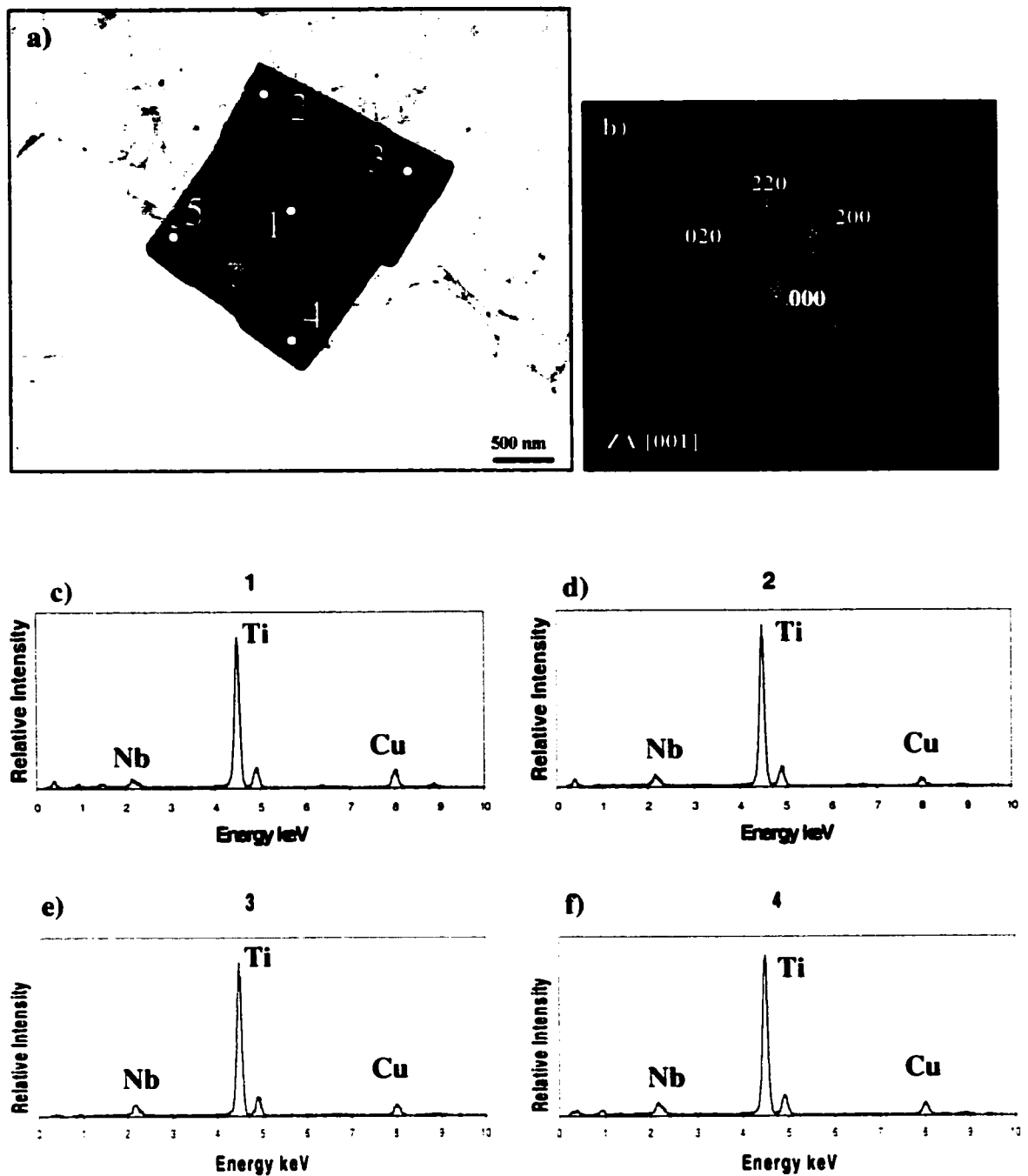


Figure 4-21 a) TEM BF image of a large cuboidal precipitate in X70. b) SAD pattern identifying it as fcc NaCl type. c)-f) Composition profiles from various positions of the precipitate as marked in a).

#### 4.4.3 Medium Sized Irregular Shaped Precipitates (30-50nm)

This class of precipitate was mostly rounded and consisted mainly of Nb with some Ti and sometimes Mo. TEM BF image of one such precipitate is shown in Figure 4-22a along with an accompanying diffraction pattern (Figure 4-22b) and EDX spectrum (Figure 4-22c). The crystal structure was again fcc, NaCl-type.

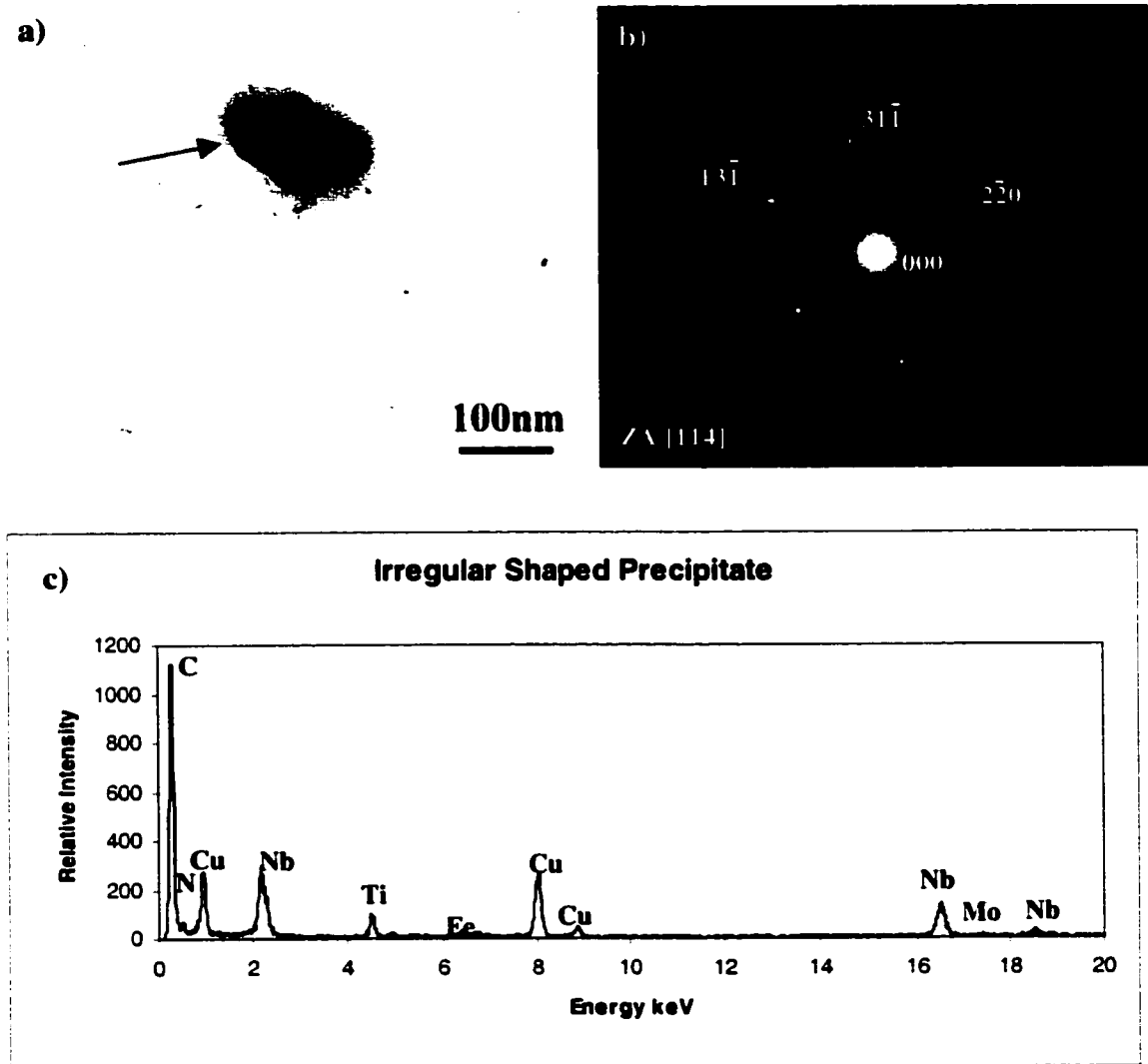


Figure 4-22 a) TEM BF of an irregular shaped precipitate in X70, b) DP identifies it to be fcc, NaCl type, lattice parameter close to NbC, c) EDX indicated presence of Nb with Ti.

Both the cuboidal (0.1 - 1.0 $\mu$ m) and irregularly shaped (30-50nm) precipitates were distributed randomly within the grains and at the grain boundaries. There did not appear to be any preferential precipitation at the grain boundaries or along any specific planes within the grains, as apparent from carbon replica method. However, this might be a limitation of the carbon replica extraction method where not all the precipitates are pulled out. Thin foils were observed to see any evidence of preferential nucleation sites for precipitation of class 2 and 3 particles but they appeared random too. Figure 4-23 shows a collage constructed of many smaller images showing the distribution of class 2 and 3 precipitates within a ferrite grain.

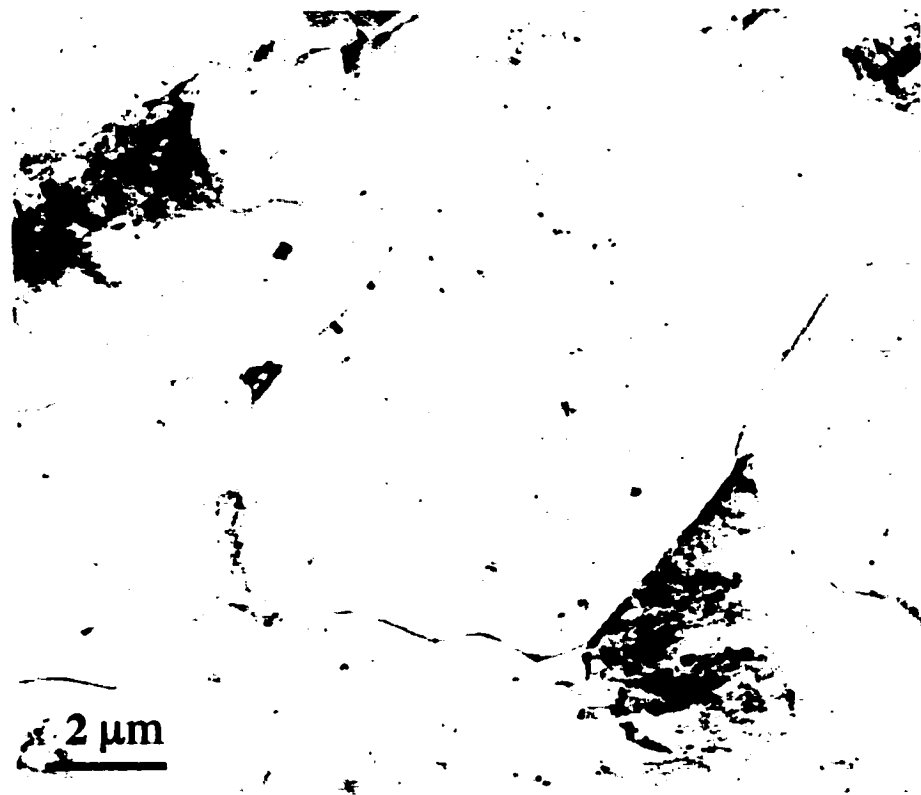


Figure 4-23 Distribution of cuboidal (0.1-1.0 $\mu$ m) and irregular shaped (30-50nm) precipitates in a ferrite grain.

#### 4.4.4 Small Spherical Precipitates ( <20nm)

These precipitates were present throughout the grains and were quite small (<20nm). Majority of these precipitates were in the 5-10nm size range, while some grew up to 20nm for X70 steel. TEM dark field (DF) images from a carbon replica (Fig. 4-24) and thin foil specimen (Fig. 4-25) show the size and distribution of these precipitates. The strain induced precipitates are also visible in Fig. 4-24 and are indicated. The precipitates often appeared as rows or sheets, which are proposed to form during the ledge growth of ferrite [Batte73]. EDX analysis indicated that they were either NbC or Nb carbonitrides. An EDX spectrum from one such precipitate is shown in Figure 4-24c. The presence of N was difficult to discern as the N peak in the EDX spectra was masked by the large C peak arising from the C support film. Molybdenum was also present. Molybdenum can partially substitute for Nb in the precipitates forming (Nb,Mo)(C,N); however, Mo levels are likely not high enough to significantly affect the amount of precipitation hardening [Kanazawa67-1][Kanazawa67-2]. Small amounts of Ti were also observed. The large Cu peak arises from the copper support grid. O is from the oxides that formed sometimes on the supporting Cu grid and was not seen generally. Molybdenum was also present in these precipitates. The iron peak arises when some matrix is pulled by the carbon film during sample preparation. Single crystal diffraction patterns were difficult to obtain. Ring patterns were obtained from a group of precipitates as shown in Figure 4-24b. The ring patterns matched closely to NbC indicating they could be either NbC or Nb carbonitrides.

The diffraction pattern in Fig. 4-25b indicated an orientation relationship between the particles and the ferrite matrix. The more intense spots in the pattern are from ferrite ([012] zone axis), while the extra spots near the center are from particles- the DF in Fig. 4-25a was taken using one of the extra spots. The following orientation dependence was determined, assuming a NaCl type structure for the precipitates.

$[1-10]$  precipitate  $\parallel$   $[012]$  ferrite and  $(110)$  precipitate  $\parallel$   $(100)$  ferrite

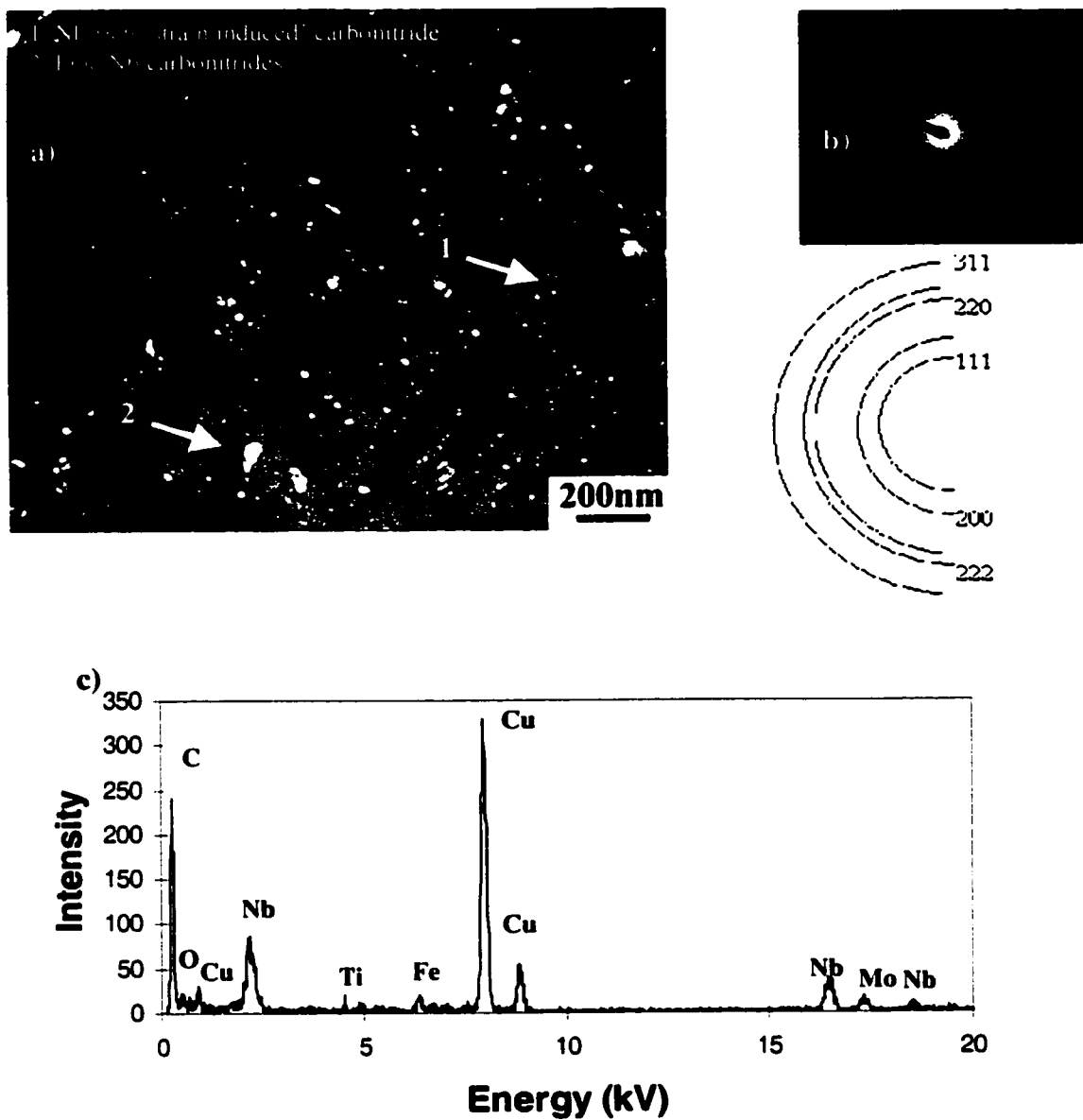


Figure 4-24 a) TEM DF image of small spherical precipitates in X70 steel. b) Ring diffraction pattern from a cluster of precipitates. c) EDX spectrum from a group of precipitates.

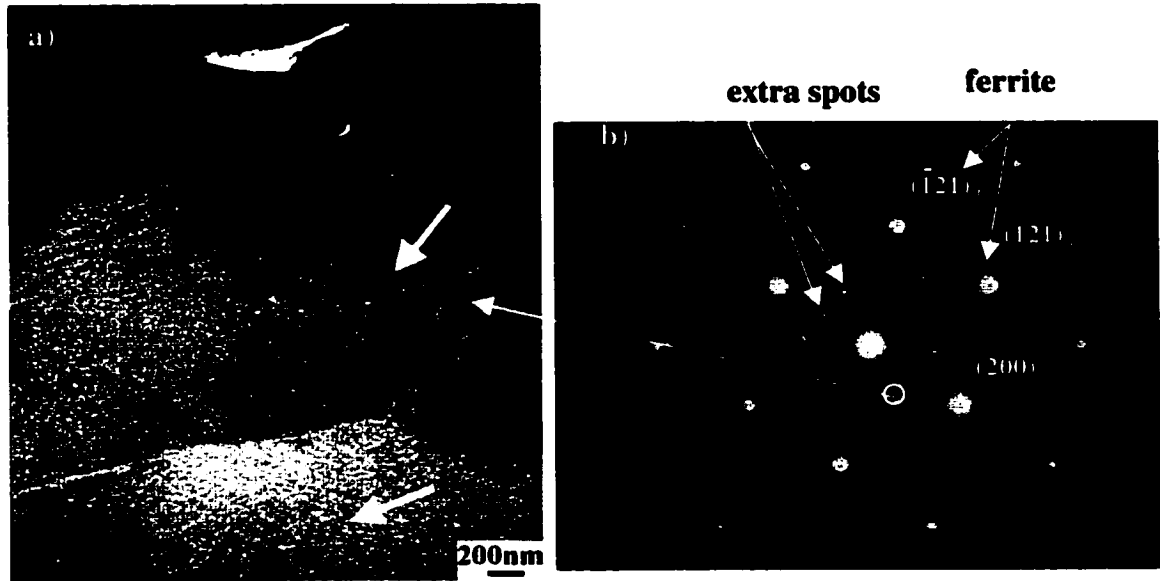


Figure 4-25 a) TEM DF image of thin foil sample of X70 showing small precipitates along a line. b) SAD pattern from central ferrite grain in (a), showing extra spots near the central spot. The spot used for obtaining the DF image is encircled.

#### 4.4.5 Very Small Precipitates (<5nm)

In addition to the four major types of precipitates already discussed, some very small (<5nm) precipitates were detected in X70 (Fig. 4-26). The precipitates form during the later stages of processing when the strip is being coiled at temperatures <600°C. At this temperature virtually all the Ti has been depleted and the Nb precipitates out with C and N by nucleating on the dislocations and at the grain boundaries, as seen in Fig. 4-10b. These finely dispersed precipitates contribute to precipitation strengthening in these steels.

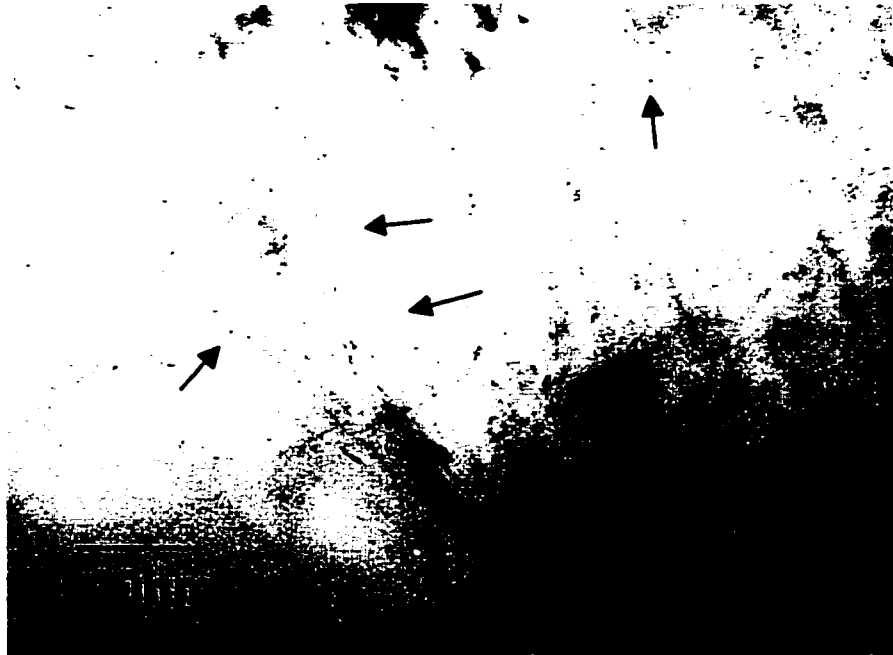


Figure 4-26 TEM BF image of thin foil sample of X70 steel showing extremely small ( $<5\text{nm}$ ) precipitates spread throughout the grain and at grain boundaries. The precipitation seems to occur along lines or sheets.

## **Chapter 5: X80 Steel: Results**

### **5.1 Introduction**

X80 steel is closely related to X70 steel in terms of chemical composition, with the main difference being the concentration of Nb which has been increased from ~0.06wt% to ~0.09wt%. The titanium level in X80 is similar to that in X70 (0.023wt%). Slight differences exist in terms of Mo, Mn and Ni, with the X80 chemistry being marginally richer than X70. The complete chemical composition for X80 steel (along with X70 and Grade80) is shown in Table 3-1. In addition to these differences in chemistry, the thermomechanical rolling schedule for X80 steel was considerably different from that of X70 and Grade80. Because of these differences a slightly different microstructure was expected and the results below summarize the various microstructural features present in X80 steel.

### **5.2 Grain Structure**

Initial microscopic examination was done in the optical microscope. Samples etched in 2% nital were used to reveal the grain structure. Figure 5-1 shows the general grain structure of X80 steel at a low magnification. The micrograph was taken in the LS orientation, from the middle of the thickness away from the centerline or edges to represent the bulk microstructure. It is apparent that, like X70 steel, the grains are highly irregular in shape and of mixed size range. However, certain differences are immediately apparent. Whereas the grain structure in X70 consisted of a substantial percentage of polygonal ferrite, in X80 the grains are more or less completely acicular or bainitic in nature. This is to be expected since the design philosophy of these microalloyed steels is for the structure to move from a ferritic-pearlitic mix to ferritic-bainitic while reducing (or eliminating) the pearlitic content as the strength levels are increased.

Figure 5-2a shows the grain structure near the center of thickness of the plate. It is evident that the grains are highly deformed and irregular in shape. Also the grains are larger and more mixed in size (i.e., both large and small) when compared with the grain structure from near the surface of the plate (Figure 5-2b). The grains are finer and more equiaxed when compared with the interior of the plate.



Figure 5-1 Optical micrograph of X80 steel etched with 2% nital, showing acicular/ferritic (AF) grain structure with mixed grain size. Small regions of polygonal ferrite (PF) are also visible.

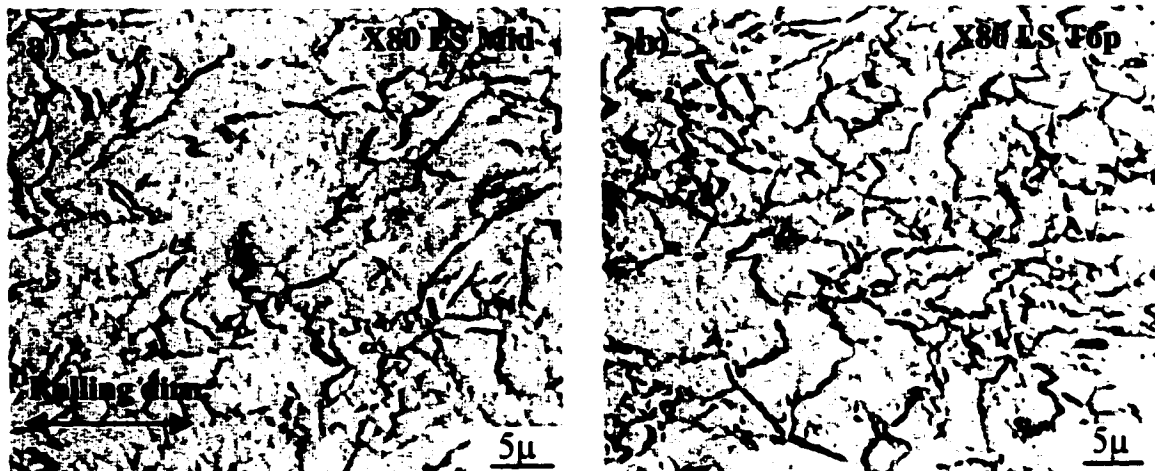


Figure 5-2 Grain structure of X80 steel in an optical microscope, a) near the center, X80-LS-mid; and b) near the surface, X80-LS-top (etched with nital).

The method of random intercepts was used to study and assign an apparent grain size as in X70. Three areas, each of  $1600\mu\text{m}^2$  were selected and 30 random lines drawn for each. The number of grains intercepted by each line was counted and the inverse of this quantity provided an estimate of the grain size. About 500 grains were counted in all (Figure 4-3). The standard deviation gives an idea of the degree of the mixed nature of grain sizes. A lower standard deviation implied that grains were more or less within a narrow size range and a large deviation reflected a mix of large and small grains. Table 5-1 shows the results obtained from near the centerline and near the surface of the plate. It is apparent that the grains are larger and of more mixed nature at the center than at the surface.

Table 5-1 Grain size as average intercept length.

Grain Size	X80	
	Center	Surface
Average intercept length ( $\mu\text{m}$ )	6.1	5.1
Standard deviation ( $\mu\text{m}$ )	1.9	1.4

To get an idea of the shape of grains, instead of randomly oriented lines, directions along the rolling direction and perpendicular to it were chosen (Figure 4-4). More than 200 grains were counted to give a statistically representative count. Table 5-2 shows that for X80 steel the grains are similarly shaped at the center and near the surface.

Table 5-2 Aspect ratio of grains for X80 steel along the LS orientation.

	<b>X80</b>	
	<b>Center</b>	<b>Surface</b>
<b>Aspect Ratio</b>	1.9	1.9

The X80 plate did not show any centerline segregation, as is evident from Figure 5-3 which shows an optical micrograph from the centerline of the plate, along the rolling direction. It is apparent that the microstructure is clean and there is no centerline banding. However, like in X70 steel, there was a greater concentration of larger, copper colored, cuboidal precipitates of TiN at the centerline, than near the surfaces of the plate.

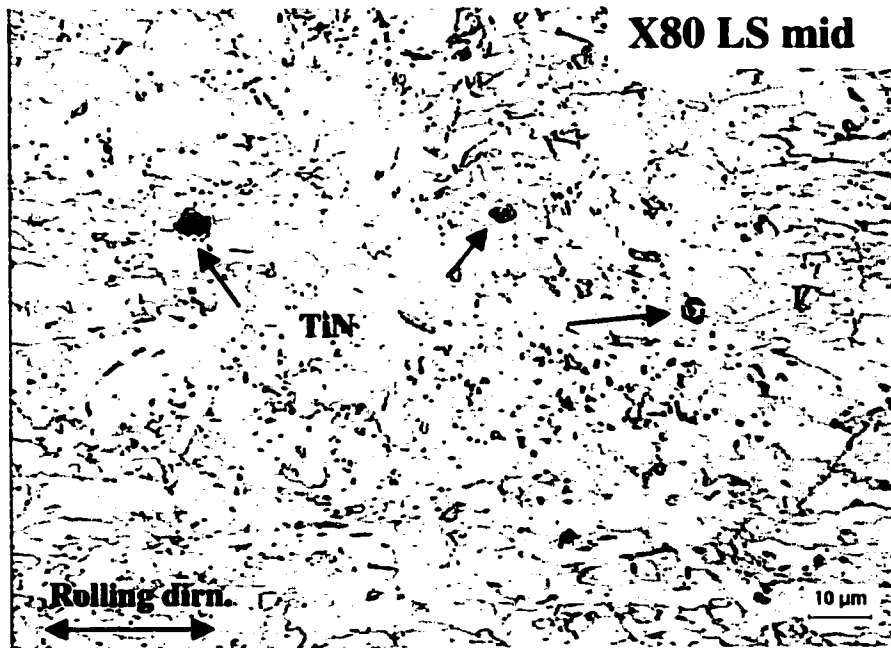


Figure 5-3 Optical micrograph of X80 steel etched with 2% nital, along the rolling direction, showing no segregation at the centerline. Some TiN cuboidal precipitates are visible.

The use of modified LaPera's etch revealed the various constituent phases in the microstructure by coloring the ferrite tan, martensite and retained austenite white and bainite/carbide black. It was found to be most useful in the identification of martensite/retained austenite constituent. This phase is not easily differentiated through other etchants like nital and picral. Figure 5-4 shows the distribution of MAC at the center of the thickness of the plate and near the surface for X80 steel. MAC was found to be concentrated more at the centerline where the MAC islands were larger and clustered together. However, tiny, finely dispersed islands were observed throughout the thickness of the plate.

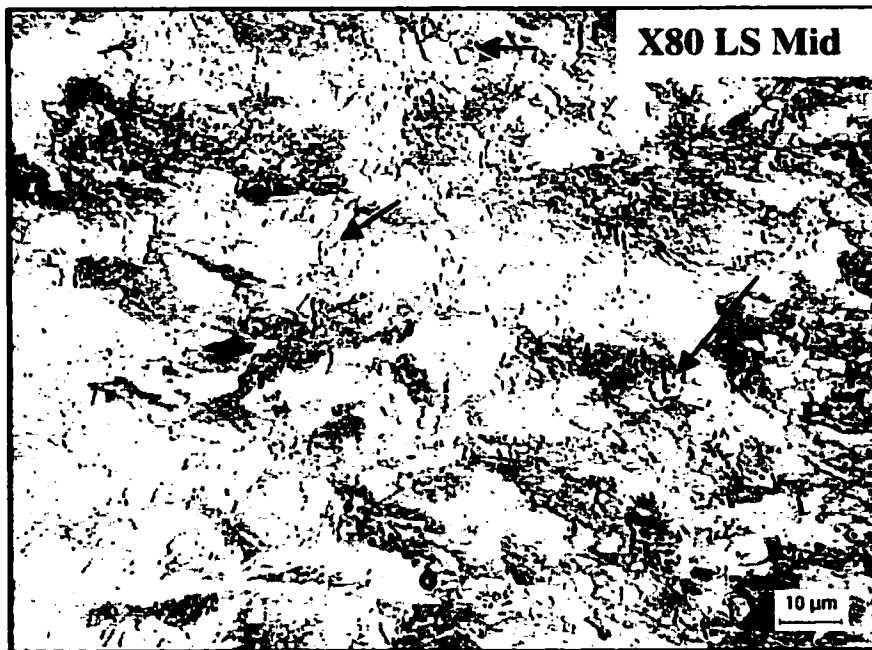
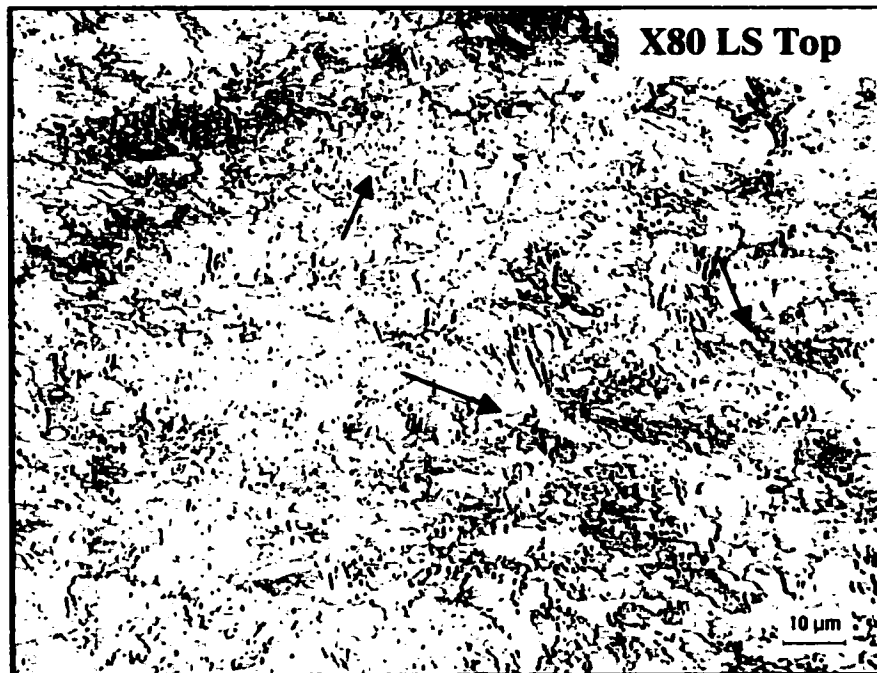


Figure 5-4 Optical micrographs of X80 steel etched with modified LaPera's etch showing the presence of martensite austenite constituent (MAC) as tiny white islands in the ferrite matrix (tan).

When etched with picral (4%) for sufficiently long times (greater than 2 min), X80 revealed pearlite-like microstructures at areas between the grains of ferrite very similar to that in X70 (Figure 4-7). Figures 5-5a and 5-5b show the relative size and distribution of these “pearlitic” regions in the center and at the surface of the X80 plate respectively. These regions were coarser and more sparsely distributed in the center as compared with the surface region.

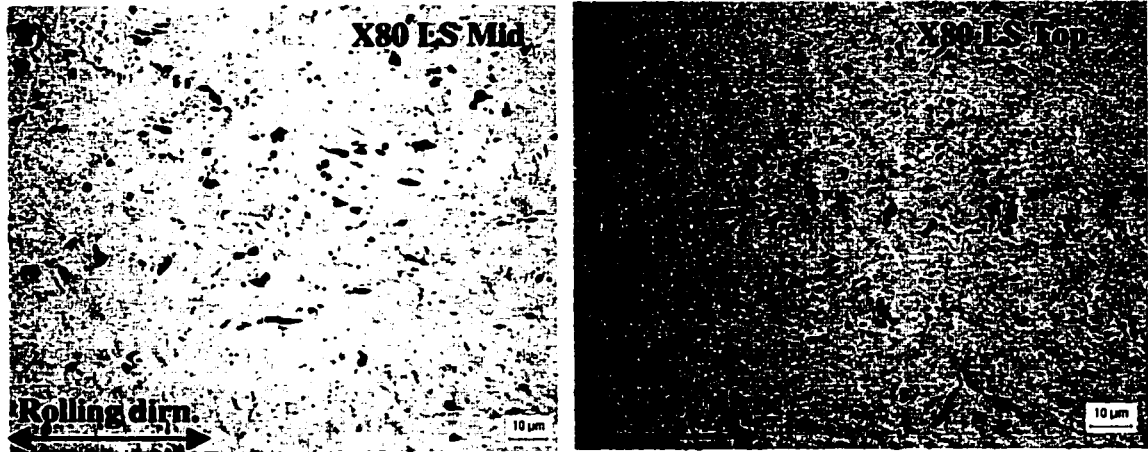


Figure 5-5 Optical micrographs of X80 LS steel etched with picral showing distribution of pearlite like microstructure at a) near the centerline and b) near the surface of plate.

To ascertain the crystal structures of the constituent phases in X80 steel, thin foils were analyzed in the TEM. A major portion of the microstructure consisted of acicular grains of bcc ferrite, with many of them exhibiting low angle grain boundaries. Like the X70 steel, clusters of subgrains within a large ferrite grain were observed. Their presence was revealed by the SAD patterns, all of which matched very closely, with slight angular misorientations (less than  $5^\circ$ ). This mismatch in orientation can be ascertained by the angular separation between the closely spaced spots in a SAD from adjoining grains. One such case is shown in Figure 5-6. Generally, the grains possessed high dislocation densities and several small precipitates were observed associated with these dislocations.

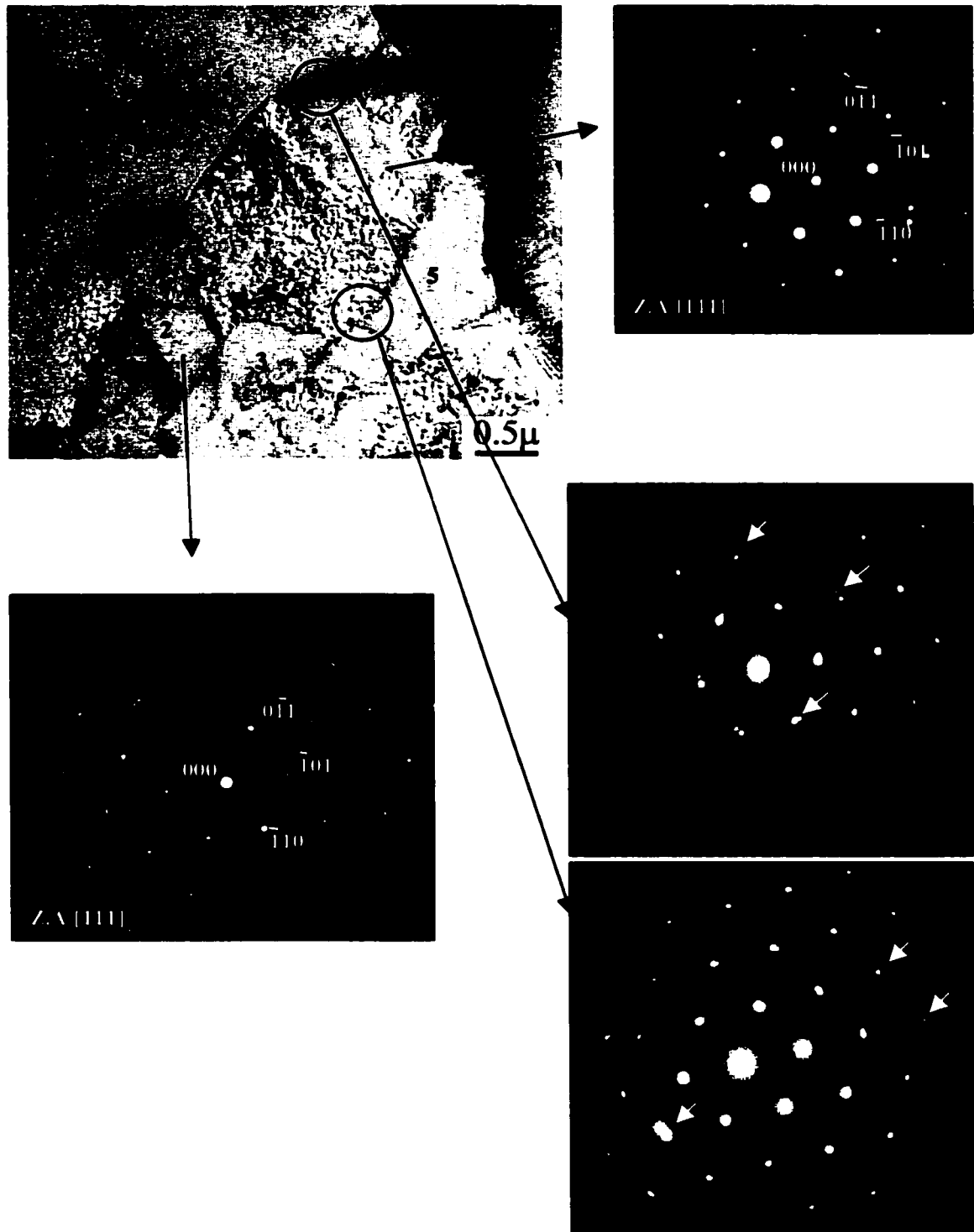


Figure 5-6 TEM BF image from a thin foil sample of X80 steel showing the presence of a polygonal ferrite grain with many smaller subgrains in it. The adjoining SAD patterns show that the subgrains are separated by low angle grain boundaries ( $\sim 2^\circ$ ).

### 5.3 Inclusions in X80 Steel

The inclusions in X80 steel were approximately rounded in shape, indicating the efficacy of S control and Ca treatment. Many of these non-metallic inclusions acted as nucleation sites for large cuboidal TiN precipitates and many attached themselves to the cuboidal TiN precipitates during casting and solidification of the slab. Figure 5-7a shows an SEM micrograph of one inclusion. EDX analysis showed the particle to consist primarily of Mn, Ca and S. However, many of the larger inclusions had some Al, Ti, Nb and Mg as well (Figure 5-7b). As explained in Section 4-3, these inclusions are most probably mixed oxides and sulfides of Ca, Mn, Al, Si and Ti. The inclusions in X80 showed larger amounts of Mn as compared to X70; however, the Mn levels in X80 (1.82wt%) are only slightly higher than in X70 (1.75wt%). Therefore this difference in observations appears to be fortuitous and may be just a sampling phenomenon.

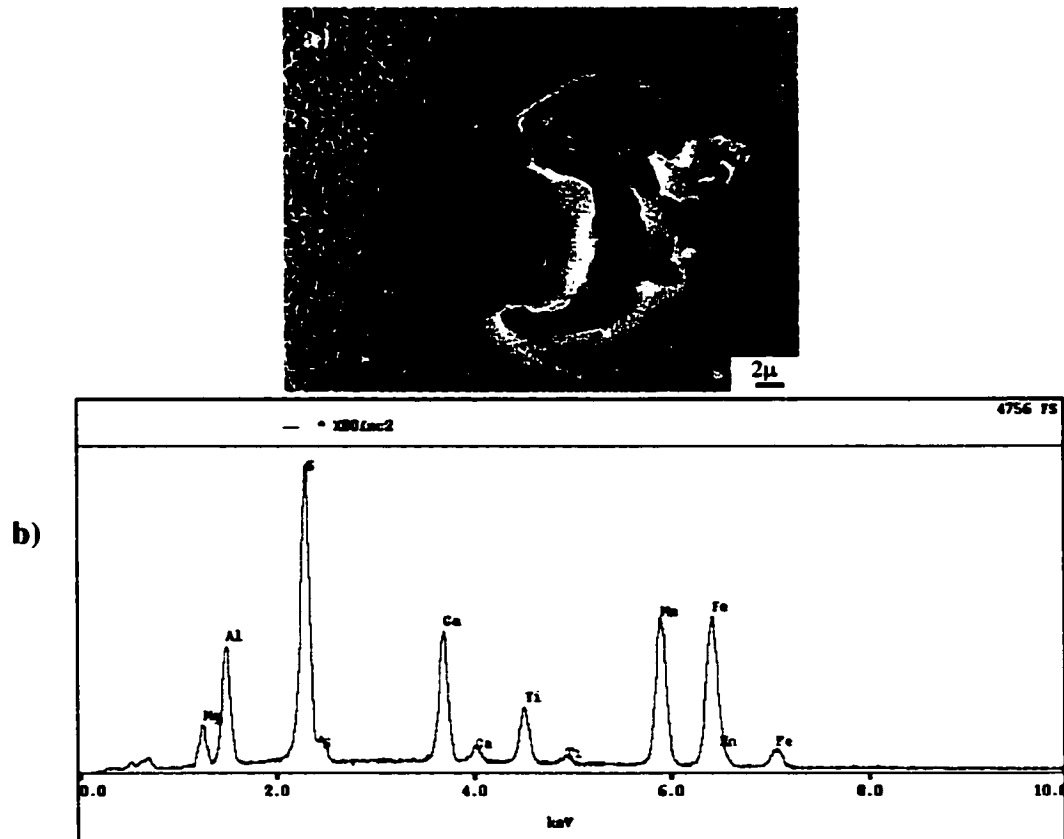


Figure 5-7 a) Secondary electron SEM micrograph of a spherical non-metallic inclusions in X80 steel, b) EDX spectrum from it shows the inclusion to be consisting mainly of Ca, Mn and S with Ti, Al, Mg, Mn. Fe is from the matrix.

Figure 5-8 shows an optical micrograph of a polished and unetched sample of X80 steel in the LS orientation. The size and distribution of the inclusions is apparent.

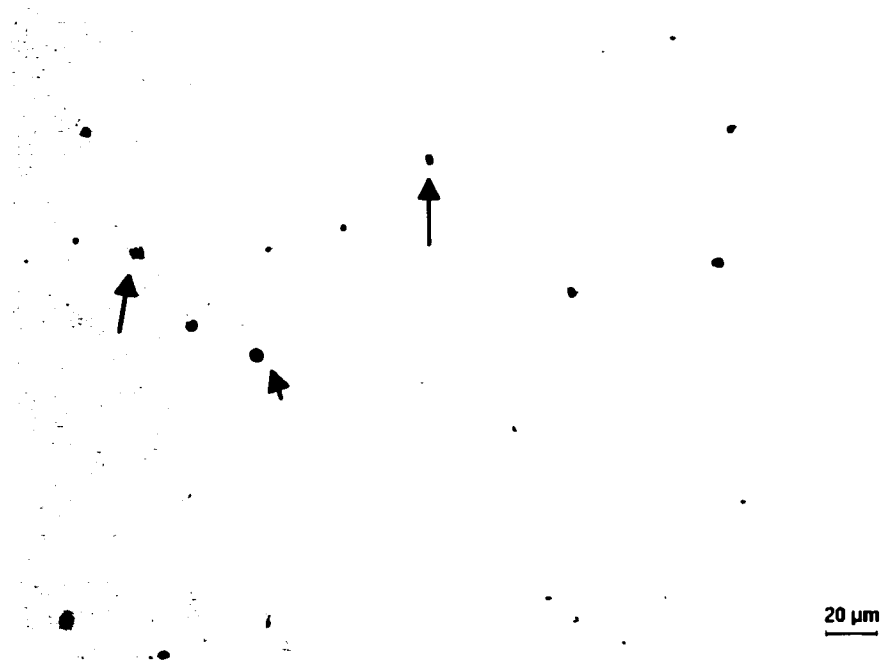


Figure 5-8 Polished and unetched X80 steel in the LS orientation depicting the size and distribution of non-metallic, Ca-Mn-S inclusions.

Image analysis was used to identify and count the inclusions present in various regions of the plate with respect to the rolling direction and thickness of the plate as depicted in Figure 3-2. Seventy observations were made on each area (e.g., LS-Top) with each observation corresponding to an area of  $1600\mu\text{m}^2$ . Statistical analysis was performed to ascertain the distribution of these inclusions in terms of size (planar intercept area) and shape (aspect ratio). When the size is measured as planar intercept areas from the two perpendicular areas (LS and ST in this case) then it directly corresponds to the volume of these spherical particles. Similarly by measuring the aspect ratio on the two perpendicular faces LS and LT a good estimate of the shape of the inclusion can be made. The plots below show the shape and size distribution of CaMnS inclusions in X80 steel (Figures 5-9 to 5-12).

The following observations can be made:

- As with X70 the inclusions are more or less spherical. There are no long stringers present in the X80 steel. The particle shape is close to being spherical; however, they are slightly elongated along the rolling direction and across the width of the plate.
- Most of the inclusions have areas  $\leq 3\mu\text{m}^2$  with about 75% of them having areas  $\leq 1\mu\text{m}^2$ .
- The nominal density of inclusions in the LS orientation is around  $1.9 \times 10^5/\text{cm}^2$ .
- There is no appreciable difference in distribution of inclusions across the thickness of the plate. This implies good mixing in the liquid steel and good casting practice.

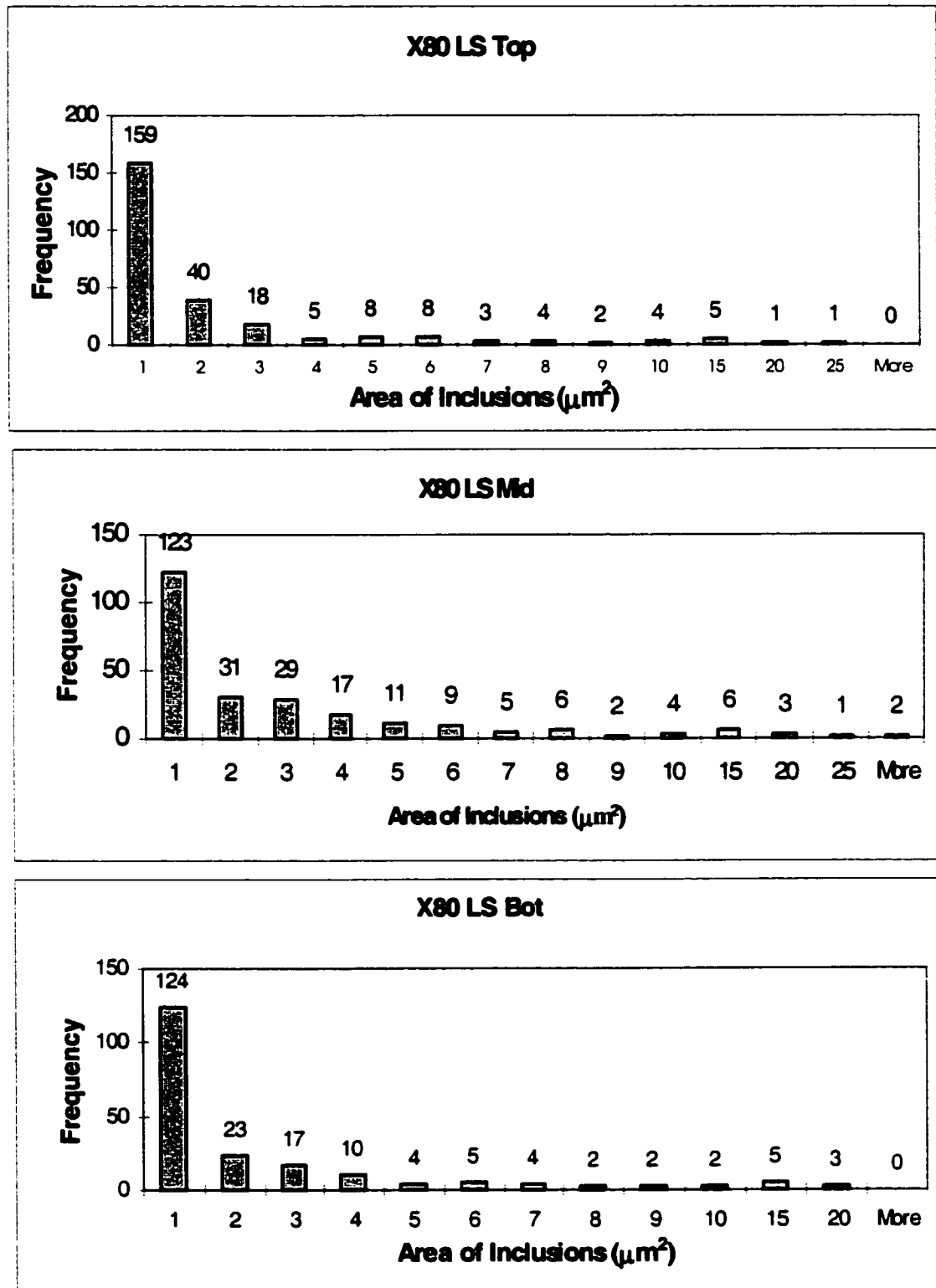


Figure 5-9 Planar intercept area of inclusions in X80 steel along the LS orientation.

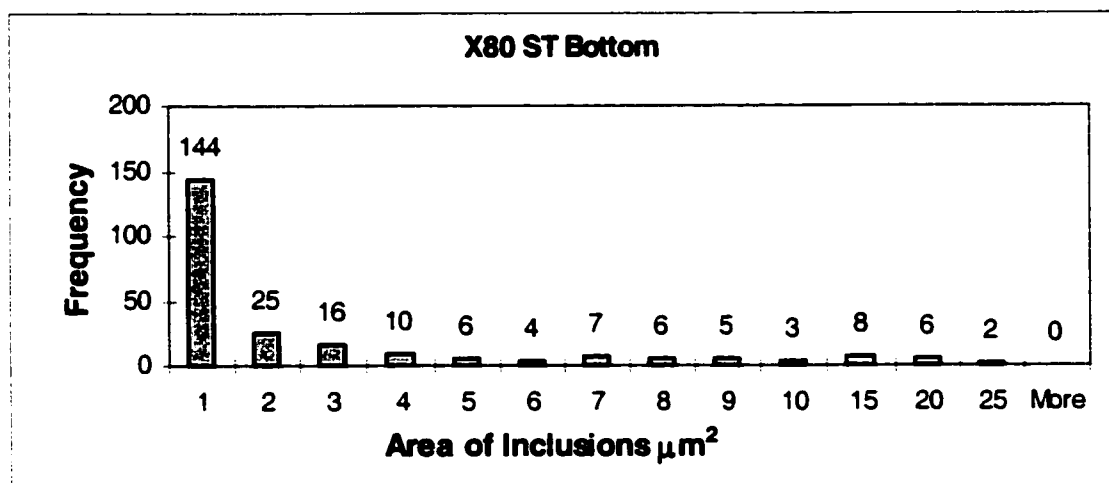
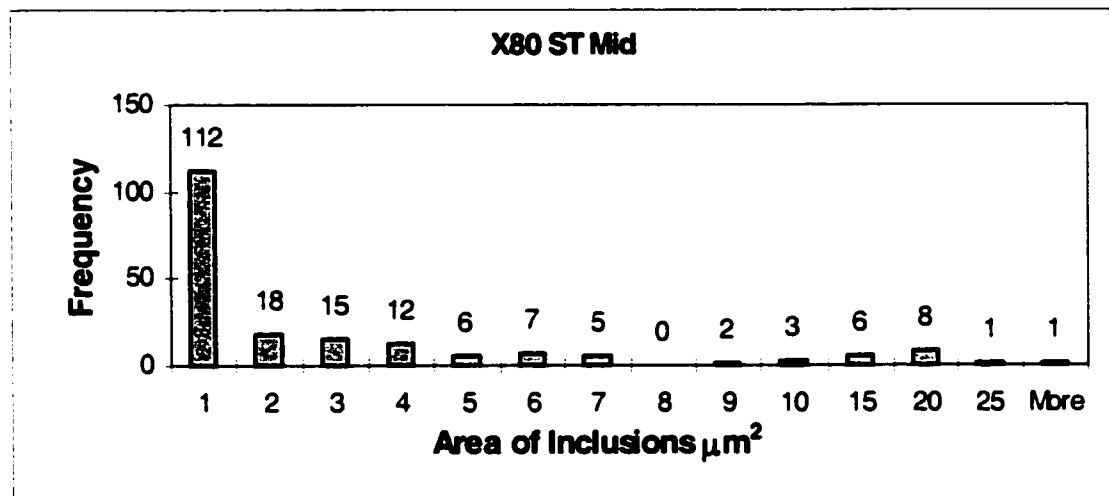
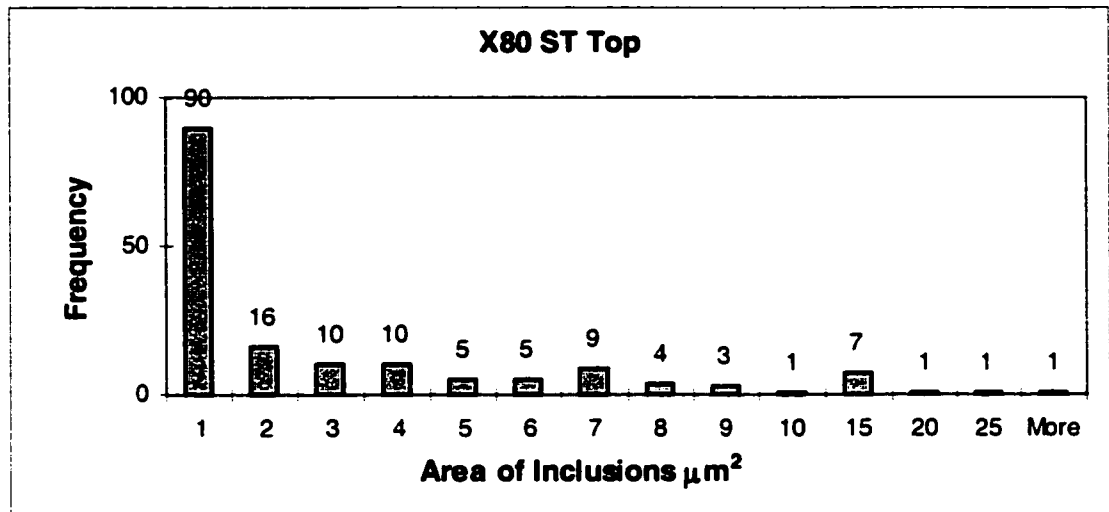


Figure 5-10 Planar intercept area of inclusions in X80 steel along the ST orientation.

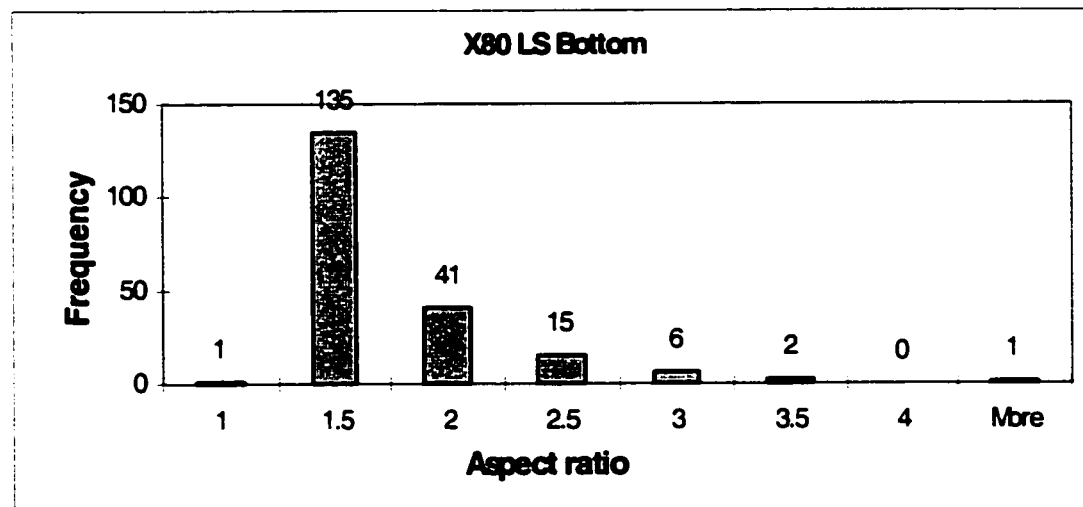
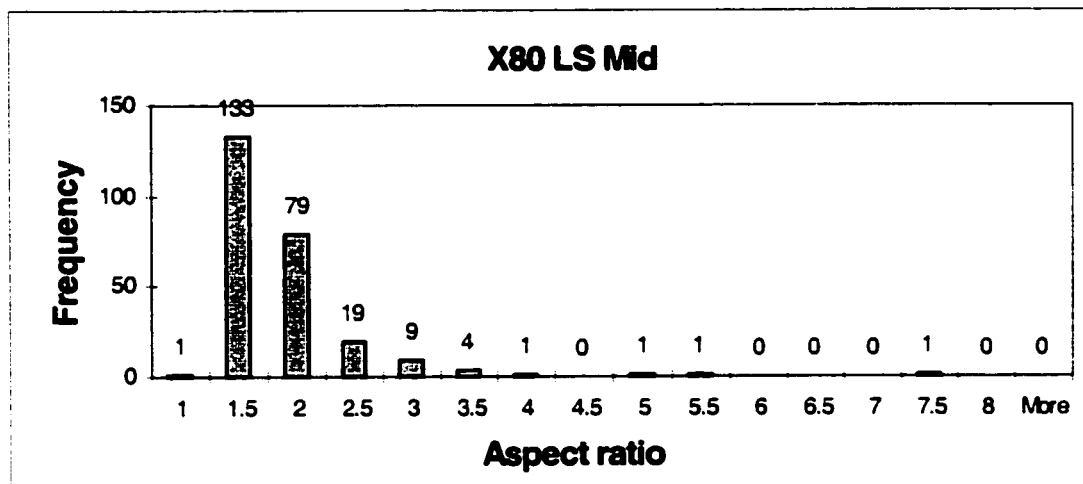
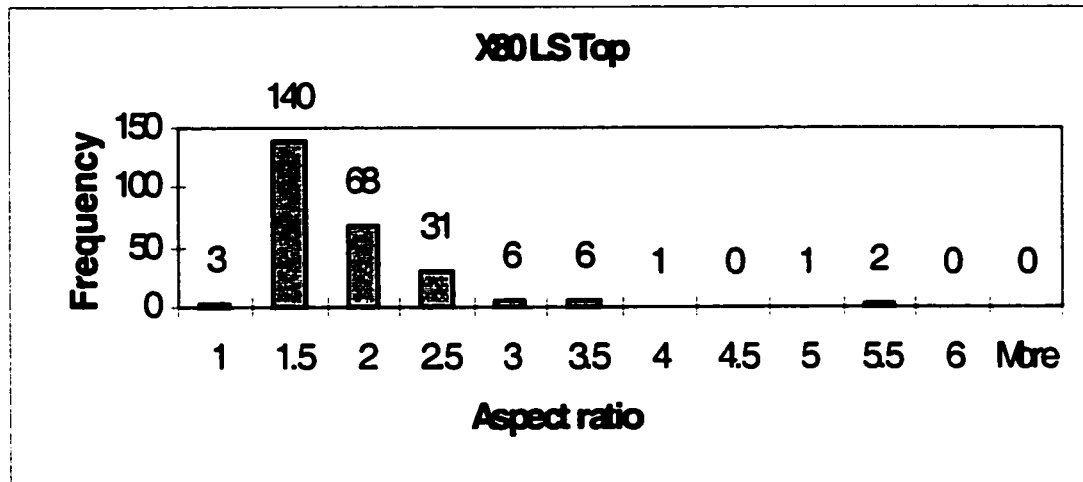


Figure 5-11 Aspect ratio of inclusions in X80 steel along the LS orientation.

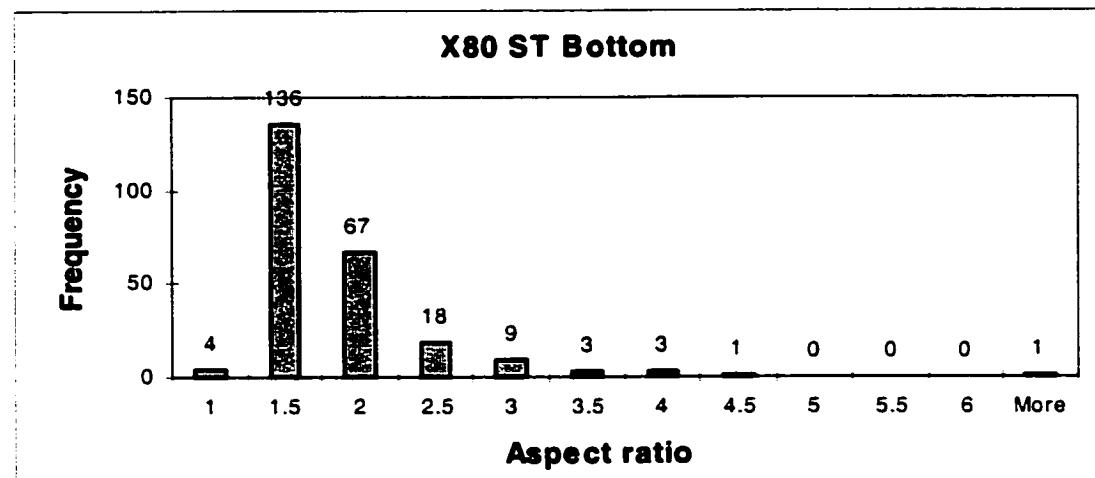
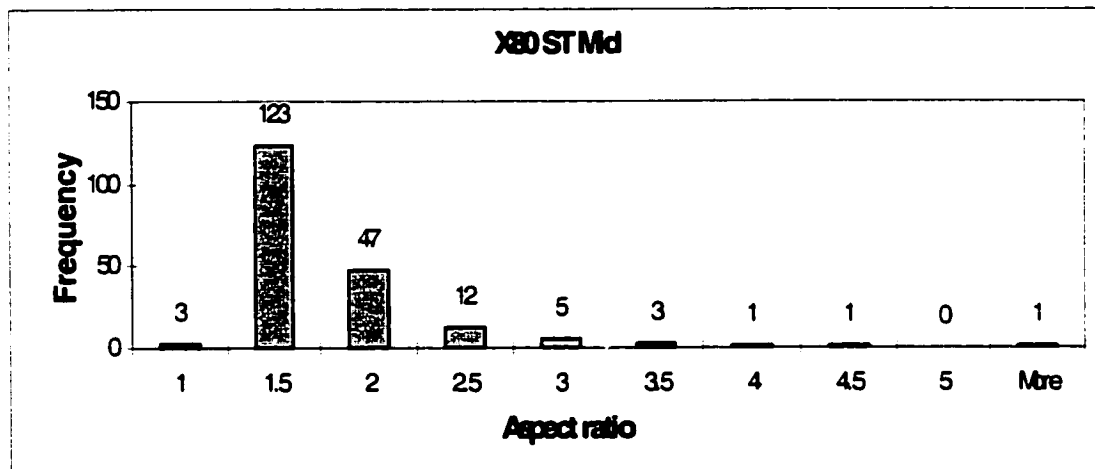
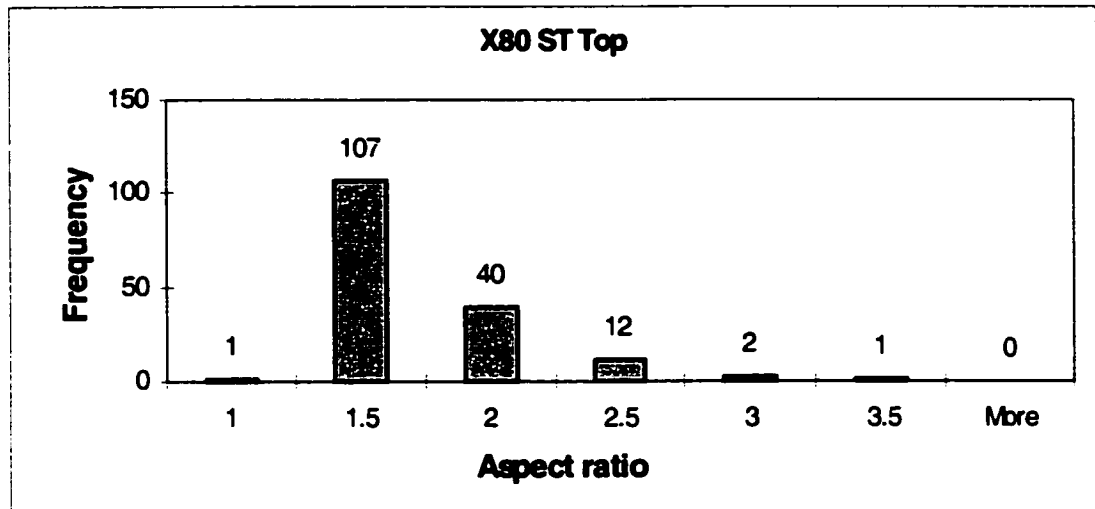


Figure 5-12 Aspect ratio of inclusions in X80 steel along the ST orientation.

## 5.4 Precipitates in X80 Steel

Similar to X70 steel, five kinds of precipitates were observed in the X80 steel. They were classified into these categories based on their size, shape, composition and the various stages of rolling during which they precipitate out from the solution.

### 5.4.1 Very Large TiN Precipitates (2-10 $\mu$ m)

As in X70 steels, this class of precipitates was large enough to be seen under low magnifications in an optical microscope. A key identifying characteristic was their copper color. These precipitates were identified to be primarily TiN (Section 4.4.1, [Itman97] and [Zhou96]). The majority of these precipitates were cuboidal in shape with a particle in their interior. The particle was later identified to be the non-metallic inclusions present in the steel. In X80 steel, in addition to inclusions at the precipitate core, there were many precipitates with spherical particles attached to their exteriors. Figure 5-13 shows an optical micrograph of X80 steel in LS orientation, depicting a copper colored, faceted precipitate with a dark particle in the interior and another large inclusion attached on the side.

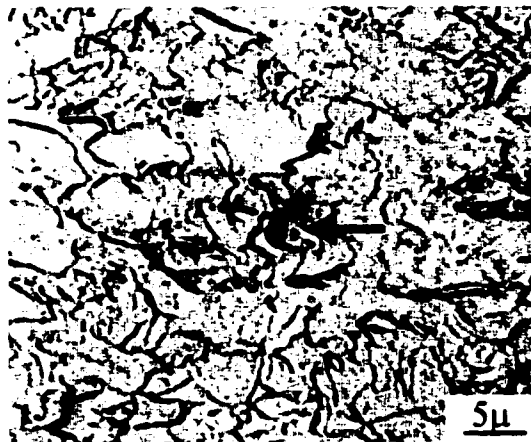


Figure 5-13 TiN cuboidal precipitate in X80 steel with a non-metallic inclusion at its interior and another attached to its side.

Figure 5-14a shows an SEM micrograph of a similar precipitate and the adjoining EDX patterns identify the different components. The cuboidal particle was Ti rich with some Nb, similar to X70. The inclusions attached to the sides contained Mn in addition to Ca and S. It appears that while in the melt the inclusions physically attached onto the already present large TiN cuboids. The large Fe peak in all the spectra is from the matrix. A general observation was that the non-metallic inclusions in X80 contained substantial amounts of Mn in addition to Ca and S, as well as trace amounts of Ti, Al and Mg.

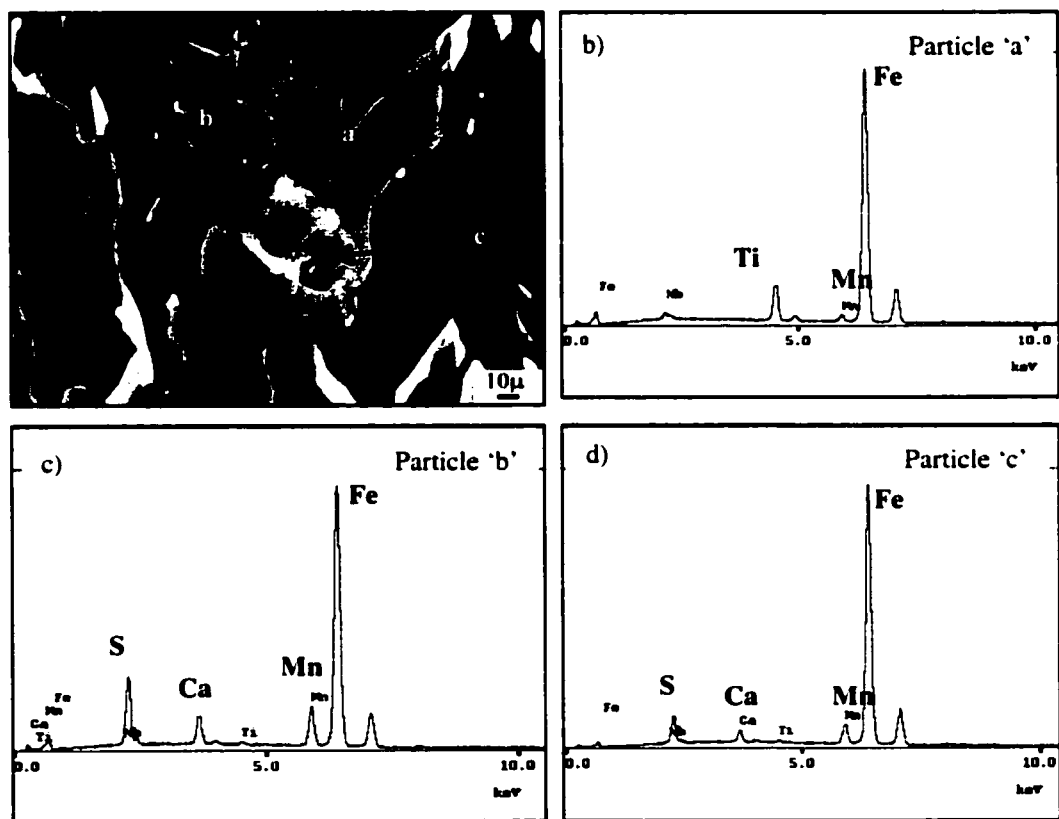


Figure 5-14 a) Secondary electron SEM micrograph of a TiN cuboidal precipitate with inclusions attached to the sides, b)-d) EDX from the various areas as marked in a).

As for X70 steel, a method of random sampling and random intercepts was followed to count the number and size of these precipitates in X80 steel. 50 areas were chosen at random near the centerline and at near the surface of the plate in the LS orientation and number of particles contained in them counted. Each area was  $1600\mu\text{m}^2$ . This gave a very crude approximation of areal density of the precipitates. The average intercept length gave an approximation of the relative sizes (Figure 4-19).

Table 5-3 shows the results for X80 steel. The large TiN precipitates were concentrated near the centerline of the plate indicating segregation effects during the solidification of the slab after continuous casting. These are discussed in more detail in Chapter 7. Precipitates size was slightly larger in the interior than at the surface.

Table 5-3 Density and size distribution of TiN precipitates across the thickness of X80 plate.

	<b>X80</b>	
	<b>Center</b>	<b>Surface</b>
<b>Density (#/cm<sup>2</sup>)</b>	<b>2500</b>	<b>900</b>
<b>Average Size (μm)</b>	<b>2.6</b>	<b>2.1</b>
<b>Std. Dev (μm)</b>	<b>0.9</b>	<b>1.0</b>

#### 5.4.2 Large Cuboidal Precipitates (0.1-1.0μm)

These precipitates were cuboidal in shape and many had additional particles growing on one of the facets (Figure 5-15a). Individual cuboidal particles were also observed but the majority of them were associated with a second particle which was irregular shaped (Figure 5-15a) or faceted (Figure 5-15b). The large, base cuboidal precipitates consisted mainly of Ti but had some Nb as well (Figure 5-16a) whereas the other particles were Nb rich with smaller amounts of Ti (Figure 5-16b). Both types of particles were fcc, NaCl type. Both particles had the same crystallographic orientation, i.e., there was epitaxial growth of smaller Nb rich precipitate on the larger, cuboidal Ti rich precipitate. Figure 5-17 shows an SAD pattern from the pair of

precipitates in Figure 5-15b. The spot splitting indicates two particles with the same crystal structure and orientation and almost the same interplanar spacing. The outer spots are from TiN and inner from NbC.

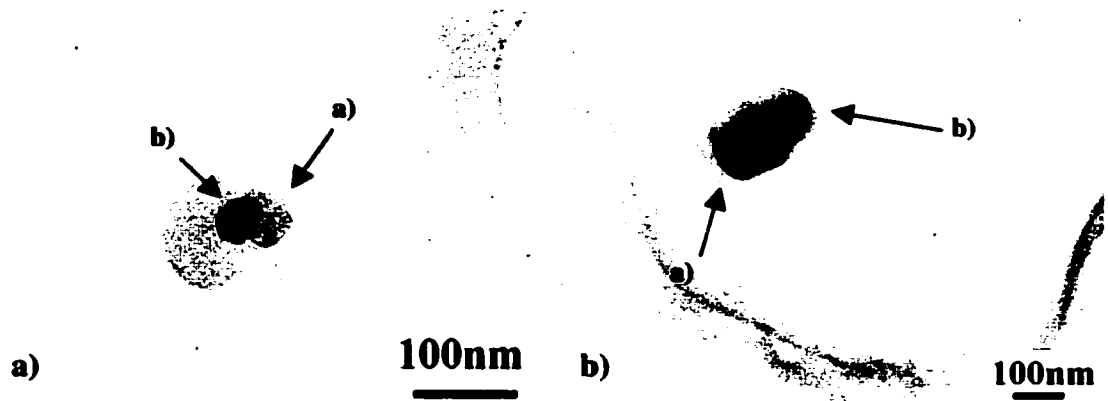


Figure 5-15 Large cuboidal precipitates in X80 associated with a second particle growing epitaxially from one of the edges: a) Irregularly shaped second particle. b) Faceted second particle.

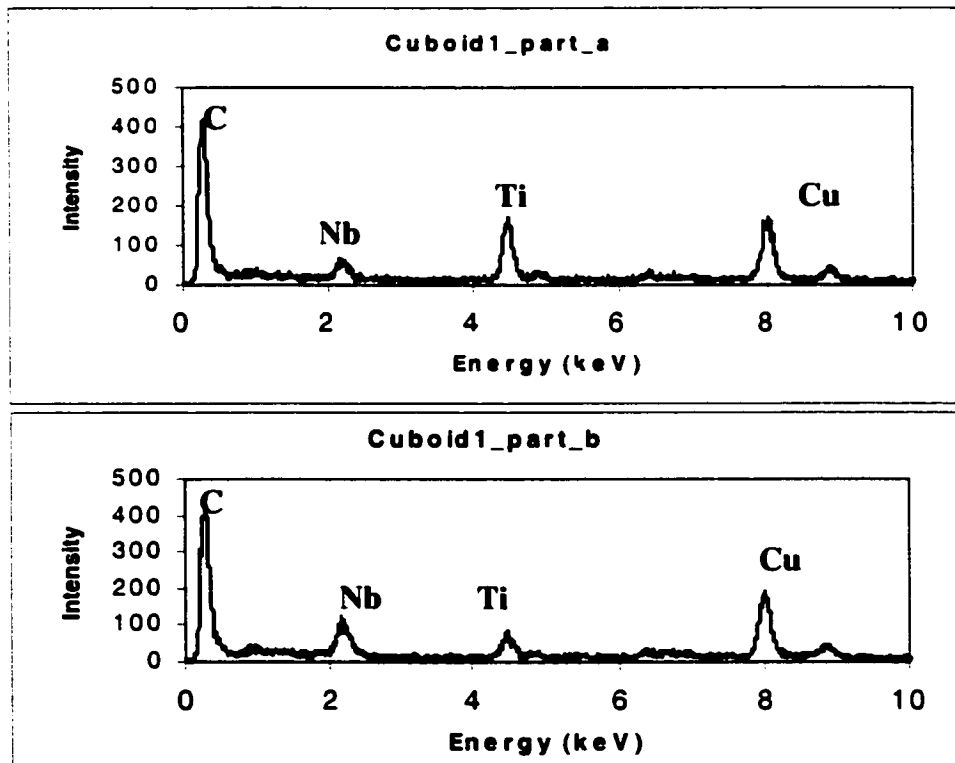


Figure 5-16 EDX spectra from the large precipitates in X80 steel (Figure 5-15a) . a) Larger, cuboidal particle which is richer in Ti and b) smaller irregularly shaped particle richer in Nb.

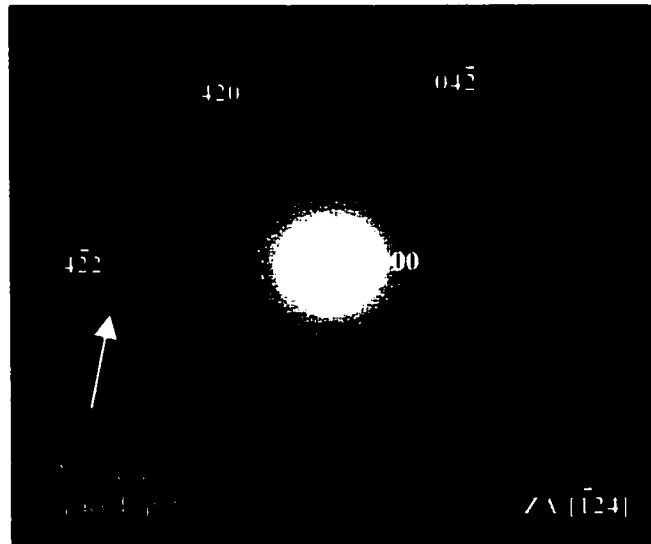


Figure 5-17 SAD pattern from the pair of precipitates from Figure 5-16b. The crystallographic orientation is the same with a slight mismatch in d spacing as shown. The outer spots are from TiN and inner from NbC. The rings are from the amorphous carbon film supporting the precipitates.

#### 5.4.3 Medium Sized Irregularly Shaped Precipitates (30-50nm)

In X80 steel, many of the Nb rich precipitates of this type were seen associated with the larger TiN particles as discussed above (Figure 5-15a). The larger precipitates act as nucleation sites for growth of the Nb-rich precipitates. However, these precipitates were also observed distributed within the grains. These precipitates come out by a 'strain induced mechanism' and act to pin the austenite grain boundaries. The crystal structure was again NaCl-type, common to Ti and Nb carbonitrides. Figure 5-18 shows a BF TEM image from a carbon replica showing several rounded and irregular shaped precipitates distributed randomly within the grain and at the grain boundaries.

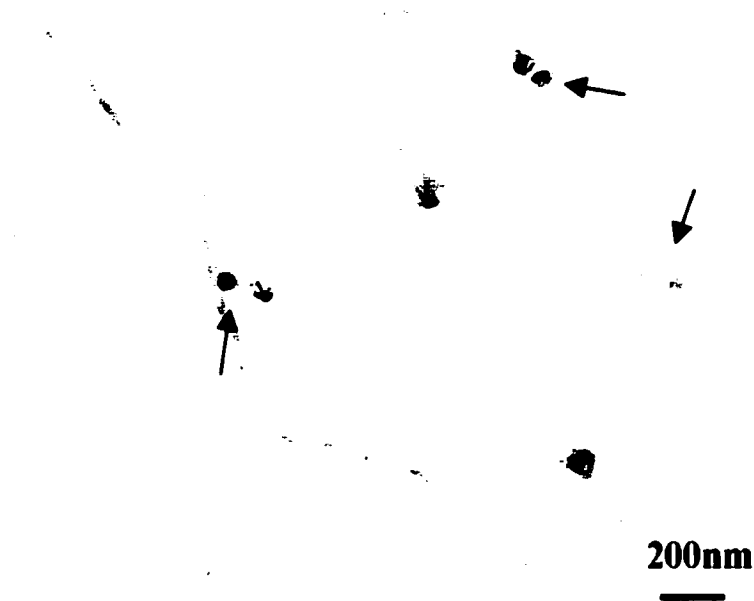


Figure 5-18 TEM BF image of X80 carbon replica showing irregular shaped, Nb rich precipitates at the grain boundaries and within the ferrite grains.

#### 5.4.4 Small Spherical Precipitates ( <20nm)

As with the X70 steel, the X80 steel possessed small rounded precipitates spread randomly throughout the grains. They were quite small ( <20nm). Most of them were in the size range 5-15nm. They consisted mainly of Nb with some Mo. The particles were identical in all respects to the ones identified in X70 steels. For details refer to Section 4-4. Figure 5-19 shows a bright field TEM micrograph of the small precipitates surrounding a medium sized cuboidal precipitate from a carbon replica sample.

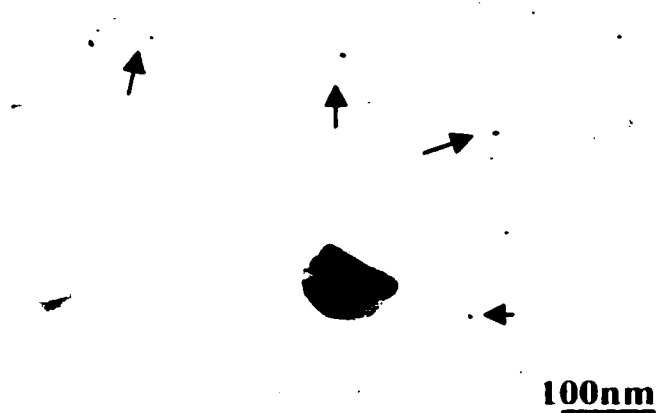


Figure 5-19 TEM BF micrograph of carbon replica from X80 steel showing presence of small (<10nm), spherical precipitates of NbC in the matrix.

#### 5.4.5 Very Small Precipitates (<5nm)

As with X70 steels, in addition to the four major types of precipitates already discussed, some very small (<5nm) precipitates were detected in X80 (Fig. 5-20). The precipitates form during the later stages of processing when the strip is being coiled at temperatures <600°C. At this temperature virtually all the Ti has been depleted and the Nb precipitates out with C and N by nucleating on the dislocations and at the grain boundaries. These finely dispersed precipitates contribute to precipitation strengthening in these steels.

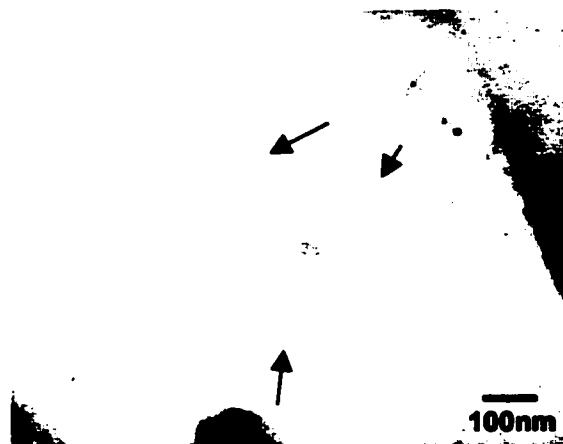


Figure 5-20 TEM BF image from thin foil X80 showing extremely small (<5nm) precipitates spread throughout the grain and at grain boundary.

## **Chapter 6: Grade80 Steel**

### **6.1 Introduction**

Grade80 steel is a plate steel. It is not employed for line pipe construction but used as a flat product. Therefore the toughness requirements are not as strict and the focus is on getting the required minimum strength levels. For the Grade80 this refers to a specified minimum yield strength (SMYS) of 80ksi or 550MPa. Consequently, sulfur control is not so critical in this steel and higher levels up to 0.01wt% are common. The chemistry of Grade80 is richer than X70 and X80 in terms of carbon (0.06wt%), Nb, Ti, Mo and residual elements like Ni, Cr and Cu. Mn levels are around 1.64wt%. Figure 2-1 gives the full chemical composition of Grade80 steel along with other linepipe grades and relevant comparisons can be drawn. Figure 2-2 lists the important physical properties of this grade of steel. It has sufficiently high strength levels (587MPa LRD) but comparatively, low fracture toughness (140J@RT LRD). The thermomechanical rolling treatment provided to Grade80 was similar to X70 linepipe grade. However, many distinctive characteristics in its microstructure were observed, mainly depending on the chemistry but also on the thermomechanical processing. These are described in the following sections.

### **6.2 Grain Structure**

The grain structure in Grade80 steel was primarily typical acicular ferritic that has been described in the previous sections (Sections 4-1 and 5-1) with amounts of bainitic ferrite along with some retained austenite and MAC. The grains were highly dislocated and irregular in shape and showed a mixed grain size ranging anywhere from 1 $\mu$ m to several tens of  $\mu$ ms in size. Compared to the X70 and X80 steel, a considerably smaller percentage of the matrix appeared to be composed of polygonal ferrite when compared to X70 and X80 steels. Figure 6-1 shows an optical micrograph of the Grade80 steel in the LS orientation and away from the edges or the centerline.

The grains are elongated and deformed and the grain boundaries are not sharply demarcated.



Figure 6-1 Optical micrograph of Grade80 steel in LS orientation, etched with nital, showing the typical grain structure. Some areas appear as massive lath shaped with poorly defined substructure, as pointed out by the upper arrow marked 'AF'. The dark spherical particles are the non-metallic inclusions present in the steel.

On observing the steel in a SEM at higher magnifications (2000X-5000X) (Figure 6-2), many of the grains which appeared as massive grains in the optical microscope could be seen to consist of smaller subgrains which had low angle grain boundaries. Since they are separated by low angle grain boundaries, a chemical etch like nital, for optical metallography, etches away the entire area as one grain. The presence of this kind of substructure has been verified by observations in the TEM. Diffraction patterns from individual subgrains showed them to be approximately of the same crystallographic orientation with very small ( $<5^\circ$ ) angular mismatches (similar to that shown in Section 5-1 for X80 steel). One instance is depicted in Figure 6-3, where

the diffraction pattern from two adjoining ferrite grains superimposes with a very slight rotational mismatch.

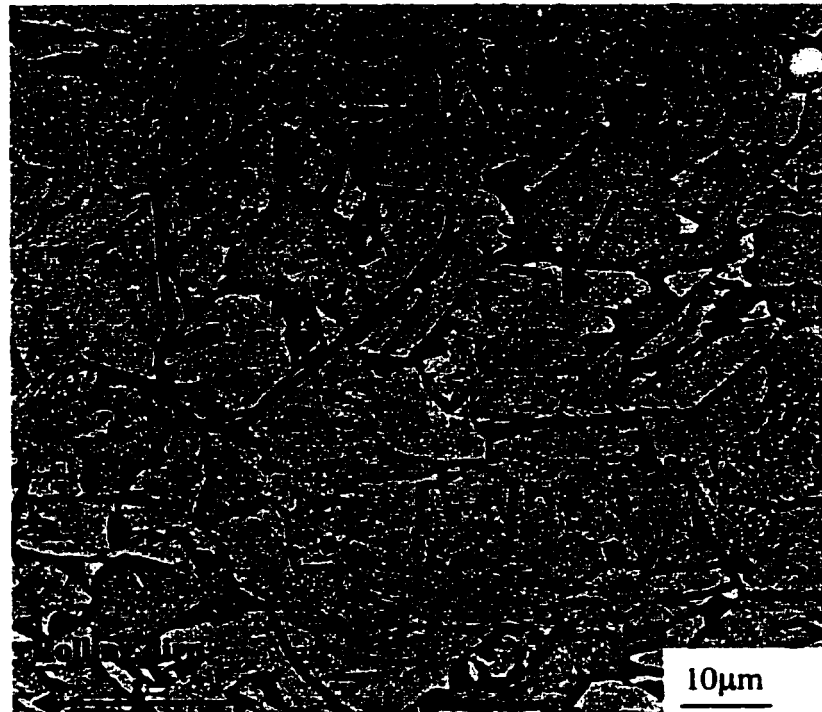


Figure 6-2 Secondary electron SEM micrograph of Grade80 steel showing subgrains in a large grain, as marked by the line.

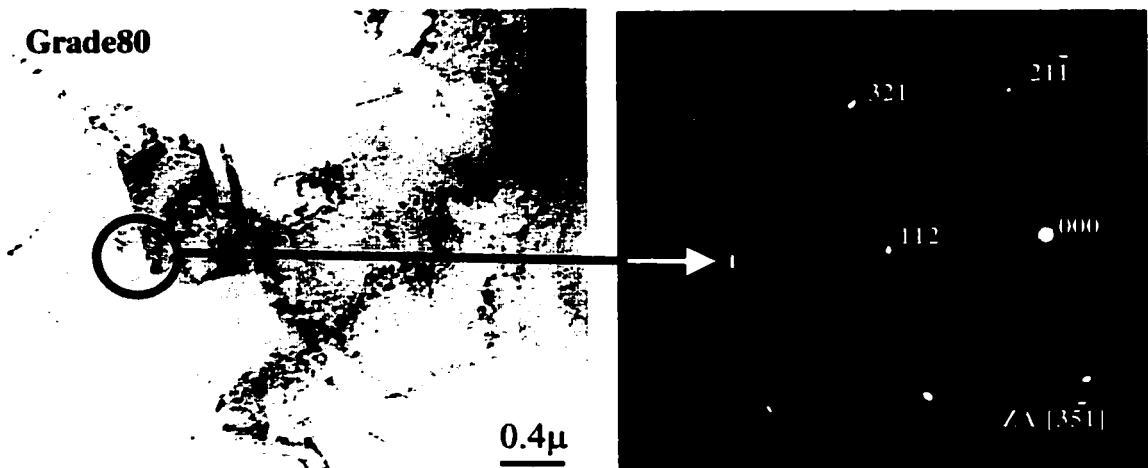


Figure 6-3 TEM BF image of a Grade80 thin foil showing a) lathlike grain structure. b) SAD pattern from adjoining grains shows presence of low angle grain boundaries through splitting of spots as marked by the arrow.

A method of random intercepts was used to study and assign an apparent grain size as outlined in the previous section (section 4-1). Three areas, each of  $1600\mu\text{m}^2$  were selected and 30 random lines drawn for each. The number of grains intercepted by each line counted and the inverse of this quantity provided an estimate of the grain size. About 500 grains were counted in all. The standard deviation gave an approximation of the degree of the mixed nature of grain sizes. A lower standard deviation implies that grains were more or less within a narrow size range and a large deviation reflected a cluster of large and small grains. Table 6-1 shows the results obtained from near the centerline and near the surface of the plate. The grains in Grade80 were larger and more mixed in size (both large and small) near the center of thickness of the plate. The grains were smaller and more equiaxed near the surface of the plate and more or less of a very narrow size range, as represented by the small standard deviation.

Table 6-1 Grain size as average intercept length for Grade80 steel in LS orientation.

Grain Size	Grade80	
	Center	Surface
Average intercept length ( $\mu\text{m}$ )	10.9	5.8
Standard deviation ( $\mu\text{m}$ )	7.7	1.3

Table 6-2 represents the aspect ratio of grains by taking average intercepts of grains along the rolling direction and perpendicular to it across the thickness of the plate. The grains are more equiaxed nearer to the surface (aspect ratio closer to one) when compared to the interior.

Table 6-2 Aspect ratio of grains for Grade80 steel along the LS orientation.

	<b>Grade80</b>	
	<b>Center</b>	<b>Surface</b>
<b>Aspect Ratio</b>	2.4	1.2

The Grade80 steel showed marked centerline segregation. Many elongated non-metallic inclusions were visible at the centerline (Figure 6-4a), as were large , shiny, cuboidal precipitates of TiN (Figure 6-4b).

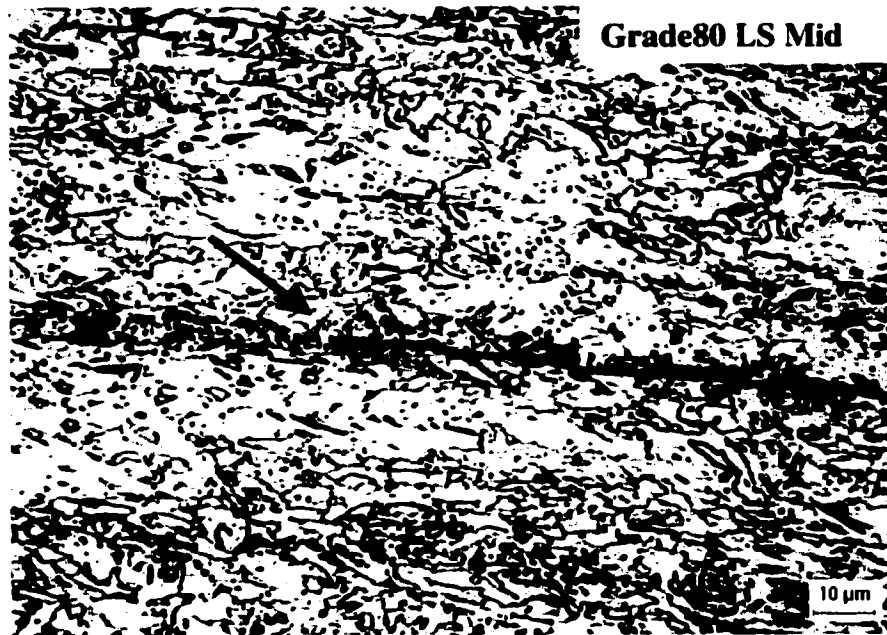


Figure 6-4 a) Centerline segregation in Grade80 steel. The presence of elongated inclusions at the centerline is indicated by the arrow (etched with nital).

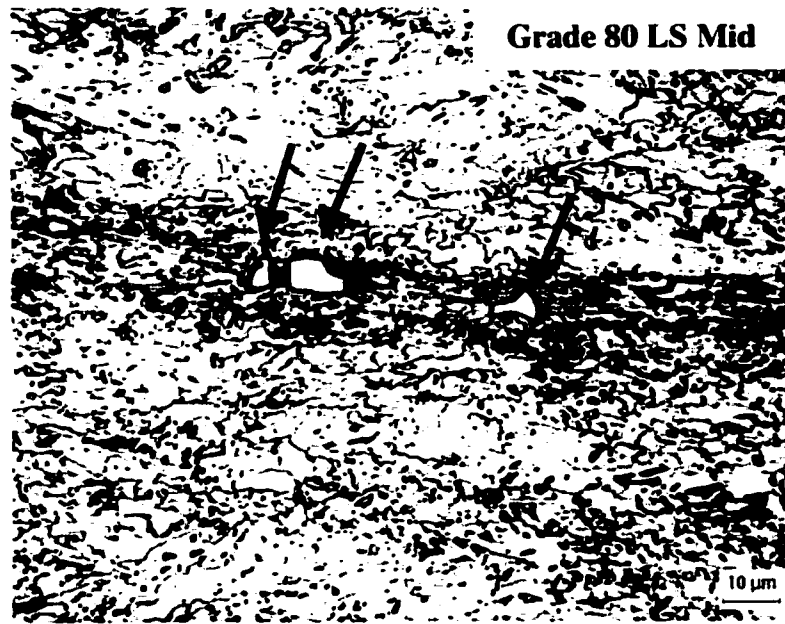


Figure 6-4 b) TiN faceted precipitates in Grade80 steel at the centerline.

When etched with picral for long times, the Grade80 steel also showed the presence of a 'pearlite-like' microstructure as observed in X70 and X80 steel (Figure 6-5). This phase was coarser and sparsely distributed in the center when compared to the surface, where it was finer in size and well dispersed.



Figure 6-5 Optical micrograph of Grade80 steel etched with picral showing presence of pearlite-like microstructural constituent.

As with the other grades of steel, TEM was used to ascertain the crystal structure of the constituent phases and observe other microstructural features like dislocations, subgrains and small precipitates, which are revealed only at high resolution and remain invisible in optical and SEM microscopy. The grains in Grade80 were mainly bcc ferrite. They were acicular in nature and possessed high dislocation densities (Figure 6-6). As with X70 and X80 steel, many of them had low angle grain boundaries with adjoining grains (Figure 6-3). Figure 6-7a shows a TEM BF image of thin foil of Grade80 in LS orientation. Elongated acicular grains are clearly visible. The adjoining diffraction pattern identifies the lathlike grain to be bcc ferrite (Figure 6-7b).



Figure 6-6 TEM BF image from a thin foil of Grade80 showing the presence of numerous dislocations in a grain of ferrite.

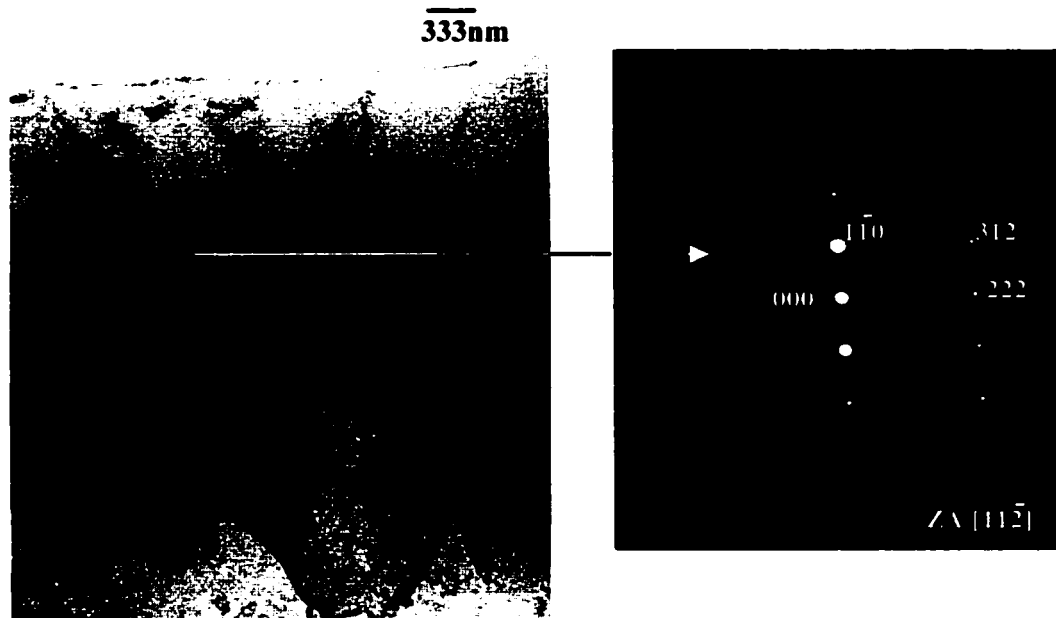


Figure 6-7 a) TEM BF micrograph of Grade80 steel showing acicular ferrite grains. b) SAD pattern from one acicular grain identifies it to be bcc ferrite.

### 6.3 Inclusions in Grade80 Steel

The Grade80 steel contained larger amounts of sulfur (0.01wt%) but similar amounts of Ca (0.002wt%) as compared to X70 and X80 grades. This resulted in the Grade80 steel having elongated inclusions, consisting mainly of Mn and S, besides rounded inclusions. The stringers were observed more along the centerline of the plate where they grew up to 50 $\mu$ m in length. The inclusions away from the centerline were smaller and in most cases rounded. However some shorter stringers were observed. Figure 6-8 illustrates this behavior. Figure 6-8a is an optical micrograph from the centerline and Figure 6-8b shows an area near the surface of the plate. Figure 6-9 shows the chemical composition of an elongated and a rounded inclusion. The elongated inclusion was found to consist mainly of Mn and S with small amounts of Ti. The large Fe peak is from the matrix (Figure 6-9a). The rounded inclusion

contained some Ca in addition to mainly Mn and S and traces of Mg, and Ti. The large peak of Al has contributions from polishing powder ( $\text{Al}_2\text{O}_3$ ), the observation being supported by a considerable O peak (Figure 6-9b). As explained in section 4.3, most probably these inclusions are a mix of oxides and sulfides of Ca, Mn, Al, Ti, Mg and Si.

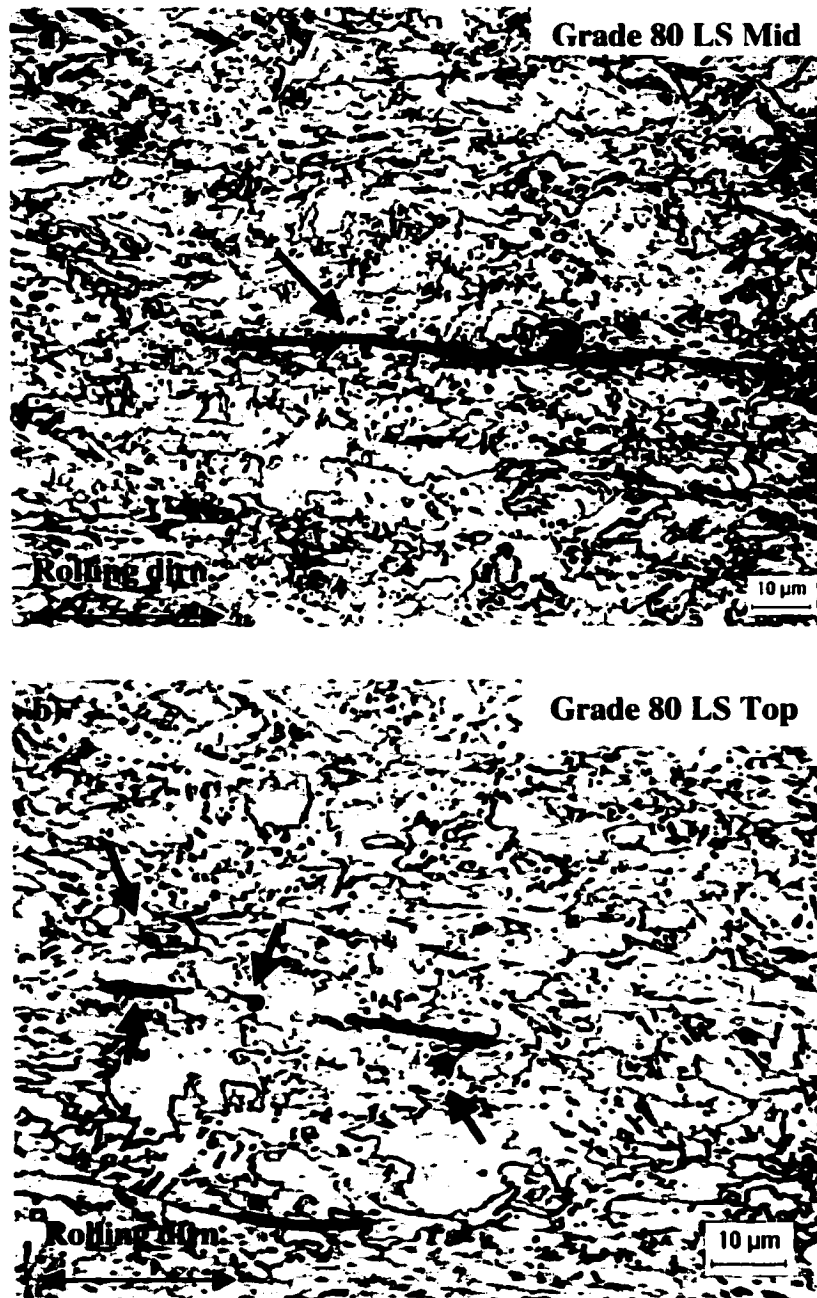


Figure 6-8 a) Optical micrograph from centerline of Grade80 steel showing a long stringer, b) near the surface of the plate the inclusions are a mix of spherical particles and short stringers. (Etched with nital).

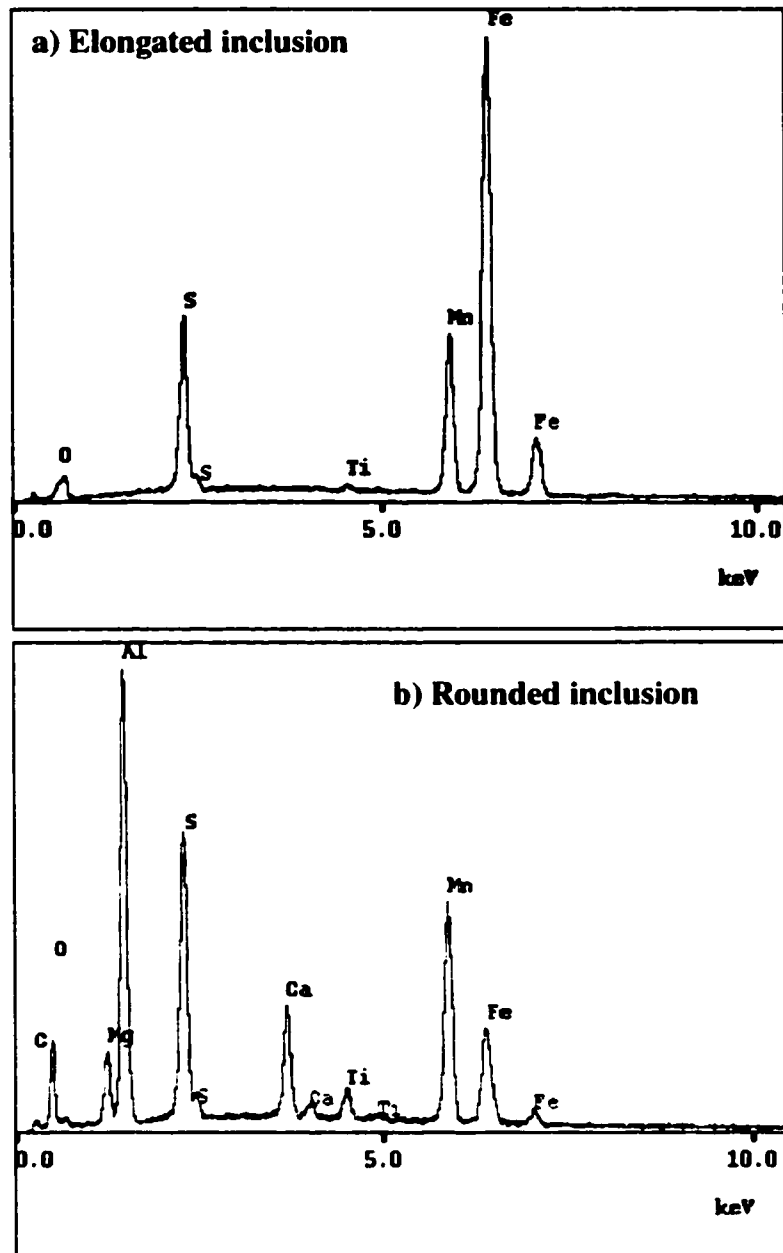


Figure 6-9 EDX spectra from inclusions in Grade80 steel. a) The elongated inclusion was composed mainly of Mn and S with traces of Ti, the large Fe peak is from the matrix; b) the small rounded inclusions consisted of considerable amount of Ca in addition to Mn and S and traces of Ti and Mg. The large Al and O peaks have contributions from the polishing powder ( $\text{Al}_2\text{O}_3$ ).

Image analysis was used to identify and count the inclusions present in various regions of the plate with respect to the rolling direction and thickness of the plate as depicted previously in Figure 3-2. However, there was one important difference in counting the inclusions in Grade80. The long stringers at the centerline of the plate could not be properly identified and delineated by the image analysis software and so they had to be counted manually. For smaller stringers and rounded inclusions away from the centerline and near the surface, the software worked fine. Seventy observations were made on each area (e.g., LS-Top) with each observation corresponding to an area of  $1600\mu\text{m}^2$ . Statistical analysis was performed to ascertain the distribution of these inclusions in terms of size (planar intercept area) and shape (aspect ratio). When the size is measured as planar intercept areas from the two perpendicular areas (LS and ST in this case) then it directly corresponds to the volume of these spherical particles. Similarly by measuring the aspect ratio on the two perpendicular faces LS and LT a good estimate of the shape of the inclusion can be made. The plots below show the shape and size distribution of inclusions in Grade80 steel (Figures 6-10 to 6-13).

The following observations can be made:

- Looking at the aspect ratios in the LS and ST direction, the presence of highly elongated inclusions is indicated near the centerline (aspect ratios as high as 50 – 100). Some elongated inclusions are also present throughout the thickness but generally their aspect ratio is  $\leq 3$ .
- Most of the inclusions away from the centerline have areas  $\leq 5\mu\text{m}^2$  however, about 20% have areas in the range  $5\text{--}25\mu\text{m}^2$ .
- The nominal density of inclusions in the LS orientation is around  $0.4 \times 10^5/\text{cm}^2$  near the centerline and  $2.2 \times 10^5/\text{cm}^2$  near the surfaces
- There is considerable segregation at the centerline. This might be due to improper mixing in the liquid steel or some casting problem, such as high superheat which provides longer times at higher temperatures for the solutes to be partitioned from solidifying grains to the interdendritic, liquid region at the center of the slab.

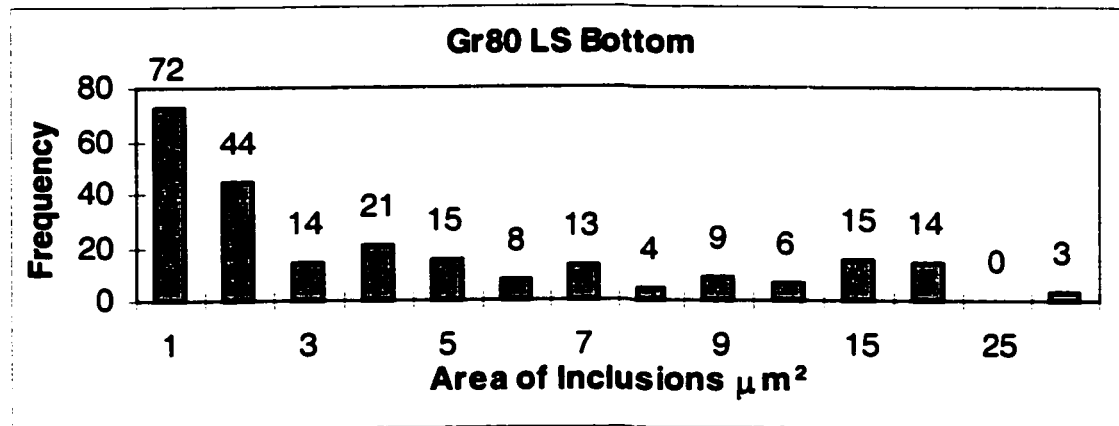
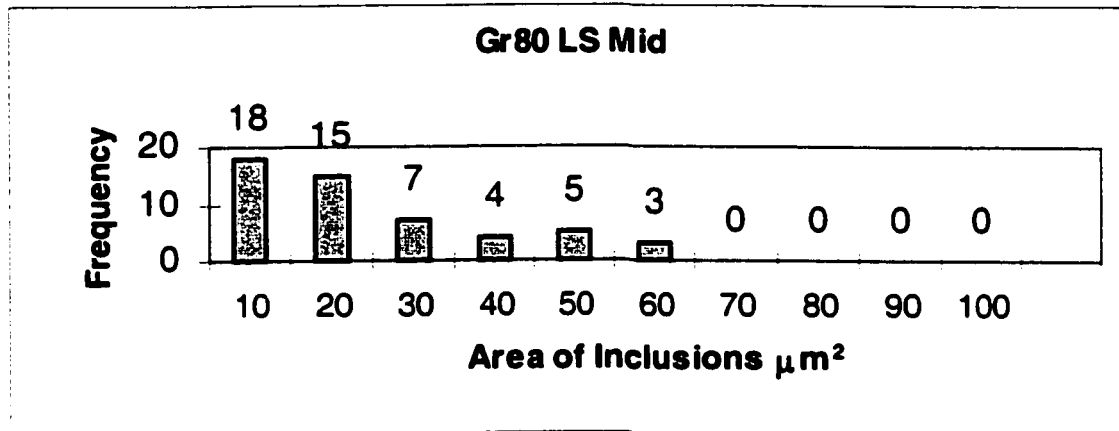
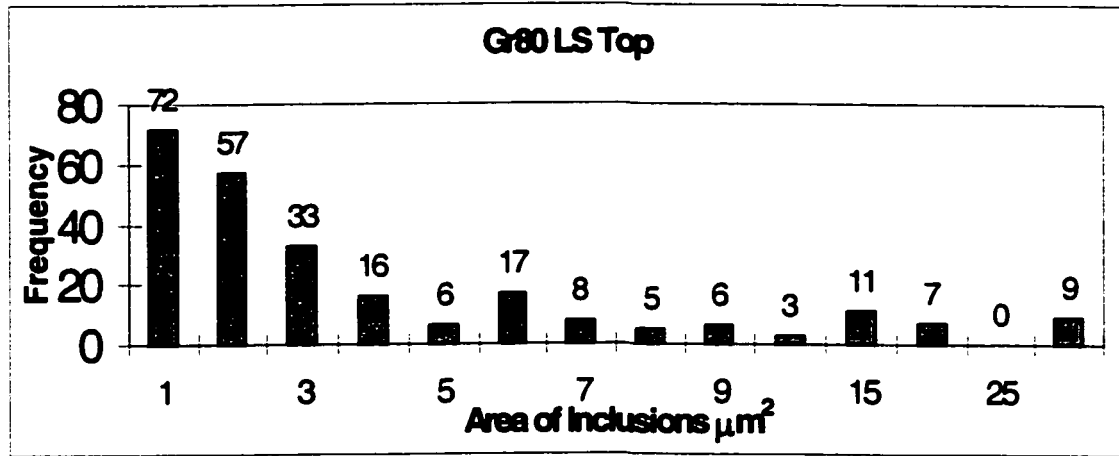


Figure 6-10 Planar intercept area of inclusions in Grade80 steel along the LS orientation.

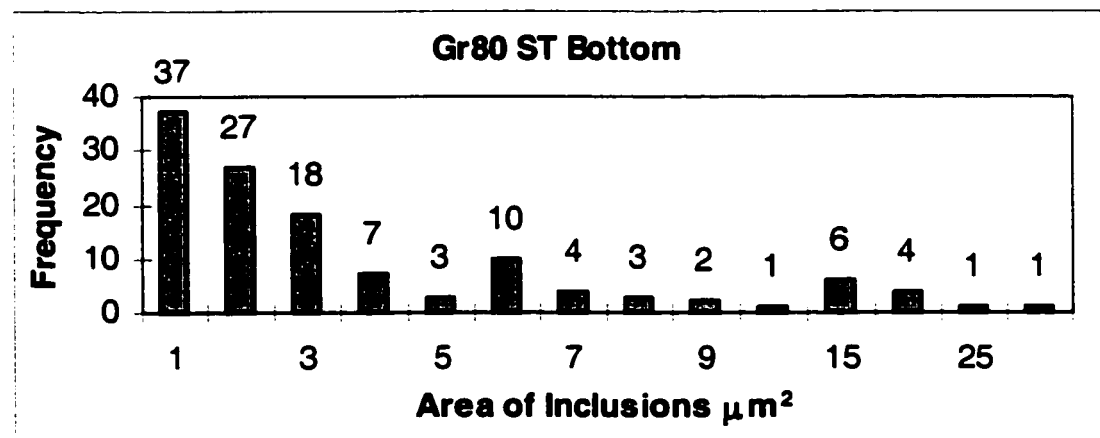
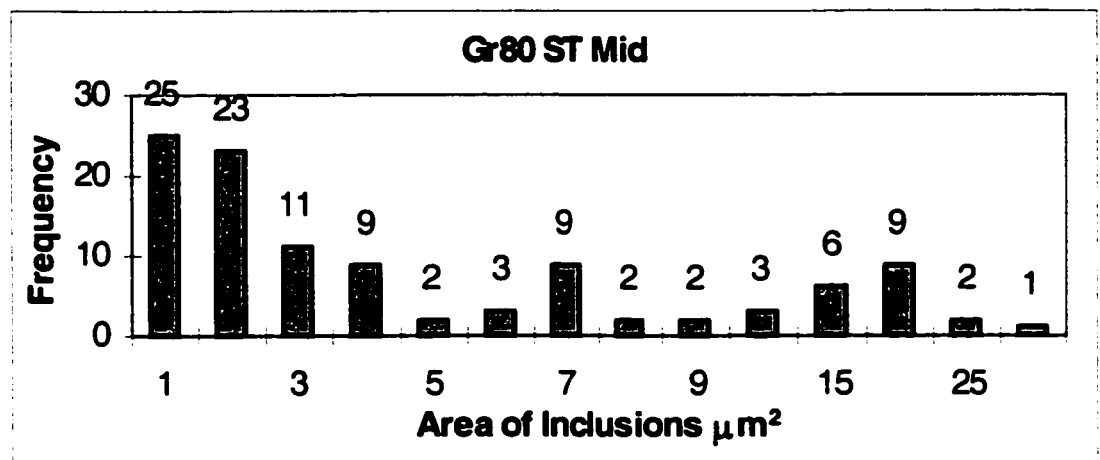
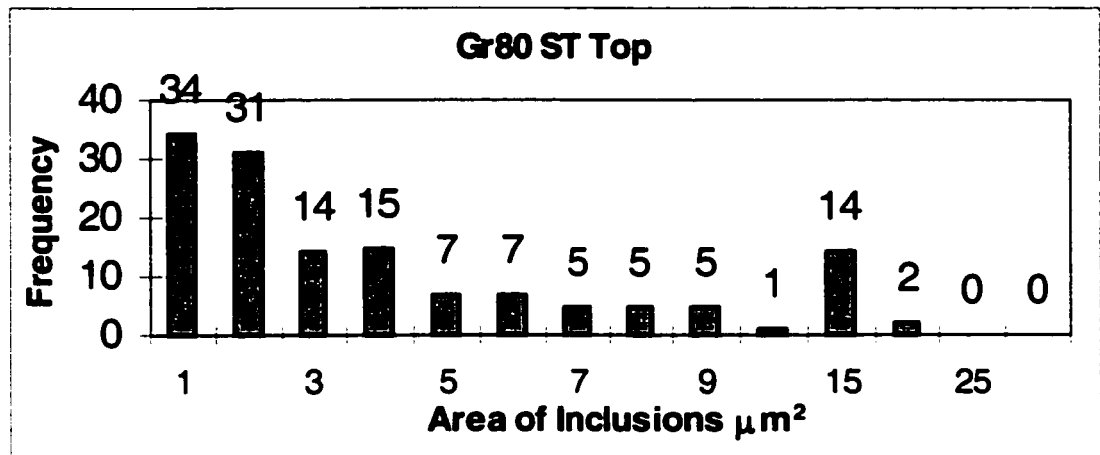


Figure 6-11 Planar intercept area of inclusions in Grade80 steel along the ST orientation.

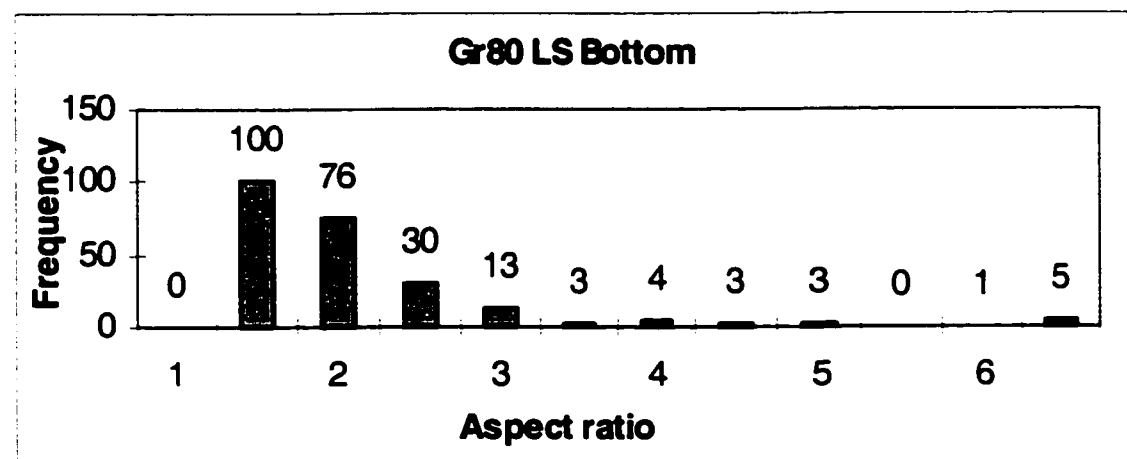
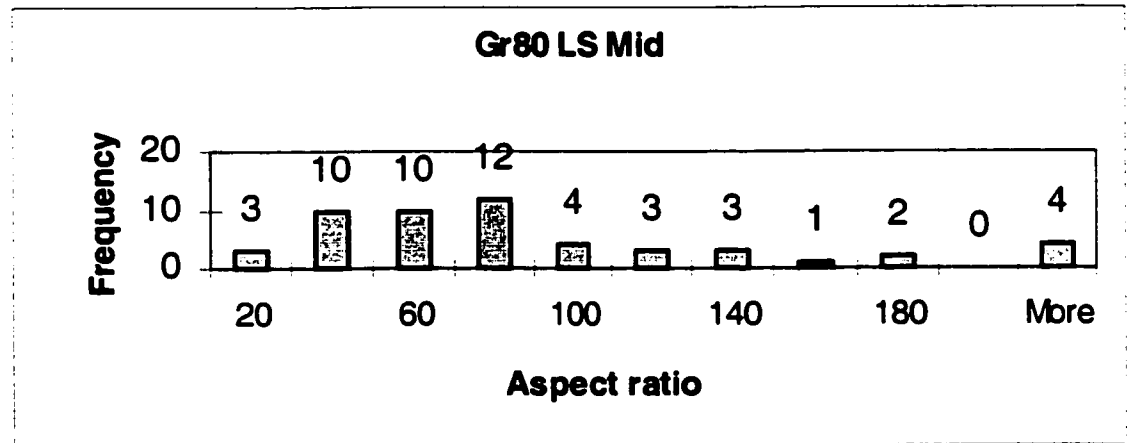
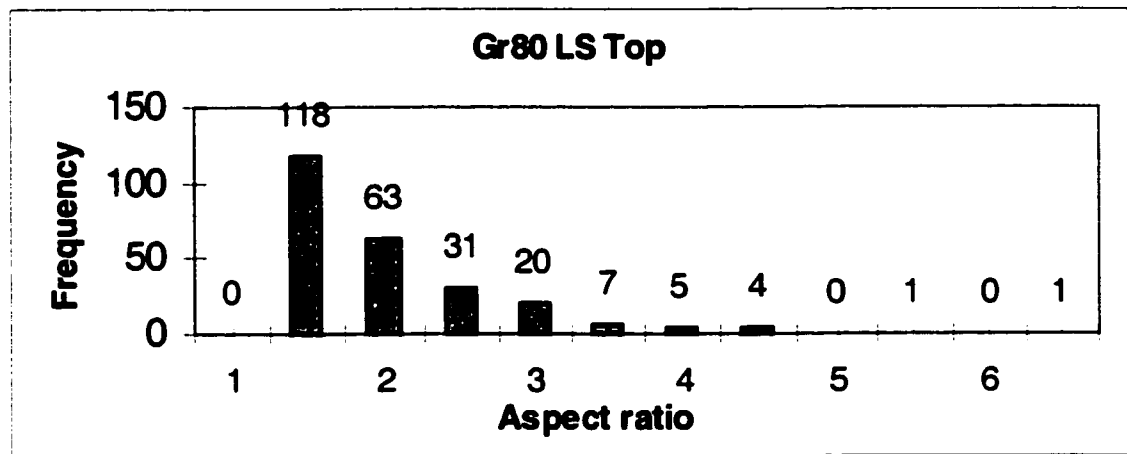


Figure 6-12 Aspect ratio of inclusions in Grade80 steel along the LS orientation.

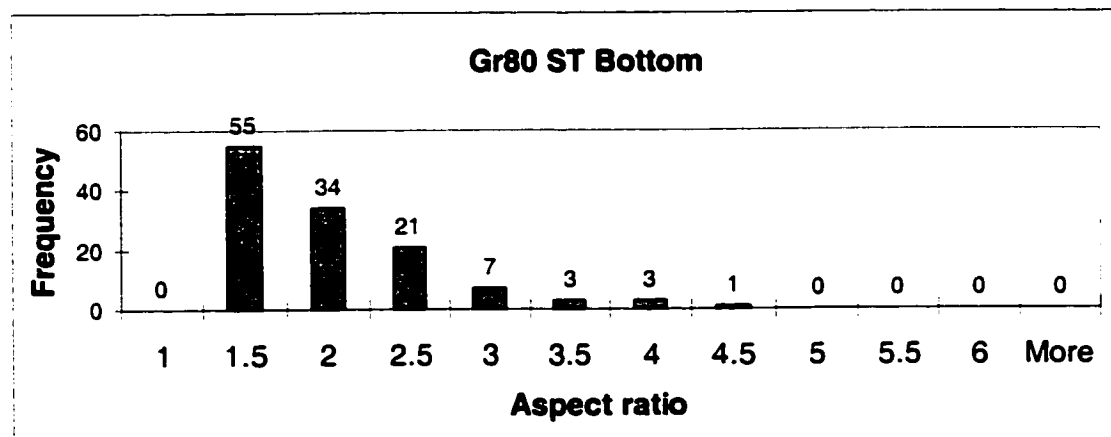
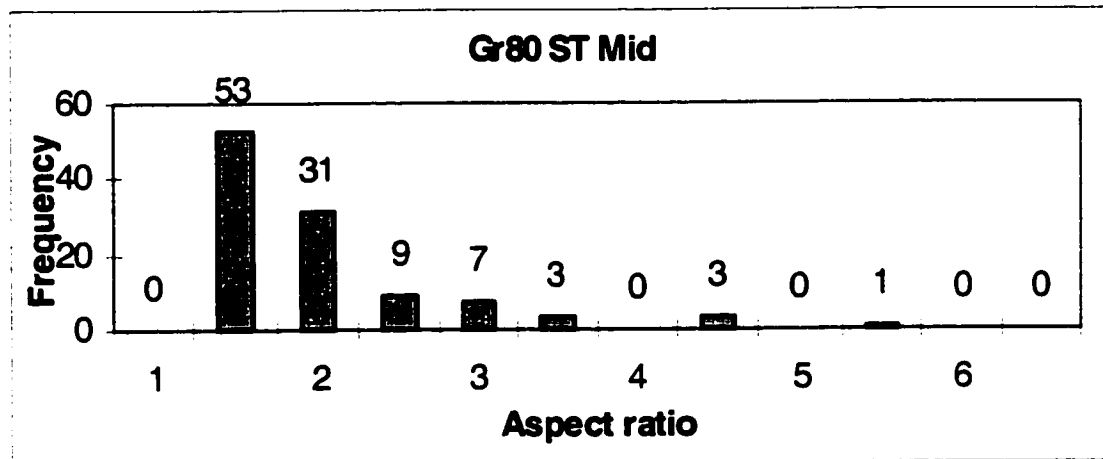
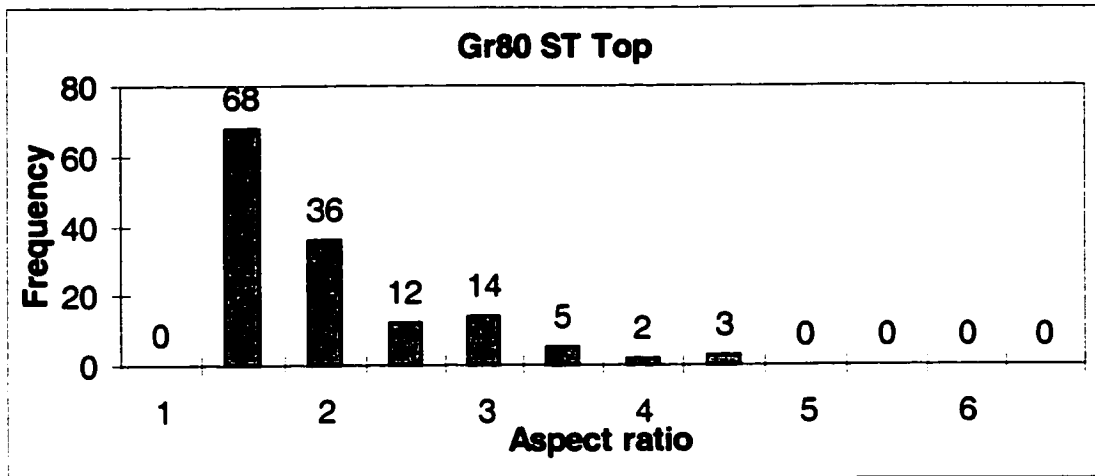


Figure 6-13 Aspect ratio of inclusions in Grade80 steel along the ST orientation.

## **6.4 Precipitates in Grade80 Steel**

As in the other grades of steel, the precipitates in Grade80 steel were classified into five main categories depending on their size, shape, composition and the various stages of processing during which they precipitate out from the solution.

### **6.4.1 Very Large TiN precipitates (2-10 $\mu$ m)**

Similar to earlier sections on X70 and X80 steel these precipitates were identified to be consisting mainly of Ti with small amounts of Nb replacing the Ti. These were shiny and copper-colored in appearance and were large enough to be easily observable in the optical microscope. Almost all of them were faceted with the majority of them cuboidal in shape. Due to instrumentation limitations and the large C peak overshadowing the N shoulder, most of the time it was difficult to ascertain the presence of N in the precipitates. However, thermodynamics of precipitation [Gladman92] predict these particles to be primarily TiN. This observation is also supported by results from Itman et al. [Itman97] and Zhou and Priestner [Zhou96] who identified similar precipitates in Nb-Ti microalloyed steels to be primarily TiN. Figure 6-4 shows the optical micrograph of a cluster of TiN particles.

The differentiating feature between these types of precipitates in the Grade80 when compared to X70 and X80 was that the majority of them did not possess a small particle at their core (Figure 6-4). This was because in Grade80 steel the main type of non metallic inclusions were elongated stringers of MnS. Many of the TiN precipitates were seen near the centerline associated with the large elongated inclusions. This might occur as explained in earlier chapter on X80 steel. The large precipitates and inclusions conglomerate in the melt. Later on rolling the soft MnS is elongated to a stringer and the hard TiN retains its shape, while still being attached to inclusion (Figure 6-8a).

A method of random intercepts and random sampling was followed to calculate the size and frequency distribution of these TiN precipitates at near the center of thickness and near the surface of the plate. For details refer to section 4-1. The results are presented in Table 6-3. It is clear that almost all of the TiN precipitates were found near the centerline. This may be due to segregation of these precipitates during solidification of the slab.

Table 6-3 Size and number distribution of TiN precipitates across the thickness of Grade80 plate.

	<b>Grade80</b>	
	<b>Center</b>	<b>Surface</b>
<b>Density (#/cm<sup>2</sup>)</b>	<b>7700</b>	<b>400</b>
<b>Average Size (μm)</b>	<b>2.4</b>	<b>0.7</b>
<b>Std. Dev (μm)</b>	<b>1.5</b>	<b>0.4</b>

#### 6.4.2 Large Cuboidal Precipitates (0.1-1.0μm)

As in the X70 steel, these precipitates were cuboidal in shape and Ti-rich suggesting them to be primarily TiN. However, some Nb replaced the Ti and therefore their lattice parameter did not exactly match that of TiN, TiC or NbN and NbC. It was somewhere between the limits. Figure 6-14a shows a TEM BF image of these precipitates from a carbon replica sample. The adjoining DP identifies the crystal structure to be NaCl-type (Figure 6-14b). The EDX spectrum from one of the precipitates (Figure 6-14c) shows it to be Ti-rich with some Nb and traces of Mo. Mo content was the highest (0.3wt%) amongst the three kinds of steels studied. The large Cu peak is from the grid supporting this sample. A small N shoulder is clearly discernible in this case.

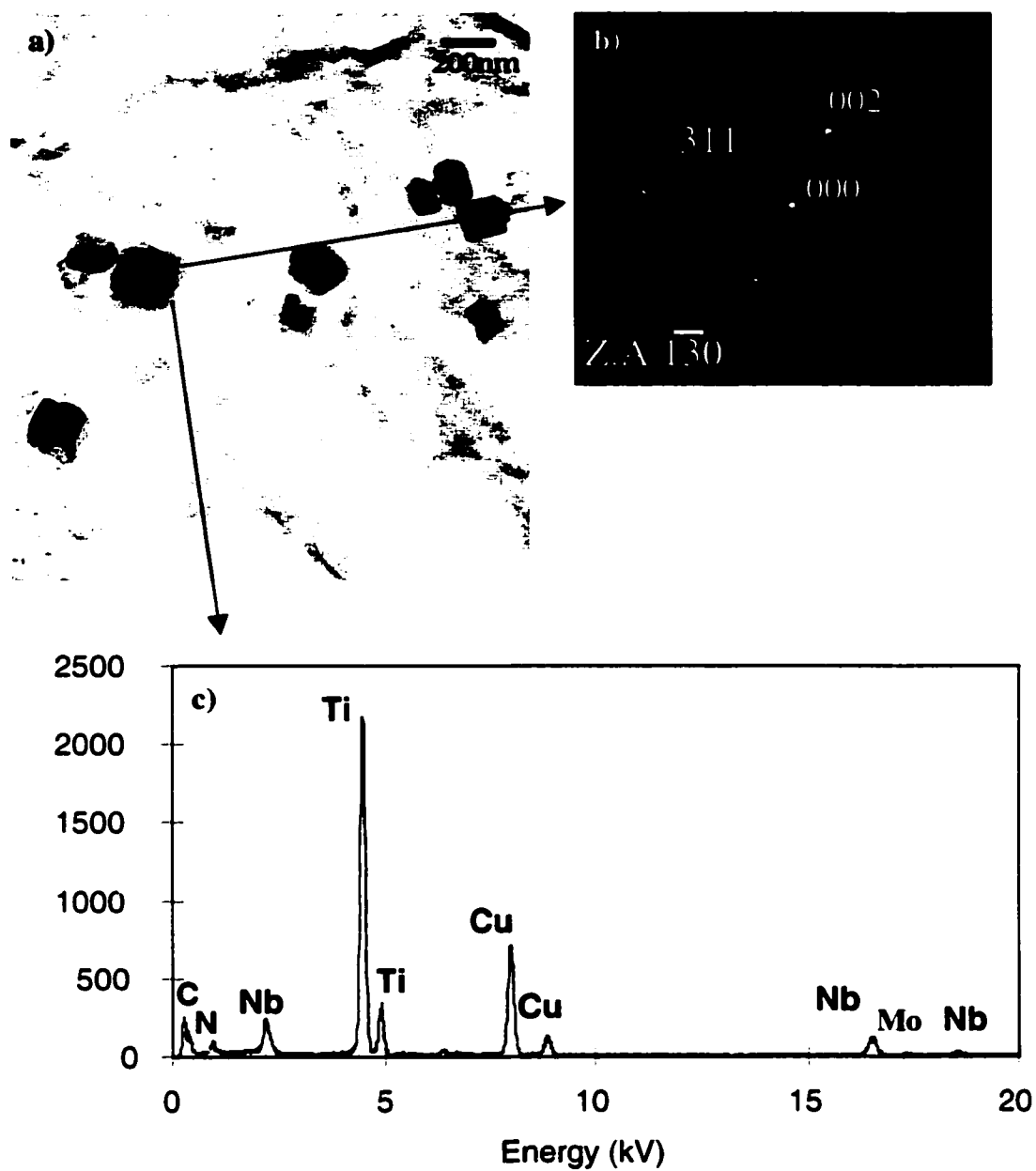


Figure 6-14 a) TEM BF image of cuboidal precipitates from a carbon replica. b) SAD pattern from one precipitate. c) EDX spectrum from the same precipitate in (b).

### 6.4.3 Medium Sized Irregular Shaped Precipitates (30–50nm)

This class of precipitates was rich in Nb but contained traces of Ti and Mo. Based on their composition and size and shape and looking at the thermodynamics of Nb precipitation in steel, it is most likely that the particles precipitate during the later stages of rolling by a 'strain induced precipitation' mechanism. This will be discussed more in the next chapter. Figure 6-15 shows 2 such irregular shaped precipitates in Grade80 steel as observed in a TEM carbon replica. The adjoining DP from precipitate 'a' identifies it to have a NaCl-type crystal structure. The EDX spectrum (Figure 6-15c) shows the precipitate to be Nb-rich with traces of Ti and Mo. The large Cu peak is from the supporting grid. The large C peak has contributions from the supporting C film in the replica in addition to the precipitate. The large C peak also masks the N shoulder.



Figure 6-15 a) TEM BF image of carbon replica from Grade80 LS showing medium sized, irregular shaped precipitates along with a cluster of smaller rounded precipitates marked by an arrow. b) Indexed SAD pattern from precipitate 'a'.

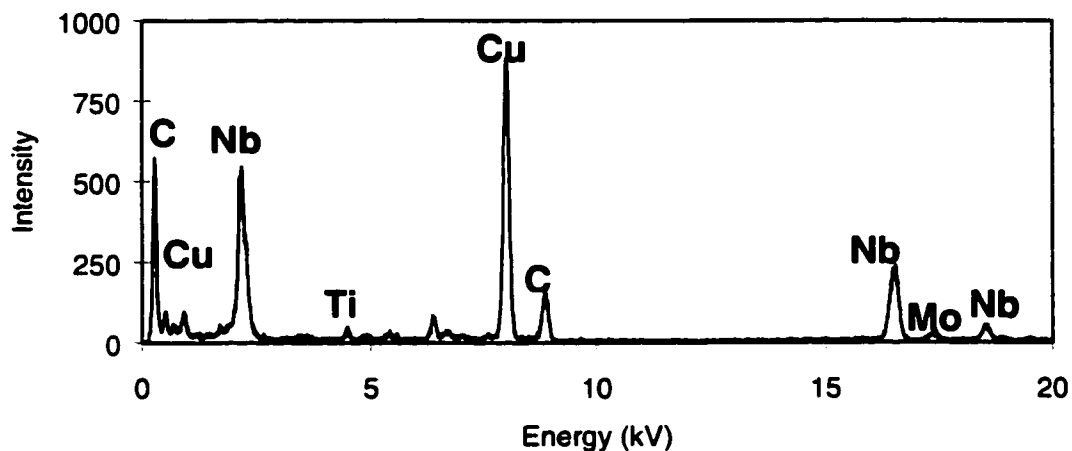


Figure 6-15 c) EDX spectrum from precipitate 'a' in (a).

#### 6.4.4 Small Spherical Precipitates (<20nm)

Very similar to X70 and X80 steel, the Grade80 steel possessed small rounded precipitates spread throughout the interior of the ferrite grains (Figure 6-16a). The precipitates often appeared as rows or sheets, which are proposed to form during the ledge growth of ferrite [Batte73]. At this time most of the Ti has precipitated from the solution and NbC or Nb carbonitride is the compound which is thermodynamically most favored for precipitation at lower temperatures. The precipitates consisted mainly of Nb with an extremely small amount of Ti and Mo (Figure 6-16c). The O peak in the spectrum is from the oxidation products formed on the supporting Cu grid. The presence of N was difficult to discern as the N peak in the EDX spectra was masked by the large C peak arising from the C support film. Molybdenum was also present. Molybdenum can partially substitute for Nb in the precipitates forming (Nb,Mo)(C,N); however, Mo levels are likely not high enough to significantly affect the amount of precipitation hardening [Kanazawa67-1][Kanazawa67-2]. It was difficult to obtain diffraction patterns from a single precipitate owing to their small size. However, a ring pattern from a cluster of these precipitates is shown and indexed in Figure 6-16b.

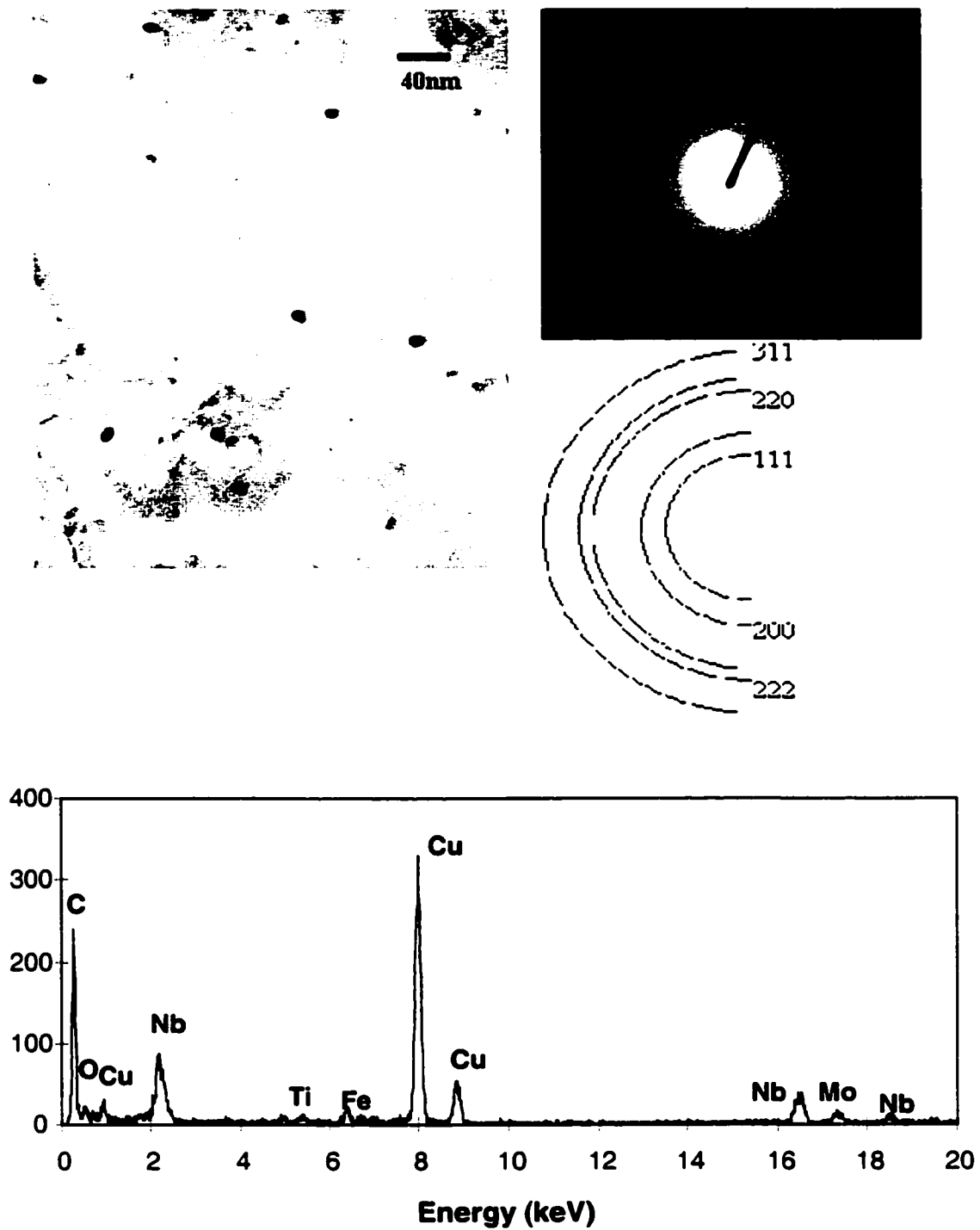


Figure 6-16 a) TEM BF image of small, rounded precipitates in Grade80 steel. b) Ring pattern from cluster of small precipitates indexed to be NbC. c) EDX spectrum from one of the small precipitate shows it to be Nb rich with traces of Mo, Ti and O. The O peak is from the oxidation products formed on Cu support grid.

#### 6.4.5 Very Small Precipitates (<5nm)

As with X70 and X80 steels, in addition to the four major types of precipitates already discussed, some very small (<5nm) precipitates were detected in Grade80. The precipitates form during the later stages of processing when the strip is being coiled at temperatures <600°C. At this temperature virtually all the Ti has been depleted and the Nb precipitates out with C and N by nucleating on the dislocations and at the grain boundaries, as seen in Fig. 6-17. These finely dispersed precipitates contribute to precipitation strengthening in these steels.

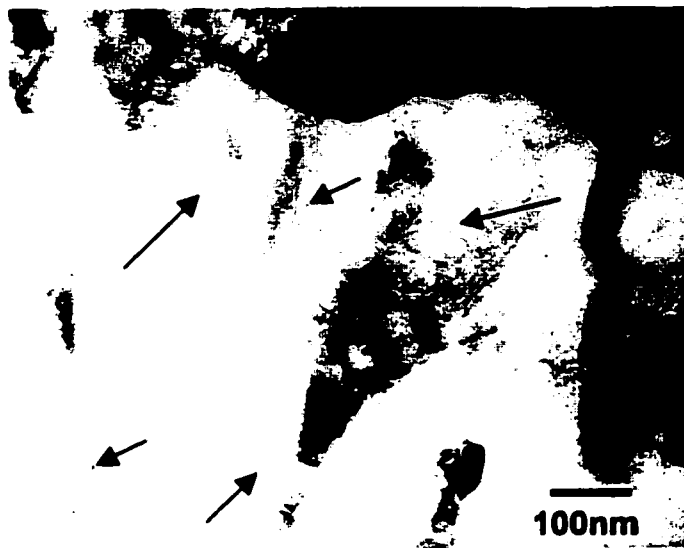


Figure 6-17 TEM BF image of a ferrite grain showing extremely small precipitates spread throughout the grain, as seen by arrows pointing to extremely small spots.

## **Chapter 7: Discussion**

### **7.1 Introduction**

In the previous chapters the three different grades of steel were characterized individually. The aim was to identify and quantify the various microstructural features. The basic microstructure was similar in all the steels, i.e., an acicular ferrite/bainitic ferrite grain structure with high dislocation densities and low angle grain boundaries, 5 kinds of precipitates, non-metallic inclusions, retained austenite and pearlite-like microconstituents. The focus of this chapter shall be to explain the evolution of a particular microstructure and the origin of differences in the microstructure based on the differences in processing history. Although the basic microstructures were similar, differences existed in terms of relative abundance or lack of certain phases, size and shape distribution of the various constituents and morphology and composition of precipitates and inclusions. These differences are the basis for differing mechanical properties observed in the final product and their origins can be traced to the particular processing schedules (coupled with the chemistry). Effort shall be made, to make an across the board comparison for the three grades of steels analyzed in this study. It is expected that by obtaining this information and quantifying the differences in microstructure in terms of various features and constituents, it will be possible to make a reasonable and rational argument for the differing mechanical properties.

### **7.2 Thermomechanical Processing**

Table 7-1 shows in concise terms, the processing conditions for individual grades. This shall be the basis for subsequent discussions. The reheating practice was the same for all grades of steel. The slabs were heated to about 1200°C-1300°C for about 3 hrs to achieve temperature uniformity and to solutionize the majority of the alloying additions. The initial thickness of the slabs was the same (about 20cm) for all grades. After reheating, the slabs were rough rolled to reduce the thickness to

about 20-40mm. This intermediate plate is called t-bar. During the roughing phase, the aim was to roll the steel above the  $T_{nr}$  (no-recrystallization temperature) of austenite, so that the austenite grains are refined by frequent reduction and recrystallization. During the finishing stages of rolling at 700°C-900°C, austenite recrystallization is retarded with two main mechanisms operating. At higher finishing temperatures, dissolved microalloying elements hinder recrystallization by a solute drag mechanism. At lower temperatures, strain induced precipitation of Nb/Ti carbonitrides at sub-grain boundaries has the effect of pinning austenite grain boundaries. Nb is particularly effective at retarding recrystallization.

[DeArdo96][DeArdo97][Itman97][Zhou96]. A fine initial austenite grain size is an important prerequisite for a final, fine ferrite grain structure [Sage83]. The t-bar gauge thickness is determined by the requirements of rolling further down the mill, i.e., reduction in Steckel mill, final gauge of coiled strip and amount of deformation required. The proper mix of toughness and strength is a function of grain size and chemistry (affecting the transformation temperatures and amount of precipitation). A large amount of deformation leads to more nucleation sites and finer grains, while faster cooling leads to more acicular ferrite and bainite. Higher contents of microalloying elements Nb & Ti, ensure sufficient retention of these in solid solution to precipitate out later during finish rolling and coiling and contribute to the strength of the steel.

Table 7-1 Processing parameters for the three grades of steel.

	<b>X70</b>	<b>X80</b>	<b>Grade80</b>
<b>Reheat temperature*</b>	1200-1300	1200-1300	1200-1300
<b>Reheat time (hrs)</b>	>2	>2	>2
<b>Initial slab thickness (cm)</b>	20.3	20.3	20.3
<b>t-bar temperature</b>	700-1000	700-1000	700-1000
<b>t-bar gauge (mm)</b>	20-40	20-40	20-40
<b>Finishing temp (avg)**</b>		-170	-40
<b>No. of passes</b>	5	5	5
<b>Coiling temp (avg)**</b>		40	20
<b>Min gauge (mm)</b>	14.6	15.6	12.8

\* all temperatures in °C

\*\* finishing and coiling temperatures are relative to those for X70 steel

### 7.3 Grain Structure

The grain structures in all the three steels were similar. The grains were highly deformed and irregular in shape. This is what is typically referred to as the acicular grain structure in linepipe terminology [Collins83]. The grains were neither equiaxed nor of uniform size. On the other hand they were highly deformed and mixed in nature. The matrix primarily consisted of acicular/bainitic ferrite with small amounts of polygonal ferrite. On etching with nital, some of the ferrite grains appeared to be raised from the surface with respect to other grains (e.g., Figure 6-2). Pereloma and Boyd [Pereloma 96] claim these grains to be a distinct form of ferrite characterized by higher hardness and dislocation density. They are also supposed to preferentially oriented with their [001] normal to the plane of polish. Islands of retained austenite were observed with modified LaPera's etch and some 'pearlite-like' microstructural constituent was revealed by etching with picral for long times.

It has been stated that the matrix was composed of acicular ferrite/bainitic ferrite. There is considerable confusion and ambiguity in the research community about the nomenclature and classification of this kind of phase (or morphology). These terms (acicular ferrite and bainite) come from welding metallurgy and high carbon steels respectively. In low carbon steels, like ours, the classical basket weave pattern (acicular ferrite) [Honeycombe96] or inter- or intra-lath carbides (upper and lower bainite) were not observed. Generally, in microalloyed steels the two terms are used interchangeably. For our case all the grains turned out to be bcc ferrite (no martensite with  $c/a > 1$  could be observed in the TEM). Many of the ferrite grains had high aspect ratios and possessed high dislocation densities. There was no preferential precipitation of iron-carbide in the inter- or intra-lath regions. This might be due to the very low carbon contents and strong carbide/nitride forming elements like Nb and Ti. However, due to their particular elongated, lath-like morphology with high dislocation densities, the grains are frequently termed acicular ferrite or bainitic ferrite.

Many researchers have tried to differentiate between the two designations by making the distinction based on aspect ratios and the thickness of the laths [Araki91][Collins83]. According to Collins bainitic ferrite can be differentiated from acicular ferrite by the criterion that in bainitic ferrite the laths are more elongated (higher aspect ratios) and are typically 0.5-0.7 $\mu$ m in width. Many of these parallel laths occur together in a bunch for bainitic ferrite.

As an illustration, two micrographs are reproduced below (Figure 7-1). The first is from the X70 steel showing an irregular shaped ferrite grain, highly dislocated and surrounded by other irregular shaped ferrite grains (Figure 7-1a). This could be classified as an acicular ferrite structure. The second micrograph shows an area of lath shaped grains, high in dislocation density and with high aspect ratios. Many of these parallel laths occur together in a packet for bainitic ferrite, with low angle boundaries between the laths (Figure 7-1b).

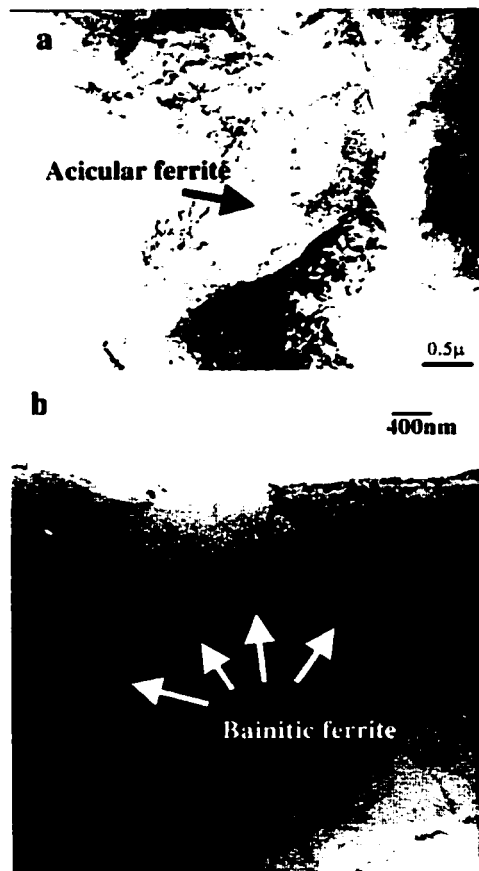


Figure 7-1 TEM BF micrographs from thin foils of X70 and Grade 80 showing differences between a) acicular ferrite and b) bainitic ferrite.

While X70 steel has a considerable fraction of polygonal ferrite along with primarily acicular ferrite (Figure 4-1), the structure in X80 is more acicular/bainitic (Figure 5-1 ), Grade80 is also highly bainitic (Figure 6-1). This is to be expected as when the strength requirements increase, it is a well established practice to move from a ferritic/pearlitic structure to a bainitic/martensitic one. A richer chemistry (more Ti, Nb and Mo), especially with higher Nb contents shifts the CCT curves to longer times and lower temperatures, leading to more bainitic ferrite content. The yield strengths increase from 545MPa(X70) to 568MPa(X80) to 587MPa (Grade80). The harder microstructure (and other effects to be discussed later) results in a toughness decrement from 375J (for X70) to 75J (for Grade80) as shown in Table 3-2.

Table 7-2 shows the amount of deformation, the final thickness and an approximation of the cooling rate for each grade of steel. As an approximation of the cooling rate it is assumed that the cooling rate is only dependant on the temperature difference at the entry and exit, the speed of the plate and inversely dependant on the thickness of the plate.

$$\frac{dT}{dt} \propto \frac{\Delta T v}{t}$$

Where

$$\frac{dT}{dt} = \text{cooling rate ( } ^\circ\text{C/s)}$$

$\Delta T$  = change in temperature;

$t$  = thickness of plate and

$v$  = velocity of plate on cooling table

Table 7-2 Comparison of deformation and cooling rates for different grades of steel.

	<b>X70</b>	<b>X80</b>	<b>Grade80</b>
<b>Deformation (mm)</b>	13.12	19.05	20.17
<b>Final thickness (mm)</b>	14.6	15.6	12.8
<b>Cooling rate (approx)*</b> <i>v = velocity of plate on cooling table</i>	235v/14.6	170v/15.6	203v/12.8
<b>Grain Structure</b>	polygonal ferrite + acicular ferrite	polygonal ferrite + acicular ferrite + bainitic ferrite	polygonal ferrite + acicular ferrite + more bainitic ferrite

\*  $v$  is approximately 25% higher for X80 compared with X70

A larger deformation coupled with a faster cooling rate, is expected to produce a larger fraction of shear assisted products, i.e., bainite and/or martensite. This is illustrated best by Grade80 steel, which has the thinnest final gauge and highest reduction in thickness along with a moderately fast cooling rate. The chemistry of the steel also plays a role in the transformation. This can be better explained through the CCT diagrams. Figures 7-2a and b show CCT curves for X70 and X80 steels respectively. The CCT diagram for X80 is shifted to the right and longer times (nose for ferrite start is  $\sim 10$ s) compared with X70 (nose for ferrite start is  $\sim 2$ s). This is due to the higher content of Nb and Mo in X80. Thus, even though the cooling rate for X80 ( $\approx 170^\circ\text{v}$  and 15.6mm) is less than that for X70 ( $\approx 235^\circ\text{v}$  and 14.6mm), it has a better chance of forming a bainitic ferrite microstructure. X80 also undergoes more deformation than X70 due to a thicker t-bar gauge, leading to more nucleation sites for ferrite and subsequent finer grain size. Thus, the observations are consistent with the processing of the steels.

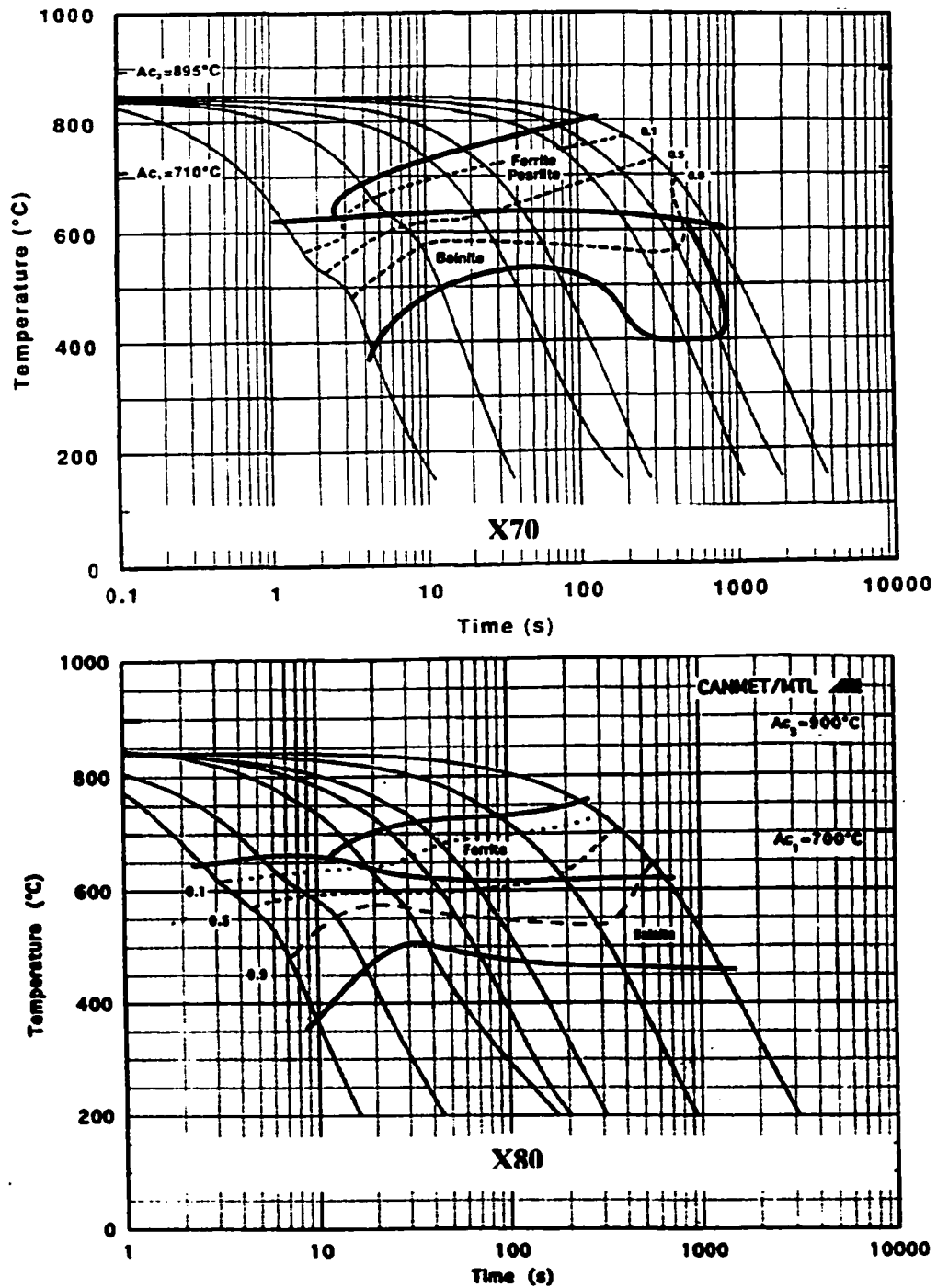


Figure 7-2 CCT diagrams for a) X70 and b) X80 steels [CANMET98].

When looking at the plates across the thickness, in the LS orientation, some general trends were observed for the three kinds of steels. The grains were larger and more elongated at the centerline, whereas the grains closer to the surface were refined and more equiaxed (Figures 4-2, 5-2 and 6-2). This is possibly because more nucleation sites are generated near the surface due to higher deformation and faster cooling rates at the surface compared with the interior of the plate. Due to particular nature of the rolling of these steels, the resultant ferrite grain structure depends on the prior austenite grain distribution. The austenite grain distribution just before transformation is reflected in the final ferrite morphology. Near the surface of the plate there is more chance for austenite recrystallization which leads to finer and more equiaxed grain distribution there, as compared to the middle of the plate. This is subsequently reflected in the ferrite grain distribution. In the interior although the cooling rates are high and deformation large, there is less chance of recrystallization of austenite and the grains remain as pancaked, elongated grains which transform to acicular and bainitic ferrite with high aspect ratios. However, it should be noted that some deformation may also occur during the  $\gamma \rightarrow \alpha$  transformation, where there is a mixture of both austenite and ferrite. Therefore the ferrite itself may undergo deformation and may, in certain favorable conditions, recrystallize. The final microstructure is a combination of both these effects.

Table 7-3 shows the grain size and shape for the interior (closer to centerline) and near the surface of the plate. It is apparent that the grains are larger near the center and fine, closer to the surfaces. A large standard deviation in the average grain size denotes a mixed structure, i.e., a cluster of large and small grains. A smaller standard deviation signifies that the grains were confined within a narrow size range. Near the surface, the grains consistently showed smaller deviations. For Grade80 steel the standard deviation in average grain size at the center was abnormally high ( $7.7\mu\text{m}$ ). This arose because in the center there were some very large, lath shaped grains, in conjunction with smaller acicular grains. This gave rise

to a high average grain size with large standard deviation. However, as discussed previously in Section 6-1, many of these apparently large grains consist of subgrains separated only by a small orientation mismatch. The chemical etchants such as nital, etch the entire region as one grain. Therefore these results have to be interpreted cautiously.

Table 7-3 Distribution of grain size and grain shape across the thickness of the plate.

	<b>X70</b>		<b>X80</b>		<b>Grade80</b>	
	<b>Center</b>	<b>Surface</b>	<b>Center</b>	<b>Surface</b>	<b>Center</b>	<b>Surface</b>
<b>Grain size (<math>\mu\text{m}</math>)</b>	9.0	6.6	6.1	5.1	10.9	5.8
<b>Std. Dev (<math>\mu\text{m}</math>)</b>	4.2	2.1	1.9	1.4	7.7	1.3
<b>Aspect Ratio</b>	2.2	1.8	1.9	1.9	2.4	1.2

Comparing the grain sizes across the different grades of steel we see that while X70 has a larger grains than X80, the grains are of mixed sizes as indicated by larger standard deviation. The grains in X80 are smaller on an average. This can be explained through the CCT diagram for X80 which is shifted to the right (when compared to X70). As a result the nucleation times are longer for a given cooling rate and a shorter time is available for grain growth. The resultant microstructure is different with higher contents of bainitic ferrite than polygonal ferrite. For Grade80 steel the grain size near the surface is comparable to the other two grades. However, at the center the grains are very large and this might be due to the limitations of the etch as explained above in the previous paragraph.

The average aspect ratio of the grains was calculated to get an estimation of the amount of acicular/bainitic ferrite content of the steel. The assumption was that the grains are elongated along the rolling direction. Measuring the average grain size along the direction of rolling and along the thickness of the plate and taking the ratio would give an apparent average aspect ratio. The grains had higher aspect ratios in the center (Table 7-3), denoting elongated grains in center and more equiaxed grains at the surfaces. Across the different grades, Grade80 had

the maximum difference with large elongated grains at the centerline (aspect ratio ~2.5) and fairly equiaxed grains at the surface (aspect ratio ~1.2). However, the large grains in center of X80 might consist of smaller subgrains as explained in Section 6.1

#### **7.4 Segregation Effects**

Segregation effects were visible in all the different grades of steels to some extent. The effects were most pronounced for Grade80 and were least pronounced for X80. X70 showed some centerline segregation. In the case of Grade80 there was severe centerline segregation in terms of solute (as indicated by RA), inclusions and large TiN precipitates. Large stringers of MnS elongated along the rolling direction were observed near the centerline. The large, copper colored TiN precipitates were frequently associated with these stringers as they acted as heterogeneous nucleation sites (Section 6-1). For the X70 and X80 steels, the inclusions were rounded and more or less equally distributed throughout the thickness. However, the TiN precipitates were preponderant at the centerline for both X70 and X80. This will be discussed in more detail in the next section on precipitates.

Modified LaPera's etch revealed islands of retained austenite/martensite (MAC) throughout the thickness of the plate. These were concentrated more at the centerline and larger in size. The islands were smaller and finely distributed near the surfaces, away from the interior of the plate (Figures 4-6, 5-4). Etching the steels with picral for long times revealed some 'pearlite-like' microstructures as shown in Figure 4-7, 5-5 and 6-5. Again these were larger at the centerline and finer and near the surface. Similar distributions of MAC and 'pearlite-like' constituent were observed for both X70 and X80.

MAC arises due to the limited solubility of C in ferrite (0.02at% at the eutectoid temperature) and other solutes (e.g., Mn etc). When the austenite to ferrite transformation is taking place, ferrite rejects excess carbon and solutes through

diffusion to the adjacent austenite grains. These small areas, which show up mainly at the grain boundary triple points, are richer in carbon and solutes and make up the MAC. The higher carbon austenite can transform to martensite on cooling or remain as retained austenite [Thompson96]. According to Collins [Collins83] 'the M/A region are the last to transform during cooling. At this point, the remaining austenite has been substantially enriched in carbon and partitioned into small rectangular blocks by ferrite formation at higher temperatures'. By similar reasoning the presence of more numerous and larger areas of MAC near the centerline can be explained. Since there is more solute segregation near the centerline and the cooling rates are lower, more time is available for solute/carbon diffusion out of the transforming grains, leading to more MAC areas. Their fewer numbers at the center and higher numbers at the surfaces are a direct reflection of the ferrite grain distribution, with greater number of transformation sites available in a finer grain structure.

It was not possible to do a precise statistical analysis, with a large data set as the image analysis software was not able to delineate these MAC islands from the rest of the matrix satisfactorily. Consequently, a manual count was performed to get an overall estimate of the relative amount of these phases in the three grades of steel. The numbers of these islands per unit area were counted. No size measurements were performed, as because of their small size the error associated would be unacceptably large. However, as has been pointed out earlier these MAC islands were smaller and finely spread out near the surfaces of the plate as compared to the centerline where they were larger. Table 7-4 presents the results.

Table 7.4 Distribution of MAC islands in the three grades of steels.

<b>No. of MAC islands/100<math>\mu\text{m}^2</math></b>		
	<b>Centerline</b>	<b>Surface</b>
<b>X70</b>	86	127
<b>X80</b>	136	238
<b>Grade80</b>	118	240

From Table 7-4 it is apparent that Grade80 has the maximum number of these MAC islands while for X70 it is the least. This is to be expected as the Grade80 has the richest chemistry of three and would lead to maximum amount of solute segregation. The anomalously low number of MAC at the center of Grade80 steel might be due to the larger grain size there as shown in Table7-3.

The distribution of the 'pearlite like' microstructure also appears to be some kind of transformation product due to solute segregation. Complete identification of this microstructure was not possible. In appearance, the morphology resembled degenerate pearlite. However, even on obtaining an EDX spectrum from a SEM equipped with a field emission gun (FEG) (i.e., a very small spot size; ~1nm), no appreciable carbon enhancement was detectable. In terms of carbon and other constituents such as Mn, Nb and Ti, the chemical composition was similar to the matrix. Hence, the name 'pearlite-like' structure. Some researchers classify this phase as bainite or martensite [Kot-Bramfitt81]. However, there was no conclusive supporting evidence either way. This may be a limitation of specimen preparation. More studies need to be performed to identify this phase. As with the MAC, it was not possible to do a precise statistical analysis with a large data set as the image analysis software was not able to delineate these 'pearlite-like' microstructure from the rest of the matrix satisfactorily. Consequently, a manual count was performed to get an overall estimate of the relative amount of this constituent in the three grades of steel. The numbers of these phase per unit area were counted. No size measurements were performed, as because of their small size and the lamellae like morphology the error associated would be unacceptably large. Table 7-5 presents the results.

Table 7.5 Distribution of 'pearlite-like' microstructure in the three grades of steels.

<b>No. of 'pearlite-like' islands/100<math>\mu</math>m<sup>2</sup></b>		
	<b>Centerline</b>	<b>Surface</b>
<b>X70</b>	34	56
<b>X80</b>	51	84
<b>Grade80</b>	93	136

## 7.5 Inclusions

The inclusions for the line pipe grades were mostly rounded and consisted primarily of Ca and S (Ca, Mn and S in the case of X80). These are most probably mixed oxides and sulfides of Ca, Mn, Al, Ti, Mg and Si (see Section 4.3 for details). No stringers were observed in these two grades. This indicates the efficacy of S control and Ca/Si treatment. It is necessary to control the S level to low values ( $<0.004\text{wt}\%$ ) to avoid formation of MnS inclusions, which are soft and get flattened into stringers on rolling. The elongated inclusions play a detrimental role in the properties by their assistance in hydrogen induced cracking (HIC). Ca is added to make the MnS harder and spherical. Ca replaces Mn in MnS and assists its removal through the slag. This process, called spheroidization, imparts sufficient hardness to the non-metallic inclusions to retain their round shape. The inclusions in X70 and X80 were both rounded but subtle differences existed. While inclusions in X70 were primarily composed of Ca and S (with small amounts of Mn), the ones in X80 showed Mn levels comparable to Ca. The Mn level in X80 is marginally higher ( $1.82\text{wt}\%$  vs.  $1.76\text{wt}\%$  for X70) but not sufficiently higher to justify it as the basis of these observations. The difference may be a sampling phenomenon as we are observing a small section of an approximately 20m plate and properties may vary along the length due to casting effects, superheat and compositional variations along the length.

The inclusions in X80 steel were finer and more numerous (Table 7-6) compared with X70. The finer size might be a sampling phenomenon. The higher density of inclusions (though of smaller size) can be attributed to marginally higher level of S and Mn in X80 (Table 3-1). The inclusions were also more spherical in X80. The aspect ratio for X80 inclusions was close to 1.5 whereas for X70 it was closer to 2. The inclusions were elongated in the rolling direction and along the width of the plate due to a decrease in thickness. However they still maintained an oval shape. The larger aspect ratio in X70 is linked to the larger inclusions, which under similar deformation forces produced a larger percentage change.

Table 7-6 Characteristics of inclusions in the various grades of steel.

	<b>X70</b>	<b>X80</b>	<b>Grade80</b>
<b>Characteristic</b>	rounded, no stringers	rounded, no stringers	stringers
<b>Composition</b>	primarily Ca-S	primarily Ca-Mn-S	MnS + CaMnS
<b>Size</b>	< 3micron <sup>2</sup> 70% near 2micron <sup>2</sup>	< 2micron <sup>2</sup> 75% near 1micron <sup>2</sup>	up to 50micron <sup>2</sup> at center equally spaced from 10-50
<b>Aspect Ratio (area intercept)</b>	1.5 to 2.5 peaks at 2	1.5 to 2.5 large peak at 1.5	as high as 50-100 at center closer to 1.5-2 at surfaces
<b>Frequency #/cm<sup>2</sup></b>	1.5x10 <sup>5</sup>	1.9x10 <sup>5</sup>	0.4x10 <sup>5</sup> at centerline 2.2x10 <sup>5</sup> at surface
<b>S (wt%)</b>	0.001	0.004	0.010
<b>Ca (wt%)</b>	0.004	0.003	0.002
<b>Mn (wt%)</b>	1.745	1.820	1.640

Compared to the line pipe grades, the Grade80 steel had numerous elongated inclusions, which were concentrated more at the centerline but were present throughout the thickness. The stringers were mainly MnS with small amounts of Ca in addition to Al, Ti, Mg and Fe. Spheroidal CaMnS inclusions were also observed away from the centerline. It is evident from Table 7-6 that Grade80 steel had a relatively large content of S, while the Ca level was low, below that in X70 and X80. Thus, only some of the inclusions in Grade80 were spherodized. The remaining MnS inclusions segregated to the centerline and were flattened into stringers during rolling. They were as long as 50µm at the centerline. The presence of these large inclusions is one of the reasons for reduced toughness of Grade80 plate.

## **7.6 Precipitates**

### **7.6.1 Very Large TiN Precipitates (2-10 $\mu$ m)**

This group of precipitates was large enough to be seen at relatively low magnifications in the optical microscope. Key identifying characteristics included their copper color and cuboidal faceted shape. Most had a particle at their core. EDX analysis of the precipitates showed traces of Nb with large amounts of Ti. The C and N levels could not be detected accurately in the SEM. Although Nb was invariably present in small amounts in all the precipitates, these have been classified as primarily TiN (and not TiC or TiNb(C,N)). This is because TiN is a phase which precipitates out early in the steel processing sequence, at temperatures  $>1200^{\circ}\text{C}$ . Thermodynamically, TiN has the maximum driving force for precipitation at elevated temperatures, amongst TiN, TiC, NbN and NbC. As illustrated by Gladman [Gladman97] (Figure 7-3), almost all the Ti precipitates out of the solid solution on cooling around  $1000\text{-}1100^{\circ}\text{C}$  as primarily TiN. TiN remains undissolved during subsequent reheating in the range  $1200\text{-}1250^{\circ}\text{C}$ . Nb is stable in the solution until lower temperatures and its precipitation becomes significant below  $1000^{\circ}\text{C}$ . As shall be explained in detail in the next paragraph, the largest precipitates are believed to have come out early in the processing sequence, even at the time of casting or solidification of the slab. Hence they are called nitrides of titanium. Other researchers have reported similar observations for these precipitates [Itman97][Zhou96].

As pointed out earlier, many of these precipitates had non-metallic inclusions at their core, which acted as nucleation sites for TiN precipitates in X70 and X80. This was also observed by Saikaly et. al. [Saikaly99] in a Ti microalloyed steel. Other inclusions attached themselves onto the outer surfaces of the TiN cored precipitates. This suggests that these TiN cuboids are formed in the melt, for other particles cannot attach to the exterior in a solid matrix. In the melt, when the steel is

being cast or in the interdendritic regions during solidification of the cast slab, the non-metallic inclusions conglomerate on the large precipitates.

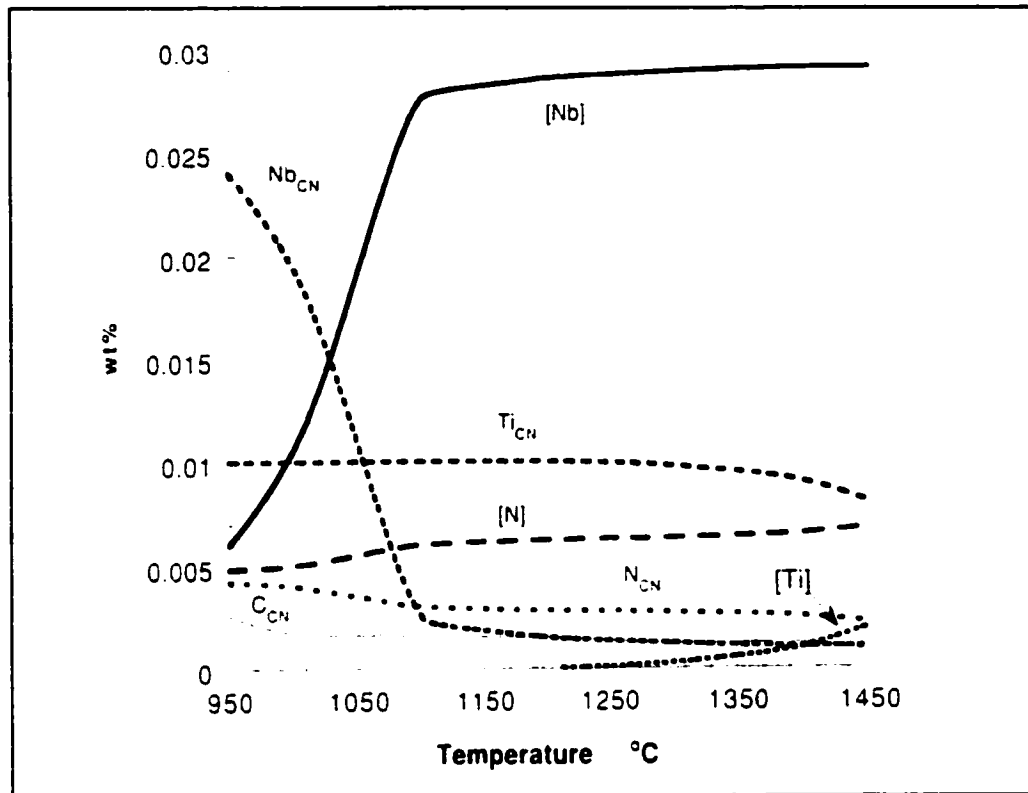


Figure 7-3 Relationship of precipitation of Ti and Nb carbides, nitrides with temperature for a microalloyed steel [Gladman97].

The density of and size distribution of the large TiN precipitates was calculated using a method of random sampling and random intercepts. The results for all three grades are reproduced in Table 7-7.

Table 7-7 Distribution of large (2-10 $\mu$ m) TiN precipitates.

	X70		X80		Grade80	
	Center	Surface	Center	Surface	Center	Surface
Density (#/cm <sup>2</sup> )	3400	1600	2500	900	7700	400
Size ( $\mu$ m)	3.9	3.1	2.6	2.1	2.4	0.7
Std. Dev. ( $\mu$ m)	1.8	0.7	0.9	1.0	1.5	0.4

More of the clusters (TiN + inclusions) were seen in X80. In Grade80 many TiN precipitates did not have any inclusions cores. That may be due to the lower number of small spherical inclusions in Grade80. Looking at Table 7-7 we see that the number of TiN precipitates is lower in X70 and X80, while for Grade80 it is much higher. The number of precipitates is slightly higher in X70. This is unexpected as the Ti and N levels in the X70 and X80 steels are almost similar with these being marginally higher the X80 steel. The difference in size may be attributed to the time of Ti addition. Titanium is added during secondary steelmaking and according to the current practices at IPSCO, i.e., time of addition of Ti, are variable in this regard. So if added earlier, more time is provided for TiN growth. Hence, sizes may vary from heat to heat within the same grade and is somewhat dependant on sampling. The Grade80 steel had similar Ti levels (0.028wt%) compared with X70 and X80 (0.023-0.024wt%). There are more particles near the centerline and they are larger when compared with the surface region. Over all the number of these precipitates were found to be higher in Grade 80. The differences in distribution of large TiN particles seem to be a sampling phenomenon and may vary across the length of the plate and from also heat to heat. More measurements need to performed for better assessment.

#### **7.6.2 Large TiN Precipitates (0.1-1.0 $\mu$ m)**

These particles, like the ones described above, were primarily cuboidal in shape and were identified as TiN, with smaller amounts of Nb. The main difference, other than the size was the absence of CaS inclusions at the core. The crystal structure corresponded to the NaCl type and was isostructural with NbC, NbN and TiC. Niobium can substitute for Ti and likely does so after initial precipitation, either during cooling after casting or during reheating [Houghton93]. Their smaller size and lack of a nucleation core indicates that these particles precipitate out later during processing, most likely when the steel is being cooled down through the austenite range and remain insoluble during subsequent reheating. The difference in precipitation sequence differentiates them from the large TiN precipitates which

come out during casting, nucleating on CaS inclusions. Itman et al. [Itman97] have identified very similar precipitates in a 0.055C-0.02Nb-0.06Ti microalloyed steel.

The particle densities were counted for X70 and X80 steel using carbon extraction replicas. The extraction method does not pull out all the precipitates, so by this method only a lower population limit is obtained [Hirsch82]. The results are presented in Table 7-8. To calculate the volume of the steel from which precipitates are extracted, assumption was made as to the thickness of the replica to be same as the size of Nb-rich precipitates pulled out of the matrix. If the sampling thickness was larger than this, then many of the smaller precipitates would have fallen off. Although, some larger (up to 0.5 $\mu$ m) precipitates have also been extracted, these are most probably the ones that were exposed upon etching and were resting on the surface with only a small part embedded in the matrix. Their volume fraction has therefore not been counted. Both X70 and X80 have similar numbers of these precipitates (Table 7-8). However, on the whole, the cuboidal TiN precipitates were larger in the X70 (closer to 500nm) when compared with X80 (100-200nm). The particles precipitate out when the steel was solidifying after casting and remain undissolved during reheating. If the Ti were added earlier in the X70 steel, for this particular heat the large TiN would have had the chance to grow larger than compared to X80. Also, the t-bar temperature for X80 after roughing and before being sent to finish rolling was about 170°C lower compared with X70. Thus, on an average, precipitates in X70 spent longer times at elevated temperatures and had a greater chance for growth through diffusion. This might also have led to their larger sizes.

Table 7-8 Density and size of precipitates in X70 and X80.

	X70		X80	
	Density ( $\mu\text{m}^{-3}$ )	Average size	Density ( $\mu\text{m}^{-3}$ )	Average size
<b>Cuboidal TiN</b>	7	0.5 $\mu\text{m}$	9	0.15 $\mu\text{m}$
<b>Nb-rich irregular shaped</b>	20	30nm	37	50nm
<b>Nb(C,N) small, rounded</b>	2060	5nm	3420	15nm

### 7.6.3 Nb-rich Irregularly Shaped Precipitates (30-50nm)

This class of precipitates was mostly rounded and contained mainly Nb with smaller amounts of Ti. These were present throughout the ferritic grains in all the three grades of steels. Specific examples are shown in Figures 4-22, 5-18 and 6-15. The crystal structure was also NaCl-type; Nb and Ti are mutually soluble as are C and N. Many of the precipitates come out by the mechanism referred to as 'strain induced precipitation' [Collins83] [Deardo97] [Itman97]. When the plate is deformed in the 800-1000°C range, large numbers of dislocations and strain bands are created within the microstructure. These provide heterogeneous sites for nucleation of precipitates [DeArdo97][Nelson97]. In this temperature range, most of the Ti has already precipitated out of the solution and there is a strong driving force for Nb precipitation, as shown in Figure7-3 [Gladman97]. This accounts for the high Nb content relative to Ti. The large TiN particles also serve as nucleation sites, as shown for X80 (Figure 5-15) where rounded carbonitride particles have grown on existing TiN particles. The growth was epitaxial, as indicated by the accompanying diffraction pattern.

The nominal densities for these irregular shaped precipitates were measured for X70 and X80 steel using the carbon replicas. The precipitates were more numerous in X80 than in X70 (Table 7-8). This is to be expected, as Nb levels in X80 are higher, 0.09wt% vs. 0.067wt% for X70. Many Nb-rich particles precipitated epitaxially on the existing TiN cuboids. Others were spread randomly throughout the grains in the interior and at the grain boundaries. Many Nb-rich precipitates were seen clustered around the large cuboidal TiN particles in both X70 and X80.

#### **7.6.4 Small Spherical Precipitates (<20nm)**

These were present throughout the grains and were quite small (<20nm in most case). Most of these were in the 5-10nm range for X70 and closer to 15nm for X80 steel (Table 7-8). As with other precipitates, the structure was the NaCl-type and the EDX analysis indicated that they were either NbC or Nb carbonitrides. The presence of N was difficult to discern as the N peak in the EDX spectra was masked by the large C peak arising from the C support film. However, ring diffraction pattern obtained from a cluster of particles matched the NbC lattice parameter well. Molybdenum was also present in these precipitates, with a higher incidence in X80 and Grade 80, which can be attributed to their higher Mo levels. Molybdenum can partially substitute for the Nb in the precipitates forming (Nb,Mo)(C,N); however, Mo levels are likely not high enough to significantly affect the amount of precipitation hardening [Kanazawa67-1][Kanazawa67-2]. Mo<sub>2</sub>C can form in higher Mo steels (≥0.5wt%), but was not detected in the steels studied. Precipitation occurs during the austenite to ferrite transformation and can be attributed to the approximately order of magnitude drop in solubility across the  $\gamma/\alpha$  interface. The precipitates often appear as rows or sheets, which are proposed to form during ledge growth of ferrite [Batte73].

Table 7-8 shows the distribution and size of small (<20nm), spherical precipitates of the type Nb(C,N) for X70 and X80. Overall the precipitates were

larger and more numerous in the X80 steel than in the X70 steel. Quantitative measurements gave an average size around 15nm for X80 compared with about 5nm for X70 steel. The precipitate density was about one and a half times higher for X80 steel. The higher levels of Nb and Mo in X80 (compared with X70) should lower the  $\gamma \rightarrow \alpha$  transformation temperature and therefore decrease the particle size, which is contrary to experimental observation. This discrepancy can be attributed to the higher coiling temperature ( $\approx 40^\circ\text{C}$  higher) for the X80 steel, which might have resulted in precipitate coarsening. Indeed the precipitate density for the next higher size range of precipitates (Nb-rich irregularly shaped precipitates) is about 2 times higher for X80 steel as compared to X70 (Table 7-8). Also the population count for small, spherical precipitates might also have a contribution from the smallest sized precipitates.

The following orientation dependence was determined, assuming a NaCl type structure for the precipitates.

$[1-10]$  precipitate  $\parallel [012]$  ferrite and  $(110)$  precipitate  $\parallel (100)$  ferrite

#### **7.6.5 Very Small Precipitates (<5nm)**

In addition to the 4 major type of precipitates, some very small (<5nm) precipitates were detected in all three grades of steels. The precipitates form during the later stages of processing when the strip is being coiled at temperatures  $<600^\circ\text{C}$ . At this temperature virtually all the Ti has been depleted, and the Nb precipitates out with C and N by nucleating on dislocations and at the grain boundaries. Due to the extremely small size of these precipitates they were easily masked by the matrix and very difficult to image. These finely dispersed precipitates contribute to precipitation strengthening in these steels.

## **7.7 Mechanical Properties**

The yield strength rises gradually from X70 (545MPa) through X80(568MPa) to Grade80(587MPa) (Table 3-2). In contrast the toughness levels fall in the opposite direction. Whereas Grade80 has a Charpy impact energy of 75J LRD @RT (150J in TRD), the X70 is a very tough steel with Charpy energies around 375@RT. For X80 steel the strength and toughness values are intermediate, 568MPa YS and 235J@RT.

The lower impact toughness of Grade80 can be related to the matrix being composed primarily of bainitic ferrite and effect of long inclusions. The bainitic ferrite phase is harder than polygonal ferrite and contains higher density of dislocations. In these grades of microalloyed steels no cementite particles were observed due to low carbon contents and the carbon and nitrogen being tied up by Ti and Nb carbo-nitride precipitation. Still, large deformation at lower temperatures and particular processing schedules coupled with accelerated cooling ensure formation of large percentages of shear assisted products like acicular ferrite/low carbon bainite. These possess high dislocation densities and various kinds of Ti.Nb carbo-nitride precipitates. Compared to the other two grades, the Grade80 has the highest alloying content and a mostly bainitic ferrite matrix. This leads to its lower toughness values. In addition the presence of large numbers of elongated inclusions present in this steel are a major factor in its low Charpy values. However, all these factors which lead to drop in toughness are an important ingredient for strength, other than elongated inclusions or stringers. Consequently highest strength levels are observed in Grade80 (586-637MPa).

In the case of X70 steel, the matrix is a mix of acicular ferrite/bainitic ferrite (~90%) with polygonal ferrite along with retained austenite and MAC. The X70 steel has low sulfur levels, which is manifest as small, rounded inclusions distributed evenly throughout the matrix. The precipitates in X70 are very similar to those in X80 and Grade80. Although the precipitates have large effects on strength

and toughness, it is believed that the precipitate density being more or less similar, the dominant factor in causing large changes in toughness is the hardness of the matrix and inclusion distribution [Shehata86]. However, in exceptional cases, like that of Grade80, centerline segregation and presence of stringers also makes a significant contribution in lowering the toughness.

The X80 is steel is similar to X70 in many respects, however there are some differences. The matrix is more bainitic ferrite for X80, i.e., harder. This may be the dominant cause of lower toughness. X80 has more precipitates in the size range 20nm to 1.0 $\mu$ m which are larger than in X70. This can be attributed to higher alloying contents of X80 and its higher coiling temperature. These also marginally lower the toughness levels. Conversely the higher density of precipitates and more bainitic microstructure raise the strength levels for X80 up to 568MPa YS from 545MPa for X70. Increased Mn content is also believed by some researchers to lead to increased yield strength and finer grain size [Bhole91]. The inclusions in X80 are more numerous and finer when compared to X70, but the differences are marginal and no large contributions to differences in properties are implied. However they are an important contributing factor in the overall strength and toughness levels when a grade is considered individually.

## **Chapter 8: Conclusions**

X70, X80 and Grade80 microalloyed steels have been characterized in terms of constituent phases, distribution of alloying elements, inclusion compositions and morphologies of various kinds of precipitates present within the microstructure. All three kinds of steels had similar microstructural constituents; however, some differences were apparent. These could be traced back to difference in their chemical composition and their particular processing schedules.

### **Grain Structure**

- The matrix of all the steels was composed mainly of acicular ferrite/bainitic ferrite with small percentages of polygonal ferrite (~ up to 10%-20%).
- Grade80 steel had the highest content of acicular/bainitic ferrite, which can be attributed to the higher alloy content (Nb, Ti and Mo) and higher cooling rates of the plate after final rolling.
- X70 steel had the lowest amount of acicular/bainitic ferrite (~70%-80%) the rest being polygonal ferrite. The structure of X80 was somewhere between the X70 and Grade80 with a higher acicular ferrite content than Grade80.
- The acicular grains were highly deformed and irregular in shape and possessed high dislocation densities. Many small precipitates of NbC were observed nucleated on these dislocation networks.
- Distinction was made between acicular and bainitic ferrite. Acicular ferrite was irregularly shaped, highly dislocated, elongated grains with high aspect ratios (but lower than bainitic ferrite). Bainitic ferrite occurred as pockets of narrow (<0.5-0.7 $\mu$ m), parallel, lath-shaped grains with high aspect ratios and high dislocation densities.
- Many grains showed substructure with characteristic low angle grain boundaries between the subgrains.
- All three steels showed coarser microstructures near the centerline of the plate, as well as segregation effects.

- Segregation effects were most notable in Grade80 steel where centerline segregation in terms of retained austenite (RA), inclusions and TiN precipitates was most pronounced.
- For X70 steels the segregation was markedly high with large amounts of retained austenite at the centerline. However, this might be a sampling phenomenon varying across the length of the plate.
- Pockets of retained austenite existed between clusters of ferrite grains. These showed a KS-OR with the adjoining ferrite.

### **Inclusions**

- The inclusions in X70 were composed mainly of Ca and S. The inclusions were rounded, small and dispersed uniformly across the thickness of the plate.
- The inclusions in X80 contained significant amounts of Mn along with Ca and S. These were also rounded and small and dispersed across the thickness of the plate.
- The inclusions in X70 and X80 were not perfectly spherical but slightly distorted along the rolling direction and across the width of the plate. The distortion was slightly more pronounced for X70 steel.
- In Grade80 steel, many elongated inclusions (stringers) of MnS were observed near the centerline along with the CaS rounded inclusions. This was due to high levels of S (0.01wt%) in Grade80 as compared with the other two grades (<0.004wt%).

### **Precipitates**

- Five types of precipitates were identified in all the three kinds of steels:
  - 1) Very large (5-10 $\mu$ m) cuboidal TiN particles nucleated on CaS inclusions;
  - 2) Large (0.1-1.0 $\mu$ m) cuboidal TiN particles;
  - 3) Medium sized (30-50nm), irregularly shaped Nb-Ti carbonitrides;
  - 4) Fine (<20nm), rounded precipitates of Nb carbonitrides with traces of Mo;

**5) Finely dispersed precipitates, <5nm in size.**

- The type 1 precipitates formed during the casting or solidification process. Many were segregated to the centerline, which was the last liquid to solidify. This segregation was most apparent for Grade80 but present in both X70 and X80 to some extent.
- The type 2 precipitates come out of solution later, either when the steel is being cooled through the austenitic region after casting or after reheating.
- The third class of precipitates were Nb-rich. They come out through the 'strain induced precipitation' mechanism.
- The type 4 precipitates come out of the solution during the austenite to ferrite transformation and can be attributed to approximately order of magnitude drop in solubility across the  $\gamma/\alpha$  interface. The precipitates often appear as rows or sheets, which are proposed to form during ledge growth of ferrite.
- The last class of precipitates, <5nm, come out during coiling, at temperatures around 600°C. Many of these precipitate on the dislocation networks. These are the major contributors to secondary strengthening
- For X80 steel many of the larger TiN precipitates were observed with Nb rich carbonitrides precipitated epitaxially on them.
- The irregularly shaped Nb-rich precipitates were found to be more numerous in X80 when compared to X70. This may be because of higher levels of Nb in X80.
- The fine Nb carbonitrides (type 4) were found to be larger and less numerous in X80 steel when compared to X70. This may be due to growth and ripening in X80 which is coiled at approximately 40°C higher than X70.

**Mechanical Properties**

- The microalloyed steels derive their high strength from a combination of microstructural factors like fine, acicular and bainitic ferrite grains, high dislocation densities and small precipitates spread throughout the matrix.

- The strength of the steels can be directly correlated to the type of matrix present. Grade80 steel has the highest content of bainitic ferrite microstructure and consequently the highest yield strength.
- The factors leading to higher strength are detrimental to toughness. The toughness values of the steels decrease from X70 to Grade80 in direct opposition to their yield strengths. Grade80 steel with the most bainitic ferrite content has the lowest fracture toughness. In addition, the presence of MnS stringers at the centerline is a major contributor to lower toughness.
- Amongst X70 and X80 steels, X80 has the higher acicular/bainitic ferrite content and also the type 3 (medium sized irregularly shaped, 30-50nm) and type 4 (small spherical, <20nm) precipitates are larger and more numerous. This leads to a lower toughness when compared to X70.

## **Chapter 9: Future Work**

A basic framework for complete microstructural characterization has been laid out in this thesis. The microstructure was divided into three main categories, matrix, precipitates and inclusions. This provided the broad headings under which almost all the microstructural features were categorized. For each of the three different grades of steels a 'microstructural map' was developed which focused on larger microstructural features down to the smallest of the precipitates. After this foundation has been laid in this thesis, there are many improvements and developments possible in the study of the microstructure and their ultimate linking to the processing on one side and the resultant physical properties on the other. Some of these ideas are detailed below.

In this study, the various grades of steel were analyzed individually. However, it is also desirable to observe the same grade in various heats. This would give a good indication of the variations occurring within the same chemistry, but different processing conditions. This approach limits the permutations of a large number of factors influencing the microstructure of the final product by limiting the focus to fewer variables. Another possible recourse would be to perform dilatometric tests on these steels. This would allow the researcher to obtain specimens from any intermediate state of thermomechanical processing by arresting the processing sequence at that particular stage. However, caution has to be practiced as this is a simulation of the actual bulk processing and although it closely approximates the real process, there may be considerable variations.

For the present work, most of the samples were taken from the center of the width of the plate. This is the area where the bulk properties of the commercial product are specified. However, since welding is an integral part of the pipe forming processes, it is desirable to know if there are variations in the microstructure across the width of the plate, particularly near the edges, which may affect hardenability and toughness.

By observing the grain structure, the ferrite grains were identified as acicular or bainitic ferrite. These terms come from welding technology and higher carbon steels. In these (X70, X80 and Grade80), low carbon steels the classical basket-weave pattern (acicular ferrite) [Honeycombe96], or inter- or intra-lath carbides (upper and lower bainite) were not observed. Considerable confusion and ambiguity exists in the research community about the nomenclature of this phase (or morphology?). Attempts have been made to make a distinction by measuring the aspect ratio and thickness of the ferrite laths. The thinner, almost parallel laths, occurring in pockets and with higher aspect ratios could be classified as bainitic ferrite, while those with lower aspect ratios as acicular. Many researchers have proposed this approach, e.g., [Collins83]. Another differing characteristic might be the dislocation density in the ferrite, with the ferrite grains with higher densities classified as bainitic. In the present work, both kind of grains were observed possessing high dislocation densities and identified as such, although no quantitative measurements were performed. This might be one of the avenues to explore.

While characterizing the precipitates in these steels, it was observed that they were never pure carbides or nitrides but a combinatorial product (carbo-nitrides). The lattice parameter also varied with Ti and Nb as well as C and N composition. With the current instrumentation limits and sample preparation methods (most notably carbon replicas), it was not possible to ascertain the actual amounts of C and N through EDX or lattice measurements. Electron energy loss spectroscopy (EELS) can be employed to overcome this difficulty as it delineates the C and N peaks quite easily and unambiguously.

A 'pearlite-like' microstructural constituent was observed, but not conclusively identified, on etching with picral for long times. This inability in proper identification might be due to limitations of the techniques used. The SEM beam has a large interaction volume (even with a FEG SEM the results were inconclusive) therefore the signals from these small areas ( $<0.5\mu\text{m}$ ) are easily swamped by the

matrix. If site specific TEM sample could be made the region could be identified unambiguously.

Lastly, difficulties were encountered in analyzing the extremely small precipitates (<5nm). With better tools, like a field emission gun (FEG) TEM that has an extremely small probe size, it might be possible to study better their chemical composition through EDX.

## References

- [Almond79] Almond, EA; Mitchell, PS; Irani, RS; *Metal Technology*, Vol. 6, No. 6, June 1979, pp. 205-214.
- [Araki91] Araki, T; Enomoto, M; Shibata, K; *Tetsu-to-Hagane (Journal of the Iron and Steel Institute of Japan)* (Japan), Vol. 77, No. 10, Oct. 1991, pp. 1544-1550.
- [Aronson67] Aronson, AH; Strunck, SS; *Welding Journal*, Vol. 46, No. 6, June 1967, pp. 266S-269S.
- [Babu91] Babu, SS; Bhadeshia, HKDH; *Materials Transactions, JIM (Japan)*, Vol. 32, No. 8, Aug. 1991, pp. 679-688.
- [Banks79] Banks, TM; Gladman, T; *Metals Technology*, Vol. 6, No. 3, Mar. 1979, pp. 81-94.
- [Batte73] Batte, AD; Honeycombe, RWK; *Metal Science Journal*, No. 7, Sept. 1973, pp. 160-168.
- [Bhole91] Bhole, SD; Yu, H; *Canadian Metallurgical Quarterly*, Vol. 30, No. 1, Jan.-Mar. 1991, pp. 45-54.
- [Bittence78] Bittence, JC; *Materials Engineering*, Vol. 87, No. 5, May 1978, pp. 39-42.
- [Brownrigg73] Brownrigg, A; *Journal of Australian Institute of Metals*, Vol. 18, No. 3, Sept. 1973, pp. 124-136.
- [Canmet98] CANMET confidential report to IPSCO 'CCT diagrams', 1999.

- [Cochrane81] Cochrane, RC; Morrison, WB; *Metal Technology*, Vol. 8, No. 12, Dec. 1981, pp. 458-465.
- [Collins83] Collins, LE; Godden, MJ; Boyd, JD; *Canadian Metallurgical Quarterly*, Vol. 22, No. 2, Apr.-June 1983, pp. 169-179.
- [Collins85] Collins, LE; Knight, RF; Ruddle, GE; Boyd, JD; *Accelerated Cooling of Steel, Pittsburgh, Pennsylvania, USA, 19-21, Aug. 1985, The Metallurgical Society/AIME*, 1986, pp. 261-282.
- [Collins88] Collins, LE; Boyd, JD; Jockman, JA; Dignard-Bailey, L; Krishnadev, MR; Dionne, S; *Accelerated Cooling of Rolled Steel, Winnipeg, Canada, 24-25 Aug. 1987, Pergamon Press*, 1988, pp. 71-84
- [Collins95] Collins, LE; Baragar, DL; Bowker, JT; Kostic, MM; Subramanian, SV; *Microalloying '95*, 1995, pp. 141-147.
- [Collins98] Collins, LE; Materials for resource recovery and transport, International Symposium on Materials for Resource Recovery and Transport, Calgary, Alberta, Canada, August 16-19, 1998, *The metallurgical society of CIM*. 1998.
- [DeArdo88] DeArdo, AJ; *Cf.: Process Technology Conference Proceedings*, Vol. 8, Dearborn, Michigan, USA, Iron and Steel Society, Inc. (USA), 23-26 Oct. 1989, pp. 67-78.
- [DeArdo88-2] DeArdo, AJ; *Canadian Metallurgical Quarterly*, Vol. 27, No. 2, Apr.-June 1988, pp. 141-154.

- [DeArdo95] DeArdo, AJ; *ISIJ International (Japan)*, Vol. 35, No. 8, 1995, pp. 946-954.
- [DeArdo96] DeArdo, AJ; *Microstructural Science*, Vol. 24. 21-24 July 1996.
- [DeArdo97] DeArdo, AJ; *THERMEC 97: International Conference on Thermomechanical Processing of Steels and Other Materials, Wollongong, Australia, 7-11 July 1997, Minerals, Metals and Materials Society/AIME (USA)*, 6 x 9 in., Illustrated, July 1997, pp. 13-29.
- [Dogan88] Dogan, B; Collins, LE; Boyd, JD; *Metallurgical Transactions A*, Vol. 19A, No. 5, May 1988, pp. 1221-1234.
- [Feng89] Feng, B; Chandra, T; Dunne, DP; *Materials Forum*, Vol. 13, No. 2, Second Quarter 1989, pp. 139-146.
- [Feng90] Feng, B; Dunne, DP; Chandra, T; *Materials Forum*, Vol. 14, No. 4, Fourth Quarter 1990, pp. 264-269.
- [Gärtner92] Gartner, AW; Graf, MK; Hillenbrand, HG; *International Conference on Pipeline Reliability. Vol. I, Calgary, Alberta, Canada, 2-5 June 1992, Gulf Publishing Company (USA)*, 1992, pp. 15.
- [Gaugry85] Verger-Gaugry, J-L; Ocampo, G; Embury, JD; *Metallography*, Vol. 18, No. 4, Nov. 1985, pp. 381-393.
- [Gladman73] Gladman, T; Dulieu, D; *Metals Science*, No. 8, Jun. 1974, pp. 167-176.

- [Gladman92] Gladman, T; *Ironmaking and Steelmaking*, Vol. 19, No. 6, 1992, pp. 457--463.
- [Gladman97] Gladman T; *The Physical Metallurgy of Microalloyed Steels*, Institute of Materials, London, 1997.
- [Goetz77] Goetz, GJ; *Journal of Metals*, Vol. 29, No. 8, Aug. 1977, pp. 12-18.
- [Hanada86] Hanada, M; Takeda, H; Fukushima, H; Koizumi, I; Noguchi, Y; *Transaction of Iron Steel Institute of Japan*, Vol. 26, No. 5, May 1986, pp. 433-438.
- [Heritier84] Heritier, B; Maitrepierre, PH; Rofes-Vernis, J; Wyckaert, A; *Cf.: HSLA Steels, Technology and Applications*, Philadelphia, Pa., U.S.A., 3-6 Oct. 1983, American Society for Metals, 1984, pp. 981-989.
- [Hilty75-1] Hilty, DC; Farrell, JW; *Iron Steelmaker*, Vol. 2, No. 5, May 1975, pp. 17-22.
- [Hilty75-2] Hilty, DC; Farrell, JW; *Iron Steelmaker*, Vol. 2, No. 6, June 1975, pp. 20-27.
- [Hirsch82] Hirsch, YC; Parker, BA; *Metals Forum*, Vol. 5, No. 1, 1982, pp. 41-47.
- [Honeycombe96] Honeycombe, RWK; Bhadeshia, HKDH; *Steel: Microstructures and Properties*, London : Arnold, 1995.

- [Houghton93] Houghton, DC; *Acta Metallurgia et Materialia (USA)*, Vol. 41, No. 10, Oct. 1993, pp.2993-3006.
- [Itman97] Itman, A; Cardoso, KR; Kestenbach, H-J; *Materials Science and Technology*, Vol. 13, Jan 1997, pp. 49-55.
- [Juarez-Islas94] Juarez-Islas, JA; Perez, R; Albarran, JL; Flores, O; Martinez, L; *Materials Letters (Netherlands)*, Vol. 21, No. 2, 15 Oct. 1994, , pp. 197-202.
- [Kanazawa67-1] Kanazawa, S; NakaShima, A; Okamoto, K; Tanabe K and Nakazawa, S; *Transactions of the Japan Institute of Metals*, Vol. 8, 1967, pp. 105-112.
- [Kanazawa67-1] Kanazawa, S; NakaShima, A; Okamoto, K; Tanabe K and Nakazawa, S; *Transactions of the Japan Institute of Metals*, Vol. 8, pp. 113-120.
- [Kestenbach89] Kestenbach, H-J; Rodriguez, JA; Dermonde, JR; *Materials Science and Technology*, Vol. 5, No. 1, Jan. 1989, pp. 29-35.
- [Kim83] Kim, NJ; *Journal of Metals*, Vol. 35, No. 4, Apr. 1983, pp. 21-27.
- [Kniessl93] Kneissl, AC; Posch, G; Garcia, CI; DeArdo, AJ; *International Symposium on Low-Carbon Steels for the 90's, Pittsburgh, Pennsylvania, USA, 18-21 Oct. 1993, The Minerals, Metals & Materials Society (TMS) (USA)*, 1993, pp. 113-119.
- [Kostic96] Kostic, MM; Cf.: *International Pipeline Conference, ASME* 1996, pp. 203-207.

- [Kot-Bramfitt81] Kot, RA; Bramfitt, BL; Cf.: *Fundamentals of Dual-Phase Steels*, Chicago, Ill., Metallurgical Society/AIME, 23-24 Feb. 1981.
- [Kramer97] Kramer, S; Knepe, G; Rosenthal, D; *Iron and Steel Engineer (USA)*, Vol. 74, No. 7, July 1997, pp. 17-26.
- [Krishnadev75] Krishnadev, MR; Galibois, A; *Metallurgical Transactions A*, Jan. 1975, 6A, (1), pp. 222-224.
- [Kuziak95] Kuziak, R; Bold, T; Cheng, Y-W; *Journal of Materials Processing Technology (Switzerland)*, Vol. 53, No.1-2, 1 Aug. 95, pp. 255-262.
- [Lawson80] Lawson, RD; Matlock, DK; Krauss, G; *Metallography*, Vol. 13, No. 1, Feb. 1980, pp. 71-87.
- [Lehtinen89] Lehtinen, B; Hansson, P; *Scandinavian Journal of Metallurgy*, Vol. 18, No. 6, 1989, pp. 295-300.
- [Liu89] Liu, WJ; Jonas, JJ; *Metallurgical Transactions A*, Vol. 20A, No. 8, Aug. 1989, pp. 1361-1374.
- [Manohar96] Manohar, PA; Chandra, T; Killmore, CR; *ISIJ International (Japan)*, Vol. 36, No. 12, Dec. 1996, pp. 1486-1493.
- [Mangonon76] Mangonon, PL; *Metallurgical Transactions A*, Vol. 7A, No. 9, Sept. 1976, pp. 1389-1400.

- [Meyer96] Meyer, L; Muschenborn, W; Hulka, K; *Transactions of the Indian Institute of Metals (India)*, Vol. 49, No. 3, June 1996, pp. 231-244.
- [Mihelich74] Mihelich, JL; Smith, JH; *Metals Progress*, Vol. 105, No. 4, Apr. 1974, pp. 39-41.
- [Mishra98] Mishra, SK; Ranganathan, S; Das, SK; Das, S; *Scripta Materialia (USA)*, Vol. 39, No. 2, 12 June 1998, pp. 253-259.
- [Morrison95] Morrison, WB; *Ironmaking and Steelmaking*, Vol. 22, No. 6, 1995, pp. 453-458.
- [Nagae92] Nagae, M; Endo, S; Mifune, N; Uchitomi, N; Hirano, O; *NKK Technical Review*, No. 99, 1992, pp. 17-24.
- [Naylor89] Naylor, DJ; *Ironmaking Steelmaking*, Vol. 16, No. 4, 1989, pp. 246-252.
- [Nelson97] Nelson, DS; Zhang, F; Boyd, JD; *THERMEC 97: International Conference on Thermomechanical Processing of Steels and Other Materials, Wollongong, Australia, 7-11 July 1997, Minerals, Metals and Materials Society/AIME (USA)*, 6 x 9 in., Illustrated, July 1997, pp. 491-497.
- [Nicholson86] Nicholson, A; Gladman, T; *Ironmaking and Steelmaking*, Vol. 13, No. 2, 1986, pp. 53-69.
- [Paju89] Paju, M; Hougardy, HP; Grabke, HJ; *Scandinavian Journal of Metallurgy*, Vol. 18, No. 5, 1989, pp. 235-242.

- [Paju91] Paju, M; Grabke, HJ; Hougardy, HP; *Scandinavian Journal of Metallurgy*, Vol. 20, No. 2, 1991, pp. 135-140.
- [Penalba96] Penalba, F; Garcia de Andres, C; Carsi, M; Zapirain, F; *Journal of Materials Science (UK)*, Vol. 31, No. 14, 15 July 1996, pp. 3847-3852.
- [Pereloma96] Pereloma, EV; Boyd, JD; *Scripta Materialia (USA)*, Vol. 34, No. 5, 1 Mar. 1996, pp. 703-706.
- [Pereloma96-2] Pereloma, EV; Bayley, C; Boyd, JD; *Materials Science and Engineering A (Switzerland)*, Vol. 210, No. 1-2, 15 June 1996, pp. 16-24.
- [Pereloma96-3] Pereloma, EV; Boyd, JD; *Materials Science and Technology (UK)*, Vol. 12, No. 12, Dec. 1996, pp.1043-1051.
- [Pontremoli86] Pontremoli, M; Bufalini, P; Aprile, A; Jannone, C; *Metals Technology*, Vol. 11, Nov. 1984, pp. 504-514.
- [Purdy84] Purdy, GR; Hillert, M; *Acta Metallurgica*, Vol. 32, No. 6, June 1984, pp. 823-828
- [Read90] Read, S; Gibbs, RK; Parker, BA; *Materials Forum*, Vol. 14, No. 4, Fourth Quarter 1990, pp. 304-307.
- [Rothville78] Rothwell, AB; Gray, JM; *Cf.: Welding of HSLA (Microalloyed) Structural Steels*, Rome, Italy, 9-12 Nov. 1976, American Society for Metals, 1978.
- [Samuel84] Samuel, FH; *Z. Metallkd.*, vol. 75, no. 12, Dec. 1984, pp. 967-972.

- [Sage83] Sage, AM; *Metal Technology*, Vol. 10, No. 6, June 1983, pp. 224-233.
- [Saikaly99] Sakaly, W; Soto, R; Bano, X; Issartel, C; Rigaut, G; Charai, A; *The European Physical Journal, Applied Physics*, No. 6, 1999, pp. 243-250.
- [Sangal92] Sangal, S; Yannacopoulos, S; *Canadian Metallurgical Quarterly (Canada)*, Vol. 31, No. 1, Jan.-Mar. 1992, pp. 55-61.
- [Sellars84] Sellars, CM; Cf.: *Deformation, Processing and Structure*, St.Louis, Mo., U.S.A., 23-24 Oct 1982, American Society for Metals, 1984, pp. 245-277.
- [Shams86] Shams, N; *Journal of Metals*, Vol. 38, No. 5, May 1986, pp. 31-33.
- [Shehata82] Shehata, MT; Boyd, JD; Cf.: *Advances in the Physical Metallurgy and Applications of Steels*, Liverpool, England, 21-24 Sept. 1981, The Metals Society, 1982, pp. 229-236.
- [Shehata82-2] Shehata, MT; Boyd, JD; *Microstructural Science, Vol. 10, San Francisco, Calif., 19-22 July 1982*, 1982, Elsevier Science Publishing Co., Inc., pp. 229-237.
- [Shehata85] Shehata, MT; Moore, V; Parsons, DE; Boyd, JD; *American Society for Metals, Corrosion, Microstructure and Metallography. (Microstructural Science)*, Vol 12, 1985, pp. 329-344.
- [Shehata86] Shehata, MT; Boyd, JD; *Second International Symposium on the Effects and Control of Inclusions and Residuals in Steels*,

*Toronto, Canada, 17-20 Aug. 1986, 1986, The Metallurgical Society of CIM, pp. III.19-III.33.*

- [Smith88] Smith, RM; Dunne, DP; *Materials Forum*, Vol. 11, 1988, pp. 166-181.
- [Snape74] Snape, E; deBarbadillo, JJ; Sulfide inclusions in steel, 7-8 Nov. 1974, ASM Metals Park. 1975.
- [Spanos94] Spanos, G; *Metallurgical and Materials Transactions A*, Vol. 25A, No. 9, Sept. 1994, pp. 1967-1980.
- [Stuart83] Stuart, H; Jones, BL; *Journal of Metals*, Vol. 35, No. 4, Apr. 1983, pp. 17-20.
- [Thompson96] Thompson, SW; Krauss, G; Colvin, DJ; *Metallurgical and Materials Transactions A (USA)*, Vol. 27A, No. 6, June 1996, pp. 1554-1568.
- [Tiwary95] Tiwary, SK; Halder, A; Sarkar, S; Chattopodhyay, RN; Chatterjee, A; *Transactions of the Indian Institute of Metallurgy*, Vol. 48, No. 3, 1995, pp. 249-252.
- [Tominaga85] Tominaga, H; Watanabe, S; Minamiya, S; Toyooka, T; *Transactions of Iron Steel Institute of Japan.*, Vol. 25, No. 4, Apr. 1985, B-123.
- [Tsukada82] Tsukada, K et al.; *Nippon Kokan Tech. Rep. (Overseas)*, No.35, Oct. 1982, pp. 24-34.

- [Wellner81] Wellner, P; Walser, B; *Cf.: Microstructural Science, Vol. 9. 13th Annual Technical Meeting, International Metallographic Society, Brighton, England, 18-22 Aug. 1980, Elsevier North-Holland, Inc., 1981, pp. 185-191.*
- [Zhou96] Zhou, C; Priestner, R; *ISIJ International (Japan), Vol. 36, No. 11, Nov. 1996, pp. 1397-1405.*
- [Zou91] Zou, H; Kirkaldy, JS; *Metallurgical Transactions A, Vol. 22A, No. 7, July 1991, pp. 1511-1524.*

# Appendix A Selected X-ray diffraction data for Fe( $\alpha$ ), Fe( $\gamma$ ), TiC, TiN, NbC and NbN

06-0696:	QM:Star	d:	I:Diffractionmeter						
Iron, syn Fe				Gray, light gray metallic. Total impurities of sample <0.0013% each metals and non-metals. X-ray pattern at 25 C. Occurs as terrestrial "iron" and in meteorites as "Kamacite". The iron used was an exceptionally pure rolled sheet prepared at the NBS [Moore, G., ITJ. Met., \RG, \BPS\RG 1443 (1953)]. It was annealed in an \H2\ atmosphere for 3 days at 1100 C and slowly cooled in a He atmosphere. a=2.8587 at -194 C to 2.8993 at 800 C. SGA-Fe (bcc)-(-910 C) SGG-Fe (fcc)=(1390 C) SGD-Fe (bcc). Opaque mineral optical data on specimen from Meteorite: RR#2R#e= 57.7, Diap.=16, VHN=158 (mean at 100, 200, 300), Color values=.311, .316, 57.9, Ref.: IMA Commission on Ore Microscopy QDP.					
Radiation : CuK $\alpha$ Calibration: Ref: Swanson et al. Natl. Bur. Stand. (U.S.), Circ. 539, 4 3 (1955)	Lambda: 1.5405 d-CutOff:	Filter: Ni I/Ic(RIR):							
System: Cubic(Powder Diffraction) Cell Parameters= 2.866 2.866 2.866 90.00 90.00 90.00 Ref: Ibid.	S.G.: Im3m (229) Z= 2 mp=								
Dx= 7.875 Dm=	Mwt= 55.85	Vol(RC)= 11.78	F(6)=225.2(.0044,6)						
ea=	nwb=	ey=	Sign:	2V=					
Ref:									
6 Reflections. Radiation: CU_1.540598. Strong Lines: 2.03/\X 1.17/3 1.43/2 0.91/1 1.01/1 0.83/1 0.00/1 0.00/1 0.00/1									
#	d(A)	I(fix)	I(var)	h	k	l	2-Theta	Theta	1/(2d)
1>	2.0268	100	100	1	1	0	44.674	22.337	0.24669
2>	1.4332	20	28	2	0	0	65.023	32.511	0.34887
3>	1.1702	30	52	2	1	1	82.335	41.168	0.42728

## Appendix A

### Selected X-ray diffraction data for Fe( $\alpha$ ), Fe( $\gamma$ ), TiC, TiN, NbC and NbN

31-0619: QM:Doubtful Quality		d: I:Film-Visual Estimate								
Iron ( Fe , C )										
Radiation : CoKa		Lambda: 1.7902	Filter:							
Calibration:		d-CutOff:	I/Ic(RIR):							
Ref: Goldschmidt. Metallurgia, 40 103 (1949)										
System: Cubic(Powder Diffraction)		S.G.: Fm3m (225)	Z= 0.39							
Cell Parameters=		3.600 3.600 3.600	90.00 90.00 90.00							
Ref: Ibid.			mp=							
Dx= 7.730 Dm=		Mwt= 562.67	Vol(RC)= 11.66							
F(6)=5.5(0.181,6)										
ea=		nwb=	ey=							
Ref:		Sign:	2V=							
6 Reflections. Radiation: CU_1.540598. Strong Lines: 2.08/X 1.80/8 1.27/5 1.08/8 1.04/5 0.90/3 0.00/1 0.00/1 0.00/1										
#	d(A)	I(fix)	I(var)	h	k	l	2-Theta	Theta	1/(2d)	1/(2d)
1>	2.0800	100	65	1	1	1	43.473	21.736	0.24038	4> 1.0830 80 100 3 1 1 90.676 45.338 0.46168
2>	1.8000	80	60	2	0	0	50.674	25.337	0.27778	5> 1.0370 50 65 2 2 2 95.944 47.972 0.48216
3>	1.2700	50	53	2	2	0	74.679	37.339	0.39370	6> 0.9000 30 45 4 0 0 117.716 58.858 0.55556

## Appendix A

### Selected X-ray diffraction data for Fe( $\alpha$ ), Fe( $\gamma$ ), TiC, TiN, NbC and NbN

32-1383:	QM:Star	d:	I:Diffractionmeter																
Kharabaevite, syn				Dark gray. The sample was obtained from Kennametal, Latrobe, Pennsylvania, USA. Pattern at 25 C. To replace 6-614 and 31-1400.															
Ti C																			
Radiation : CuK $\alpha$ Lambda: 1.540598 Filter:																			
Calibration: Internal (W) d-CutOff: I/Ic(RIR):																			
Ref: Natl. Bur. Stand. (U.S.) Monogr. 25, 18 73 (1981)																			
System: Cubic (Powder Diffraction) S.G.: Fm3m (225) Z= 4																			
Cell Parameters= 4.327 4.327 4.327 90.00 90.00 90.00 mp=																			
Ref: Ibid.																			
Dx= 4.911 Dm= Mwt= 59.91 Vol (RC)= 20.26 F(10)=97.5 (.0103,10)																			
ee= nwB= ey= Sign: 2V=																			
Ref:																			
10 Reflections. Radiation: Cu $_{1.540598}$ . Strong Lines: 2.16/ $\lambda$ 2.50/8 1.53/6 1.30/3 0.97/3 0.88/3 1.25/2 0.83/2 0.99/1																			
#	d(A)	I(fix)	I(var)	h	k	l	2-Theta	Theta	1/(2d)	#	d(A)	I(fix)	I(var)	h	k	l	2-Theta	Theta	1/(2d)
1>	2.4990	80	69	1	1	1	35.907	17.953	0.20008	6>	1.0818	10	20	4	0	0	90.804	45.402	0.46219
2>	2.1637	100	100	2	0	0	41.711	20.855	0.23109	7>	0.9927	13	28	3	3	1	101.785	50.892	0.50368
3>	1.5302	60	84	2	2	0	60.450	30.225	0.32675	8>	0.9677	25	55	4	2	0	105.502	52.751	0.51669
4>	1.3047	30	49	3	1	1	72.371	36.186	0.38323	9>	0.8834	25	61	4	2	2	121.377	60.688	0.56599
5>	1.2492	17	29	2	2	2	76.141	38.071	0.40026	10>	0.8327	16	41	5	1	1	135.355	67.678	0.60046

## Appendix A

### Selected X-ray diffraction data for Fe( $\alpha$ ), Fe( $\gamma$ ), TiC, TiN, NbC and NbN

38-1420:	QM:Star	d:Diffractionmeter	I:Diffractionmeter	The sample was obtained from City Chemical Corporation, New York, USA. The structure was determined by Christensen (1). Dark greenish brown. The mean temperature of data collection was 26.2 C. To replace 6-642 (2). No impurity found by SEM with Energy Dispersive Spectrometer (EDS).															
Osbornite, syn																			
Ti N																			
Radiation : CuK $\alpha$				Lambda: 1.5405981															
Calibration: Internal (Si)				Filter: Graph															
Ref: Wong-Ng, W., McMurdie, H., Paretzskin, B., Hubbard, C., Dragoo, A., NBS (USA)				d-CutOff: 17.7 I/Ic(RIR):															
ICDD Grant-in-Aid (1987)																			
System: Cubic (Powder Diffraction)				S.G.: Fm3m (225)															
Cell Parameters=				Z= 4															
Ref: Hubbard, C., Dragoo, A.H., Paretzskin, B.,				mp=															
Powder Diffraction, 2 200 (1987)																			
Dx= 5.388 Dm=				Vol(RC)= 19.08 F(10)=176.2 (.0057,10)															
Mwt= 61.91																			
ea=				Sign:															
Ref:				2V=															
10 Reflections.				Strong Lines: 2.12/X 2.45/7 1.50/5 1.28/2 0.95/1 1.22/1 0.87/1 0.82/1 0.97/1															
Radiation: CU 1.540598.																			
#	d(A)	I(fix)	I(var)	h	k	l	2-Theta	Theta	1/(2d)	#	d(A)	I(fix)	I(var)	h	k	l	2-Theta	Theta	1/(2d)
1>	2.4492	72	62	1	1	1	36.663	18.331	0.20415	6>	1.0604	5	10	4	0	0	93.172	46.586	0.47151
2>	2.1207	100	100	2	0	0	42.597	21.299	0.23577	7>	0.9730	6	13	3	3	1	104.677	52.339	0.51385
3>	1.4997	45	63	2	2	0	61.814	30.907	0.33341	8>	0.9485	14	31	4	2	0	108.611	54.306	0.52716
4>	1.2789	19	31	3	1	1	74.070	37.035	0.39095	9>	0.8658	12	29	4	2	2	125.678	62.839	0.57752
5>	1.2245	12	20	2	2	2	77.964	38.982	0.40833	10>	0.8164	7	18	5	1	1	141.320	70.660	0.61247

## Appendix A

### Selected X-ray diffraction data for Fe( $\alpha$ ), Fe( $\gamma$ ), TiC, TiN, NbC and NbN

30-1364;	QM:Star	d:Diffractionmeter	I:Diffractionmeter	The mean temperature of the data collection was 25.5 C. The structure of NbC was determined by Rudy et al. (1). The sample was from Alfa Products, Danvers, Massachusetts, USA. To replace 10-181 (Private Communication). Black.															
Niobium Carbide				Spectroscopic analysis indicated impurities of Ta 0.02%, Ti 0.01%, and Fe 0.07%.															
Nb C																			
Radiation : CuK $\alpha$				Lambda: 1.5405981				Filter: Graph											
Calibration: Internal (Si)				d-Cutoff: 17.7				I/Ic(RIR):											
Ref: Wong-Mg, W., McMurdie, H., Paretzkin, B., Hubbard, C., Dragoo, A., NBS (USA)																			
ICDD Grant-in-Aid (1986)																			
System: Cubic (Powder Diffraction)				S.G.: Fm3m (225)				Z= 4											
Cell Parameters=				4.470 4.470 4.470 90.00 90.00 90.00				mp=											
Ref: Hubbard, C., Dragoo, A.H., Paretzkin, B.,																			
Powder Diffraction, 3 55 (1988)																			
Dx= 7.804 Dm=				Wt= 104.92				Vol(RC)= 22.33				F(10)=139.5 (.0072,10)							
ea=				nb=				ey=				Sign: 2V=							
Ref:																			
10 Reflections.				Radiation: CU_1.540598. Strong Lines: 2.58/X 2.24/8 1.58/4 1.35/3 1.00/1 1.29/1 1.03/1 0.91/1 0.86/1															
#	d(A)	I (fix)	I (var)	h	k	l	2-Theta	Theta	1/(2d)	#	d(A)	I (fix)	I (var)	h	k	l	2-Theta	Theta	1/(2d)
1>	2.5809	100	100	1	1	1	34.731	17.365	0.19373	6>	1.1176	5	11	4	0	0	87.342	43.571	0.44739
2>	2.2352	80	92	2	0	0	10.317	20.159	0.22369	7>	1.0253	7	17	3	3	1	97.405	48.702	0.48766
3>	1.5804	35	57	2	2	0	58.339	29.170	0.31637	8>	0.9994	10	25	4	2	0	100.844	50.422	0.50030
4>	1.3477	26	49	3	1	1	69.720	34.860	0.37101	9>	0.9124	7	19	4	2	2	115.183	57.591	0.54800
5>	1.2903	9	18	2	2	2	73.308	36.654	0.38750	10>	0.8603	6	18	5	1	1	127.127	63.563	0.58122

## Appendix A

### Selected X-ray diffraction data for Fe( $\alpha$ ), Fe( $\gamma$ ), TiC, TiN, NbC and NbN

38-1155: QM:Not Indexed d:Calculated I:Calculated				Light yellow. Sublattice occupancy (t): Nb 97, N 97. All data were yielded by extrapolation of experimental values to N/Nb=1.000.															
Niobium Nitride Nb M1.000																			
Radiation : CuK $\alpha$ Lambda: 1.54056 Filter: Calibration: External(Si) d-Offset: I/Ic(RIR): Ref: Lengauer, W., Tech. Univ. of Vienna, Inst. for Chem. Tech. of Inorg. Mater. Private Communication (1986)																			
System: Cubic() Cell Parameters= 4.393 4.393 4.393 90.00 90.00 90.00 S.G.: Fm3m (225) Z= 4 Ref: Lengauer, W., Ettmayer, P. mp= Monatsh. Chem., 117 275 (1986) Dx= 8.378 Dm= 8.153 Mwt= 106.91 Vol(RC)= 21.19 F(10)=31.7(0.032,10)																			
ea=		nvB=		ay=		Sign:		2V=											
Ref:																			
11 Reflections. Radiation: CU 1.540598. Strong Lines: 2.54/ $\lambda$ 2.20/9 1.55/5 0.78/6 1.32/4 0.85/4 0.90/3 0.98/3 1.01/2																			
#	d(A)	I(fix)	I(var)	h	k	l	2-Theta	Theta	1/(2d)	#	d(A)	I(fix)	I(var)	h	k	l	2-Theta	Theta	1/(2d)
1>	2.5360	100	48	1	1	1	35.365	17.683	0.19716	7>	1.0080	21	25	3	3	1	99.669	49.835	0.49603
2>	2.1960	86	48	2	0	0	41.069	20.535	0.22769	8>	0.9820	30	37	4	2	0	103.334	51.667	0.50916
3>	1.5530	54	42	2	2	0	59.472	29.736	0.32196	9>	0.8970	32	44	4	2	2	118.353	59.177	0.55741
4>	1.3240	41	38	3	1	1	71.154	35.577	0.37764	10>	0.8450	36	52	5	1	1	131.454	65.727	0.59172
5>	1.2680	18	17	2	2	2	74.817	37.408	0.39432	11>	0.7770	63	100	0	0	0	164.939	82.470	0.64350
6>	1.0980	9	10	4	0	0	89.103	44.551	0.45537										